Local structure characterization of amorphous and nanoscale systems using X-ray Absorption Spectroscopy (XAS)

Yuanpeng Zhang

Supervisor: Dr. Andrei V. Sapelkin

Advisor: Prof. Martin T. Dove

School of Physics and Astronomy
Queen Mary, University of London

This dissertation is submitted for the degree of
Doctor of Philosophy

Queen Mary September 2016

To my loving parents . . .

Declaration

I certify that this work contains no material which ahs been accepted for the award of any other degree or diploma in my name, in any university or other tertiary institution and, to the best of my knowledge and belief, contains no material previously published or written by another person, except where due reference has been made in the text. In addition, I certify that no part of this work will, in the future, be used in a submission in my name, for any other degree or diploma in any university or other tertiary institution withour prior approval of Queen Mary, University of London and where applicable, any partner institution responsible for the joint-award of this degree.

I give consent to this copy of my thesis, when deposited in the University Library, being made available for loan and photocopying, subject to the provisions of the Copyright Act 1988.

I also give permissions for digital version of my thesis to be made available on the web, via the University's digital research repository, the Library Search and also through web search engine, unless permission has been granted by the University to restrict access for a period of time.

Name: Yuanpeng Zhang

Signature: _____

Date: 08/23/2016

Acknowledgements

First of all, I would like to show the greatest thanks to my dear parents. Their cares and support have been always togethter with me.

I would like to show my thanks and respect to my primary supervisor – Dr. Andrei V. Sapelkin, who opens the door of the research world for me and guides me to learn the X-ray absorption spectroscopy. We had many fruitful discussions about both the research topics and general condensed matter physics. Especially, I was impressive with his introduction to the synchrotron radiation facilities (which I never got in touch with before Ph.D.) and his own old experience at synchrotron radiation, when we were at Diamond Light Source for experiments. Those days were interesting and unforgetable when we did measurements together at the beamline days and nights.

I would like to specially thank Ali Karatutlu and Osman Ersoy from our group. Without the samples prepared by them, all the data analysis and simulation work given in this thesis have nowhere to base. I also want to thank William Little from our group for the Matlab code for the Raman spectra analysis. N. R. Corsini should also be acknowledged for his work on DFT calculation for Ge quantum dots under high pressure.

I highly appreciate the help and support for the research on amorphous modelling and molecular dynamics simulation from Prof. Martin T. Dove (my second supervisor) and Anthony Phillips. Besides, I learned a lot from Martin about general aspects of doing research, such as writing, presentation, and among others. I also enjoy the coffee time every morning in our physics museum proposed by Martin. I like the atmosphere people talking about everything from social life to science in a relaxed way during the coffee time. And also, that was indeed a good chance for me to promote my English communication skill.

I would like to thank all the beamlines scientists and staff, including Ginnantonio Cibin, Diego Gianolio, Andy Dent and all the others whose names are not given here, for all

the support they provided for our experiments at Diamond Light Source. I also want to acknowledge the sponsor of my Ph. D. study – China Scholarship Council (CSC).

Finally, I want to give my special thanks to a special person, a girl who has been accompanying me through most of the time during last three years. When we were together, everytime I came across difficulty she would always be by my side and comfort me. Because of her, the life abroad away from home has never been lonely.

Abstract

X-ray absorption spectroscopy (XAS) was used as the main technique to explore the local structure of Ge quantum dots (QDs) systems. The extended X-ray absorption fine structure (EXAFS), together with several other techniques, such as transmission electron microscopy (TEM), Raman and X-ray diffraction (XRD), was used to examine both the long range order and local structural information, including the bond length and angle distribution, static and dynamic disorder (Debye-Waller factor). For colloidally prepared matrix-free Ge QDs (2-5 nm), it was found that as-prepared samples are best described by a core-shell model with a small nano-crystalline core and an amorphous outer layer terminated either with oxygen or hydrogen depending on the synthesis route (with different reduction precursor). Furthermore, a combination of EXAFS, photoluminescence and Raman spectroscopy together with *ab initio* simulations were employed to look into the remarkable behaviour of the matrix-free Ge QDs under hydrostatic compression. It was found that the phase behaviour of small Ge QDs under high pressure is drastically different from both larger nanoparticles and bulk Ge. We discovered that the application of pressure drives surface-induced amorphization leading to Ge-Ge bond over-compression and eventually to a polyamorphic semiconductor-to-metal transformation.

To further extend the applicability of EXAFS to highly disordered systems, a Fortran package combining molecular dynamics (MD) simulation and FEFF calculation (for EXAFS spectra simulation) was developed. Using this package, the initial input model was evolved using an MD simulation to take into account of the thermal effect. The generated model from MD was loaded into FEFF. The EXAFS spectra were then calculated and compared to the experimental data. The combined simulation was then applied to the Ge QDs system, for which a WWW code and its revised version were used to generate the theoretical amorphous and the aforementioned core-shell models, respectively. It was found that the result from the combined MD-FEFF approach is consistent with the proposed core-shell model for the structure and morphology of the matrix-free Ge QDs.

The near-edge portion of the XAS spectra, i.e. the X-ray absorption near-edge structure (XANES, extends to around 50 eV above the absorption edge) is known to be very sensitive to medium-range order and electronic properties of materials. Such sensitivity was utilized to investigate the local symmetry of Ge QDs system. The FDMNES package was used to calculate the theoretical XANES spectra that were compared with the experimental data. Such approach was applied to the matrix-free Ge QDs system. It was found that XANES data for as-prepared Ge QDs can only be adequately described if the second coordination shell of the diamond-type structural model is included in the FDMNES calculations. This is in contrast to the EXAFS data that show only the first-shell signal. These results suggest that the as-prepared small Ge quantum dots retain their diamond-type symmetry beyond the first shell. Furthermore, we utilized this sensitivity of XANES to local symmetry to study annealed Ge quantum dots and found evidence for significant structural distortion which we attribute to the existence of surface disorder in the annealed oxygen-free Ge quantum dots. In addition, by utilizing the optically detected XAS (ODXAS) we obtained structural data correlated to light emission signals and thus have been able to link light emission with the atomic-level structure. For the oxygen-terminated Ge QDs, it was found that it is the oxide-rich regions that play a key role in the light emission. In oxygen-free samples we found that pure Ge regions contribute to the light emission. Detailed OD-XANES analysis shows a similar result to the transmission-detected XANES, which indicates the retaining of diamond-type local symmetry extending to the second coordination shell.

Publication list

Y. P. Zhang, O. Ersoy, A. Karatutlu and A. Sapelkin. Local structure of amorphous and nanoscale systems by numerical XANES analysis, *J. Non-Cryst. Solids*, 2015. DOI: 10.1016/j.jnoncrysol.2016.07.001

A. Karatutlu, W. Little, O. Ersoy, **Y. P. Zhang**, I. Seker and A. Sapelkin. Laser-induced particle size tuning and structural transformations in germanium nanoparticles prepared by stain etching and colloidal synthesis route, *J. Appl. Phys.*, 2015, **118**, 244303.

Y. P. Zhang, O. Ersoy, A. Karatutlu, W. Little and A. Sapelkin. Local structure of Ge quantum dots determined by combined numerical analysis of EXAFS and XANES data, *J. Synchrotron Radit.*, 2015, **23**, 253-259.

N. R. C. Corsini, **Y. P. Zhang**, W. R. Little, A. Karatutlu, O. Ersoy, P. D. Haynes, C. Molteni, N. D. M. Hine, I. Hernandez, J. Gonzaiez, F. Rodriguez, V. V. Brazhkin and A. Sapelkin. Pressure-induced amorphization and a new high density amorphous metallic phase in matrix-free Ge nanoparticles, *Nano Lett.*, 2015, **15**, 7334-7340.

M. Y. Song, A. Karatutlu, O. Ersoy, Y. Zhou, Y. X. Yang, **Y. P. Zhang**, W. R. Little, A. P. Wheeler and A. V. Sapelkin. Spectroscopic super-resolution fluorescence cell imaging using ultra-small Ge quantum dots, *arXiv:1503.09151*, 2015.

A. Karatutlu, M. Song, A. P. Wheeler, O. Ersoy, W. R. Little, **Y. P. Zhang, et al.**, P. Puech, F. S. Boi, Z. Luklinska and A. V. Saplekin. Synthesis and structure of free-standing germanium quantum dots and their application in live cell imaging, *RSC Adv.*, 2015, **5**, 20566-20573.

Y. P. Zhang, A. Karatutlu, O. Ersoy, W. Little, G. Cibin, A. Dent, and A. Sapelkin. Structure and effects of annealing in colloidal matrix-free Ge quantum dots, *J. Synchrotron Radit.*, 2015, **22**, 105-112.

Table of contents

List of figures xi

List of tables xviii

Nomenclature xix

1 Introduction 1

1.1 Nanomaterials . . . 1

1.2 Quantum dots . . . 3

1.2.1 Quantum confinement effect . . . 4

1.2.2 Group IV quantum dots . . . 8

1.3 Structure characterization for QDs system . . . 9

1.4 XAS for structure characterization . . . 12

References . . . 15

2 Synchrotron radiation and XAS 26

2.1 Overview of synchrotron radiation . . . 26

2.2 A brief history of XAS . . . 28

2.3 The application of XAS . . . 30

References . . . 32

3 XAS techniques 36

3.1 Fundamentals of XAS . . . 36

3.2 XAS spectra measurement . . . 40

3.2.1 Transmission mode . . . 41

3.2.2 Fluorescence mode . . . 42

3.2.3 Optical detection mode . . . 44

3.3 The EXAFS formulation . . . 45

3.4 EXAFS data analysis . . . 51

3.4.1 Background subtraction and normalization 51
3.4.2 Spectra fitting 54
3.4.3 EXAFS analysis beyond Athena and Artemis 64
3.5 Introduction to XANES 65
References 70

4 XANES theoretical calculation 74
4.1 Finite difference method (FDM) for XANES 75
4.2 Challenges and advances in XANES calculation 79
References 81

5 Structure of colloidal matrix-free Ge quantum dots 83
5.1 Experiment 83
5.1.1 Synthesis 83
5.1.2 Characterization 84
5.2 Results and Discussion 85
5.3 Conclusions 92
References 94

6 Phase transition of matrix-free Ge quantum dots under hydrostatic compression 96
6.1 Methodology 97
6.2 Results and Discussion 98
6.3 Conclusion 102
References 103

7 MD+FEFF simulation for Ge QDs 105
7.1 Methodology 106
7.2 Results and Discussion 108
7.3 Conclusion 114
References 116

8 Local structure of bulk amorphous GaSb and Ge quantum dots by XANES 117
8.1 Experiment and Calculation 118
8.2 Bulk aGaSb as the reference system 118
8.3 Local symmetry in matrix-free Ge QDs 120
8.4 Structural origins of PL in Ge QDs by OD-XANES 124

8.5 Conclusion 127
References 128

9 Conclusion and Future work **130**
9.1 Summary 130
9.2 Future work 132
References 133

Appendix A Nyquist-Shannon theorem **134**
References 138

Appendix B Multiple scattering theory **139**
B.1 Quantum scattering theory 139
B.1.1 Lippmann-Schwinger equation 139
B.1.2 Scattering amplitude 141
B.1.3 Born approximation 142
B.1.4 Partial-wave expansion 144
B.1.5 Phase shift 146
B.2 Scattering theory in FEFF 148
B.2.1 Basic theoretical formulation 148
B.2.2 Scattering potential in FEFF 153
B.2.3 Determination of Phase shift, amplitude factor and EMFP 154
References 156

Appendix C Green's function method **157**
References 163

Appendix D Finite difference method **164**
References 170

Appendix E MD2FEFF Codes **171**
References 174

List of figures

1.1 Photograph showing the color changing of Lycurgus cup as light is shine through from internally. Reproduced from Ref. [2]. 2

1.2 Density of states in one band of semiconductor as a function of dimension [40]. 5

1.3 The discretization of energy levels and the size dependence of the band-gap in Ge QDs. The blue dotted line indicate the band-gap in bulk Ge [44]. 6

1.4 (a) Optical absorption spectra for CdSe QDs with different sizes [47]. (b) Size-tunable light emission from CdSe QDs [48]. 7

1.5 The unit cell of Ge (a) diamond, (b) BC8 and (c) ST12 phase. For each structure, the rings formed by the local atoms are labelled out. 9

1.6 Powder XRD patterns of Ge QDs produced by conventional heating method (with various heating temperature) compared to Ge reference pattern [72]. . . . 10

1.7 Calculated total and partial X-ray PDFs for $PbVO_3$, showing the overlapping of PDF peaks. Source from Ref. [79]. 11

2.1 The comparison of X-ray source brilliance between the synchrotron and Bremsstrahlung radiation [2]. 27

2.2 The first Fourier transform pattern of the EXAFS spectra, for crystalline and amorphous Ge [11]. 29

3.1 Depiction of photon absorption. 37

3.2 An example of XAFS spectra. The two shaded regions (with different color) indicates the XANES and EXAFS regime, respectively. The inset energy diagram illustrates the transition corresponding to different absorption edges. The black-white strip shown at the bottom is an example for the absorption spectra recorded on the photographic film, which shows the white line corresponding to the absorption edge. 38

3.3 (a) Example XAFS spectra of crystalline GaSb with background absorption. (b) Normalized spectra together with the background signal. (c) Spectra in k-space. (d) Fourier transform of the spectra. 39

3.4 The illustration of the transmission detection mode for XAS measurement. . . . 41

3.5 (a) The energy diagram showing the decay of photoelectron through fluorescence. (b) Illustration for the fluorescence measurement, showing the incident (θ) and exit (ϕ) angle. Reproduced from Ref. [1]. 42

3.6 The illustration for optically detected XAS signal collection. 45

3.7 The illustration for the system disorder. The solid dot refers to the atomic equilibrium position. The arrows indicates the disorder of the system, and the open dot refers to the dynamic position of atoms. 48

3.8 (a) Athena data importing window. (b) Athena main window 51

3.9 The comparison of plot options in k- (left) and R-space (right). 54

3.10 The Artemis window. 55

3.11 The Fourier transform (red) of square window function (blue) with different width. The Fourier transform of broad window function is closer to δ-function, which will bring in less artificial effect when convoluted with the Fourier transform of the experimental data – Imagine the window with infinite width – The Fourier transform will give δ-function which brings in no artificial effect at all. 57

3.12 The combined MD and RMC approach for EXAFS data analysis. Reproduced from Ref. [29]. 65

3.13 The (A) pre-edge, (B) edge and (C) post-edge regions of the XANES spectra. The overall arctan background function is also shown. The inset figures shows the background subtraction specifically for the pre-edge region for further analysis [33]. 66

3.14 Cr K-edge XANES for Cr^{3+} and Cr^{6+} oxides [1]. 66

3.15 The photoelectron MFP $\lambda(k)$ [1]. 67

3.16 Ti K-edge XANES spectra for various Ti oxide compounds with (a) fourfold, (b) fivefold and (c) sixfold coordinated Ti [36]. 68

3.17 (a) Examples of curve fits for mineral phases containing Fe^{2+} and Fe^{3+} [33]. (b) The XANES spectra of Au nanoclusters embedded in silica matrix, compared with the simulated spectra of a 13-atom cluster in SiO_2 and under vacuum [37]. 69

4.1 The illustration for the division of the calculation cluster to three zones in FDMNES. The small circle (zone-1) represents the region surround the atomic ion core where the potential is assumed to be spherically symmetric. Outside the small circle (zone-2), it is where the FDM was used to solve the Schrödinger equation on the grid points. Outside the big circle (zone-3), the potential is assumed to be constant (flat). Here it should be pointed out that the solid and open dots refer to the grid points but not the atoms [6]. 76

5.1 (a,b) TEM and size distribution of CS1 as-prepared sample; (c,d) TEM and size distribution of CS2 as-prepared sample; (e,f) Raman spectrum for CS1 and CS2 as-prepared samples, respectively. 85

5.2 Background-subtracted PXRD patterns (X-ray energy = 8047 eV) for all as-prepared and annealed CS1 (a – c) and CS2 (d – f)samples; reference for diamond-type Ge (JCPDS No. 4-545) is shown as blue marks at the bottom. 'Hex' in the sample name means a suspension in hexane; 'Ar' means synthesis with Ar gas protection and 'H2Ar' for a mixture of H_2 and Ar. The inset image is scanning electron microscope (SEM) image for CS1 annealed 600. 86

5.3 Comparison if CS2 as-prepared sample PXRD pattern with Ge related phase: (a) diamond, (b) mC16, (c) BC8, (d) ST12. Gaps in the original data are due to dead areas between XRD detector segments. 88

5.4 (a,b) EXAFS fitting result for CS1 Hex Ar and CS1 Hex H_2Ar, respectively; (c,d) EXAFS fitting result for CS1 Ar annealed 450 and CS1 Ar annealed 600, respectively. 89

5.5 (a,b) EXAFS fitting result for CS2 Hex Ar, CS2 Hex H_2Ar, respectively; (c) EXAFS fitting result for CS2 annealed 450. (d) The unit cell of diamond Ge. . 90

5.6 Five general possibilities for as-prepared homogeneous and inhomogeneous Ge QDs. (a) Crystalline. (b) Amorphous. (c) Mixture of crystalline and amorphous QDs. (d) Mixed crystalline-amorphous within one single QD. (e) Single QD with nano-crystalline core and amorphous shell. 92

6.1 The cross section of a Bridgeman-type Diamond Anvil Cell. The culet where the diamond faces make contact with sample is typically $\sim$ 0.6mm. The applied pressures is increased by tightening the screws. The ruby is present for calibrating the pressure. The gasket compromised of a hard metal foil is to prevent the diamond faces from coming into contact [10]. 97

6.2 (a) White light transmission through the sample as a function of pressure. (b) Evolution of the Raman spectra. (c) The Raman peak position extracted from the experimental data (blue circles) together with the DFT simulation result (green circles). The Raman peak position for the bulk c-Ge (red circles) linearly extrapolated beyond 11 GPa is also shown. The inset figures shows the changing of the FWHM of the experimental Raman peak as a function of pressure. (d) Pressure dependence of the photoluminescence peak position (blue circles) compared to the calculated HOMO-LUMO gaps for $Ge_{71}H_{60}$ (green circles) and $Ge_{181}H_{110}$ (purple circles) hydrogen-terminated clusters [16]. 99

6.3 (a) Ge-Ge nearest-neighbour distance obtained from EXAFS analysis and DFT simulations. The horizontal dashed line indicates the value of stability of Ge-Ge distance in crystalline bulk Ge. (b) DW factor of Ge-Ge bonding from EXAFS analysis. For (a) and (b), the corresponding behaviour of the crystalline [18] and amorphous [19] bulk Ge is also shown for comparison. (c) The 1st shell coordination number from EXAFS analysis and DFT simulation. (d) The changing of volume per atom as the function of pressure calculated from DFT. The corresponding $Ge_{71}H_{60}$ cluster and the bond angle distribution (the grey bars correspond to the β-Sn phase) are shown as the inset figures. 100

7.1 The GaSb phonon dispersion curve fitting with Morse and screened harmonic three-body potential. The phonon frequencies (in dots) for GaSb (taken at 300 K) are from Ref. [7]. The reduced wave vector is given as: $\zeta = a_0 q/2\pi$, where the lattice constant $a_0 = 6.0959$ Å. 106

7.2 The relaxation curve for the ART running. The inset figures are the finally obtained aGaSb model, together with the PDF pattern corresponding to the initial (green) and final (blue) structural configuration. 109

7.3 The comparison of the Ga K-edge EXAFS experimental spectra (measured at 78 K) with the theoretical spectra obtained from MD2FEFF running for (a) the initial random aGaSb model and (b) the aGaSb model after $\sim$ 3500 steps relaxation as the input structural model. The numerical difference between the experimental and the theoretical spectra is also presented for each model in (a) and (b), respectively. 110

7.4 The Ge (a) crystalline (b) amorphous and (c) core-shell (with the 90% crystalline region, atoms shown in red color) structural models and the corresponding PDF pattern for each model. The green arrow in (c) indicates contribution from the amorphous portion of the model as compared to that of the crystalline model. . 111

7.5 The comparison of experimental EXAFS spectra for annealed Ge QDS with the theoretical spectra obtained from MD2FEFF running for (a) Ge core-shell model with 90% core crystalline region and (b) crystalline Ge model. The numerical difference (from $k = 3.5$ Å^{-1} to $k = 14.0$ Å^{-1}) between the experimental and theoretical spectra is also presented for each model in (a) and (b), respectively. . 112

7.6 The comparison of experimental EXAFS spectra for as-prepared Ge QDs with the theoretical spectra obtained from MD2FEFF running for (a) Ge amorphous model, (b) Ge core-shell model with 20% core crystalline region and (c) Ge core-shell model with 30% core crystalline region. The numerical difference (from $k = 3.5$ Å^{-1} to $k = 14.0$ Å^{-1}) between the experimental and theoretical spectra is also presented for each model in (a) - (c), respectively. 113

8.1 (a) GaSb zinc blende (ZB) (b) GaSb β-tin (BT) unit cell together with the 7.0 Å cluster for XANES spectra calculation with Ga and Sb as the absorbing atom, respectively. 119

8.2 (a) Ga K-edge XANES for GaSb compound at $T = 78$ K, together with the corresponding simulated XANES for zinc blende (ZB) structure. (b) The Ga K-edge XANES of both crystalline and amorphous GaSb compounds at $T = 78$ K, together with the corresponding simulated XANES spectra where the calculation cluster was set to 3.0 Å, 5.0 Å and 7.0 Å, respectively. 120

8.3 The XANES spectra of CS1 Ge QDs, together with the reference spectra of $aGeO_2$ and the linear combination of aGe and $aGeO_2$ (aGe – 50%, $aGeO_2$ – 50%). 121

8.4 (a) Comparison of XANES spectra for as-prepared, annealed Ge QDs, amorphous Ge [4], bulk (diamond-type) Ge references, theoretical calculation with diamond-type [5], BC8 [6] and ST12 [7] Ge phases (with the calculation cluster size $r = 7.0$ Å). The energy value corresponding to feature 'A' to 'C' is given at the bottom. (b) Simulated XANES spectra for diamond-type Ge structure by FDMNES using FDM mode, where the calculation cluster size was set from 3.0 Å to 7.0 Å. The arrows indicate the second main feature position in each spectrum. 122

8.5 Comparison of experimental XANES spectra of as-prepared Ge QDs with simulation, for which only the first two shells are included in the calculation cluster (radius $r = 4.2$ Å) using FDM mode. 123

8.6 Position of features in the XANES spectra of annealed Ge QDs and the diamond-type Ge reference. The feature in the middle cannot be observed in the reference XANES spectrum. The positions were obtained by taking the derivatives of the XANES spectra. The inset is an illustration of the proposed core-shell model for annealed Ge QDs. 124

8.7 (a) and (b) The two PL windows ($350-450$ nm and $500-650$ nm) used to collect the OD-XANES spectra for CS1 and CS2 sample, respectively. (c) and (d) The comparison of OD-XANES (with PL window selected around 400 nm and 550 nm, respectively) and XANES (detected in transmission mode) spectra for CS1 and CS2 sample, respectively. 125

A.1 The illustration for the Fourier transform of (a) the original continuous signal (in time domain) and (b) the sampled signal. The picture was reproduced based on the original image: [1] 136

A.2 The illustration for the sampling theorem using three artificial signals in (a), (b) and (c), respectively. The blue lines indicate the sampling points in time domain. 137

B.1 Depiction of the full potential and the muffin-tin potential. Reproduced from Ref. [4]. 149

B.2 The illustration for the single and multiple scattering paths. 150

B.3 Illustration of four-leg multiple scattering. Circles represent the scatterers, and line represents the Green's propagator connecting each two adjacent atoms. λ is the spherical expansion index and the dashed line represents the separable representation of the Green's propagator for each leg. Reproduced from Ref. [5]. 152

B.4 Illustration for the building up of the muffin-tin potential in 2D space. The idea for 3D situation is similar. Reproduced from Re. [7]. 154

C.1 The electric field caused by the electrostatic charge distribution in space. 158

D.1 Example of the discretization of the domain. 165

E.1 The flowchart of MD2FEFF code. 172

List of tables

3.1 Parameters of B18 beamline at Diamond Light Source 40

5.1 d-spacing (in Å) calculated from PXRD patterns compared with JCPDS database for α-quartz, rutile GeO_2 and diamond-type Ge. 87

5.2 Comparison of two extra diffraction peaks in CS1 annealed samples with Ge metastable phases. 88

5.3 EXAFS fitting result for CS1 samples. 90

5.4 EXAFS fitting result for CS2 samples. 91

7.1 The fitted Morse and screened harmonic three-body potential for GaSb. 107

7.2 Tersoff potential parameters for Ge system. 108

7.3 The first and second shell distances for the initial and relaxed (for 3500 steps) aGaSb model, together with those for cGaSb [11] and aGaSb [12] reference. . . 109

Nomenclature

Acronyms / Abbreviations

AFM Atomic Force Microscope

ART Activation Relaxation Technique

BC Boundary Condition

BSR Bethe-Salpeter Equation

BT β-tin

BW Bandwidth

CB Conduction Band

CI Configuration Interaction

CNTs Carbon Nanotubes

CS Colloidal Synthesis

DAC Diamond Anvil Cell

DFT Density Functional Theory

DOS Density Of States

DW Debye-Waller Factor

EDX Energy Dispersive X-ray Spectroscopy

EMFP Electron Mean Free Path

ESRF European Synchrotron Radaition Facility

EXAFS Extended X-ray Absorption Fine Structure

FDM Finite Difference Method

FIB Focused Ion Beam

FLAWP Full Linear Augmented Plane Wave

FMS Full Multiple Scattering

FPMS Full Potential Multiple Scattering

FSR Final State Rule

FWHM Full Width at Half Maximum

GDY Graphdiyne

HDA High Density Amorphous

HOMO Highest Occupied Molecular Orbital

KKR Koringa-Kohn-Rostoker method

LDA Local Density Approximation

LDA Low Density Amorphous

LOR Long-Range Order

LUMO Lowest Unoccupied Molecular Orbital

MD Molecular Dynamics

MS Multiple Scattering

MW Molecular Weight

NSLS National Synchrotron Light Source

ODXAS Optically Detected X-ray Absorption Spectroscopy

PCA Primary Component Analysis

PCBM Phenyl-C61-butyric acid methyl ester

PC Percentage of Crystalline

PDF Pair Distribution Function

PEC Photoelectrochemical

PL Photoluminescence

PVP Polyvinylpyrrolidone

PWA Plane Wave Approximation

PXRD Powder X-ray Diffraction

QC Quantum Confinement

QDs Quantum Dots

RDF Radial Distribution Function

RMC Reverse Monte Carlo

SEM Scanning Electron Microscope

SRO Short-Range Order

SRS Synchrotron Radiation Source

SSRF Shanghai Synchrotron Radiation Facility

STEM Scanning Transmission Electron Microscope

STM Scanning Tunnelling Microscope

TEM Transmission Electron Microscope

TMCs Transition Metal Chacolgenides

VB Valence Band

WWW Wooten-Winter-Weaire method

XAFS X-ray Absorption Fine Structure

XANES X-ray Absorption Near-Edge Structure

XAS X-ray Absorption Spectroscopy

XEOL X-ray Excited Optical Luminescence

XPDF X-ray Pair Distribution Function

XRD X-ray Diffraction

ZB Zinc Blende

Chapter 1

Introduction

For nanomaterials, or even for any functional materials, knowledge of their structure is crucial for understanding and improving physical properties. This thesis is about utilization of X-ray absorption technique to explore the local structure of Ge nanoparticles. In this first chapter, some background knowledge about nanomaterials and quantum dots will be given in section-1.1 and 1.2, respectively. In section-1.3, the difficulty in exploring the structure for nano-systems will be addressed, which will then be followed by the introduction to our approach based on X-ray absorption spectroscopy to explore the structure of nano-systems (section-1.4).

1.1 Nanomaterials

Nanomaterials refer to those materials with size in either of the three dimensions between 1 and 100 nm. Materials in this size regime show properties or behaviours intermediate between that of a macroscopic and that of an atomic or molecular system. For example, when the size of metallic particles is down to nano-scale, the onset of the surface plasmon resonance (SPR) effect will influence the color of metallic nanoparticles. The color could be further tuned by controlling the size of particles [1]. As a matter of fact, the coloring of metallic nanoparticles with different size has already been used in ancient times. The most famous example of one such application is the Lycurgus cup (stored in British Museum [2]). The color of the cup will change from green to wine red as light shines through from internally, as is shown in Fig. 1.1. Modern analysis has shown that the observed optical properties are due to the Ag and Au nanoparticles ($\sim$ 70 nm) found in this cup [3].
Owing to the size scale of nanomaterials, they have different physical and chemical properties from the bulk counterparts. First of all, the large surface-to-volume ratio of nanomaterials

Fig. 1.1 Photograph showing the color changing of Lycurgus cup as light is shine through from internally. Reproduced from Ref. [2].

implies that there is a substantial fraction of atoms located on the surface. Atoms at the surface are commonly not fully coordinated, leading to the formation of the so-called dangling bonds. Therefore the large portion of the surface atoms for nanomaterials indicates high chemical reactivity which implies potential application on catalysts [4–7]. Nanomaterials also hold peculiar thermal, mechanical, electrical and optical properties. For example, there are experimental results showing the decrease of melting point with the reduction of nanoparticle size [8]. As for mechanical properties, in the nano-size regime, the inverse Hall-Petch relation was observed [8], in contrast to the normal Hall-Petch effect where the hardness and yield strength increases with the reduction of the grain size [9, 10]. The peculiarity of electrical and optical properties (e.g. the blue shift of luminescence with the size reduction) of nanomaterials is mainly attributed to the changing of energy band structure, e.g. the Kubo effect for metallic nanomaterials and the quantum confinement effect for nano-sized semiconductors.

Nanoscale systems can be roughly divided into three basic categories: 0D, 1D and 2D according to either their three, two or one dimension is in the nano-regime. The most common representation of 0D nanomaterials is nanoparticles or quantum dots when the size in each dimension is down to less than 10 nm. Typical examples involve the early work on Cu halide microcrystals by Ekimov and Efros, et al. [11, 12] and semiconductor quantum dots (QDs) such as CdSe QDs by Alivisatos, et al. [13, 14]. One typical example of the 1D nanomaterials are carbon nanotubes (CNTs), which were first discovered in 1990s by Iijima [15, 16], and are now still a widely studied 1D system. As for the 2D nanomaterials, the research into graphene has received a great deal of attention for the last 10 years owing to its superior properties, e.g. zero electron effective mass [17]. As a typical example, for the research upon graphene, the National Graphene Institute (NGI) based in Manchester,

UK, is receiving £38m from EPSRC and £23m from ERDF [18], respectively. As part of the China-UK corporation project, Chinese IT company Huawei also provides millions of funding to NGI for graphene research and commercialization [19].
Beneficial from the development of nanotechnology, including sample preparation techniques such as the focused ion beam (FIB) lithography [20], photo lithography [21] and sample characterization techniques, such as atomic force microscope (AFM) [22] and scanning tunnelling microscope (STM) [23], researchers are now able to touch the '*plenty of room*' as mentioned in Feymann's famous lecture given in 1959 [24]. Devices based on nanomaterials have also already been fabricated. For example, the CNTs-based transistor fabricated by IBM has been reported [25].
Following a general overview upon the nanomaterials, the next section will specifically focus on one of the typical representatives of 0D nanomaterials as mentioned earlier – semiconductor quantum dots (QDs).

1.2 Quantum dots

Generally, the QDs refer to small nanoparticles ($\sim$ 10 nm) which shows distinctive properties as compared to their bulk counterparts. There are various applications of QDs of different kinds, including Group III-V (GaAs, InP, GaSb, etc.) [26, 27], II-VI (ZnO, ZnS, CdSe, etc.) [28, 29] and Group IV (Si, Ge, $Si_{1-x}Ge_x$, etc.) [30, 31] QDs, etc. First of all, as mentioned before, the large surface-to-volume ratio of QDs promises wide application in catalysis processes, such as electrocatalysis and photocatalysis. For example, the surface-functionalized CdSe QDs, with the novel large π-conjugated carbon material – graphdiyne (GDY) – were proven to be potentially applicable to fabricating an effective photoelectrochemical (PEC) device for water splitting by solar energy [32]. Moreover, the extraordinary optical property (e.g. the strong light-harvesting capability) owing to the QC effect of QDs also attracts diverse interest of research upon the application in QDs solar cells, [33] QDs lasers [34] and QDs-based spintronics [27]. It's noteworthy that the superb light-harvesting property of QDs has been further extended to be coupled with other media to further promote the quantum efficiency [35] or for other optical applications. For example, the CdSe/CdS core-shell QDs were used to launch the surface plasmon mode of gold, which was then further coupled to the photonic modes of the TiO_2 waveguide [36].
The application of QDs in biological imaging, where they have several clear advantages over other standard techniques, is promising. The commonly used fluorescent imaging techniques rely on photoluminescent dyes [37, 38]. These dyes can be targeted by using chemical

labels, but they have a limited lifespan of seconds to minutes before degrading and ceasing to luminance, thus limiting the types of phenomena that can be studied [39]. Dyes rely on the structural change as part of the mechanism for their optical activity. Therefore they suffer from the problem of photobleaching, limiting their application primarily to short-term experiments [39]. Semiconductor QDs, however, do not suffer from the photobleaching problem as their photoluminescence is completely due to the electronic transitions. A further advantage of semiconductor QDs over dyes is the tunability of their emission wavelength. Dyes emit at a single wavelength, and so for each required colour a new dye is needed. Different colour dyes are completely different molecules and as such will have different properties, such as stability, efficiency, toxicity, lifetime, etc. The optical emission wavelength from the semiconductor QDs, however, can be controlled through simply changing the size alone.

Due to their comparable size with atoms, QDs are called artificial atoms. Indeed, it is the small size effect that brings superb properties, e.g. high chemical activity due to large surface-to-volume ratio, to QDs, and especially the quantum confinement (QC) effect makes the optical property significantly different from that of the bulk materials. Therefore the following introduction about QDs will start with a basic overview of the QC effect.

1.2.1 Quantum confinement effect

For semiconductor QDs materials, when an electron is excited to the conduction band (CB), it will leave off holes in the valence band (VB). The generated electron-hole pair is know as *exciton*, and the physical separation between the electron and hole is referred to as the Bohr exciton radius (r_B). In the bulk semiconductor, the overall size of material is much larger than r_B, therefore the migration of exciton is not spatially restricted. However, when the size (in either of the three dimensions) of semiconductors is comparable to the corresponding r_B, it will give rise to the QC effect – QD is confined in three dimensions, a quantum wire is confined in two dimensions (1D system) and a quantum well is confined in one dimension (2D system).

First of all, the QC effect is reflected in the density of states $\rho(E)$ (DOS) defined as the number of states per unit volume (N) per unit energy:

$$\rho(E) = \frac{\partial N}{\partial E} \tag{1.1}$$

In Fig. 1.2, the illustration for DOS of 0D to 3D systems is given, from which one can inspect the discretization of the DOS in low-dimensional materials. For example, for a simple

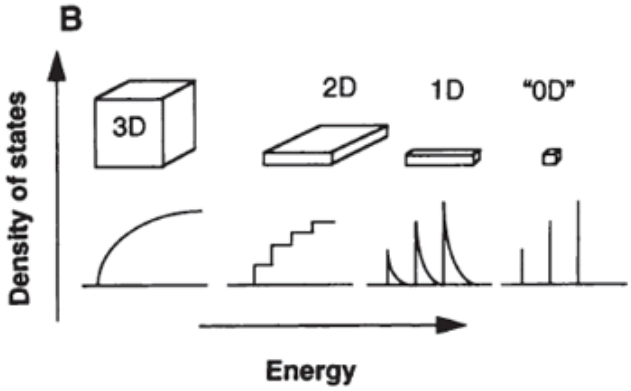

Fig. 1.2 Density of states in one band of semiconductor as a function of dimension [40].

one-dimensional system, the allowed k-values are given as $k = 2n\pi/L$ ($n = 1,2,3,\cdots$), where L is the size of the one-dimensional wire. When L is large (corresponding to the bulk material), the k-space can be regarded as continuous. As L approaches the quantum confinement regime, the k-space can no longer be viewed as continuous, which then further leads to the discretization of the energy band and DOS.

The QC effect is also reflected in the size-dependence of the band-gap, which will influence the electronic and optical properties of low-dimensional semiconductors. By applying the effective mass approximation (EMA), Efros et al. [41] derived the size-dependence of the band-gap of QDs:

$$E_n = E_g + \frac{h^2\pi^2}{2\mu R^2} \tag{1.2}$$

where E_g is the band-gap of the bulk semiconductors, μ the reduced mass of the exciton given by $m_e m_h/(m_e + m_h)$ where m_e and m_h are the masses of the electron and hole, respectively, and R is the radius of QDs. Brus [42] and Kayanuma [43] further extended the model to account for the Coulomb interaction of excitons and the correlation energy to give:

$$E_n = E_g + \frac{h^2\pi^2}{2\mu R^2} - \frac{1.786e^2}{\varepsilon R} + 0.284E_R \tag{1.3}$$

where the third term corresponds to the Coulomb interaction, and E_R is the Rydberg correlation energy of the bulk semiconductor as given by:

$$E_R = \frac{\mu e^4}{2\varepsilon^2\varepsilon_0^2 h^2} \tag{1.4}$$

where ε_0 is the vacuum permittivity and ε is the dielectric constant. In Fig. 1.3, the discretization of energy band and the widening of the band-gap for Ge QDs with different sizes is shown, as compared to the Ge bulk system. Further details about the exciton/biexciton

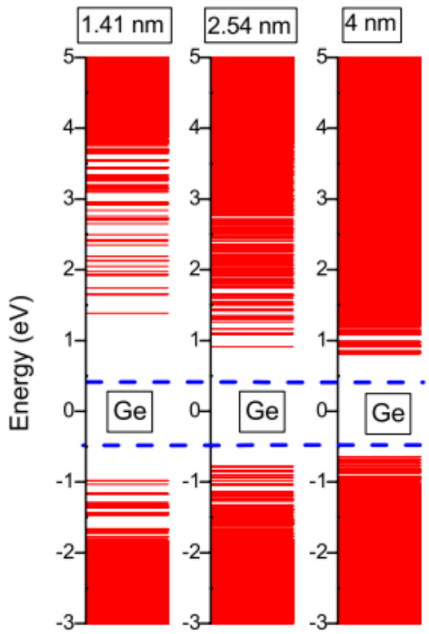

Fig. 1.3 The discretization of energy levels and the size dependence of the band-gap in Ge QDs. The blue dotted line indicate the band-gap in bulk Ge [44].

effect in QDs will not be covered in this thesis, and the corresponding discussion can be found in Ref. [45] and section-I.A.3 of Ref. [46]. However, here it's worth pointing out that the exciton effect (the third term on the right in Eq. 1.3) does not play a significant role in nanostructures with small size, where the excitation energy (the first term on the right in Eq. 1.3) and the quantinization effect (the second term on the right in Eq. 1.3) is much larger than the exciton energy. Therefore for materials with larger Bohr exciton radii, the corresponding nanostructures encompass a larger regime of the QC effect, where the exciton effect can be important [46]. This adds to tunability of the band structure for QDs materials with large Bohr exciton radii.

The influence of the quantum confinement effect on the band structure is further reflected in the massive change (as compared to the bulk counterparts) and the size-dependence of the optical properties of QDs materials. The electronic transitions shift to higher energy with the reduction of the QDs size. Fig. 1.4 shows the changing of both the optical absorption (Fig.

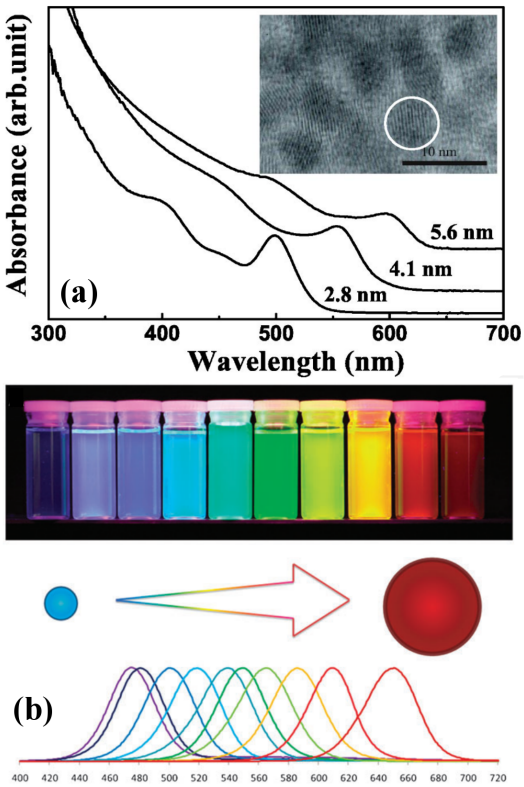

Fig. 1.4 (a) Optical absorption spectra for CdSe QDs with different sizes [47]. (b) Size-tunable light emission from CdSe QDs [48].

1.4a, CdSe QDs) and photoluminescence (Fig. 1.4b, CdSe QDs) wavelength as the function of QDs size.

The other important consequence of the QC effect is the breaking of k-selection rule (conservation of momentum) in optical transition. Si and Ge are both indirect band-gap semiconductors, which means the conduction band (CB) minima and valence band (VB) maxima do not coincide with each other in k-space. Therefore for bulk Si and Ge, the optical transition can only happen through the interaction with phonon, which makes the light emission inefficient. However, for quantum confined systems (e.g Si and Ge QDs), the reduction of the system dimension tends to increase the spread of the electron/hole wavefunction, according to the Heisenberg uncertainty principle. Such spreading of the wavefunction in k-space will make it possible to observe the pseudo-direct optical transition without the assistance of phonon. The breaking of the k-selection rule is stronly size and shape dependent, and it can happen in any materials, especially in those with large Bohr radii where it can be observed for large particle size, and over wide size ranges [46]. Another mechanism which could possibly

contribute to breaking of the k-selection rule is the Brillouin zone (BZ) folding, which again, is attributed to the reduction of size. When the dimension of nanostructures is reduced to be comparable with the Bohr exciton radius, the size of material then significantly influences the periodicity – the introduction of a supercell larger than the original primitive unit cell. This will then reconstruct the Brillouin zone, and for indirect band-gap semiconductors, in some situation the BZ is rebuilt in such a way that the otherwise non-coinciding CB minima and VB maxima meet in k-space [46]. Therefore in such cases, the originally indirect band-gap bulk semiconductors becomes direct band-gap quantum systems.

1.2.2 Group IV quantum dots

Synthesis, properties and application of the group IV QDs have attracted great interest over the past 20 to 30 years, ever since reports by Canham et al. (1991) on the light emission in the porous Si [49]. Interest originally started because of the promise of adding optical capabilities to an already widely used electronic material – Si. As mentioned before, the QC effect of the QDs system could improve quantum efficiency significantly for group IV materials. Also size tunable optical and electric properties make the group IV QDs attractive for application in multi-junction solar cells [50, 51], photodetectors [52] and field-effect transistors [53, 54]. For example, it was recently reported that the coupling of Si QDs with graphene for high-performance photodetectors [55]. Moreover, potential applications of Ge nanocrystals (NCs) on printing electronics [56] and organic-inorganic hybrid photoelectric devices [57] have been reported. Specifically for Ge QDs, which will be the focus of this thesis, the research into it started at about the same time with that for Si to explore the optical emission from Ge NCs and porous Ge [58–61]. Here, there are two main reasons why we focus on Ge system in this thesis. First of all, the large Bohr exciton radius (24 nm [62] compared to 5 nm of Si [63]) leaves plenty of space for tuning optical properties by changing the QDs size owing to the strong exciton effect in QDs with large size. Secondly, Ge system is much easier to study with X-ray absorption spectroscopy than Si, especially under high pressure.

The superb property (e.g. no photobleaching) of QDs materials makes them more suitable (as compared to traditionally used dyes) for bio-applications, for which the toxicity and bio-compatibility should be among the primary considerations, alongside the optical properties. For group IV QDs, the low toxicity and excellent bio-compatibility is of advantage over other QDs materials, such as those group II-VI and group III-V QDs, for bio-applications. Here it's worth mentioning the work from our own group, where the Ge QDs were used

for spectroscopic super-resolution fluorescence cell imaging [64]. Also the potential bio-applications of Ge nanoparticles on cell imaging, labelling and photothermal therapy have been reported [65, 66].
Following the general introduction to nanomaterials and quantum dots, the next section will focus on the structure characterization for the small-size nano-systems, especially the QDs systems. Both the importance and the difficulty in looking at the structure for nano-systems will be addressed.

1.3 Structure characterization for QDs system

All the exciting optical properties useful for the application of QDs are defined by electronic structures. These, in turn, are defined by the atomic structure. Hence knowledge of the atomic structure is paramount in understanding the electronic and optical properties and informing synthesis [67–69]. Moreover, information about the link between the atomic-level structure and the electronic-optical properties of materials can provide further guidance in developing the synthesis routes that provide desired outcomes.

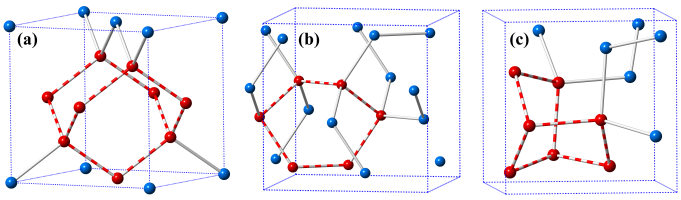

Fig. 1.5 The unit cell of Ge (a) diamond, (b) BC8 and (c) ST12 phase. For each structure, the rings formed by the local atoms are labelled out.

For nano-systems, especially when the size in either of the three dimensions is down to the QC regime, lack of long-range order in the structure makes it crucial to look into the local structure (i.e. the local atomic arrangement). Specifically for the group IV QDs (e.g. Ge, Si QDs), most samples prepared under mild synthesis conditions seem to be amorphous-like due to the relatively high crystallization temperature [65]. Upon further processing (e.g. heating, compressing), the as-prepared QDs may undergo phase transition. Therefore in such situation it's important to look into the local environment for exploring the structural changes accompanying the corresponding phase transition. For Ge QDs systems, upon thermal or high pressure conditions, various lattice structures including some metastable phases such as ST12 [56], BC8 [70] and mC16 [71] have been reported (see Fig. 1.5).

The large surface-to-volume ratio (due to the small size) of nanomaterials lead to high surface energy. High surface energy plays a significant role in structure transformation, which could possibly lead to the stabilization of metastable phase at ambient conditions. For example, the ST12 metastable phase was reported to exist at ambient condition in Ge QDs [56]. All of these metastable phases have different local symmetry. For example, both BC8 and ST12 structures are composed of distorted tetrahedral units. But the BC8 structure is composed of sixfold rings (Fig. 1.5b). Three of the four nearest atoms are at 2.39(1) Å and the other one is at 2.30(1) Å [70]. For ST12, the atoms exist in five- or seven- fold rings (Fig. 1.5c), and the four nearest-neighbor bonds appear to be closer in length, with two at 2.49(4) Å, one at 2.48(4) Å, and the other one at 2.49(5) Å [70]. Therefore for better understanding the structural configuration of Ge QDs, information about local symmetry is indeed crucial.

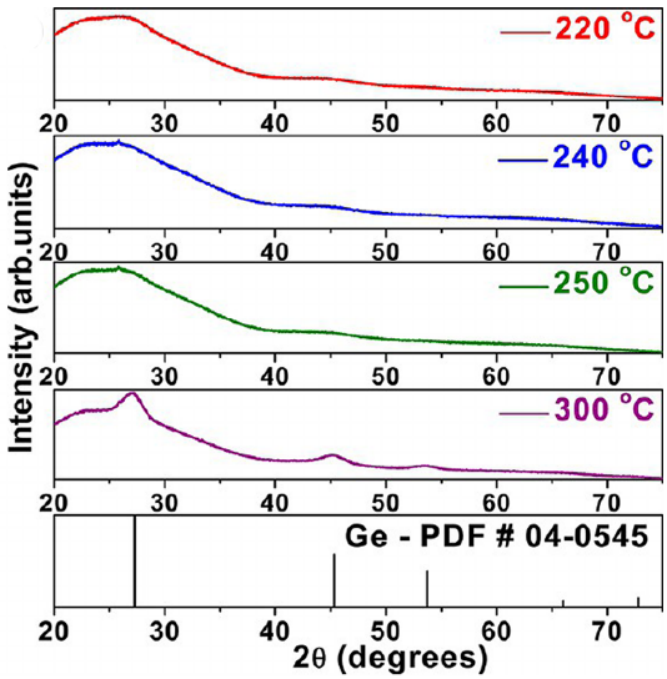

Fig. 1.6 Powder XRD patterns of Ge QDs produced by conventional heating method (with various heating temperature) compared to Ge reference pattern [72].

However, characterizing the ultra-small QDs (below 10 nm) becomes challenging and often comes with a degree of uncertainty [73], due to the significant surface, interface [74–76] and size effects [77], etc. In the case of Ge QDs, as mentioned before, the as-prepared sample is, in most situations, amorphous. Therefore the sparse and broad Bragg peaks due to the limited structural coherence makes it difficult to extract useful structural information using

the traditional scattering techniques, such as the powder X-ray or neutron diffraction [78]. Fig. 1.6 shows an example of the powder X-ray diffraction (PXRD) pattern of Ge QDs from a report by Kauzlarich et al. [72], from which one can clearly see little information concerning the structural evolution can be extracted (especially the local environment changing) as the heating temperature increases. In recent years, the analysis of the pair distribution

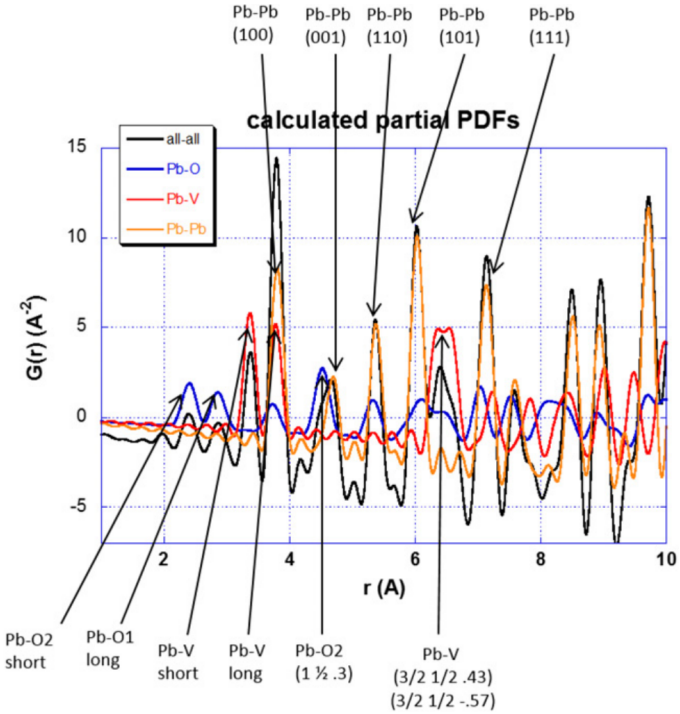

Fig. 1.7 Calculated total and partial X-ray PDFs for $PbVO_3$, showing the overlapping of PDF peaks. Source from Ref. [79].

function (PDF) based on X-ray or neutron total scattering has made a significant progress [80]. The total scattering technique combined with the PDF analysis can in principle yield local, medium and long range structural information [81, 78]. However, the PDF method suffers from problems when the system is complex, involving many distinctive chemical sites. In such situation, the overlap of PDF peaks is often the case, for which Fig. 1.7 gives an example showing the calculated partial and overall X-ray PDFs for $PbVO_3$ compounds [79]. To deal with such a problem, the chemically specific partial PDF can be obtained based on the X-ray anomalous scattering technique, where the energy of X-ray in use is close to the absorption edge of the element of interest. However, it should be pointed out that the extraction of PDF patterns with high resolution in real space requires that the scattering pattern should be measured over a wide range of Q-values ($Q = 4\pi sin\theta/\lambda$), which requires

high energy (thus small λ and large Q) of X-ray. This makes the anomalous X-ray total scattering inapplicable for those systems containing elements for which the corresponding energy of the absorption edge is too low (e.g. lower than the in-house Ag X-ray energy for X-ray PDF measurement – $\sim$ 22 keV) to meet the high-energy requirement imposed by the X-ray PDF resolution. Other commonly used techniques to characterize nanomaterials include transmission electron microscope (TEM), Raman, etc. Both TEM and Raman suffer from the problem of annealing samples [77, 82–86], to some extent, which makes it tricky to deal with the amorphous systems due to the amorphous-to-crystalline phase transition. Moreover, not much information can be directly obtained for amorphous systems from TEM, apart from the influence on samples. Raman can be used to determine the size of nanocrystals employing the well known Richter model [87, 88], but could be problematic for very small nanoparticles (e.g. QDs) [89]. As mentioned before, the surface-to-volume ratio of nanoparticles increases with the decreasing of the nanoparticle size. Atoms on the surface of nanoparticle are either passivated by being capped with atoms of other elements (e.g. hydrogen, oxygen) or exist with dangling bonds. Hence the force environment for surface atoms is different from those in the core region. This will lead to a change in bond length and strength which determines the phonon behaviour and thus the observed Raman spectra. Therefore the significant surface effect for small-size QDs tends to make it difficult to carry out Raman spectra fitting based on the Richter model, due to the mixing-up of the contribution from the core and surface region.

Therefore in this thesis, X-ray absorption spectroscopy (XAS) was used as the main technique to probe the local environment of Ge QDs. In XAS, the core electron is excited by the incoming X-ray to become propagating photoelectron, which provides an opportunity to explore the local structure by looking at the interaction with the local surroundings. A general introduction about our approach to probe the local structure mainly using XAS will be presented in next section.

1.4 XAS for structure characterization

X-ray absorption spectroscopy (XAS) has long been recognised as a powerful alternative method to traditional diffraction and PDF based techniques due to its sensitivity to local structure [90–92]. Most importantly, when considering its site selectivity, XAS offers a potential advantage over the PDF based methods. Also as compared to TEM and Raman methods, X-rays have little effect on samples in the XAS measurement. Indeed, owing to the development of the modern theory of the X-ray absorption fine structure, the extended

part (EXAFS, between 50-1000 eV above an x-ray absorption edge) of the overall XAS signal has been successfully used in characterizing both the bulk [93–95] and nano- systems [96–101]. This success is due to the important and unique structural information EXAFS can yield including coordination numbers, interatomic distances, dynamic and static disorder around specific types of atoms in a multicomponent system.

However, while the analysis of EXAFS is a powerful method of choice for structural characterization, traditional EXAFS data analysis relies on the structural parameters fitting and does not directly return a structural model as the output. Moreover, the commonly used EXAFS spectra fitting algorithm may encounter problems when dealing with highly disordered systems (e.g. some amorphous or liquid systems). For example, the cumulant expansion used in the IFEFFIT algorithm may become inadequate or fail altogether to describe the experimental EXAFS spectra [102–104]. Therefore, as the supplementary to the conventionally used parameters fitting based EXAFS analysis technique, the EXAFS spectra simulation (using FEFF9.6 [105]) can be carried out by combining with the molecular dynamics (MD) simulation (using DL_POLY_4 [106]). For the combined simulation, an initial structural model can be used as the input for the EXAFS spectra calculation, which will then be followed by the structure evolution with MD simulation. Here the purpose of the MD simulation is to take into account of thermal effect of the system. The configuration and step-wise average is calculated after each cycle of the combined simulation, which is then compared to the experimental spectra on-the-run. As the output, a structural model, together with the corresponding agreement with the experimental EXAFS spectra will be generated.

Furthermore, EXAFS could provide inadequate or no information about the local symmetry of disordered samples due to the limited (usually to the first coordination shell) structural information. In nanomaterials, there are added problems of the complex nanoscale morphology [107–109], possible contribution to the signal from the metastable phases [77, 110, 71], surface effect, etc. As compared to EXAFS, another portion of the overall XAS signal – the X-ray absorption near-edge structure (XANES) is of advantage in looking at the local symmetry and the medium-range order [111, 112]. This is mainly the result of the low kinetic energy (therefore long electron mean free path (EMFP) [112, 113]) of the photoelectron in the XANES region. Recent developments in the computational power and the codes capable of sufficiently accurate XANES calculations make it possible to obtain quantitative structural and electronic information through the comparison between theoretical and experimental results. Here, the numeric analysis of XANES data for Ge QDs will be carried out, specifically, to demonstrate the capability of numerical XANES analysis and its potential to be extended to complex systems.

The next chapter will start from the background introduction to the synchrotron radiation together with the history and application of XAS techniques, e.g. data measurements and analysis (Chapter-2 and 3). Brief introduction to the theoretical method used for the XANES simulation based on the finite difference method (FDM) used in FDMNES [114] will be given in Chapter-4. Chapter-5 to 8 includes the specific case study – Chapter-5 will discuss the utilization of EXAFS together with PXRD, TEM and Raman to explore the structure of colloidal Ge QDs, Chapter-6 will discuss the phase transition of Ge QDs under hydrostatic high pressure using EXAFS, Raman and density funcitonal theory simulation, Chapter-7 will focus on the combined EXAFS-MD simulation for the Ge QDs systems using the self-developed MD2FEFF code, and Chapter-8 will introduce the exploration of the local structure of Ge QDs by numerical XANES analysis.

References

[1] F. Bradley. *Materials Chemistry*. Springer, 2011.

[2] The lycurgus cup. http://www.britishmuseum.org/research/collection_online/collection_object_details.aspx?objectId=61219&partId=1&searchText=lycurgus&page=1, April 2016. online; accessed 09-April-2016.

[3] S. Horikoshi and N. Serpone. *Microwaves in Nanoparticle Synthesis: Fundamentals and Applications*. Wiley-VCH Verlag GmbH & Co. KGaA, 2013.

[4] D. Curcio, L. Omiciuolo, M. Pozzo, P. Lacovig, S. Lizzit, N. Jabeen, L. Petaccia, D. Alfe, and A. Baraldi. Molecular lifting, twisting, and curling during metal-assisted polycyclic hydrocarbon dehydrogenation. *J. Am. Chem. Soc.*, 138:3395–3402, 2016.

[5] J. B. Ding, L. Z. Bu, S. J. Guo, Z. P. Zhao, E. B. Zhu, Y. Huang, and X. Q Huang. Morphology and phase controlled construction of Pt–Ni nanostructures for efficient electrocatalysis. *Nano Lett.*, 16:2762–2767, 2016.

[6] N. Zhu, X. Hao, J. Ulstrup, and Q. J. Chi. Single-nanoparticle resolved biomimetic long-range electron transfer and electrocatalysis of mixed-valence nanoparticles. *ACS Catal.*, 6:2728–2738, 2016.

[7] Z. Q. Liu, H. Cheng, N. Li, T. Y. Ma, and Y. Z. Su. $ZnCo_2O_4$ quantum dots anchored on nitrogen-doped carbon nanotubes as reversible oxygen reduction/ evolution electrocatalysts. *Adv. Mater.*, 28:3777–3784, 2016.

[8] V. Pokropivny, R. Lohmus, I. Hussainova, A. Pokropivny, and S. Vlassov. *Introduction to nanomaterials and nanotechnology*. University of Taru, 2007.

[9] E. O. Hall. The deformation and ageing of mild steel: Iii discussion of results. *Proc. Phys. Soc., Ser. B*, 64:747–753, 1951.

[10] N. J. Petch. The cleavage strength of polycrystals. *J. Iron Steel Inst.*, 174:25–28, 1953.

[11] A. I. Ekimov. Optical properties of semiconductor quantum dots in glass matrix. *Phys. Scr.*, T39:217–222, 1991.

[12] A. I. Ekimov and AL. L. Efros. Optics of zero dimensional semiconductors systems. *Acta. Phys. Pol. A*, 79:5–14, 1991.

[13] A. P. Alivisatos, T. D. Harris, L. E. Brus, and A. Jayaraman. Resonance Raman-scattering and optical-absorption studies of CdSe microclusters at high-pressure. *J. Chem. Phys.*, 89:5979–5982, 1988.

[14] V. L. Colvin and A. P. Alivisatos. CdSe nanocrystals with a dipole-moment in the 1st excited-state. *Phys. Rev. Lett.*, 97:730–733, 1992.

[15] S. Iijima. Helical microtubules of graphitic carbon. *Nature*, 354:56–58, 1991.

[16] S. Iijima and T. Ichihashi. Single-shell carbon nanotubes of 1-nm diameter. *Nature*, 363:603–605, 1993.

[17] K. S. Novoselov, A. K. Geim, S. V. Morozov, D. Jiang, Y. Zhang, S. V. Dubonos, I. V. Grigorieva, and A. A. Firsov. Electric field effect in atomically thin carbon films. *Science*, 306:666–669, 2004.

[18] Huawei signs partnership with university to develop graphene-based technologies. http://www.manchester.ac.uk/discover/news/huawei-signs-partnership-with-university-to-develop-graphene-based-technologies, October 2015. online; accessed 11-April-2016.

[19] China to invest £30bn in uk plc: how the deals break down. http://www.telegraph.co.uk/finance/china-business/11943880/China-to-invest-30bn-in-UK-plc-how-the-deals-break-down.html, October 2015. online; accessed 11-April-2016.

[20] B. Cui. *Recent Advances in Nanofabrication Techniques and Applications*. Intech, 2011.

[21] J. J. Dong, Liu J, G. G. Kang, J. H. Xie, and Y. T. Wang. Pushing the resolution of photolithography down to 15 nm by surface plasmon interference. *Sci. Rep.*, 4:srep05618, 2014.

[22] L. Ding, Y. Li, H. B. Chu, X. M. Li, and J. Liu. Creation of cadmium sulfide nanostructures using AFM dip-pen nanolithography. *J. Phys. Chem. B*, 109:22337–22340, 2005.

[23] S. W. Hia. Scanning tunneling microscopy single atom/molecule manipulation and its application to nanoscience and technology. *J. Vac. Sci. Technol. B*, 23:1351–1360, 2005.

[24] R. P. Feymann. There's plenty of room at the bottom. *Eng. & Sci.*, 23:22, 1960.

[25] Ibm: Commercial nanotube transistors are coming soon. https://www.technologyreview.com/s/528601/ibm-commercial-nanotube-transistors-are-coming-soon/, July 2014. online; accessed 11-April-2016.

[26] Y. H. Huo, B. J. Witek, S. Kumar, J. R. Cardenas, J. X. Zhang, N. Akopian, R. Singh, E. Zallo, R. Grifone, D. Kriegner, R. Trotta, F. Ding, J. Stangl, V. Zwiller, G. Bester, A. Rastelli, and O. G. Schmidt. A light-hole exciton in a quantum dot. *Nat. Phys.*, 10:46–51, 2014.

[27] T. A. Baart, M. Shafiei, T. Fujita, C. Reichl, W. Wegscheider, and L. M. K. Vandersypen. Single-spin CCD. *Nat. Nanotechn.*, 11:330–335, 2016.

[28] W. Y. William and X. G. Peng. Formation of high-quality CdS and other II-VI semiconductor nanocrystals in noncoordinating solvents: Tunable reactivity of monomers. *Angew. Chem. Int. Ed.*, 41:2368–2371, 2002.

[29] A. Nurmikko. What future for quantum dot-based light emitters? *Nat. Nanotechn.*, 10:1001–1004, 2015.

[30] A. Alkhatib and A. Nayfeh. A complete physical germanium-on-silicon quantum dot self-assembly process. *Sci. Rep.*, 3:srep02099, 2013.

[31] S. Ilday, F. O. Ilday, R. Hübner, T. J. Prosa, I. Martin, G. Nogay, I. Kabacelik, Z. Mics, M. Bohn, D. Turchinovich, H. Toffoli, D. Toffoli, D. Friedrich, B. Schmidt, K. H. Heinig, and R. Turan. Multiscale self-assembly of silicon quantum dots into an anisotropic three-dimensional random network. *Nano Lett.*, 16:1942–1948, 2016.

[32] J. Li, X. Gao, B. Liu, Q. L. Feng, X. B. Li, M. Y. Huang, Z. F. Liu, J. Zhang, C. H. Tung, and L. Z. Wu. Graphdiyne: A metal-free material as hole transfer layer to fabricate quantum dot-sensitized photocathodes for hydrogen production. *J. Am. Chem. Soc.*, 138:3954–3957, 2016.

[33] Z. J. Ning, O. Voznyy, J. Pan, S. Hoogland, V. Adinolfi, J. X. Xu, M. Li, A. R. Kirmani, J. P. Sun, J. Minor, K. W. Kemp, H. P. Dong, L. Rollny, A. Labelle, G. Carey, B. Sutherland, I. Hill, A. Amassian, H. Liu, J. Tang, O. M. Bakr, and E. H. Sargent. Air-stable n-type colloidal quantum dots solids. *Nat. Mater.*, 13:822–828, 2014.

[34] J. F. Ho, J. Tatebayashi, S. Sergent, and C. F. Fong. A nanowire-based plasmonic quantum dot laser. *Nano Lett.*, 16:2845–2850, 2016.

[35] B. H. Kim, C. H. Cho, J. S. Mun, M. K. Kwon, T. Y. Park, J. S. Kim, C. C. Byeon, J. Lee, and S. J. Park. Enhanced of the external quantum efficiency of a silicon quantum dot light-emitting diode by localized surface plasmon. *Adv. Mater.*, 20:3100–3104, 2008.

[36] J. C. Weeber, K. Hammani, G. C. Francs, A. Bouheller, J. Arocas, A. Kumar, F. Eloi, S. Buil, X. Quélin, J. P. Hermier, M. Nasiiowski, and B. Dubertret. Colloidal quantum dot integrated light sources for plasmon mediated photonic waveguide excitation. *ACS Photonics*, 3:844–852, 2016.

[37] S. Antic and D. Zecevic. Optical signals from neurons with internally applied voltage-sensitive dyes. *J. Neurosci.*, 15:1392–1405, 1995.

[38] B. J. Baker, E. K. Kosmidis, D. Vucinic, C. X. Falk, L. B. Cohen, M. Djurisic, and D. Zecevic. Imaging brain activity with voltage- and calcium- sensitive dyes. *Cell. Mol. Neuroviol.*, 25:245–282, 2005.

[39] U. Resch-Genger, M. Grabolle, S. Cavaliere-Jaricot, R. Nitschke, and T. Nann. Quantum dots versus organic dyes as fluorescence labels. *Nat. Meth.*, 5:763–775, 2008.

[40] A. P. Alivisatos. Semiconductor clusters nanocrystals and quantum dots. *Science*, 216:933–937, 1996.

[41] A. L. Erfos. Interband absorption of light in a semiconductor sphere. *Sov. Phys. Semicond.*, 34:772, 1982.

[42] L. E. Brus. On the development of bulk optical properties in small semiconductor crystallites. *J. Lumin.*, 31-2:381–384, 1984.

[43] Y. Kayanuma. Quantum-size effects of interacting electrons and holes in semiconductor microcrystals with spherical shape. *Phys. Rev. B*, 38:9797–9805, 1988.

[44] C. Bulutay. Interband, intraband, and excited-state direct photon absorption of silicon and germanium nanocrystals embedded in a wide band-gap lattice. *Phys. Rev. B*, 76:205321, 2007.

[45] Al. L. Efros and M. Rosen. The electronic structure of semiconductor nanocrystals. *Annu. Rev. Mater. Sci.*, 30:475–521, 2000.

[46] E. G. Barbagiovanni, D. J. Lockwood, P. J. Simpson, and L. V. Goncharova. Quantum confinement in Si and Ge nanostructures: Theory and experiment. *Appl. Phys. Rev.*, 1:011302, 2014.

[47] S. Neeleshwar, C. L. Chen, C. B. Tsai, Y. Y. Chen, C. C. Chen, S. G. Shyu, and M. S. Seehra. Size-dependent properties of CdSe quantum dots. *Phys. Rev. B*, 71:201307(R), 2005.

[48] P. Zrazhevskiy, M. Sena, and X. H. Gao. Designing multifunctional quantum dots for bioimaging, detection, and drug delivery. *Chem. Soc. Rev.*, 39:4326–4354, 2010.

[49] A. G. Cullis and L. T. Canham. Visible light emission due to quantum size effects in highly porous crystalline silicon. *Nature*, 353:335–338, 1991.

[50] E. Canovas, D. F. Marron, A. Marti, A. Luque, A. W. Bett, F. Dimroth, and S. P. Philipps. Photoreflectance analysis of a GaInP/GaInAs/Ge multijunction solar cell. *Appl. Phys. Lett.*, 97:203504, 2010.

[51] W. Guter, J. Schone, S. P. Philipps, M. Steiner, G. Siefer, A. Wekkeli, E. Welser, E. Oliva, A. W. Bett, and F. Dimroth. Current-matched triple-junction solar cell reaching 41.1% conversion efficiency under concentrated sunlight. *Appl. Phys. Lett.*, 94:223504, 2009.

[52] S. Assefa, F. N. Xia, and Y. A. Viasov. Reinventing germanium avalanche photodetector for nanophotonic on-chip optical interconnects. *Nature*, 464:80–U91, 2010.

[53] R. Pillarisetty. Academic and industry research progress in germanium nanodevices. *Nature*, 479:324–328, 2011.

[54] Y. Kamata. High-k/Ge MOSFETs for future nanoelectronics. *Mater. Today*, 11:30–38, 2008.

[55] T. Yu, F. Wang, Y. Xu, L. L. Ma, X. D. Pi, and D. R. Yang. Graphene coupled with silicon quantum dots for high-performance bulk-silicon-based schottky-junction photodetectors. *Adv. Mater.*, 2016.

[56] S. J. Kim, O. K. Quy, L. S. Chang, E. A. Stach, C. A. Handwerker, and A. Wei. Formation of the ST12 phase in nanocrystalline Ge at ambient pressure. *J. Mater. Chem.*, 20:331–337, 2010.

[57] D. J. Xue, J. J. Wang, Y. Q. Wang, S. Xin, Y. G. Guo, and L. J. Wan. Facile synthesis of germanium nanocrystals and their application in organic-inorganic hybrid photodetectors. *Adv. Mater.*, 23:3704–3707, 2011.

[58] Y. Mawda. Visible photoluminescence from nanocrystalline Ge embedded in a glassy SiO_2 matrix: evidence in support of the quantum-confinement mechanism. *Phys. Rev. B*, 51:1658–1670, 1995.

[59] Y. H. Ye, J. Y. Zhang, X. M. Bao, X. L. Tan, and L. F. Chen. Visible photoluminescence from Ge^+-implanted SiO_2 films thermally grown on crystalline si. *Appl. Phys. A*, 67:213–217, 1998.

[60] S. Okamoto and Y. Kanemitsu. Photoluminescence properties of surface-oxidized Ge nanocrystals: surface localization of excitons. *Phys. Rev. B*, 54:16421–16424, 1996.

[61] R. Venkatasubramanian, D. P. Malta, M. L. Timmons, and J. A. Hutchby. Visible light emission from quantized planar Ge structures. *Appl. Phys. Lett.*, 59:1603–1605, 1991.

[62] D. J. Xue, J. J. Wang, and Y. Q. Wang. Facile synthesis of germanium nanocrystals and their application in organic-inorganic hybrid photodetectors. *Adv. Mater.*, 23:3704–3707, 2011.

[63] T. Y. Kim, N. M. Park, K. H. Kim, G. Y. Sung, Y. W. Ok, T. Y. Seong, and C. J. Choi. Quantum confinement effect of silicon nanocrystals in situ grown in silicon nitride films. *Appl. Phys. Lett.*, 85:5355–5357, 2004.

[64] M. Y. Song, A. Karatutlu, O. Ersoy, Y. Zhou, Y. X. Yang, Y. P. Zhang, W. R. Little, A. P. Wheeler, and A. V. Sapelkin. Spectroscopic super-resolution fluorescence cell imaging using ultra-small ge quantum dots. *arXiv:1503.09151*, 2015.

[65] D. D. Voughn, J. F. Bondi, and R. E. Schaak. Colloidal synthesis of air-stable crystalline germanium nanoparticles with tunable size and shapes. *Chem. Mater.*, 22:6103–6108, 2010.

[66] L. J. Hope-Weeks. Time dependent size and shape control of germanium nanocrystals. *Chem. Commun.*, 24:2980–2981, 2003.

[67] D. Bera, L. Qian, T. K. Tseng, and P. H. Holloway. Quantum dots and their multimodal applications: A review. *Materials*, 3:2260–2345, 2010.

[68] D. C. Lee, J. M. Pietryga, I. Robel, D .J. Werder, R. D. Schaller, and V. I. Klimov. Colloidal synthesis of infrared-emitting germanium nanocrystals. *J. Am. Chem. Soc.*, 131:3436–3437, 2009.

[69] W. Little, A. Karatutlu, D. Bolmatov, K. Trachenko, A. V. Sapelkin, G. Cibin, R. Taylor, F. Mosselmans, A. J. Dent, and G. Mountjoy. Structural origin of light emission in germanium quantum dots. *Sci. Rep.*, 4:7372, 2014.

[70] R. J. Nelmes, M. I. McMahon, N. G. Wright, D. R. Allan, and J. S. Loveday. Stability and crystal-structure of BC8 germanium. *Phys. Rev. B*, 48:9883–9886, 1993.

[71] D. Selli, I. A. Baburin, R. Martonak, and S. Leoni. Novel metastable metallic and semiconducting germaniums. *Sci. Rep.*, 3:1466, 2013.

[72] E. Muthuswamy, A. S. Iskandar, M. M. Amador, and S. M. Kauzlarich. Facile synthesis of germanium nanoparticles with size control: Microwave versus conventional heating. *Chem. Mater.*, 25:1416–1422, 2013.

[73] K. Lu. *Nanoparticulate materials: synthesis, characterization and processing*. John Wiley and Sons, New Jersey, 2012.

[74] D. Ferrer, D. A. Blom, L. F. Allard, S. Mejia, E. Perez-Tijerina, and M. Jose-Yacaman. Atomic structure of three-layer Au/Pd nanoparticles revealed by aberration-corrected scanning transmission electron microscopy. *J. Mater. Chem.*, 18:2442–2446, 2008.

[75] J. R. Weber, A. Janotti, and C. G. Van de Walle. Dangling bonds and vacancies in germanium. *Phys. Rev. B*, 87:035203, 2013.

[76] V. A. Yuryev, L. V. Arapkina, M. S. Storozhevykh, V. A. Chapnin, K. V. Chizh, O. V. Uvarov, V. P. Kalinushkin, E. S. Zhukova, A. S. Prokhorov, I. E. Spektor, and B. P. Gorshunov. Ge/Si(001) heterostructures with dense arrays of Ge quantum dots: morphology, defects, photo-emf spectra and terahertz conductivity. *Nanoscale Res. Lett.*, 7:414, 2012.

[77] H. W. Chiu, S. M. Kauzlarich, and E. Sutter. Thermal behaviour and film formation from an organogemernium polymer/nanoparticle precursor. *Langmuir*, 22:5455–5458, 2006.

[78] T. Proffen, S. J. L. Billinge, T. Egami, and D. Louca. Structural analysis of complex materials using the atomic pair distribution function – a practical guide. *Z. Kristallogr.*, 218:132–143, 2003.

[79] P. Bordet. Local structure studies using the pair distribution function. *Eur. Phys. J.*, 104:01003, 2015.

[80] R. E. Dinnebier and S. J. L. Billinge. *Powder Diffraction: Theory and Practice*. Royal Society of Chemistry, 2008.

[81] T. Proffen, K. L. Page, S. E. Mclain, B. Clausen, T. W. Darling, J. A. TenCate, S. Y. Lee, and E. Ustundag. Atomic pair distribution function analysis of materials containing crystalline and amorphous phases. *Z. Kristallogr*, 22:1002–1008, 2005.

[82] D. Tomanek and M. A. Schluter. Structure and bonding of small semiconductor clusters. *Phys. Rev. B*, 23:1208–1217, 1987.

[83] N. H. Chou, K. D. Oyler, N. E. Molt, and R. E. Schaak. Colloidal synthesis of germanium nanocrystals using room-temperature benchtop chemistry. *Chem. Mater.*, 21:4105–4107, 2009.

[84] C. A. Moore, J. J. Rocca, T. Johnson, G. J. Collins, and P. E. Russel. Large area electron-beam annealing. *Appl. Phys. Lett.*, 43:290–292, 1983.

[85] S. G. Ryu, I. Gruber, C. P. Grigoropoulos, D. Poulikakos, and S. J. Moon. Large area crystallization of amorphous Si with overlapping high repetition rate of laser pulses. *Thin Sold Films*, 520:6724–6729, 2012.

[86] W. Tseng, Dietrich H, J. Davey, A. Chrisou, and W. T. Anderson. The effects of ion-implantation and pulsed electron-beam anneal on Ge films grown epitaxially on (100) GaAs. *J. Electr. Mater.*, 9:685–692, 1980.

[87] H. Richter and Z. P. Wang. The one phonon Raman-spectrum in microcrystalline silicon. *Solid State Commun.*, 39:625–629, 1981.

[88] I. H. Campbell and P. M. Fauchet. The effects of microcrystal size and shape on the one phonon Raman-spectra of crystalline semiconductors. *Solid State Commun.*, 58:739–741, 1986.

[89] G. Gouadec and P. Colomban. Raman spectroscopy of nanomaterials: How spectra relate to disorder, particle size and mechanical properties. *Prog. Cryst. Growth Charact. Mater.*, 53:1–56, 2007.

[90] T. J. Penfold, C. J. Milne, and M. Chergui. Recent advances in ultrafast x-ray absorption spectroscopy of solutions. *Adv. Chem. Phys.*, 153:1–41, 2013.

[91] H. Wende. Recent advances in x-ray absorption spectroscopy. *Rep. Progr. Phys.*, 67:2105–2181, 2004.

[92] J. Yano and V. K. Yachandra. X-ray absorption spectroscopy. *Photosynth. Res.*, 102:241–254, 2009.

[93] F. Jiao, A. Harrison, J. C. Jumas, A. V. Chadwick, W. Kockelmann, and P. G. Bruce. Ordered mesoporous Fe_2O_3 with crystallite walls. *J. Am. Chem. Soc.*, 128:5468–5474, 2006.

[94] S. T. Oyama. Novel catalysts for advanced hydropocessing: transition metal phosphides. *J. Catal.*, 216:343–352, 2003.

[95] I. E. Wachs. Recent conceptual advances in the catalysis science of mixed metal oxide catalytic materials. *Cata. Today*, 100:79–94, 2005.

[96] X. L. Li, G. Pan, Y. W. Qin, T. D. Hu, Z. Y. Wu, and Y. N. Xie. EXAFS studies on absorption-desorption reversibility at manganese oxide-water interfaces II. Reversible absorption of zinc on delta-MnO_2. *J. Coll. Interf. Sci.*, 271:35–40, 2004.

[97] S. C. Liou, S. Y. Chen, H. Y. Lee, and J. S. Bow. Structural characterization of nano-sized calcium deficient apatite powders. *Biomaterials*, 25:189–196, 2004.

[98] F. Maillot, G. Morin, Y. H. Wang, D. Bonnin, P. Ildefonse, C. Chaneac, and G. Calas. New insight into the structure of nanocrystalline ferrihydrite: EXAFS evidence for tetrahedrally coordinated iron (III). *Geochim. Cosmochim. Acta*, 75:2708–2720, 2011.

[99] G. Pan, Y. W. Qin, X. L. Li, T. D. Hu, Z. Y. Wu, and Y. N. Xie. EXAFS studies on absorption-desorption reversibility at manganese oxides-water interfaces I. Irreversible absorption of Zinc onto manganite (gamma-MnOOH). *J. Coll. Interf. Sci.*, 271:28–34, 2004.

[100] M. Sasaki, M. Osada, N. Sugimoto, S. Inagaki, Y. Fukushima, A. Fukuoka, and M. Ichikawa. Novel templating fabrication of nano-structured Pt clusters and wires in the ordered cylindrical mesopores of FSM-16 and their unique properties in catalysis and magnetism. *Microp. Mesop. Mater.*, 21:597–606, 1998.

[101] Y. P. Zhang, O. Ersoy, A. Karatutlu, W. Little, and A. V. Sapelkin. Local structure of dots determined by combined numerical analysis of EXAFS and XANES data. *J. Synchrotron Radiat.*, 23:253–259, 2015.

[102] P. D'Angelo and A. Di Nola. An extended x-ray absorption fine structure study of aqueous solutions by employing molecular dynamics simulations. *J. Chem. Phys.*, 100:985–994, 1994.

[103] A. Filipponi and A Di Cicco. Short-range order in crystalline, amorphous, liquid, and supercooled germanium probed by x-ray-absorption spectroscopy. *Phys. Rev. B*, 51:12322–12336, 1995.

[104] S. W. T. Price, N. Zonias, C. K. Skylaris, A. E. Russel, and B. Ravel. The application of molecular dynamics to fitting EXAFS data. *J Phys. Conf. Ser.*, 430:012009, 2013.

[105] J. J. Rehr and R. C. Albers. Theoretical approaches to x-ray absorption fine structure. *Rev. Mod. Phys.*, 72:621, 2000.

[106] I. T. Todorov, W. Smith, K. Trachenko, and M. T. Dove. DL_POLY_3: new dimensions in molecular dynamics simulations via massive parallelism. *J. Mater. Chem.*, 16:1911–1918, 2006.

[107] R. Ke, X. Zhang, L. Wang, C. Zhang, H. Niu, C. Mao, J. Song, B. Jin, and Y. Tian. Enhanced electrochemiluminescence of cdse quantum dots coupled with MoS_2-chitosan nanosheets. *J. Solid State Eletrochem.*, 19:1633–1641, 2015.

[108] A. Samavati, M. K. Mustafa, Z. Othaman, and S. K. Ghoshal. Ge nanoislands grown by radio frequency magnetron sputtering: comprehensive investigation of surface morphology and optical properties. *J. Nanomater.*, 2015:681242, 2015.

[109] A. Samavati, Z. Othaman, S. K. Ghoshal, and M. K. Mustafa. Effects of annealing temperature on shape transformation and optical proerpties of germanium quantum dots. *Chin. Phys. B*, 24:028103, 2015.

[110] R. J. Nelmes, M. I. McMahon, N. G. Wright, D. R. Allan, and J. S. Loveday. Stability and crystal structure of BC8 germanium. *Phys. Rev. B*, 48:9883–9886, 1993.

[111] D. Norman. X-ray absorption spectroscopy (EXAFS and XANES) at surfaces. *J. Phys. C-Solid State Phys.*, 19:3273–3311, 1986.

[112] S. Pin, V. Letilly, B. Alpert, and R. Cortes. XANES spectroscopy sensitivity to small electronic changes. case of carp azidomethemoglobin. *Febs. Lett.*, 242:401–404, 1989.

[113] M. Newville. Fundamentals of XAFS. *Rev. Mineral. Geochem.*, 78:33–74, 2014.

[114] Y. Joly. X-ray absorption near-edge structure calculations beyond the muffin-tin approximation. *Phys. Rev. B*, 63:125120, 2001.

Chapter 2

Synchrotron radiation and XAS

In this chapter, the history and current state of XAS technique will be described. XAS experiments are most commonly carried out at a synchrotron radiation source (SRS), hence a brief introduction to SRS and its relevance to XAS will be addressed. Indeed, the synchrotron radiation source plays an important role in scientific activities today, supporting not only XAS but also other research including macromolecular crystallography, small angle X-ray scattering, X-ray total scattering and microscopic imaging. Historically, it was just owing to the setup of XAS beamline at SRS that helped to finalise the theoretical description of EXAFS and boosted the application of XAS as a powerful structure probing technique.

2.1 Overview of synchrotron radiation

For the measurement of X-ray absorption spectra, an X-ray source with continuous energy is necessary. Before the age of synchrotron radiation sources for XAS measurements the only continuous X-ray source was lab-based Bremsstrahlung radiation. However, the low brightness of the Bremsstrahlung radiation restricted the development and application of XAS technique in early days.

The situation was significantly changed with the synchrotron radiation beamline for XAS experiments starting to be built – the first operating XAS beamline was set up during the early 1970s by Stern, et al. [1]. The synchrotron radiation has several important properties and advantages over the traditional light sources, including: (1) high intensity, (2) broad spectral range, (3) high polarization, (4) natural collimation. For example, as can be seen from Fig. 2.1, the brilliance of the X-ray source from the synchrotron radiation is a great advantage over the traditional light source based on the Bremsstrahlung radiation.

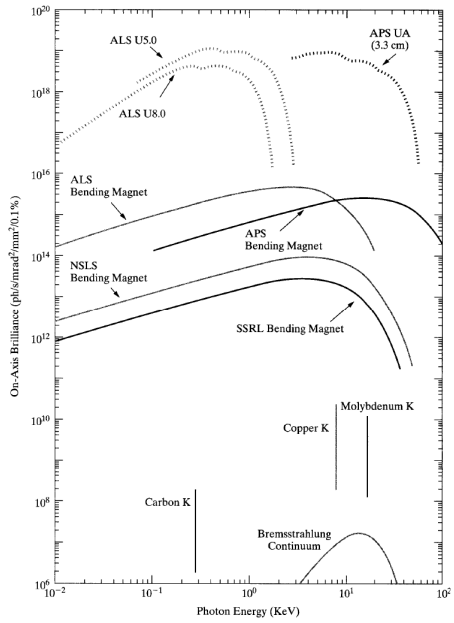

Fig. 2.1 The comparison of X-ray source brilliance between the synchrotron and Bremsstrahlung radiation [2].

The first generation of the synchrotron radiation source dates back to 1950-1960s. [3], which, however, was not primarily designed or operated as the source of radiation for the spectroscopy measurements, but instead served mainly for high-energy or nuclear physics. With growing interest in applying synchrotron radiation for the solid-state research, the storage ring, as a source of the radiation, was gradually developed in 1970s. It was until 1974 that the first machine designed specifically for generating the synchrotron radiation was commissioned in Japan [3].

With the growing of the user group and experimental demand in 1970s-1980s, reports and proposals for setting up facilities dedicated for the synchrotron radiation had been submitted to government or other foundations in many countries, such as US, European Science Foundation, Japan and China. Following such trends, the second generation of the synchrotron radiation sources (the dedicated source) were built around the world. For example, the US National Synchrotron Light Source (NSLS) at the Brookhaven National Laboratory was approved in 1976 and construction was completed in 1981. The 2-GeV electron storage ring at Daresbury Laboratory in UK started to serve users in 1981, among others [4].

Starting from 1990s, the synchrotron radiation source came to its third generation, which is the one currently in use. For the third generation, the storage ring was designed to include the

insertion devices such as wigglers and undulators for the purpose of optimizing the brightness of the radiation beam. The European Synchrotron Radiation Facility (ESRF) in France was the first third generation hard X-ray source, which came on line for users with a 6 GeV storage ring in 1994 [4]. The Diamond Light Source in UK, the one that our beamtime was mainly based in, was formally opened to users in October, 2007. In my own country China, the Shanghai Synchrotron Radiation Facility (SSRF) started to be built in 2004 and the first synchrotron light was seen in 2007, and 'the $176 million is China's biggest investment in a single science facility to date (2009)', according to a report from Nature [5]. Information about the currently available third generation synchrotron radiation sources around the world can be found in the following reference: [6].
Following the overview of synchrotron radiation sources, a brief introduction to the history and application of XAS will be given in the following two sections.

2.2 A brief history of XAS

The early theoretical description for XAS dates back to the 1930s, when Kronig gave his explanation for the fine structure well beyond the absorption edge based on long-range order (LRO) theory [7]. Essentially, Kronig attributed fine structure to the changing of DOS at the Brillouin zone, which was derived from the Bloch band structure theory [8]. Owing to the explanation by Kronig, the fine structure of the extended region of XAS spectra was called Kronig structure in early days [7]. However, it is now well known that EXAFS is dominated by the short-range order (SRO) and the LRO theory based explanation turns out to be wrong [1]. As a matter of fact, Kronig did develop the SRO theory for the fine structure, but only for molecules (LRO theory for crystals). Beyond Kronig's work, in 1941, Kostarev proposed that the SRO theory should be used for both solids and molecules. However, Kronig's explanation had been predominant until late in the 1960s [1]. For example, it was only until the late 1950s that Farrel W. Lytle, one of the pioneers of the modern XAS theory, started to realize that the fine structure is an SRO related phenomenon [7]. During the late 1960s, experiments were carried out, attempting to distinguish between the SRO and LRO theory, but the controversy still was not clarified [9, 10]. The main restriction in developing XAS theory comes from the experimental side, since it is necessary to obtain data if high enough quality to test the predictions from different theoretical descriptions. For example, experiments on a series of perovskites by Perel et al. (1970) was carried out, which was designed to distinguish the LRO and SRO theories. But the conclusion was drawn that neither LRO nor SRO theory is supported by their data [10].

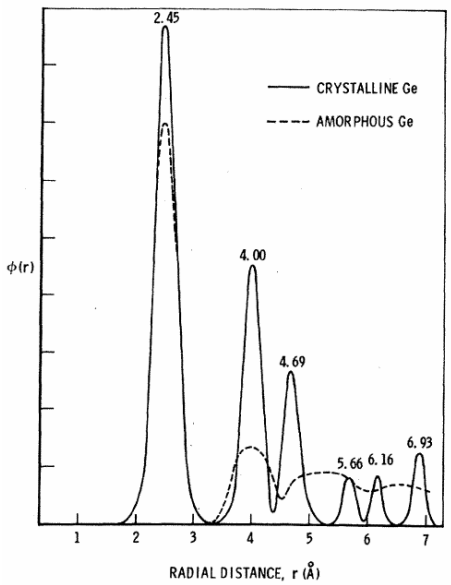

Fig. 2.2 The first Fourier transform pattern of the EXAFS spectra, for crystalline and amorphous Ge [11].

The controversy between the LRO and SRO theories came to an end in the early 1970s, when the collaboration between Edward A. Stern, Dale Sayers and Farrel W. Lytle brought EXAFS to its modern era. First of all, during the late 1960s, the experimental work in Lytle's laboratory showed that the simple Kronig theory does not work [7]. In 1969, the first version of the modern EXAFS theory was published [12], in which the EXAFS was treated as the result of the interaction (interference) between the ejected outgoing and scattered (by the neighbouring atoms as the point scatters) photoelectron wave. Soon after that, Dale Sayers simplified the obtained EXAFS equation and started to carry out the Fourier transform of the EXAFS spectra. In 1971, Sayers, et al. published the Fourier transform method for analysing the EXAFS spectra on *Phys. Rev. Lett.* [11]. Since then, not only was the appropriate EXAFS theory available, but also EXAFS spectra can be further transformed to real space to obtain a pattern similar with the radial distribution function (RDF) for unknown structure analysis. Fig. 2.2 shows the first reported Fourier transform pattern presented in Sayers's paper, for crystalline and amorphous Ge.

The modern EXAFS theory is based on the scattering theory, for which the scattering amplitude and the phase shift corresponding to the scattering from neighbour atoms are crucial parameters for the theoretical description and further structural analysis. Early theoretical analysis only relied on the transferring of these parameters from the known to unknown structure, and the quantitative calculation of the EXAFS spectra started from a

theory development by Lee and Pendry in 1975, including the multiple scattering effect [13]. Following that, endeavours have been devoted to improvement on the reliability of the quantitative theoretical calculation, and one of the most typical examples is the development of the FEFF code by Rehr, et al. [14], which is now widely used in the XAS world for theoretical description and data analysis. For example, the Demeter package [15] developed by Bruce Ravel, et al. (2005), which was intended for extracting structural parameters based on the FEFF calculation and IFEFFIT fitting algorithm, has become one of the standard tools for the EXAFS data analysis. On the experimental side, the importance of the SRS should be mentioned, which provides the high-quality continuous X-ray source for the XAS measurements and thus boosted the application of XAS as a powerful local structure probing technique.
In the next section, an overview of the XAS in modern scientific research will be given.

2.3 The application of XAS

The theoretical development and application of synchrotron radiation sources brought XAS to to the modern era, opening up the XAS technique to wide scientific research. As one of the main techniques for probing local structure of materials, it has been widely used in the areas of catalysts [16, 17], bio-chemistry [18, 19], electrochemistry [20, 21], earth and environmental science [22, 23], nano- [24, 25] and amorphous materials [26, 27]. For example, XAS has been used in the area of state-of-the-art catalyst research – the single atom catalysis such as the single-atom catalysis of CO oxidation using Pt_1/FeO_x [28]. In our own work, the XAS technique was employed to explore the local structure of Ge quantum dots [29, 30].
Site selectivity of XAS makes it a more suitable choice when looking into the complicated chemical environment, as compared to other commonly used techniques such as PDF based methods. For example, XAS was employed to probe the complex interfacial water chemistry on gold electrodes, reported in 2014 in *Science* [31]. Moreover, the possibility of very fast measurements (down to microseconds) makes XAS an ideal choice for exploring chemical processes in batteries, catalysis, nanomaterials, and among others, using the *in situ* and/or *operando* measurements [32–34]. For example, the *in situ* XAS was used to look into the initial kinetic nucleation of gold nanoparticles [35]. Especially in recent years, with the development of the X-ray free electron laser, the picosecond or even femtosecond time-resolved XAS has already been realized for various systems [36–38].

Nowadays, the synchrotron radiation sources promise high-quality XAS experimental data with high signal-to-noise ratio, and the maturing theoretical description also allows more and more accurate analysis for the experimental results. Also the powerful data analysis tools are available, such as the aforementioned Demeter package which contains Athena for background subtraction and Artemis for parameters fitting. All of these make it possible to carry out comprehensive and complicated structural analysis based on XAS alone. For example, an advanced fitting technique for EXAFS spectra analysis was developed by A. Frenkel, et al. (2012) to work on bimetallic systems for characterizing the core-shell structure [39]. Also reported by A. Frenkel, et al. (2014), a strategy to derive the nanoparticle size based on the comprehensive EXAFS analysis and atomic structure modelling was developed, which agrees well with the average size of the representative nanoparticles obtained by scanning transmission electron microscope (STEM) [40].
Moreover the XAS technique can be combined with other commonly used techniques for comprehensive structural characterization. For example, the X-ray scattering could provide the LRO information that is not accessible by XAS. In our own work, several techniques were combined with XAS to look into the structure of QDs and amorphous systems. From the perspective of theoretical description, the calculation of either EXAFS or XANES benefits a lot from the first-principle (e.g. DFT) and molecular dynamics (MD) simulations. In our own work, the combined MD-FEFF simulation was carried out on QDs and amorphous systems to explore the structural configurations.

In the next chapter, the discussion will move on to specific introduction to the XAS techniques, including the spectra measurement and the basic data analysis.

References

[1] E. A. Stern. Musings about the development of XAFS. *J. Synchrotron Rad.*, 8:49–54, 2001.

[2] Properties of x-ray. http://web.stanford.edu/group/glam/xlab/MatSci162_172/LectureNotes/, Jan 2016. online; accessed 08-July-2016.

[3] H. Winick and S. Doniach. *Synchrotron Radiation Research*. Plenum Press · New York and London, 1980.

[4] et al. A. C. Thompson. *X-ray Data Booklet*. Lawrence Berkley National Laboratory, 2009.

[5] E. Marris. China joins world-class synchrotron club. *Nature*, 459:16–17, 2009.

[6] Lightsources of the world. http://www.lightsources.org/regions, Jul 2016. online; accessed 08-July-2016.

[7] F. W. Lytle. The EXAFS family tree: a personal history of the development of extended X-ray absorption fine structure. *J. Synchrotron Rad.*, 6:123–134, 1999.

[8] E. A. Stern. Dale Sayers Festschrift. *AIP Conf. Proc.*, 882:3–9, 2007.

[9] L. V. Azaroff and D. M. Pease. *X-ray Spectroscopy*. New York: McGraw-Hill, 1974.

[10] J. Perel and R. D. Deslattes. Extended fine structure in x-ray absorption spectra of certain perovkites. *Phys. Rev. B*, 2:1317–1323, 1970.

[11] D. E. Sayers, E. A. Stern, and F. W. Lytle. New technique for investigating nanocrystalline structures: Fourier analysis of the extended x-ray-absorption fine structure. *Phys. Rev. Lett.*, 27:1204–1207, 1971.

[12] *BSRL document D1-82-0880*, Boeing, USA, 1969.

[13] J. J. Rehr and A. L. Ankudinov. Progress and challenges in the theory and interpretation of x-ray spectra. *J. Synchrotron Rad.*, 8:61–65, 2001.

[14] J. J. Rehr and R. C. Albers. Theoretical approaches to x-ray absorption fine structure. *Rev. Mod. Phys.*, 72:621, 2000.

[15] B. Ravel and M. Newville. ATHENA, ARTEMIS, HEPHAESTUS: data analysis for x-ray absorption spectroscopy using IFEFFIT. *J. Synchrotron Rad.*, 12:537–541, 2005.

[16] K. Mori, K. Miyawaki, and H. Yamashita. Ru and Ru-Ni nanoparticles on TiO_2 support as extremely active catalysts for hydrogen production from ammonia-borane. *ACS Catal.*, 6:3128–3135, 2016.

[17] K. R. Yang, A. J. Matula, G. Kwon, J. Hong, S. W. Sheehan, J. M. Thomsen, G. W. Brudvig, R. H. Crabtree, D. M. Tiede, L. X. Chen, and V. S. Batista. Solution structures of highly active molecular Ir water-oxidation catalysts from density functional theory combined with high-energy x-ray scattering and EXAFS spectroscopy. *J. Am. Chem. Soc.*, 138:5511–5514, 2016.

[18] H. Ade and H. Sroll. Near-edge x-ray absorption fine-structure microscopy of organic and magnetic materials. *Nat. Mater.*, 8:281–290, 2009.

[19] G. Hähner. Near edge x-ray absorption fine structure spectroscopy as a tool to probe electronic and structural properties of thin organic films and liquids. *Chem. Soc. Rev.*, 35:1244–1255, 2006.

[20] X. S. Liu, D. D. Wang, G. Liu, V. Srinivasan, Z. Liu, Z. Hussain, and W. L. Yang. Distinct charge dynamics in battery electrodes revealed by in situ and operando soft x-ray spectroscopy. *Nat. Commun.*, 4:2568, 2013.

[21] T. A. Pascal, K. H. Wujcik, J. Velasco-Velez, C. H. Wu, A. A. Teran, M. Kapilashrami, J. Cabana, J. H. Guo, M. Salmeron, N. Balsara, and D. Prendergast. X-ray absorption spectra of dissolved polysulfides in lithium-sulfur batteries from first-principles. *Phys. Chem. Lett.*, 5:1547–1551, 2014.

[22] Y. Ping, F. Coppari, D. G. Hicks, B. Yaakobi, D. E. Fratanduono, S. Hamel, J. H. Eggert, J. R. Rygg, R. F. Smith, D. C. Braun, T. R. Boehly, and G. W. Collins. Solid iron compressed up to 560 GPa. *Phys. Rev. Lett.*, 111:065501, 2013.

[23] B. Thalmann, A. Voegelin, U. V. Gunten, R. Behra, E. Morgenroth, and R. Kaegi. Effect of ozone treatment on nano-sized silver sulfide in wastewater effluent. *Environ. Sci. Technol.*, 49:10911–10919, 2015.

[24] S. Alayoglu, P. Zavalij, B. Eichhorn, Q. Wang, A. I. Frenkel, and P. Chupas. Structural and architectural evaluation of bimetallic nanoparticles: A case study of Pt-Ru core-shell and alloy nanoparticles. *ACS Nano*, 10:3127–3137, 2009.

[25] B. J. Hwang, L. S. Sarma, J. M. Chen, C. H. Chen, S. C. Shih, G. R. Wang, D. G. Liu, J. F. Lee, and M. T. Tang. Structural models and atomic distribution of bimetallic nanoparticles as investigated by x-ray absorption spectroscopy. *J. Am. Chem. Soc.*, 127:11140–11145, 2005.

[26] A. M. Shahin, F. Grandjean, G. J. Long, and T. P. Schuman. Cerium L_{III}-edge XAS investigation of the structure of crystalline and amorphous cerium oxides. *Chem. Mater.*, 17:315–321, 2005.

[27] A. V. Sapelkin, S. C. Bayliss, A. G. Lyapin, V. V. Brazhkin, and A. J. Dent. Structure of bulk amorphous GaSb: a temperature-dependent EXAFS study. *Phys. Rev. B*, 56:11531–11535, 1997.

[28] B. T. Qiao, A. Q. Wang, X. F. Yang, L. F. Allard, Z. Jiang, Y. T. Cui, J. Y. Liu, J. Li, and T. Zhang. Single-atom catalysis of CO oxidation using Pt1/FeO_x. *Nat. Chem.*, 3:634–641, 2011.

[29] Y. P. Zhang, A. Karatutlu, O. Ersoy, W. Little, G. Cibin, A. Dent, and A. Sapelkin. Structure and effects of annealing in colloidal matrix-free ge quantum dots. *J. Synchrotron Rad.*, 22:105–112, 2015.

[30] Y. P. Zhang, O. Ersoy, A. Karatutlu, W. Little, and A. Sapelkin. Local structure of Ge quantum dots determined by combined numerical analysis of EXAFS and XANES data. *J. Synchrotron Rad.*, 23:253–259, 2016.

[31] J. J. Velasco-Velez, C. H. Wu, T. A. Pascal, L. F. Wan, J. H. Guo, D. Prendergast, and M. Salmeron. The structure of interfacial water on gold electrodes studied by x-ray absorption spectroscopy. *Science*, 346:831–834, 2014.

[32] C. J. Pelliccione, E. V. Timofeeva, and C. U. Segre. Potential-resolved in situ x-ray absorption spectroscopy study of Sn and SnO_2 nanomaterial anodes for lithium-ion batteries. *J. Phys. Chem. C*, 120:5331–5339, 2016.

[33] Y. Gorlin, B. Lassalle-Kaiser, J. D. Benck, S. Gul, S. M. Webb, V. K. Yachandra, J. Yano, and T. F. Jaramillo. In situ x-ray absorption spectroscopy investigation of a bifunctional manganese oxide catalyst with high activity for electrochemical water oxidation and oxygen reduction. *J. Am. Chem. Soc.*, 135:8525–8534, 2012.

[34] K. Yu, T. Yao, Z. Y. Pan, S. Q. Wei, and Y. Xie. Structural evolution in the nanoscale diffusion process: a Au-Sn bimetallic system. *Dalton Trans.*, pages 10353–10358, 2009.

[35] T. Yao, Z. H. Sun, Y. Y. Li, Z. Y. Pan, H. Wei, Y. Xie, M. Normura, Y. Niwa, W. S. Yan, Z. Y. Wu, Y. Jiang, Q. H. Liu, and S. Q. Wei. Insights into initial kinetic nucleation of gold nanocrystals. *J. Am. Chem. Soc.*, 132:7696–7701, 2010.

[36] Y. Obara, T. Katayama, Y. Ogi, T. Suzuki, N. Kurahashi, S. Karashima, Y. Chiba, Y. Isokawa, T. Togashi, Y. Inubushi, M. Yabashi, T. Suzuki, and K. Misawa. Femtosecond time-resolved x-ray absorption spectroscopy of liquid using a hard x-ray free electron laser in a dual-beam dispersive detection method. *Opt. Express*, 22:1105–1113, 2014.

[37] H. T. Lemke, C. Bressler, L. X. Chen, D. M. Fritz, K. J. Gaffney, A. Galler, W. Gawelda, K. Haldrup, R. W. Hartsock, H. Ihee, J. Kim, K. H. Kim, J. H. Lee, M. M. Nielsen, A. B. Stickrath, W. K. Zhang, D. L. Zhu, and M. Cammarata. Femtosecond x-ray absorption spectroscopy at a hard x-ray free electron laser: Application to spin crossover dynamics. *J. Phys. Chem. A*, 117(4):735–740, 2013.

[38] F. Zamponi, T. J. Penfold, M. Nachtegaal, A. L*ü*bcke, J. Rittmann, C. J. Milne, M. Chergui, and J. A. Bokhoven. Probing the dynamics of plasmon-excited hexanethiol-capped gold nanoparticles by picosecond x-ray absorption spectroscopy. *Phys. Chem. Chem. Phys.*, 16:23157, 2014.

[39] A. I. Frenkel. Applications of extended x-ray absorption fine-structure spectroscopy to studies of bimetallic nanoparticle catalysts. *Chem. Soc. Rev.*, 41:8163–8178, 2012.

[40] J. Q. Wang, Q. Wang, X. H. Jiang, Z. N. Liu, W. M. Yang, and A. I. Frenkel. Determination of nanoparticle size by measuring the metal-metal bond length: The case of palladium hydride. *J. Phys. Chem. C*, 119:854–861, 2014.

Chapter 3

XAS techniques - Theory basics and Experiments

This chapter will focus on the theoretical and experimental fundamentals of the XAFS technique, from the theoretical description and formulation, data processing, to the experimental measurements of XAFS spectra. An overview of XAS spectra will be presented in section-3.1, and section-3.2 considers the various measurement modes of XAFS spectra. Section-3.3 and 3.4 will present the formulation, data processing and analysis for the EXAFS spectra. The last section then focuses on another important portion of the XAFS spectra – XANES, of which the advantage upon exploring the local environment of nano- and amorphous systems will be discussed.

3.1 Fundamentals of XAS

A typical absorption process is illustrated in Fig. 3.1. The incident electromagnetic radiation (I_0) falls on the sample, some fraction is absorbed and some transmitted (I). By introducing the linear attenuation coefficient μ, the absorption process can be described as:

$$\frac{dI}{I_0} = -\mu dx \tag{3.1}$$

where μ is defined as the absorption (attenuation) coefficient. By rearranging equation-(3.1) and integrating on both sides, it is straightforward to obtain the expression for the light intensity I as the function of penetrating depth x:

$$I = I_0 e^{-\mu x} \tag{3.2}$$

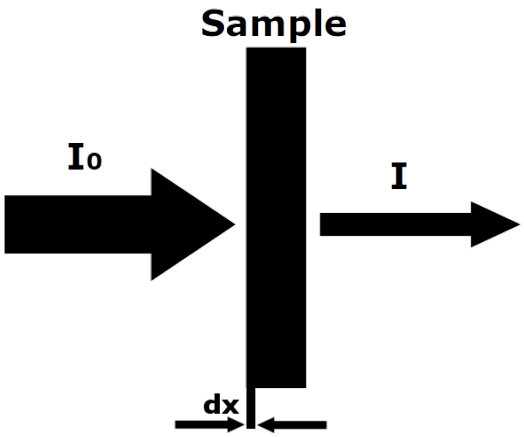

Fig. 3.1 Depiction of photon absorption.

For X-ray absorption, the attenuation coefficient μ is a function of the incident X-ray photon energy E. In general, $\mu(E)$ decreases as the energy E increases, approximately as $1/E^3$, as shown in Fig. 3.2. At a certain energy value, there is a sudden jump of the absorption coefficient which is called the *absorption edge*. This corresponds to the electron transition from the core level (e.g. 1s, 2s, 2p, etc.) to conduction band (CB) induced by the incident X-ray photons. According to the different initial core levels, the absorption edge is named as K-edge (1s excitation), L-edge (2s and 2p excitation), etc., as illustrated in Fig. 3.2. Historically, the X-ray absorption spectra was recorded on strips of the photographic film, and the intense absorption peaks showed up as a heavily exposed lines on the developed film, leaving white lines on the film as shown at the bottom of in Fig. 3.2. Therefore the absorption edge is also called a *white line*. With the absorption edge as a reference, the whole XAFS spectra can be divided to two main portions – XANES (X-ray absorption near-edge structure), which extends to ~30 eV above the absorption edge and EXAFS (extended X-ray absorption fine structure), which can extend to 500 – 1000 eV beyond the edge.
In general, the absorption coefficient μ is linked to the cross section σ (cm^2/g, effective light-matter interaction area) and density ρ (g/cm^3):

$$\mu = \rho\sigma \approx \sum_i \rho_i \sigma_i \tag{3.3}$$

where the sum is over all elements in the material. For XAFS, equation-(3.3) only describes the background absorption, which refers to the situation of isolated atoms. However the utility of XAFS relies on the fact that the absorption coefficient is strongly modulated, as a function of energy, by the proximity of neighbouring atoms. Therefore for further analysis

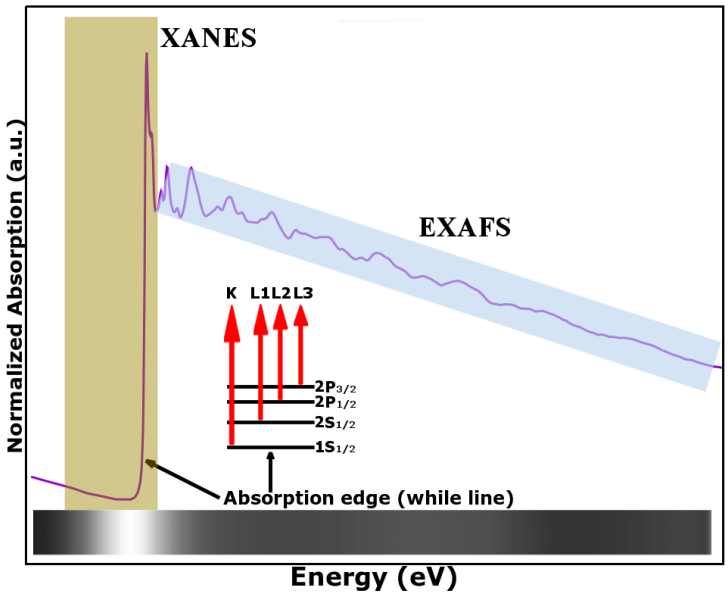

Fig. 3.2 An example of XAFS spectra. The two shaded regions (with different color) indicates the XANES and EXAFS regime, respectively. The inset energy diagram illustrates the transition corresponding to different absorption edges. The black-white strip shown at the bottom is an example for the absorption spectra recorded on the photographic film, which shows the white line corresponding to the absorption edge.

of the XAFS spectra (especially for EXAFS) to extract the local structural information, the background absorption should be subtracted to focus on the fine wiggling structures. An example of the XAFS spectra for GaSb with the corresponding background absorption is shown in Fig. 3.3 (a). To directly compare the experimental XAFS spectra with theory, and also to regularize the data with respect to variation in experimental set-ups including sample thickness, concentration, detector settings and any other aspects of the measurements, the XAFS spectra should be normalized before the background subtracted. In practice, the background subtraction and normalization process can be packaged together into a single expression:

$$\chi(E) = \frac{\mu(E) - \mu_0(E)}{\Delta\mu(E)} \tag{3.4}$$

where $\mu(E)$ and $\mu_0(E)$ are the raw spectra and background absorption, respectively, and $\Delta\mu(E)$ in the denominator refers to the edge step as presented in Fig. 3.3 (a). Here the edge step instead of the absolute absorption coefficient at the edge is used for the normalization. The reason for that is in some cases (e.g. gold hydroxide), the experimental measurement

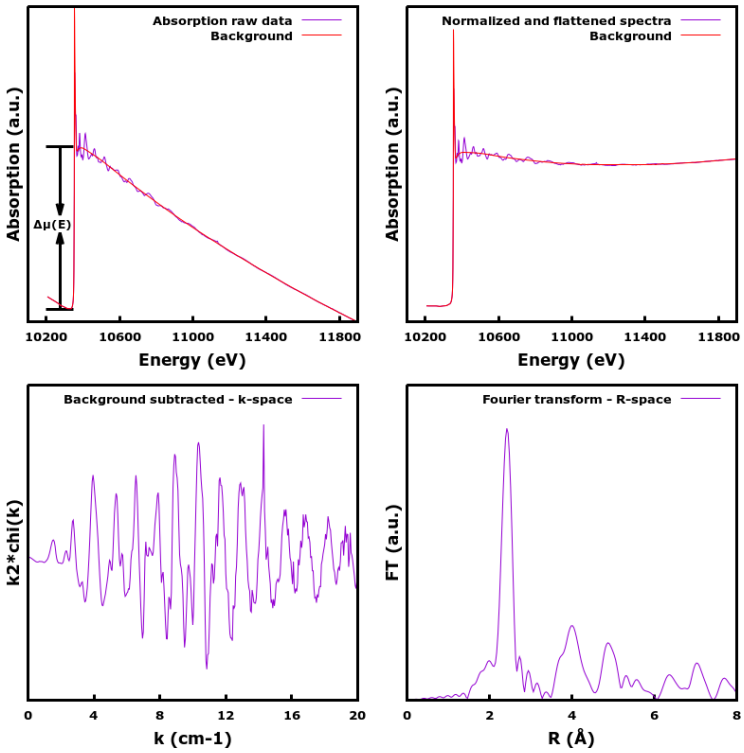

Fig. 3.3 (a) Example XAFS spectra of crystalline GaSb with background absorption. (b) Normalized spectra together with the background signal. (c) Spectra in k-space. (d) Fourier transform of the spectra.

will give negative absorption due to the strong excited emission. Then using the absolute absorption coefficient will lead to the phase inversion of the extracted $\chi(E)$ spectra. The normalized XAFS spectra is shown in Fig. 3.3 (b), for which the flattening algorithm is also applied to bring the originally tilting pre- and post-edge spectra to their horizontal positions for visualization.

After the normalization and background subtraction, the $\chi(E)$ spectra could be obtained, which can be further transformed into the $\chi(k)$ spectra in k-space by applying the following $E-k$ relation:

$$k = \sqrt{\frac{2m(E-E_0)}{\hbar^2}} \tag{3.5}$$

where E_0 refers to the absorption edge position in energy. The $E-k$ transformation is necessary, which makes it straightforward to compare with the theoretical calculation that is directly based on wavenumber (k) rather than energy. A more important reason lies in that the Fourier transform of the spectra in k-space will give the RDF-like pattern in R-space, which

then can be directly linked to the structure. The example XAFS spectra (for GaSb) in k-space and the following Fourier transform result are shown in Fig. 3.3 (c) and (d), respectively.
In the next section, the introduction to the several measurement modes for XAS spectra will be presented, including the transmission mode, fluorescence mode and the optical detection mode.

3.2 XAS spectra measurement

The modern XAFS spectra measurements at synchrotron radiation source (SRS) are relatively straightforward, provided the intense and energy tunable source of X-rays. The experimental techniques and facilities available at SRS allows the XAFS measurements with high energy resolution, high spatial resolution, and under extreme conditions of temperature and pressure. The specific characteristics of SRS and experimental station determine the energy range,

Table 3.1 Parameters of B18 beamline at Diamond Light Source

Beamline parameters	
Energy range (keV)	2.05 – 35
Energy resolution ($\Delta E/E$)	Si-111 : 1.4×10^{-4} (2.05 – 20 keV) Si-311 : 3×10^{-5} (4 – 35 keV)
Flux @ 8 keV at sample (ph/s, Si-111)	5×10^{11}
Beam size at sample (μm)	200 (H) $\times$ 250 (V)
Beam divergence at sample (FWHM, mrad)	1.9 (H) $\times$ 0.22 (V)
Source parameters	
Electron energy	3 GeV
Beam current	500 mA
Beam emittance	2.7 nm·rad
Dipole magnetic field	1.4 T
Dipole bending radius	7.148 m
Critical energy	8.39 keV
Brightness at 10 keV (ph/sec/mm^2/mrad^2/0.1%BW/300 mA)	3.8×10^{15}

beam sizes and intensities which often puts practical limitations on the XAFS measurements [1]. Here the typical parameters of B18 beamline at Diamond light source, where our XAFS experiments are mainly based, is given in Table. 3.1.
In practice, there are several available detection modes for XAS spectra measurement, including the transmission mode and fluorescence mode. Also in our experiments, the X-ray

excited optical luminescence (XEOL) was measured to extract the corresponding XAFS spectra, which is for the purpose of exploring the sub-structure responsible for the light emission in the QDs system. In general, the detection method for an XAS experiment could be chosen according to a specific sample situation and/or experimental purpose. Here an overview of the three detection modes mentioned above will be given.

3.2.1 Transmission mode

The transmission detection mode is the simplest method for XAFS spectra measurement, where the intensity of the incident and outgoing beam are measured directly using the ion chamber, as illustrated in Fig. 3.4. The absorption coefficient then can be obtained by

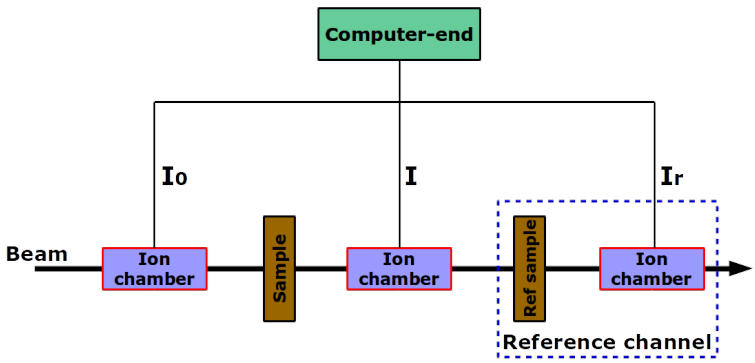

Fig. 3.4 The illustration of the transmission detection mode for XAS measurement.

simply inserting the measured I and I_0 into equation-(3.2). The compartment within the dashed box in Fig. 3.4 refers to the reference channel in some situations. Usually the sample as the reference should be a standard foil, which will yield consistently high-quality data for all measurements taken at different time. With such a reference channel alongside the sample measurements, it becomes convenient to align experimental data from different measurements, even for data measured years apart at different synchrotrons [2].

In general, to use the transmission mode for the XAS measurement, the sample should be made uniform on a scale determined by the *absorption length* of the material. The absorption length is defined as:

$$\text{absorption length} \equiv \frac{1}{\mu} \tag{3.6}$$

which refers to the distance over which the intensity of the incident X-ray decreases by $1/e \approx 37\%$. The absorption coefficient (and the absorption length) can be estimated for

specific material using equation-(3.3), and in principle the thickness of sample should be kept below $\sim 2-3$ absorption lengths to minimize the thickness effect in transmission mode. Moreover, the transmission mode favours concentrated samples, which is beneficial for getting a signal with high signal-to-noise ratio. For our XAS measurement at ambient condition, the Ge QDs sample was suspended in organic solvents, such as ethanol and hexanol, forming a dense solution. Therefore the transmission mode was mainly used. In principle, the non-uniform thickness distribution effect should also be taken into consideration for inhomogeneous samples (see detailed introduction in G. Bunker's book: Ref. [3]). However as mentioned above, our Ge QDs samples for the XAS measurement are often in the colloidal form, and therefore the thickness effect is not the main factor.

3.2.2 Fluorescence mode

After being excited by the incident X-ray, there are several possible ways for the photoelectrons to decay. One of the decay processes is the jumping back to the core-level to emit fluorescence, as shown in Fig. 3.5 (a). In principle, the intensity of the fluorescence induced

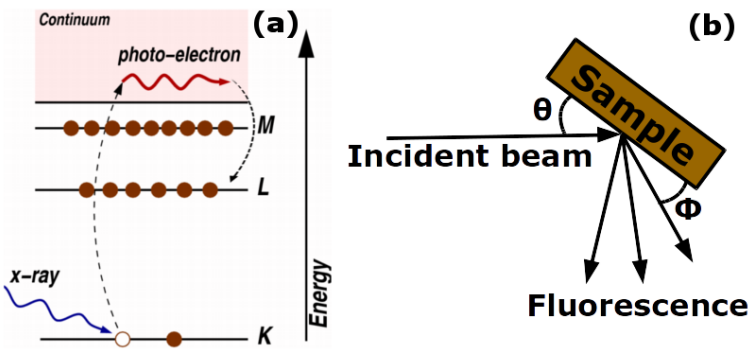

Fig. 3.5 (a) The energy diagram showing the decay of photoelectron through fluorescence. (b) Illustration for the fluorescence measurement, showing the incident (θ) and exit (ϕ) angle. Reproduced from Ref. [1].

by X-ray excitation is proportional to the absorption coefficient, therefore fluorescence can be used to measure the XAFS spectra. However for the fluorescence measurement mode, the attenuation of the measured XAFS oscillations due to the *self-absorption* effect should be taken into account. Basically, fluorescence X-rays tend to be absorbed again by the material, which then will trigger continuous fluorescence to be detected alongside the initial fluorescence. Such processes tend to dampen the XAFS oscillations. In the worst case of a

thick sample with a pure element, the incident X-ray will all be absorbed. Since the escape length of fluorescence X-ray is much longer than the penetration depth of incident X-ray, all the fluorescence X-ray can be detected. Therefore in such situations, the measured XAFS spectra will simply change with the energy as $1/E^3$ without any fine structures – a disaster for further XAFS analysis.

In fact, considering the self absorption effect and the incident and exit angle as shown in Fig. 3.5 (b), the exact expression of the fluorescence intensity is given as [1]:

$$I_f = I_0 \frac{\varepsilon \Delta\Omega}{4\pi} \frac{\mu_\chi(E)\{1 - e^{-[\mu_{tot}(E)/sin\theta + \mu_{tot}(E_f)/sin\phi]t}\}}{\mu_{tot}(E)/sin\theta + \mu_{tot}(E_f)/sin\phi} \tag{3.7}$$

where ε is the fluorescence efficiency, $\Delta\Omega$ the solid angle of the detector, and the whole term $\varepsilon\Delta\Omega/4\pi$ can be regarded as constant, E_f is the photon energy of the fluorescence, t is the thickness of the sample, $\mu_{tot}(E)$ and $\mu_\chi(E)$ are the total absorption of the sample and that from the element of interest, respectively. In practical XAFS measurements, there are two limit situations – thin sample and thick-dilute sample – where equation-(3.7) can be simplified, making the fluorescence measurement mode straightforward to follow. For thin sample, $\mu \ll 1$, therefore:

$$\begin{aligned} &[\mu_{tot}(E)/sin\theta + \mu_{tot}(E_f)/sin\phi]t \ll 1 \\ &\Downarrow \\ 1 - e^{-[\mu_{tot}(E)/sin\theta + \mu_{tot}(E_f)/sin\phi]t} &\sim 1 - \{-[\mu_{tot}(E)/sin\theta + \mu_{tot}(E_f)/sin\phi]t\} \\ &= -[\mu_{tot}(E)/sin\theta + \mu_{tot}(E_f)/sin\phi]t \end{aligned} \tag{3.8}$$

This will cancel out the term on the denominator of equation-(3.7), giving:

$$I_f \sim I_0 \mu_\chi(E) t \tag{3.9}$$

As for the thick-dilute sample, $\mu t \gg 1$ and $\mu_\chi(E) \ll \mu_{tot}(E)$, therefore:

$$\begin{aligned} &[\mu_{tot}(E)/sin\theta + \mu_{tot}(E_f)/sin\phi]t \gg 1 \\ &\Downarrow \\ 1 - e^{-[\mu_{tot}(E)/sin\theta + \mu_{tot}(E_f)/sin\phi]t} &\sim 1 \end{aligned} \tag{3.10}$$

Furthermore, since $\mu_\chi(E) \ll \mu_{tot}(E)$, the variation of $\mu_\chi(E)$ does not have much effect on $\mu_{tot}(E)$, therefore the energy dependence of $\mu_{tot}(E)$ can be ignored, which then gives:

$$I_f \sim I_0 \mu_\chi(E) \tag{3.11}$$

From expression-(3.9) and (3.11), it can be seen that the thin or thick-dilute sample is most suitable for XAFS measurements using fluorescence mode.

3.2.3 Optical detection mode

When a sample is photoluminescent, the X-ray excited optical luminescence (XEOL) signal can be collected. Using the fact that the XEOL signal is sensitive to photoelectron generation in the X-ray absorption process near and above the X-ray absorption edge, the XEOL signal can be used as the indication to record the X-ray absorption spectra. The corresponding optically detected XAS (ODXAS) spectra could be obtained. Mathematically, the XEOL signal intensity is given by [4, 5]:

$$dI_{XEOL}(x) = \mu\eta I(x)dx \tag{3.12}$$

where μ is the absorption coefficient, η is the light emission coefficient, $I(x)$ is the intensity of the incident X-rays at depth x in the sample. Substituting $I(x)$ given by (3.2) and integrating over x for a sample thickness d gives:

$$I_{XEOL} = I_0\eta(1-e^{-d\mu}) \tag{3.13}$$

where I_0 is the intensity of the incident X-ray beam. In the limit of small d (e.g. the thin limit), the exponential term in (3.13) can be expanded, giving:

$$I_{XEOL} = I_0\mu_0\eta d(1+\frac{\Delta\mu}{\mu_0}\chi) \tag{3.14}$$

where μ has been expanded in terms of (3.4).
As shown in Fig. 3.6, the XEOL-related X-ray absorption signal is measured by recording the integral PL yield within a selected wavelength range. Therefore the obtained OD-XAS spectra is concerned with a subset of atomic sites related to the light emission. In another word, the optically detected XAS allows further discrimination by reducing the signal collected from every atom of a particular element, to a subset of those which are luminescent. Thus the signal can offer insight into what environment the luminescent atoms are in and so what type of environment is conductive to the optical emission behaviour.
The following two sections will move on to the discussion about the basic EXAFS spectra processing and analysis. Before introducing the technical details about the EXAFS data

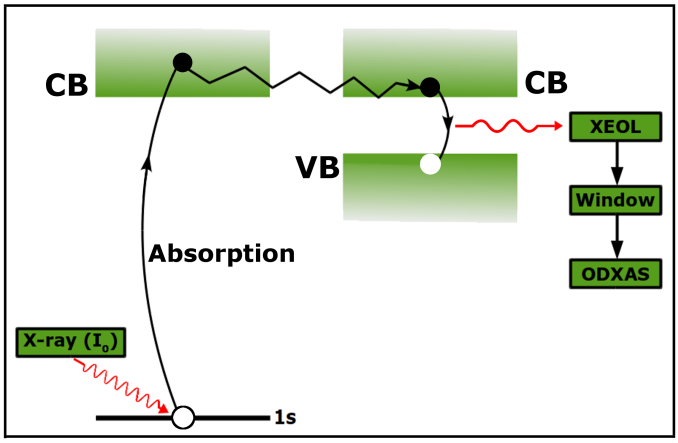

Fig. 3.6 The illustration for optically detected XAS signal collection.

analysis, the following section will briefly cover the basic EXAFS formulation, on which the EXAFS data analysis is based.

3.3 The EXAFS formulation

First of all, the X-ray absorption coefficient $\mu(E)$ can be described by the Fermi's golden rule:

$$\mu(E) \propto |\langle i|\mathscr{H}_{if}|f\rangle|^2 \tag{3.15}$$

where i indicates the initial state (core-level, without photoelectron excited) and f refers to the final state (X-ray absorbed, photoelectron excited, leaving a hole in the core level – core-hole), $\mathscr{H}_{if}$ is the interaction term. According to the quantum radiation theory, the overall Hamiltonian for a charged particle in an electromagnetic field is given by:

$$\mathscr{H} = \frac{1}{2m}(\vec{p} + \frac{e}{c}\vec{A})^2 + V(\vec{r}) \tag{3.16}$$

$$= \frac{p^2}{2m} + \frac{e}{mc}\vec{A}\cdot\vec{p} + \frac{e^2}{2mc^2}A^2 + V(\vec{r}) \tag{3.17}$$

Here $\vec{A}$ is the vector potential corresponding to the applied electromagnetic field, and it could be noticed that in (3.17) only the second term concerns the interaction between the applied field and photoelectron ($\vec{p}$ is directly linked to the wavevector $\vec{k}$ of the photoelectron), therefore contributing to the X-ray absorption. The $\vec{A}\cdot\vec{p}$ term can be further reduced to be proportional to e^{ikr}, the derivation for which will not be covered in this thesis. Detailed

discussion can be found in the 'Radiation in Atoms' section of the online quantum mechanics textbook by Jim Branson: Ref. [6].
Furthermore, the final state $|f\rangle$ can be divided to two parts:

$$|f\rangle = |f_0\rangle + |\Delta f\rangle \tag{3.18}$$

where $|f_0\rangle$ refers to the situation of isolated absorbing atom, and $|\Delta f\rangle$ corresponds to the influence (basically, the scattering) of the surrounding atoms, which is the interesting part here. Mathematically:

$$\begin{aligned}
|\langle i|\mathscr{H}_{if}|f\rangle|^2 &= |\langle i|\mathscr{H}_{if}|f_0+\Delta f\rangle|^2 \\
&= \langle i|\mathscr{H}_{if}|f_0+\Delta f\rangle\langle i|\mathscr{H}_{if}|f_0+\Delta f\rangle^* \\
&= [\langle i|\mathscr{H}_{if}|f_0\rangle + \langle i|\mathscr{H}_{if}|\Delta f\rangle][\langle i|\mathscr{H}_{if}|f_0\rangle^* + \langle i|\mathscr{H}_{if}|\Delta f\rangle^*] \\
&= |\langle i|\mathscr{H}_{if}|f_0\rangle|^2 + \langle i|\mathscr{H}_{if}|\Delta f\rangle^*\langle i|\mathscr{H}_{if}|f_0\rangle + \langle i|\mathscr{H}_{if}|\Delta f\rangle\langle i|\mathscr{H}_{if}|f_0\rangle^* \\
&\quad + |\langle i|\mathscr{H}_{if}|\Delta f\rangle|^2 \qquad (3.19) \\
&\approx |\langle i|\mathscr{H}_{if}|f_0\rangle|^2(1 + \langle i|\mathscr{H}_{if}|\Delta f\rangle\frac{\langle f_0|\mathscr{H}_{if}|i\rangle}{|\langle i|\mathscr{H}_{if}|f_0\rangle|^2} + C.C.) \qquad (3.20)
\end{aligned}$$

In (3.20), $C.C.$ refers to the complex conjugate of the previous term. It should be pointed out that from (3.19) to (3.20), the following two relations are used:

$$\langle i|\mathscr{H}_{if}|f_0\rangle^* = \langle f_0|\mathscr{H}_{if}|i\rangle \tag{3.21}$$

$$|\langle i|\mathscr{H}_{if}|\Delta f\rangle|^2 \approx 0 \tag{3.22}$$

For (3.21),

$$\begin{aligned}
(\phi_i, \mathscr{H}_{if}\phi_f)^* &= (\phi_i^*, \mathscr{H}_{if}^*\phi_f^*) \\
&= (\mathscr{H}_{if}\phi_f, \phi_i) \qquad (3.23)
\end{aligned}$$

Since the Hamiltonian operator $\mathscr{H}_{if}$ is Hermitian operator, therefore:

$$(\mathscr{H}_{if}\phi_f, \phi_i) = (\phi_f, \mathscr{H}_{if}\phi_i) \tag{3.24}$$

$$\Downarrow$$

$$\langle i|\mathscr{H}_{if}|f_0\rangle^* \iff (\phi_i, \mathscr{H}_{if}\phi_f)^* = (\phi_f, \mathscr{H}_{if}\phi_i) \iff \langle f_0|\mathscr{H}_{if}|i\rangle \tag{3.25}$$

As for (3.22), the term $|\langle i|\mathscr{H}_{if}|\Delta f\rangle|^2$ can be ignored, considering $|\langle i|\mathscr{H}_{if}|\Delta f\rangle|$ is small, i.e. approximation to only the first order. Furthermore, the relation between the overall absorption $\mu(E)$, the background absorption $\mu_0(E)$ and the fine structure $\chi(E)$ is given as:

$$\mu(E) = \mu_0(E)[1+\chi(E)] \tag{3.26}$$

By comparing (3.20) and (3.26), it can be deduced that:

$$\chi(E) \propto \langle i|\mathscr{H}_{if}|\Delta f\rangle \tag{3.27}$$

Then if treating the initial state as a delta function (localized core levels) $\delta(r)$ and designating the scattered wavefunction as $\psi_{scatt}(r)$ in real space, equation-(3.26) becomes:

$$\chi(E) \propto \int dr\delta(r)e^{ikr}\psi_{scatt}(r) = \psi_{scatt}(0) \tag{3.28}$$

Equation-(3.28) says the absorption fine structure $\chi(E)$ is proportional to the scattered wavefunction at the absorbing atom. Assuming the outgoing (and back-coming) wave as spherical:

$$\psi(\vec{k},\vec{r}) = \frac{e^{i\vec{k}\cdot\vec{r}}}{r} \tag{3.29}$$

Then the single scattering from an atom at $\vec{r} = \vec{R}$ will give the scattered wavefunction at $\vec{r} = 0$ as:

$$\psi(\vec{k},\vec{r}=0) = \frac{e^{i\vec{k}\cdot\vec{R}}}{kR}kf(k)e^{i\delta(k)}\frac{e^{i\vec{k}\cdot\vec{R}}}{kR} \tag{3.30}$$

Here the first and last term correspond to the outgoing and scattered-back spherical wave, respectively, and k in the denominator accounts for the decrease of the absorption coefficient as k increases. The k in the middle term then compensates the over dampening (two k from the first and last term makes k^2 thus over dampening) of the signal. $f(k)$ and $\delta(k)$ in the middle term refers to the amplitude and phase shift caused by the scattering atom. Considering the practical measurement signal should be real, the following expression for $\chi(k)$ could be used:

$$\begin{aligned}\chi(k) &= Im[\frac{e^{i\vec{k}\cdot\vec{R}}}{kR}kf(k)e^{i\delta(k)}\frac{e^{i\vec{k}\cdot\vec{R}}}{kR}] \\ &= Im[\frac{f(k)}{kR^2}e^{2i\vec{k}\cdot\vec{R}}e^{i\delta(k)}]\end{aligned} \tag{3.31}$$

The expression for $\chi(k)$ given by (3.31) accounts only for an ideal situation, where all atoms stay at their equilibrium position. In reality, the disorder of the system should be considered, which contains static (atoms away from the crystallographic sites) and dynamic (thermal vibration) contributions. As shown in Fig. 3.7, the mathematical form for describing the

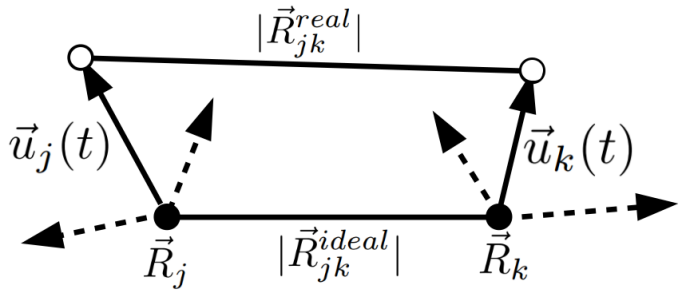

Fig. 3.7 The illustration for the system disorder. The solid dot refers to the atomic equilibrium position. The arrows indicates the disorder of the system, and the open dot refers to the dynamic position of atoms.

system disorder could be given as:

$$\vec{R}_j(t) = \vec{R}_j + \vec{u}(t) \tag{3.32}$$

where $\vec{R}_j(t)$ is the instantaneous position of atom j, $\vec{R}_j$ refers to the equilibrium position and $\vec{u}(t)$ corresponds to the disorder (static and dynamic). Considering the disorder of atomic arrangement, (3.32) should be put into the middle term of (3.31) to give:

$$e^{\langle 2i\vec{k}\cdot\vec{R(t)}\rangle} = e^{2i\vec{k}\cdot\vec{R}} e^{\langle 2i\vec{k}\cdot\vec{u}\rangle} \tag{3.33}$$

where the term $e^{\langle 2i\vec{k}\cdot\vec{u}\rangle}$ can be expanded as:

$$e^{\langle 2i\vec{k}\cdot\vec{u}\rangle} = 1 + 2i\langle\vec{k}\cdot\vec{u}\rangle - \langle(\vec{k}\cdot\vec{R})^2\rangle + \cdots \tag{3.34}$$

Since the atomic displacements are uncorrelated and random, the second term in (3.34) equals zero. As for the third term, it can be further simplified:

$$-\langle(\vec{k}\cdot\vec{u})^2\rangle = -k^2\langle u^2\rangle\langle cos^2\theta\rangle \tag{3.35}$$

where $\langle cos^2\theta\rangle$ gives:

$$\begin{aligned}\langle cos^2\theta\rangle &= \frac{\int_0^{R_x}\int_0^{\pi}\int_0^{2\pi} cos^2\theta\cdot r^2 sin\theta dr d\theta d\phi}{\frac{4}{3}\pi R_x^3} \\ &= \frac{1}{3}\end{aligned} \tag{3.36}$$

Therefore if ignoring all the higher terms, (3.34) becomes:

$$e^{\langle 2i\vec{k}\cdot\vec{u}\rangle} = 1 - \frac{1}{3}k^2\langle u^2\rangle \tag{3.37}$$

Considering the following Taylor series:

$$e^{-\frac{1}{3}k^2\langle u^2\rangle} = 1 - \frac{1}{3}k^2\langle u^2\rangle + \cdots \tag{3.38}$$

one can see the right hand sides of (3.37) and (3.38) are identical (if ignoring the higher order terms), therefore:

$$e^{\langle 2i\vec{k}\cdot\vec{u}\rangle} = e^{-\frac{1}{3}k^2\langle u^2\rangle} \tag{3.39}$$

$$\Downarrow$$

$$e^{\langle 2i\vec{k}\cdot\vec{R(t)}\rangle} = e^{2i\vec{k}\cdot\vec{R}}e^{\langle 2i\vec{k}\cdot\vec{u}\rangle} = e^{2i\vec{k}\cdot\vec{R}}e^{-\frac{1}{3}\langle u^2\rangle k^2} \tag{3.40}$$

By defining the Debye-Waller (DW) factor σ^2 as:

$$\sigma^2 = \frac{1}{6}\langle u^2\rangle \tag{3.41}$$

and putting (3.40) back to (3.31), the equation for $\chi(k)$ becomes:

$$\chi(k) = Im[\frac{f(k)}{kR^2}e^{-2\sigma^2k^2}e^{2i\vec{k}\cdot\vec{R}+i\delta(k)}] \tag{3.42}$$

Here it should be pointed out that the way of defining DW factor as given by (3.41) follows the way used in diffraction related formulation therefore the factor $\frac{1}{6}$ instead of $\frac{1}{3}$ was used, bringing in an extra factor '2' in the exponential of the DW term in (3.42).

Up until now, the scattering of the photoelectron is considered to be elastic, however in practice, the energy loss as photoelectrons propagate should be considered. Moreover, the lifetime of the core-hole is not infinite, therefore if the core has already been filled before the photoelectron is scattered back, the absorption signal should be dampened as well. To account for both of the effects, an extra term containing the electron mean free path (EMFP) was introduced. The EMFP refers to the average distance travelled by the photoelectrons before being inelastically scattered and before the core-hole is filled. Taking EMFP into account, the expression for $\chi(k)$ becomes:

$$\chi(k) = Im[\frac{f(k)}{kR^2}e^{-2\sigma^2k^2}e^{2R/\lambda(k)}e^{2i\vec{k}\cdot\vec{R}+i\delta(k)}] \tag{3.43}$$

Equation-(3.43) corresponds to one scattering path only, and the the overall $\chi(k)$ signal should be the sum of all the scattering paths. Also, to account for the degeneracy of the scattering paths and all the other effects influencing the scattering amplitude, another two parameters N and S_0^2 are introduced for each path, respectively. The final EXAFS equation is given as:

$$\begin{aligned}\chi(k) &= \sum_j Im[\frac{N_j S_0^2 f_j(k) e^{-2\sigma_j^2 k^2} e^{2R_j/\lambda(k)}}{kR_j^2} e^{2i\vec{k}\cdot\vec{R}_j + i\delta(k)}] \\ &= \sum_j \frac{N_j S_0^2 f(k) e^{-2\sigma^2 k^2} e^{2R/\lambda(k)}}{kR_j^2} sin[2kR_j + \delta(k)] \end{aligned} \tag{3.44}$$

Equation-(3.44) is just the classic EXAFS equation of Stern, Lytle and Sayers [7]. With the theoretical description for EXAFS spectra, it is plausible to carry out further structural analysis. First of all, it can be seen from (3.44) the basic EXAFS formula contains the sine function. Therefore it is natural to assume that the Fourier transform will give the corresponding frequency component and hence the RDF-like pattern in R-space. In fact, it was just based on the theoretical expression of the EXAFS that Stern, et al. (1971) proposed the Fourier transform technique for EXAFS analysis [8]. More importantly, if the scattering amplitude $f_j(k)$ and phase shift $\delta(k)$ can be obtained, the structural parameters (R_j, σ_j^2, etc.) can be extracted by fitting the theoretical expression to the experimental result. Historically, the scattering amplitude and phase shift were garnered through transferring from the known to unknown systems. However modern development of the theoretical description for XAS already allows the calculation of the scattering amplitude $f_j(k)$ and phase shift $\delta(k)$ in the *ab initio* way. Details about the scattering amplitude and phase shift within the framework of quantum scattering theory and its implementation in FEFF can be found in Appendix-B. Meanwhile, various tools/packages, such as Demeter [9], DL_Excurve [10], GNXAS [11], are already available to carry out the structural parameters fitting based on the theoretical calculation. In this thesis, the Demeter package will be used, including Athena for the background subtraction together with the normalization and Artemis for structural parameters fitting.

Before heading to the next section, it should be pointed out that the classic equation-(3.44) applies only for single scatterings in principle, which can be inspected from the derivation procedures given above. However, Rehr, et al. (1990) proposed that the form of equation-(3.44) could be kept unchanged if replacing the single scattering amplitude with the corresponding effective scattering amplitude for the multiple scattering problem [12]. That's what the

developed program for theoretical calculation of XAFS spectra – FEFF – was named after – 'F' stands for the scattering amplitude $f(k)$ and 'eff' stands for 'effective'.
In the next section, the technical details about the EXAFS data processing and analysis will be introduced on the basis on the EXAFS formulation given in current section.

3.4 EXAFS data analysis

3.4.1 Background subtraction and normalization

The experimentally measured EXAFS spectra should be processed before any further analysis to extract structural information. First of all, the raw EXAFS spectra should be normalized to make it plausible to compare between experiments. Then background absorption should be subtracted to focus on the fine structure only and also to compare with the theoretical calculation or to fit the structural parameters. All of the processes can be done using the Athena program, the main window of which is shown in Fig. 3.8. As shown in Fig. 3.8

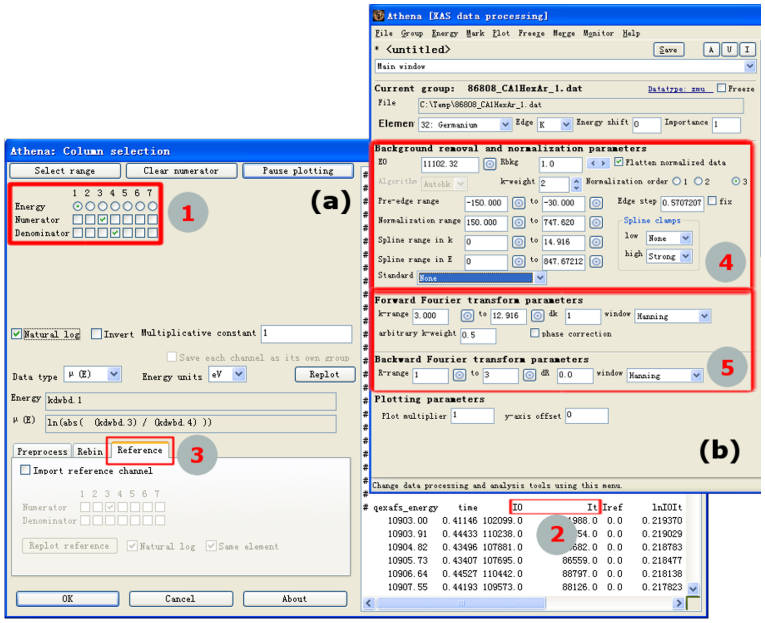

Fig. 3.8 (a) Athena data importing window. (b) Athena main window .

(a), the first step of the processing is to import the raw data. According to the different detection modes for the measurement, the corresponding box within the No. 1 red box should be checked, and the data is shown alongside for inspecting (No. 2 red box). It's worth

mentioning here that if the transmission mode was used, the transmitted intensity I_t should be selected as the denominator and I_0 checked as the numerator, according to equation-(3.2). The No. 3 red box labels out the reference tab, therefore if the reference channel was used along with the measurement, the 'Import reference channel' box should be checked. As illustrated in Fig. 3.4, the transmitted X-ray from the sample is the incident beam for the reference channel, therefore the column selection for the reference channel should be: I_t – Numerator and I_r – Denominator. After proper column selection for importing the raw data, the main Athena window shows up with all the adjustable parameters for normalizing and background subtraction (No. 4 red box in Fig. 3.8) and the Fourier transform (No. 5 red box in Fig. 3.8). Introduction about the data normalization and background subtraction algorithm (AUTOBK) and the corresponding parameters adjustment can be found in the Athena user manual: [2], and details will not be covered in this thesis. In the following discussion, only two aspects will be the focus – the R_{bkg} parameter for background subtraction, together with the phase correction in Athena.

3.4.1.1 R_{bkg} parameter

The AUTOBK algorithm is used in Athena for the background subtraction, for which a series of k points (spline points) are selected at first to separate the whole range of data to individual pieces. The background signal is built up through fitting a polynomial within each separate piece of data, and all of the polynomials for each single piece of data will be connected smoothly at the selected spline points. The R_{bkg} parameter introduced in Athena then controls how the k spline points are going to be selected, therefore controlling the build of the background signal.

R_{bkg} is defined as the largest possible R value corresponding to the background components (i.e. the highest frequency component in k-space that the background signal can possibly contain). Therefore in k-space when selecting the splines points for background approximation, the sampling interval $2dk$ (the factor '2' here comes from the expression for EXAFS, in which the sine function contains '$2kR$'term, see equation-(3.44)) should follow the relationship as required by the Nyquist-Shannon sampling theorem (see Appendix-A):

$$2\pi\frac{1}{2dk} > 2R_{bkg} \tag{3.45}$$

$$\Downarrow$$

$$dk < \frac{\pi}{2R_{bkg}} \tag{3.46}$$

Hence the total number of spline knots N_{knots} in k-space should meet:

$$N_{knots} \geq \frac{k_{max} - k_{min}}{dk} = \frac{\Delta k R_{bkg}}{\pi} \tag{3.47}$$

where k_{max} and k_{min} specifies the spline range in k-space, as can be found within the No. 4 red box in Fig. 3.8. In practice, if the R_{bkg} parameter is set too low, the number of spline knots may not be enough to resemble the real background absorption, which means there could exist higher frequency signals (that should belong to the background) falling in between the spline knots wrongly being taken as the real structure-related signal. Furthermore, from (3.47), it can be seen that the requirement of Nyquist-Shannon only sets the lower bound for the number of spline knots in k-space. However, this does not mean that N_{knots} can be set to any value higher than the lower limit, since there is an additional consideration of not taking any higher-frequency (than the R_{bkg}) component of the real signal as the background. Therefore in practice, the equal sign is taken as the way to determine the number of spline knots in k-space for building up the background signal.
Following the logic above, it can be inferred that the R_{bkg} should also not be set too high, since otherwise part of the real signal may be taken as the background. As a result, the intensity of the first peak in R-space will be severely dampened, which will further influence the following spectra fitting to extract structure parameters. Although there is a general rule for setting the R_{bkg} value according to the Athena User's Guide (see Ref. [2]) – 'R_{bkg} *should be about half the distance to the nearest neighbor*', it indeed needs careful consideration, especially when dealing with noisy data.

3.4.1.2 Phase correction in Athena

Besides the background removal, Athena also provides the option to carry out the Fourier transform of the obtained background subtracted spectra (in k-space) to get the RDF-like pattern in R-space. It should be pointed out that the obtained $\chi(k)$ data is treated as the real part of a complex fine structure $\tilde{\chi}(k)$ and the corresponding imaginary part is set to zero by default in Athena – such setting is purely a matter of convention [13]. That's why in Athena the $\chi(k)$ data can only be plotted with magnitude, which is not like in R-space where the options to plot with 'magnitude', 'real part' and 'imaginary part' are available as shown in Fig. 3.9. However according to (3.44), the phase information $\delta(k)$ is crucial for the Fourier transform to extract R-space pattern that is comparable to the real structure. In practice, the default Fourier transform tends to give the R-space pattern for which the peak position is down-shifted as compared to the real structure. In Athena, an option is provided to

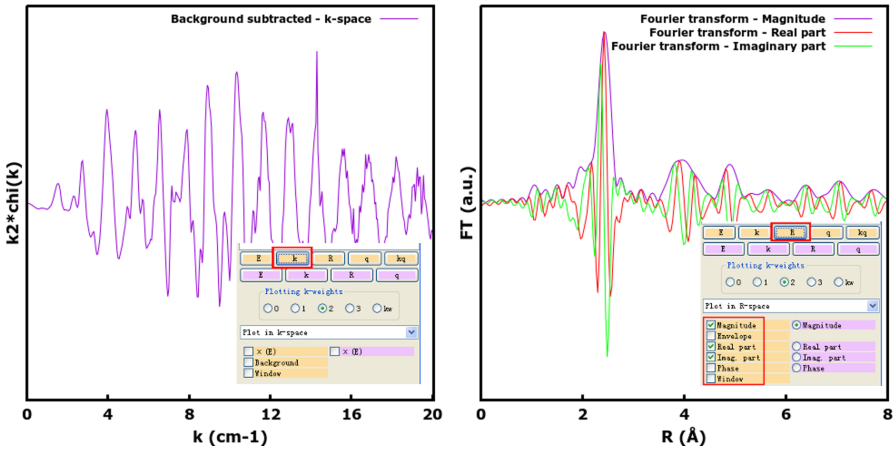

Fig. 3.9 The comparison of plot options in *k*- (left) and *R*-space (right).

carry out the phase corrected Fourier transform to account for the phase problem. However, only the phase of the central atom, which is provided in the form of table (embedded in Athena, from FEFF8 calculation), is used for the correction. [14] Therefore the phase used for the correction in Athena is not the accurate representation of the actual phase shift. The obtained Fourier transform pattern does not exactly correspond to the real structure in question. The exact theoretical phase shift can only be obtained through FEFF calculation to give the accurate Fourier transform pattern in *R*-space, which will be talked about in the next sub-section.

3.4.2 Spectra fitting

Currently, the commonly used tool in the XAFS world for EXAFS data fitting is Artemis. This section will mainly focus on the basic and some advanced usage of the Artemis software. First of all, the background subtracted EXAFS spectra (the Athena project file obtained from last step) should be imported to Artemis (No. 1 in Fig. 3.10). The next step is to define the structure (No. 2 in Fig. 3.10) and carry out the path calculation using the embedded FEFF (version 6, No. 3 in Fig. 3.10). For the defining of the structure, both '.inp' (can be downloaded from the online database: Ref. [15]) and '.cif' file (can be downloaded in the ICSD database) could be used. Also the structure can be manually input using the embedded 'Atoms' program in Artemis (the first tab in the No. 3 window in Fig. 3.10). Once the atomic structure is ready for further theoretical calculation of the corresponding EXAFS signal, running the atoms (there is an option of 'Run atoms' in the 'Atoms' tab of the No. 3 window

in Fig. 3.10) will then prepare the input file for the following FEFF calculation which can be done in the 'FEFF' tab in the No. 3 window.

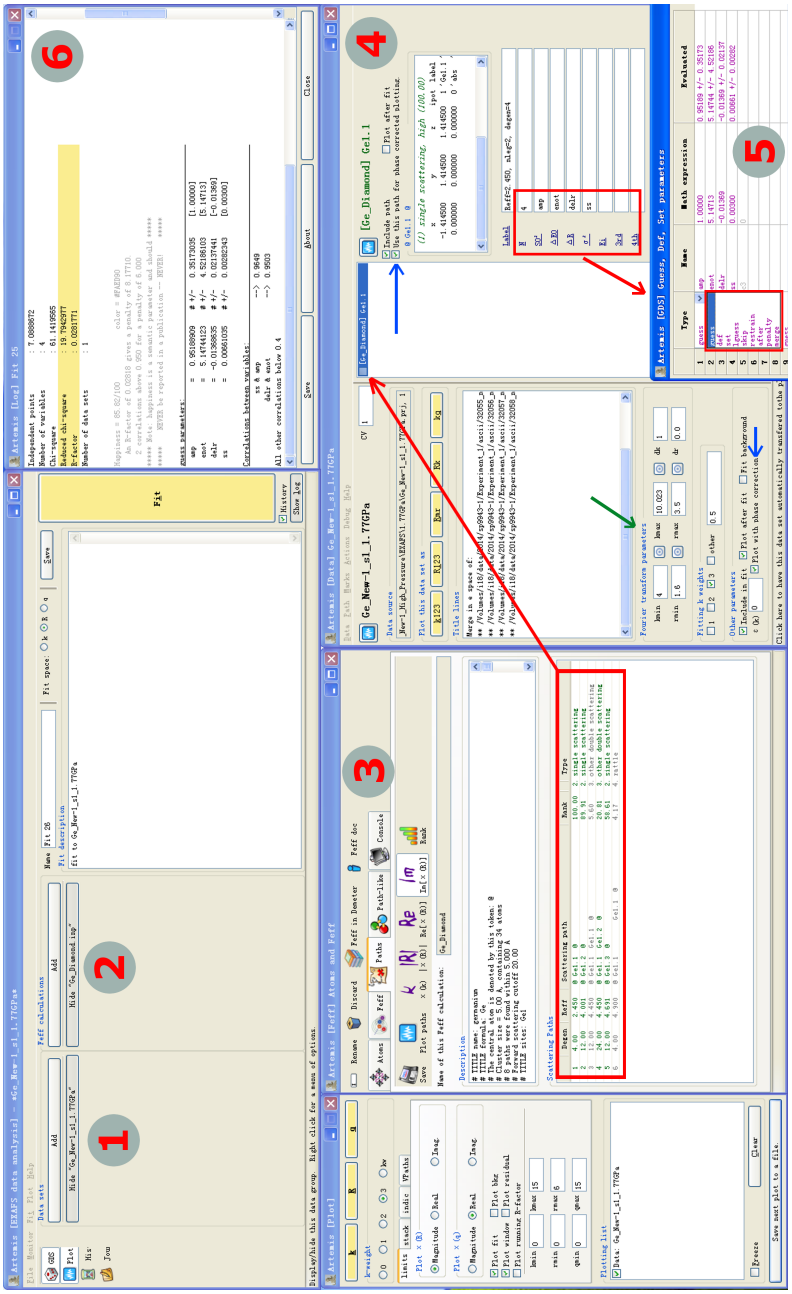

Fig. 3.10 The Artemis window.

Here the embedded FEFF6 in Artemis does provide reasonable calculation result for the scattering amplitude and phase shift that are necessary for the structural parameters fitting. However if the calculation results from the external FEFF calculation (e.g. that from FEFF9.6) are going to be used in Artemis, it is only possible in the old version (earlier than the one shown in Fig. 3.10, refer to Ref. [16]). For the old version, the whole saved Artemis project

was just a zip file where the FEFF paths calculation results (files with the name in such format 'feff*nnnn*.dat') are stored in the directory 'data0.feff0'. Therefore the paths calculation result from the external FEFF calculation can be directly copied to the 'data0.feff0' directory, replacing the old ones. Although the new version of Artemis also saves the whole project as zip file, the data storage was re-structured and the YAML data format (see Ref. [17]) was used for the convenience of program serialization and program language independence. Therefore it's impossible to directly import the external FEFF calculation in the new version of Artermis. Instead, the command-line based IFEFFIT program can be used for the EXAFS spectra fitting, for which the importing of FEFF paths calculation results is straightforward, and details can be found in the IFEFFIT tutorial by Newville: [13].
After the FEFF calculation, all the non-degenerate paths (shorter than the pre-defined upper limit of the path length) will be presented in the 'Paths' tab of the No. 3 window (see Fig. 3.10) as labelled out by the red box. Then the appropriate paths to be used for the spectra fitting (either single or multiple shell fitting) should be chosen by comparing the 'Reff' (half the total length of the scattering path) values with the peak positions in the Fourier transform pattern of the experimental spectra. The chosen paths then should be dragged to the No. 4 window, following which the parameters should be defined for each single selected path, as shown in the red box (in the No. 4 window). Here the parameters (that could be fitted) include those in equation-(3.44) such as S_0^2, DW factor σ^2, etc., together with the absorption edge position and higher order cumulants. Then the 'GDS' window should be brought up (by clicking on the 'GDS' button on the top left corner of the No. 1 window) to specify the type ('guess', 'def', etc., see the No. 5 window in Fig. 3.10) and initial values of the previously define parameters, as shown in the No. 5 window.
The fitting should be ready and by clicking the 'Fit' button, Artemis will start the fitting, after which the results will be shown in the log window – No. 6 in Fig. 3.10. All the main steps for the EXAFS spectra fitting with Artemis are already covered, and further introduction to each procedure and related issues can be found in the Artermis User's guide: [18]. More details about the spectra fitting procedures will not be covered here and in the following part of the current subsection, only several important issues concerning the EXAFS spectra fitting will be discussed, together with brief introductions to several advanced fitting schemes.

3.4.2.1 Fourier transform in Artemis

The phase shift information is available in Artemis through the theoretical FEFF paths calculation. As indicated by blue arrows in Fig. 3.10, certain path can be selected of which the phase shift will be used for the phase corrected Fourier transform.

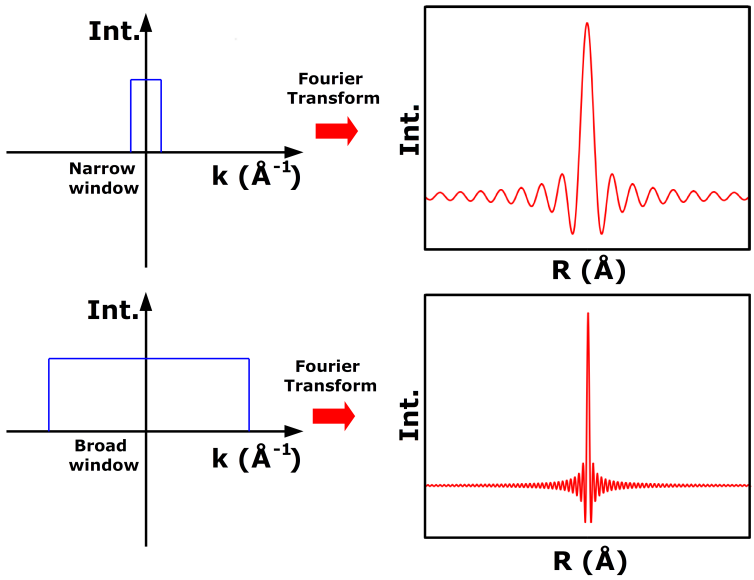

Fig. 3.11 The Fourier transform (red) of square window function (blue) with different width. The Fourier transform of broad window function is closer to δ-function, which will bring in less artificial effect when convoluted with the Fourier transform of the experimental data – Imagine the window with infinite width – The Fourier transform will give δ-function which brings in no artificial effect at all.

The region indicated by the green arrow then specifies the range (in both k- and R-space) for the spectra fitting and also the Fourier (and inverse Fourier) transform. In Athena processing, the R_{bkg} parameter determines the upper limit of the background signal. Therefore, in Artemis it is not allowed to set the lower limit of R range (r_{min} in the green arrow indicated region in Fig. 3.10) for the fitting to be smaller than R_{bkg}. Such restriction does make sense since the background signal should definitely be excluded from the fitting target. The effective k-range is also specified in Athena (see No. 5 red box in Fig. 3.8), and the k-range in Artemis should not exceed that defined in Athena, on either end.

Here it's worth mentioning the importance of the k-range. On one hand, it determines the largest number of independent parameters that can be defined for the fitting, which will be discussed later in this sub-section. On the other hand, it influences the quality of the Fourier transform to give the R-space pattern greatly. First of all, the k-range directly determines the upper limit of the resolution in R-space. Secondly, the window function was introduced in both Athena and Artemis to deal with the finite k-range. Narrower k-range corresponds to narrower window, of which the Fourier transform is further away from the

δ-function (see Fig. 3.11). Since the window function is multiplied to the experimental data in k-space, the resulted R-space spectra is thus the convolution of the Fourier transform for the window function and that for the real experimental data. Therefore in principle, the width of the window function should be set as large as possible to make the corresponding Fourier transform as close to δ-function as possible, which then avoids the artificial effect (introduced by the applied window function) in the resulted R-space spectra.

3.4.2.2 Einstein model and correlated Debye model for DW factor

Although the DW factor can be refined independently for each shell/path, it is frequently convenient to introduce the theoretical model describing the dependence of the DW factor on the interatomic distances. This benefits reducing the number of the parameters to be refined, therefore making it easier to relax to the global minima in the parameter space for the refinement. The reason for that is that when fewer parameters are set for the refinement, fewer correlations would be introduced for the refinement thus reducing errors.
Artemis provides two theoretical models accounting for the DW factor, based on the consideration of thermodynamics of the system – the Einstein model [19, 20] and the correlated Debye model [21]. The formula of the DW factor given by Einstein model is as following:

$$\sigma^2 = \frac{\hbar^2}{2\mu k_B \Theta_E} coth(\frac{\Theta_E}{2T}) + \sigma_0^2 \tag{3.48}$$

where Θ_E is the Einstein temperature (to be fitted in Artemis), which is a characteristic thermal property of materials, μ is the reduced mass of specific atom, k_B is the Boltzmann's constant, σ_0 refers to the static disorder, and T is the system temperature.
The formulation of the correlated Debye model accounting for the DW factor is a bit more complicated as:

$$\sigma^2 = \frac{\hbar}{2\mu} \int \frac{2\omega^2}{(\frac{k_B\Theta_D}{\hbar})^3} \left[1 - \frac{sin(\frac{\hbar\omega R_j k_D}{k_B\Theta_D})}{\frac{\hbar\omega R_j k_D}{k_B\Theta_D}}\right] coth(\frac{\hbar\omega}{2k_B T}) \frac{d\omega}{\omega} \tag{3.49}$$

where ω refers to the phonon frequency, Θ_D is the Debye temperature (to be fitted), which can be interpreted as the temperature at which the highest-frequency vibration mode (hence every mode) is excited, R_j is the half length of the corresponding scattering path, and k_D is defined as the Debye wave vector:

$$k_D = (\frac{6\pi^2 N}{V}) \tag{3.50}$$

where N/V gives the number density of atoms.
Here it should be pointed out that in the Einstein model, all atoms are treated as individual, non-interacting harmonic oscillators. In contrast, the Debye model treats the vibration of atomic lattice as phonons. From the perspective of practical application, the Debye model gives a better description for the behaviour of systems at low temperatures [22].

3.4.2.3 High order cumulants

From the basic EXAFS formula given by 3.44, it can be seen that if only the harmonic approximation of the DW factor is used to account for the disorder of the system, the corresponding EXAFS peak profile in R-space should be rigorously Gaussian. In the EXAFS spectra fitting, to account for the non-Gaussian peak profile of the spectra in R-space, so-called high order cumulants should be introduced. In G. Bunker's book on EXAFS [23], the way to treat the non-Gaussian peaks in R-space was discussed, which is based on a Taylor expansion (around $k = 0$) of the EXAFS formula (for one scattering path) in the following way:

$$\frac{NS_0^2 f(k)}{k} e^{i\delta(k)} \sum_0^\infty C_n \frac{(2ik)^n}{n!} = \frac{NS_0^2 f(k)}{k} e^{i\delta(k)} ln\Big(\int_0^\infty \frac{p(r)}{r^2} e^{-2r/\lambda} e^{2ikr} dr\Big) \tag{3.51}$$

where $p(r)$ refers to the distribution of the atomic positions. Here the coefficients C_n are called the cumulants, among which the first and second one are not new – the mean position and the mean square width (DW factor) of the distribution, respectively. Those coefficients of the higher order terms then accounts for the non-Gaussian shape of the peak in R-space. C_3 is related to the skewness and C_4 measures how much weight is in the tail of the peak. Both C_3 and C_4 can be introduced in Artemis for the spectra fitting. Here the above Taylor expansion assumes that the EMFP λ is constant. Details about the situation where λ varies as the function of k, together with more advanced topics about the treatment of high order cumulants, can be found in appendix-2 of G. Bunker's book [23].

3.4.2.4 Number of independent parameters

Once the k-range ($\Delta k = k_{max} - k_{min}$) is specified for the fitting, then the theoretical limit of the resolution in R-space can be obtained as:

$$dR = \frac{2\pi}{2\Delta k} \tag{3.52}$$

according to the principle of the Fourier transform. Here the factor '2' in the denominator corresponds to the '2kR' term in the *sine* function of (3.44). Then the theoretical upper limit of the independent number of points in real space is given by:

$$\begin{aligned} N_p &= \frac{2\Delta R}{dR} \\ &= \frac{2\Delta k \Delta R}{\pi} \end{aligned} \tag{3.53}$$

where the factor '2' in the numerator of (3.53) accounts for both the real and imaginary part of the R-space signal. Such theoretical limitations for the number of points in R-space should definitely be transferred to the parameter space for the fitting, therefore we have a limit for the number of independent fitting parameters specified by N_p as given in (3.53). To understand the transferring of the limit N_p from point space to parameter space, one can think of the basic demonstration that two points can be best fitted with a line which requires no more than two parameters. In such a case any other kinds of fitting requiring more than two parameters should be regarded as an over-interpretation of the data.

3.4.2.5 Statistics of fitting

The Levenberg-Marquardt non-linear least-squares fitting was used by IFEFFIT (the kernel program of Artemis), and two parameters are defined to characterize the quality of the fitting – χ^2 and $\mathscr{R}$. The deviation parameter χ^2 is given as:

$$\chi^2 = \frac{N_{idp}}{\varepsilon N_{data}} \sum_i \left[[Re(\chi_d(r_i) - \chi_t(r_i))]^2 + [Im(\chi_d(r_i) - \chi_t(r_i))]^2 \right] \tag{3.54}$$

where N_{idp} and N_{data} refers to the largest number of independent parameters and the total points number of the data, respectively, ε is the experimental measurement uncertainty, $\chi_d(r_i)$ and $\chi_t(r_i)$ corresponds to the $\chi(r)$ value of the data and the theoretical fitting, respectively. Furthermore, the reduced-χ^2 parameter χ_v^2 is defined as:

$$\chi_v^2 = \frac{\chi^2}{\nu} \tag{3.55}$$

where $\nu = N_{idp} - N_{var}$ and N_{var} is the number of parameters used for the fitting. The $\mathscr{R}$ parameter is defined to characterize the relative deviation of the fitting result, as compared to the data:

$$\mathscr{R} = \frac{\sum_i \left[[Re(\chi_d(r_i) - \chi_t(r_i))]^2 + [Im(\chi_d(r_i) - \chi_t(r_i))]^2 \right]}{\sum_i \left[[Re(\chi_d(r_i)]^2 + [Im\chi_t(r_i))]^2 \right]} \tag{3.56}$$

The value of the two parameters can be found in the log window as presented in the No. 6 window in Fig. 3.10. It should be mentioned that the reduced-χ^2 parameter χ_v^2 should be approximately 1 for the perfect fitting, according to the least-square fitting theory [24]. However, this is always not the case in Artemis, in which χ_v^2 will always be much larger than 1. The reason for that resides in the determination of the measurement uncertainty ε in (3.54). In IFEFFIT, the ε is determined from the data by performing the Fourier transform of $\chi(k)$ and then computing the root mean square of the magnitude of $\chi(R)$ between 15 and 25 Å. Such approximation for the measurement uncertainty does make sense since EXAFS is local structure concerned technique and the real EXAFS signal cannot extend to that region. Therefore any spectral content in that R range could be regarded as the noise, i.e. the measurement uncertainty. However, the measurement uncertainty of the real EXAFS experiment is much larger than the approximated value following the way as described above, owing to various contributions such as the detector non-linearity, sample inhomogeneity, and among others. Therefore due to the underestimation of the measurement uncertainty ε, the value of χ_v^2 is always much larger than 1, even for a good fit.
In a non-linear least-square fitting, the Hessian matrix can be obtained along with the fitting. The inverse of the Hessian matrix is called the Covariance matrix which directly characterizes the correlation between the fitting parameters. (refer to Ref. [25]) The diagonal elements of the Covariance matrix are the fitting errors for each corresponding parameter. For each element of the Covariance matrix, the measurement uncertainty ε appears in the numerator (in the form of $\sqrt{\varepsilon}$). As mentioned above, IFEFFIT in fact underestimates ε, therefore the fitting error of parameters are also underestimated in Artemis. The way that IFEFFIT uses to deal with such problem is to assume that the just finished fitting is indeed a good fit, i.e. the large χ_v^2 is purely due to the underestimation of ε but not because the fitting is bad. Then the error bars are multiplied by the square root of the obtained χ_v^2 to get the corrected estimation [26].

3.4.2.6 Extraction of the coordination number

As can be seen in the standard EXAFS equation-(3.44), the degeneracy parameter N (for the first shell, the degeneracy is just the coordination number) is completely correlated to the amplitude factor S_0^2. Therefore it's impossible to directly determine the coordination number based on a single fit for the sample in question. In fact, the coordination number N is fixed at the theoretical value in Artemis and only the amplitude factor S_0^2 can be fitted. To extract the coordination number, it is necessary to measure the EXAFS spectra for a reference sample. For example, if the first shell Ge-Ge coordination is to be extracted, the reference crystalline

Ge sample should be measured. Here the diamond-type Ge reference sample is selected, since the comprehensive structure analysis result from EXAFS, XANES, etc. points to the diamond-type local symmetry for the Ge-related phase in our Ge QDs. The EXAFS spectra should be fitted for both the sample and the reference and the by comparing the fitted S_0^2 value, the coordination number of the sample can be obtained:

$$N_{sample} = N_{Ref} \frac{S^2_{0Sample}}{S^2_{0Ref}} \tag{3.57}$$

where N_{sample} and N_{Ref} refers to the coordination number for the sample and the reference (theoretical value), respectively, $S^2_{0Sample}$ and S^2_{0Ref} corresponds to the refined amplitude parameter for the sample and the reference, respectively.

3.4.2.7 The restraint fitting

In the EXAFS spectra fitting, the error analysis for the refined parameters must take into account the correlation between parameters as this, in general, will affect the value of errors, usually making them larger. Also in some cases, the fitted parameter value may be non-physical, e.g. negative DW factor. To reduce the fitting error bars, or to avoid the non-physical fitted parameter value, some prior-knowledge about the sample (e.g. the coordination number) and consideration of physics (e.g. DW factor should be positive) is beneficial. Then the so-called restraint fitting can be carried out in Artemis to restrict the value of parameters within a region around the value that it is expected to be. Here it should be clarified again that to do the restraint fitting, one should have strong confidence in the expected value of parameters, since otherwise this method of restraint fitting becomes cheating.

The first way of doing the restraint fitting is through defining the fitting parameter as 'def' type (see the red box in No. 5 window in Fig. 3.10). For example, for the fitting of amplitude factor S_0^2, instead of defining a guess parameter (e.g. 'amp') in the 'S_0^2' box (see red box in No. 4 window in Fig. 3.10), the following way of defining parameters could be followed:

$$\begin{aligned} guess \quad temp &= 0.9 \\ def \quad amp &= min(max(0.7, a), 1.0) \end{aligned}$$

That means the parameter 'temp' is defined as the 'guess' type (thus can be adjusted freely) and the 'amp' parameter (corresponding to S_0^2) is defined in such a way that if the fitted value of 'temp' is between 0.7 and 1.0 then it will be assigned to 'amp' (thus to S_0^2). Otherwise the

'amp' parameter will take either 0.7 (if 'temp' smaller than 0.7) or 1.0 (if 'temp' larger than 1.0). Another approach to do the restraint fitting is a bit gentler than the first method, and the parameters can be defined as following (again, taking the fitting for S_0^2 as the example):

$$
\begin{aligned}
&guess && amp_guess = 0.9 \\
&set && amp_target = 0.9 \\
&set && scale = 100 \\
&restrain && res = abs(amp_guess - amp_target) * scale
\end{aligned}
$$

Here the parameter 'amp_guess' is assigned to S_0^2 and is defined as the 'guess' type as usual. The 'amp_target' is defined as the 'set' type (the value is fixed during the fit), which is the target (the expected value for S_0^2) of the fitting. The tricky part here is the defining of the 'res' parameter as the 'restrain' type, which adds a punishment for the fitting if the guessed 'amp_guess' parameter is away from the 'target'. The 'scale' parameter controls the scale of the punishment. By defining the fitting parameters in such a way, Artemis will then try to fit the S_0^2 parameter as close to the target as possible, with respect to the defined magnitude of the 'pushing force' (the 'scale' parameter).

3.4.2.8 An example of complex fitting model

Before the end of the current sub-section, a typical EXAFS fitting technique applied to the bi-metallic systems will be briefly introduced, according to the report by A. Frenkel, et al [27]. This fitting technique reflects the utilization of the chemical and structural configuration knowledge of the system to impose constraints upon the EXAFS spectra fitting. For the bi-metallic systems, general constraints should be imposed for the fitting:

$$N_{AB} = \frac{x_B}{x_A} N_{BA} \tag{3.58}$$

$$R_{AB} = R_{BA},\ \sigma_{AB}^2 = \sigma_{BA}^2 \tag{3.59}$$

Here A and B indicate the two differenet elements in the system, N_{AB} refers to the partial coordination number of B around A (similarly for N_{BA}), x_A and x_B refer to the molar fractions of element A and B, respectively, R_{AB} and σ_{AB}^2 refer to the bond length and the corresponding DW factor of $A-B$ bond, when element A is measured as the absorber, similarly for R_{BA} and σ_{BA}. The fitting for the two sets of experimental spectra, where A and B is measured as the absorbing atoms respectively, should be fitted cocurrently. Such constraint fitting was applied to NiIr system in the report by Sasaki, et al. [28], where the fitting parameters were

defined in the following way:

$$R_{Ir-Ni} = R_{Ni-Ir} \tag{3.60}$$

$$\sigma^2_{Ir-Ni} = \sigma^2_{Ni-Ir} \tag{3.61}$$

$$\frac{N_{Ir-Ni}}{N_{Ni-Ir}} = \frac{x_{Ni}}{x_{Ir}} \tag{3.62}$$

$$N_{Ir-Ir} = 11 - N_{Ir-Ni} \tag{3.63}$$

$$N_{Ni-Ni} = 11 - N_{Ni-Ir} \tag{3.64}$$

Here besides the constraints mentioned in (3.58) and (3.59), the constraints specified by (3.63) and (3.64) were based on the theoretical modelling for the NiIr system which indicates the complete coordination number of 11, for Ni and Ir atom. As for the molar fraction ratio in (3.62), it was obtained through the energy dispersive X-ray (EDX) spectroscopy. The obtained results from the cocurrent fitting was further utilized for the discussion of the possible structural configuration (alloy, core-shell, etc.) of the bi-metallic system [28]. Hereby it should be noticed that the site-selectivity of XAS technique was particularly useful in the above mentioned work on the bimetallic system by Frenkel and Sasaki, et al.

3.4.3 EXAFS analysis beyond Athena and Artemis

First of all, it should be mentioned that besides the graphical user interface based Athena and Artemis program for the EXAFS data processing and analysis, the command line based version of IFEFFIT is also available, as already mentioned earlier in this section. With the command line based tool, it is sometimes convenient to carry out analysis for a lot of data at the same time through scripting.

Besides the IFEFFIT algorithm based package, there have been various choices of tools for EXAFS data processing and/or analysis. For example, the PySpline program [30] is an alternative tool for the EXAFS spectra background removal, with which the spline points for building up the background signal can be adjusted manually, not like the evenly spaced spline points automatically set in Athena. As for the structural analysis tool, two alternatives are already mentioned in the early discussion – DL_Excurve and GNXAS. Recently, new tools or approaches have been developed for EXAFS data analysis. For example, the miXAFS program was developed by Ikemoto's group [31] for the purpose of the batch processing of a lot of data. Also the new version of the IFEFFIT package for the EXAFS spectra analysis was embedded in the recently developed comprehensive platform Larch [32] to process the X-ray spectroscopic and scattering data obtained at the modern synchrotron sources.

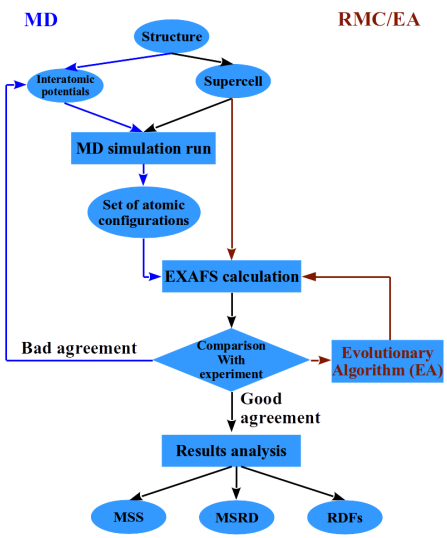

Fig. 3.12 The combined MD and RMC approach for EXAFS data analysis. Reproduced from Ref. [29].

Also, the application of MD in EXAFS analysis is becoming increasingly common. In Fig. 3.12, a proposed algorithm is shown [29], which is for evolving the structure configuration with reference to the experimental EXAFS spectra using MD simulation. This was further extended to combine with the evolutionary algorithm using reverse Monte Carlo (RMC) method. For the introduction of the structural evolution (using MD) to the EXAFS spectra analysis, external programs need to be developed to combine the MD simulation with the EXAFS spectra calculation, seamlessly. During the final year of my Ph.D., I have been working on developing the MD2FEFF code for this purpose and trying to apply this technique to Ge QDs system for the structural configuration analysis. As for the RMC approach, the RMCProfile, which is probably better known for its application in scattering problems, is capable of structural configuration analysis based on EXAFS data.
Besides EXAFS, the near-edge region of the X-ray absorption spectra – XANES – is another important portion. In the following section, we will introduce XANES, which can provide important information about the local structure, where the explanation for EXAFS becomes ambiguous.

3.5 Introduction to XANES

The XANES region in XAFS spectra extends to ~ 30 eV above the absorption edge. Formally, the region can be subdivided into three regions – the pre-edge, absorption edge and post-edge,

as shown in Fig. 3.13. For XANES, the background removal may not be that important

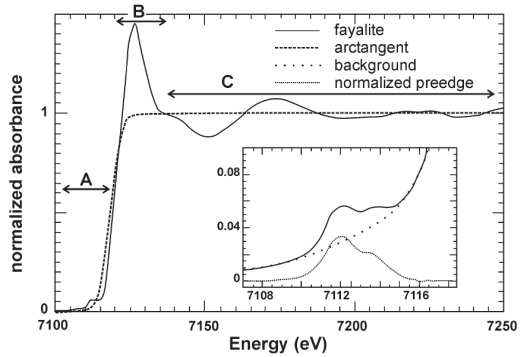

Fig. 3.13 The (A) pre-edge, (B) edge and (C) post-edge regions of the XANES spectra. The overall arctan background function is also shown. The inset figures shows the background subtraction specifically for the pre-edge region for further analysis [33].

as it is for EXAFS, since no further Fourier transform is required for the XANES analysis. Usually, some sort of arctan (as shown in Fig. 3.13) or error function could be used for removing the background [34, 35]. Specifically for the pre-edge region, further correction for the background needs to be applied prior to the analysis and interpretation of the features. This can be done by fitting a polynomial such as a spline function that smoothly follows the slope of the pre-edge data, as shown in the inset of Fig. 3.13 [33].

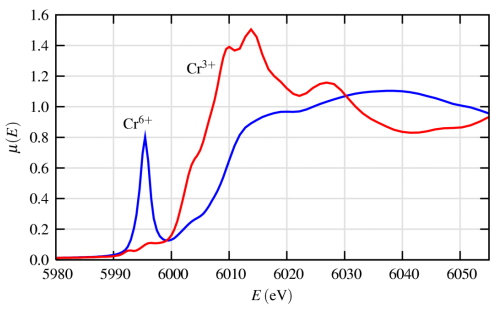

Fig. 3.14 Cr K-edge XANES for Cr^{3+} and Cr^{6+} oxides [1].

Generally, the features of the XANES spectra will be strongly correlated to the available states around the Fermi level. For example, transition metals usually have unfilled (thus available) 3d bands and filled p bands near the Fermi level. According to transition selection rule, the K-edge absorption for the transition metal elements is expected to be featureless. However in practice, sometimes features of the XANES spectra of the transition metal K-edge can be

observed, especially in the pre-edge region, which corresponds to the 1s to 3d band transition. There are two main aspects contributing to the otherwise forbidden transition, and the first aspect is the direct 1s3d quadrupole transition beyond the electric dipole approximation. The other aspect is the hybridization between the 3d and p-like orbitals, which always happen in the transition metal oxides (TMO). Generally for the TMO, the different oxidation state of the transition metal corresponds to different types or extents of the orbital hybridization, which then influences the features of the corresponding XANES feature of the transition metal element. Therefore, the XANES spectra can be regarded as the fingerprint for different oxidation state of the transition metals, as illustrated by the example of Cr K-edge XANES spectra with different oxidation states shown in Fig. 3.14.

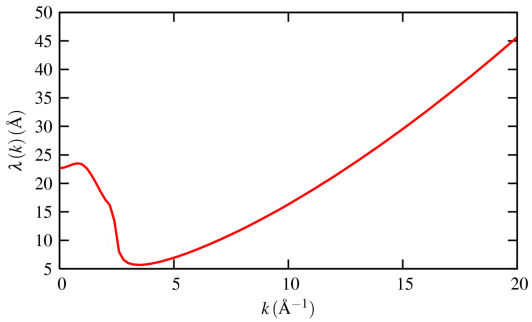

Fig. 3.15 The photoelectron MFP $\lambda(k)$ [1].

Besides the electronic structure around the Fermi level, XANES also contains the contribution from multiple scattering. As compared to EXAFS, the energy of the excited photoelectron corresponding to the XANES spectra is low, which leads to long EMFP, as presented in Fig. 3.15. Thus the single and multiple scattering effects can bring in more information about the local symmetry as compared to EXAFS. As a result, XANES is sensitive to the local environment (coordination environment, local symmetry, etc.). As shown in Fig. 3.16, in all the presented compounds, the Ti element is with the valence of +4. However the different coordination environment and local symmetry brings in distinctive features for the corresponding XANES spectra. Such sensitivity of XANES to the local surroundings is an advantage over EXAFS for looking at the local coordination environment. Furthermore, the XANES part of the XAS signal yields much higher signal-to-noise ratio as compared to EXAFS [1] and hence can be applicable, for example, to samples where satisfactory EXAFS data cannot be obtained.

For the theoretical calculation of the XANES spectra, the standard equation for EXAFS breaks down due to the divergent term $1/k$ (see equation-(3.44)). The domination of multiple

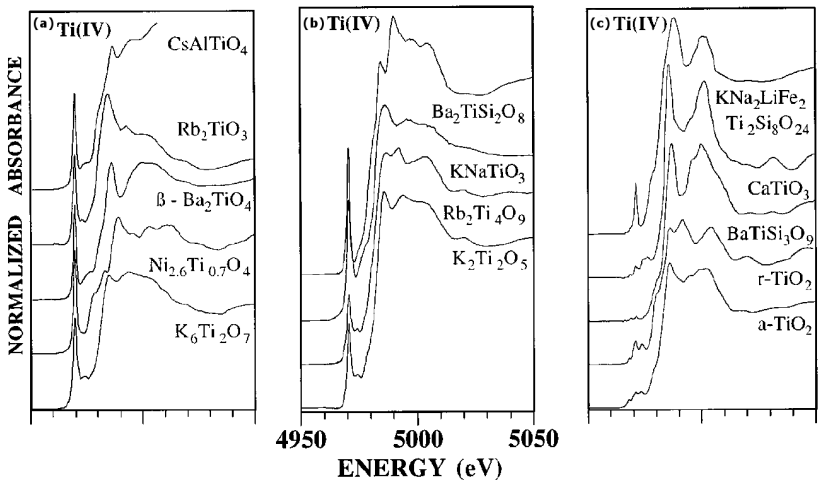

Fig. 3.16 Ti K-edge XANES spectra for various Ti oxide compounds with (a) fourfold, (b) fivefold and (c) sixfold coordinated Ti [36].

scattering brought in by the long EMFP at very low-k adds to the difficulty of the XANES theory. Especially for the L-edge (or M-edge) XANES, which corresponds to the transition involving the 2s and 2p (or 3s) electrons, the overlapping between the core and valence electrons wavefunctions cannot be ignored. Then the so-called *multiplet effect* which takes into account of the core-valence electron-electron interaction and the corresponding spin-orbital coupling makes it dramatically complex for the theoretical description of the XANES spectra.

However, in spite of the complexity in theoretical description and lack of simple analytical expression (like the standard EXAFS equation-(3.44)), the intensity and edge position of the XANES spectra can still be analysed in depth to extract the local structural information based on both the qualitative and quantitative analysis. For example, as shown in Fig. 3.17 (a), the Gaussian or pseudo-Voigt peak profiles fitting for the XANES pre-edge peaks could be used to extract the quantitative numbers for the oxidation state and coordination environment [33]. Also XANES can be used for the sample composition analysis through the linear combination fitting and the primary component analysis (PCA), both of which are available in Athena. Moreover, with the development of the theoretical calculation method and the computation power, it is already possible to carry out quantitative calculation to help predicting the local structure based on the XANES analysis. For example, the FitIt program [38] is available for fitting the structural model to the experimental spectra based on the theoretical XANES calculation and polynomial interpolation. Also shown in Fig. 3.17 (b),

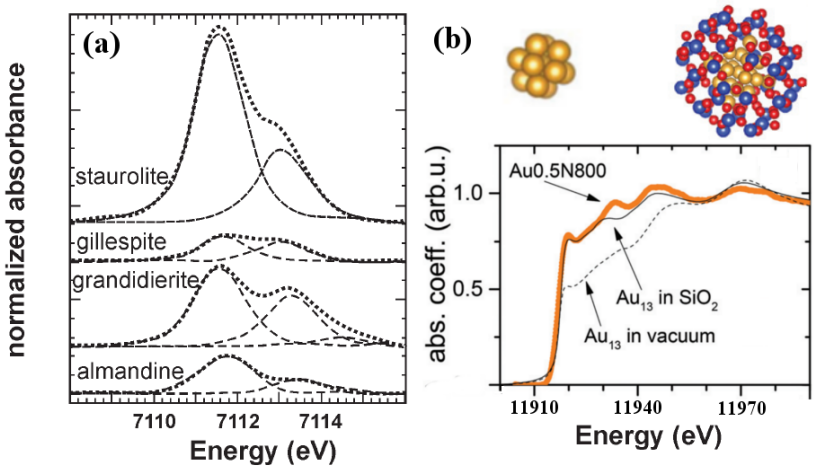

Fig. 3.17 (a) Examples of curve fits for mineral phases containing Fe^{2+} and Fe^{3+} [33]. (b) The XANES spectra of Au nanoclusters embedded in silica matrix, compared with the simulated spectra of a 13-atom cluster in SiO_2 and under vacuum [37].

the quantitative XANES calculation (using FDMNES package) was utilized to confirm the interaction between the Au nanoparticles with the supporting SiO_2 matrix. In Fig. 3.17 (b), the model on the left refers to the isolated Au_{13} model and the right-hand side model is the Au_{13} model embedded in the silica matrix. The comparison with the experimental XANES spectra (Fig. 3.17 (b), the thick orange line) shows better agreement with the latter model (Fig. 3.17 (b), solid black line) thus confirming the interaction between the Au nanoclusters with the supporting silica matrix [37]. Moreover in the articles by Y. Lei, et al. (2011), the effect of the particle size and adsorbates (CO and hydrogen) on the L-edge (L_2 and L_3) XANES spectra of the Pt nanoparticles through the theoretical simulation (using CASTEP) for the XANES spectra and the related DOS was reported [39]. Finally, it should be mentioned that in our own work, the numerical XANES calculation was utilized to look into the local symmetry of the Ge QDs system.

In the following chapter, the theoretical treatment of XANES spectra calculation based on the finite difference method (FDM) will be covered.

References

[1] M. Newville. Fundamentals of XAFS. *Rev. Mineral. Geochem.*, 78:33–74, 2014.

[2] Athena: A user's guide. http://bruceravel.github.io/demeter/aug/index.html, 2015. online; accessed 30-April-2016.

[3] Preparation of XAFS samples. http://gbxafs.iit.edu/training/XAFS_sample_prep.pdf. online; accessed 22-Jul-2016.

[4] C. M. Hessel, E. J. Henderson, J. A. Kelly, R. G. Cavell, T. K. Sham, and J. G. C. Veinot. The origin of luminescence from silicon nanocrystals: a near edge x-ray absorption fine structure (NEXAFS) and x-ray excited optical luminescence (XEOL) study of oxide-embedded and freestanding systems. *J. Phys. Chem. C*, 112:14247–14254, 2008.

[5] J. T. P. Goulon, P. M. Lemonnier, and J. Dexpert-Ghys. On a site-selective EXAFS experiment using optical emission. *Chem. Phys.*, 78:347–356, 1983.

[6] Quantum physics. http://quantummechanics.ucsd.edu/ph130a/130_notes/130_notes.html, Apr 2003. online; accessed 08-July-2016.

[7] E. A. Stern. Theory of the extended x-ray-absorption fine structure. *Phys. Rev. B*, 8:3027–3037, 1974.

[8] D. E. Sayers, E. A. Stern, and F. W. Lytle. New technique for investigating nanocrystalline structures: Fourier analysis of the extended x-ray-absorption fine structure. *Phys. Rev. Lett.*, 27:1204–1207, 1971.

[9] B. Ravel and M. Newville. ATHENA, ARTEMIS, HEPHAESTUS: data analysis for x-ray absorption spectroscopy using IFEFFIT. *J. Synchrotron Rad.*, 12:537–541, 2005.

[10] S. Tomic, B. G. Searle, A. Wander, N. M. Harrison, A. J. Dent, J. F. W. Mosselmans, and J. E. Inglesfield. *New tools for the analysis of EXAFS: the DL_EXCURVE package*. CCLRC Technical Report DL-TR-2005-001, 2004.

[11] A. Filipponi and A. D. Cicco. GNXAS: a software package for advanced EXAFS multiple-scattering calculations and data-analysis. *Task Quart.*, 4:575–669, 2000.

[12] J. J. Rehr and R. C. Albers. Scattering-matrix formulation of curved-wave multiple-scattering theory: application to x-ray-absorption fine structure. *Phys. Rev. B*, 41:8139–8149, 1990.

[13] The IFEFFIT tutorial. http://cars9.uchicago.edu/xafs_school/Material/Docs/Ifeffit_Tutorial/tutor.pdf, March 2001. online; accessed 03-May-2016.

[14] Athena: other features. http://cars9.uchicago.edu/xafs_school/APS_2005/CD/Docs/Athena/athena_misc.html, July 2005. online; accessed 03-May-2016.

[15] The atoms.inp archive. http://cars9.uchicago.edu/~newville/adb/search.html. online; accessed 08-July-2016.

[16] Demeter: XAS data processing and analysis. http://bruceravel.github.io/demeter/#old, 2015. online; accessed 08-July-2016.

[17] The official YAML web site. http://www.yaml.org/. online; accessed 08-July-2016.

[18] Artemis users' guide. http://bruceravel.github.io/demeter/artug/, 2015. online; accessed 08-July-2016.

[19] A. I. Frenkel and J. J. Rehr. Thermal-expansion and x-ray-absorption fine-structure cumulants. *Phys. Rev. B*, 48:585–588, 1993.

[20] Thermal effect on EXAFS. http://alpha.science.unitn.it/~rx/raggi_x/fornasini/pdf_JXAFS_09.pdf, September 2009. online; accessed 22-August-2016.

[21] E. Sevillano, H. Meuth, and J. J. Rehr. Extended x-ray absorption fine-structure debye-waller factors.1. monatomic crystals. *Phys. Rev. B*, 20:4908–4911, 1979.

[22] C. Kittel. *Introduction of solid state physics*. John Wiley and Sons, 2004.

[23] G. Bunker. *Introduction to XAFS: A Practical Guide to X-ray Absorption Fine Structure Spectroscopy*. Cambridge University Press, 2010.

[24] Chi-square: testing for goodness of fit. http://maxwell.ucsc.edu/~drip/133/ch4.pdf, March 2003. online; accessed 05-May-2016.

[25] A casual introduction to least-square fitting: a 'mostly' descriptive approach. http://www.aps.anl.gov/Xray_Science_Division/Powder_Diffraction_Crystallography/3LeastSquaresIntro/3LeastSquaresIntro.pdf, October 2012. online; accessed 05-May-2016.

[26] IFEFFIT measurement uncertainty. http://millenia.cars.aps.anl.gov/pipermail/ifeffit/2002-October/000148.html, October 2002. online; accessed 05-May-2016.

[27] A. I. Frenkel. Applications of extended x-ray absorption fine-structure spectroscopy to studies of bimetallic nanoparticle catalysts. *Chem. Soc. Rev.*, 41:8163–8178, 2012.

[28] K. Sasaki, K. A. Kuttiyiel, L. Barrio, D. Su, A. I. Frenkel, N. Marinkovic, D. Mahajan, and R. R. Adzic. Carbon-supported irni core-shell nanoparticles: synthesis, characterization, and catalytic activity. *J. Phys. Chem. C*, 115:9894–9902, 2011.

[29] A. Kalinko, M. Bauer, J. Timoshenko, and A. Kuzmin. Molecular dynamics and reverse Monte Carlo modeling of scheelite-type AWO_4 (A=Ca, Sr, Ba) EXAFS spectra. Karlsruhe, Germany, 23–28, August 2015. Karlsruhe Institute of Technology, 16th International Conference on X-ray Absorption Fine Structure.

[30] Adam Tenerholt, Britt Hedman, and Keith O. Hodgson. PySpline: A Modern, Cross-Platform Program for the Processing of Raw Averaged XAS Edge and EXAFS Data. In *AIP Proceedings, 13th International Conference on X-ray Absorption Fine Structure - XAFS13*, 2007.

[31] miXAFS. http://www.sci.u-toyama.ac.jp/phys/3ken/childlen/miXAFS/index-miXAFS.htm, March 2011. online; accessed 06-May-2016.

[32] Larch: data analysis tools for x-ray spectroscopy. http://xraypy.github.io/xraylarch/, 2012. online; accessed 24-Jul-2016.

[33] G. S. Henderson, F. M. F. Groot, and B. J. A. Moulton. X-ray absorption near-edge structure (XANES) spectroscopy. *Rev. Mineral. Geochem.*, 78:75–138, 2014.

[34] B. Poe, C. Romano, and G. S. Henderson. Raman and XANES spectroscopy of permanently densified vitreous silica. *J. Non-Cryst. Solids*, 341:162–169, 2004.

[35] T. Höche, M. Mäder, S. Bhattacharya, G. S. Henderson, T. Gemming, R. Wuth, C. Rüssel, and I. Avramov. $ZrTiO_4$ crystallization in nanosized liquid-liquid phase-separation droplets in glass – a quantitative XANES study. *CrystEngComm*, 13:2550–2556, 2011.

[36] F. Farges, G. E. Brown Jr., and J. J. Rehr. Ti K-edge XANES studies of Ti coordination and disorder in oxide compounds: comparison between theory and experiment. *Phys. Rev. B*, 56:1809–1819, 1997.

[37] C. Maurizio, T. Cesca, G. Perotto, B. Kalinic, N. Michieli, C. Scian, Y. Joly, G. Battaglin, P. Mazzoldi, and G. Mattei. Core-shell-like Au sub-nanometer clusters in Er-implanted silica. *Nanoscale*, 7:8968–8977, 2015.

[38] G. Smolentsev and A. V. Soldatov. FitIt: new software to extract structural information on the basis of xanes fitting. *Comp. Matter. Science*, 39:569–574, 2007.

[39] Y. Lei, J. Jelic, L. C. Nitsche, R. Meyer, and J. Miller. Effect of particle size and adsorbates on the L_3, L_2 and L_1 X-ray absorption near structure of supported *p*t nanoparticles. *Top Catal.*, 54:334–348, 2011.

Chapter 4

XANES theoretical calculation

The traditional method for the theoretical calculation of XAFS spectra (both EXAFS and XANES) based on scattering theory relies on the so-called *muffin-tin* approximation for the scattering potential, where the potential around the scatterers (i.e. atoms) is treated as spherically symmetric. In the interstitial region between scatterers the potential is set to be flat (i.e. constant). Such approximation works well for the EXAFS calculation but may fail to reproduce the XANES spectra. For the near-edge region, the corresponding energy of the photoelectron is comparable to the interstitial potential, therefore the variation of potential does matter. Also, the strong multiple scattering effects due to the long EMFP corresponding to the near-edge region leads to the accumulation of errors caused by the approximate treatment of the scattering potential. Moreover, for systems like carbon, the highly anisotropic charge density and the weak atomic potential scattering (therefore the interstitial potential scattering is comparatively strong) requires accurate treatment of the scattering potential.

To go beyond the limitation of the muffin-tin approximation, there have been several available approaches, such as the discrete variational method [1], the full-potential Koringa-Kohn-Rostoker (KKR) approach [2, 3], and the full linear augmented plane wave (FLAPW) method [4], etc. It's also worth mentioning the recently developed full potential multiple scattering (FPMS) approach by Natoli's group , which gives much better agreement with experiment as compared to the standard multiple scattering calculations in the muffin-tin approximation [5]. Another approach to calculate the XANES spectra is based on the finite difference method (FDM), which avoids the muffin-tin approximation by solving the Schrödinger equation using the local density approximation (LDA). For this thesis, the FMD based package FDMNES for XANES calculation developed by Y. Joly [6] was mainly used. Therefore in this chapter

the theoretical implementation of the FDM approach in the FDMNES program will be briefly covered.
At the end of this chapter, the complexity and recent advances in the theoretical description for the L-edge XANES spectra in some transition-metals contained systems will also be briefly addressed.

4.1 Finite difference method (FDM) for XANES

First of all, according to the Fermi's golden rule (see (B.43) in Appendix-B), if the absorption coefficient is going to be evaluated directly (unlike in the scattering theory framework where the Green's function method is used), it is crucial to evaluate both the initial and final states. The initial state can be represented by an atomic core orbital. Therefore it can be obtained from *ab initio* calculation without difficulty. Whereas the calculation for the final state is difficult (since it is not ground state any more), and it is the evaluation of the final state that is performed through the FDM. Generally in FDM, the whole calculation region is discretized over a grid of points, and the derivative function at each point is evaluated approximately with the function value of neighbouring points (more details about the FDM is given in Appendix-D). Specifically for the Schrödinger equation as following,

$$\hat{\mathscr{H}}\psi = (-\frac{\hbar^2}{2m}\Delta + V)\psi = E\psi \tag{4.1}$$

the Laplacian in the Hamiltonian can be written in its discrete form:

$$\Delta\psi_i = \frac{1}{h^2}(\frac{4}{3}\sum_{j,\varepsilon}\psi_j^{\varepsilon} - \frac{1}{12}\sum_{j,\varepsilon}\psi_j^{\varepsilon\varepsilon} - \frac{15}{2}\psi_i) \tag{4.2}$$

where symbol i indicates the discrete grid points and ψ_i represents the value of the wavefunction on each grid point, ψ_j^{ε} and $\psi_j^{\varepsilon\varepsilon}$ are the values of wavefunction on the first and second neighbouring grid points in the direction labelled by εj, h is the distance between the grid points. If the discrete form of the Laplacian operator Δ is denoted as l_{ij}, the Schrödinger equation corresponding to grid point i is given as:

$$(-l_{ii} + V_i - E)\psi_i + \sum_{j}^{neighbour} -l_{ij}\psi_j = 0 \tag{4.3}$$

where V_i represents the potential on the node point of i and the second term (the summation

over dummy variable j) corresponds to the contribution to the photoelectron kinetic energy (on grid point i) from wavefunction on all the neighbouring grid points. In FDMNES, the

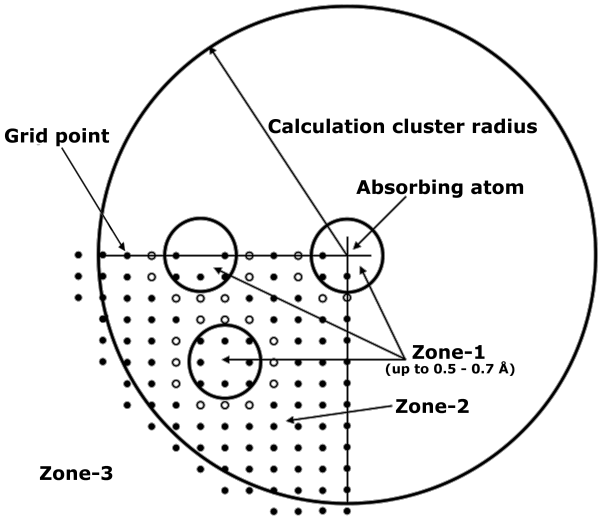

Fig. 4.1 The illustration for the division of the calculation cluster to three zones in FDMNES. The small circle (zone-1) represents the region surround the atomic ion core where the potential is assumed to be spherically symmetric. Outside the small circle (zone-2), it is where the FDM was used to solve the Schrödinger equation on the grid points. Outside the big circle (zone-3), the potential is assumed to be constant (flat). Here it should be pointed out that the solid and open dots refer to the grid points but not the atoms [6].

potential is built up based on the local density approximation (LDA) and also the Hedin-Lundqvist potential [7] is introduced to account for the exchange-correlation interaction. Specifically, since the photoelectron is high in kinetic energy when close to the ion core and much lower in between ion cores, the potential within small sphere (up to 0.5 Å $-$ 0.7 Å in radius) around the atomic ion core is assumed to be spherically symmetric and is further expanded in spherical waves. Here it should be pointed out that the region with the assumed spherically symmetric potential in FDMNES is much smaller than the spheres in a muffin-tin formulation ($\sim$ 1.0 Å).

To solve the Schrödinger equation corresponding to the final excited states, the calculation cluster in FDMNES is divided into three different regions as shown in Fig. 4.1. The final states calculation is then carried out separately in the three different kinds of regions. For zone-1, the assumed spherically symmetric potential can be written as a multipole expansion

around the atomic ion core:

$$V(\mathbf{r}) = \sum_L V_L(r) Y_L(\Omega) \tag{4.4}$$

where r is the distance away from the atomic centre and Ω refers to the angular position, Y_L is the spherical harmonics where L stands for the index (l,m) of the corresponding harmonics component. Correspondingly, the overall solution for the wavefunction $\psi(\mathbf{r})$ can be written as the linear combination of the solution for each independent angular component:

$$\psi(\mathbf{r}) = \sum_L a_L \phi_L(\mathbf{r}) \tag{4.5}$$

Here the coefficients a_l of the linear combination are the introduced unknowns, which will be finally obtained by connecting the solution at the boundary between zone-1 and zone-2 (see later discussion). The independent solution $\phi_L(\mathbf{r})$ can be further expanded in a similar way as the multipole expansion of the potential:

$$\phi_L(\mathbf{r}) = \sum_{L'} \varphi_{L'L}(r) Y_{L'}(\Omega) \tag{4.6}$$

Then the expansion of the potential (4.4) and independent wavefunctions (4.6) can be inserted into the Schr$\ddot{o}$dinger equation (inside zone-1):

$$\begin{aligned}
&\Big[-\frac{1}{r^2}\frac{d}{dr}\big(r^2\frac{d}{dr}\big) + \frac{l'(l'+1)}{r^2} + \sum_L V(r) Y_L(\Omega)\Big] \sum_{L'} \varphi_{L'L}(r) Y_{L'}(\Omega) \\
&\quad = E \sum_{L'} \varphi_{L'L}(r) Y_{L'}(\Omega)
\end{aligned} \tag{4.7}$$

$$\Downarrow$$

$$\begin{aligned}
&\Big[\frac{1}{r^2}\frac{d}{dr}\big(r^2\frac{d}{dr}\big) + E - \frac{l'(l'+1)}{r^2}\Big] \sum_{L'} \varphi_{L'L}(r) Y_{L'}(\Omega) \\
&\quad = \sum_L V_L(r) Y_L(\Omega) \sum_{L'} \varphi_{L'L}(r) Y_{L'}(\Omega)
\end{aligned} \tag{4.8}$$

By left multiplying another spherical harmonics function $Y^*_{L''}$ ('*' here represents the complex conjugate) and integrating over Ω on both sides of (4.8), one could then have the following coupled equations that functions $\phi_{L'L}(r)$ should satisfy:

$$\Big[\frac{1}{r^2}\frac{d}{dr}\big(r^2\frac{d}{dr}\big) + E - \frac{l'(l'+1)}{r^2}\Big] \varphi_{L'L}(r) = \sum_{L''L''^\dagger} C^{L'}_{L''L''^\dagger} V_{L''^\dagger}(r) \varphi_{L''L''^\dagger}(r) \tag{4.9}$$

where the real Gaunt coefficients $C^{L'}_{L''L''^{\dagger}}$ are given as:

$$C^{L'}_{L''L''^{\dagger}} = \int Y^{*}_{L''}(\Omega) Y_{L'}(\Omega) Y_{L''} d\Omega \tag{4.10}$$

Here it should be noticed the dummy summation index L and L' in (4.8) is changed to L'' and $L''^{\dagger}$ in (4.9). From (4.5) to (4.10), it can be seen that the only unknowns for the wavefunctions within zone-1 are the amplitudes a_L of the corresponding harmonics component (see (4.5)), given the assumed spherically symmetric potential in this region.

The wavefunction in zone-1 are evaluated together with that in zone-2, where the Shcr$\ddot{o}$dinger equation is discretized following the approach given in (4.2) – (4.3). The continuity at the zone boundary (solid dots within the small circle in Fig. 4.1) is then applied to connect the wavefunctions of zone-1 and zone-2. To solve the only unknowns a_L, Y. Joly [6] further applies equation-(4.5) over the grid points just outside the boundary of zone-1 (empty dots in Fig. 4.1), and the continuity of the Fourier transform is applied there for setting up the correct number of equations to solve the only unknowns a_L (detailed discussion can be found in Joly's paper: Ref. [6]).

As for the outer space beyond the calculation cluster (zone-3 in Fig. 4.1), the potential is taken as constant and the corresponding solution of the wavefunction can be given by Bessel and Hankel (or Neumann) function:

$$\psi^{f}_{Bessel-Hankel} = J_{L_f}(\mathbf{r}) + i \sum_{L} \tau^{f}_{L} H^{(1)}_{L}(\mathbf{r}) \tag{4.11}$$

$$\psi^{f}_{Bessel-Neumann} = J_{L_f}(\mathbf{r}) + \sum_{L} \eta^{f}_{L} N_{L}(\mathbf{r}) \tag{4.12}$$

where J_L, $H^{(1)}_L$ and N_L are the generalized Bessel, Hankel and Neumann functions, respectively, and τ_L (or η_L) is the introduced new unknowns. Again, the continuity at the boundary between zone-2 and zone-3 should be applied to solve the unknowns, following similar approach as for the situation of zone-1 and zone-2 – therefore both the continuity of the wavefunction and the Fourier transform should be considered.

Following the procedures described aove, one could finally get a general matrix containing all the unknowns in the wavefunctions (both atomic core and outer space) as presented in Ref. [6]. Therefore the overall solution for the final states based on the FDM approach can be obtained, beyond the muffin-tin approximation for the potential.

Here it concludes the introduction to the application of the FDM approach for the XANES spectra calculation. In the next section, the still existing challenges for the theoretical description of XANES together with the corresponding advances will be briefly addressed.

4.2 Challenges and advances in XANES calculation

For both of the FDM based approach introduced in this chapter and the multiple scattering theory based methods (e.g. FEFF) in the XANES calculation, the X-ray photon absorption is treated as the single-electron problem, where the 'single-electron' refers to the 'single core electron excitation'. By ignoring the direct coupling between the core hole and the excited photoelectron, the core-hole effect within the single-electron framework is usually treated following the so-called *final state rule* (FSR), i.e. the $(Z+1)$ approximation. For the FSR, the energetic positions of the spectral features are determined by the properties of the final state [8, 9], i.e. a core-hole (the positive charge of which is added to the nucleus to give the equivalent $(Z+1)$ nucleus charge), an excited photoelectron and the absorbed X-ray photon. For example, in both FEFF and FDMNES, the core-hole effect is treated following the FSR by default.

The single-electron and FSR approach often works well for K-edge absorption problem, but the $L_{2,3}$ absorption, especially for transition-metal (TM) systems, are poorly described [10]. This is mainly due to the so-called *multiplet effects*, including the core and valence wavefunctions overlapping and spin-spin coupling, that cannot be ignored owing to the small lifetime broadening of L-edge absorption spectra as compared to the K-edge. To go beyond the limitation of the single-electron approach, quite a few approaches have been proposed to account for the many-body interactions. One of the main methods is based on the multiplet model, for example, the CTM4XAS program developed by F. Groot, et al (2010) embeds the multiplet model to take care of the multiplet effects for the TMs L-edge XAFS spectra calculation [11]. Recently, a novel multi-channel multiple scattering method, which takes account of the multiplet effects within the multiple-scattering framework, was reported by P. Krüger and Natoli, et al. [12, 13]. Such an approach was successfully applied to the L-edge problems in various systems, e.g. the Ti $L_{2,3}$ spectra in TiO_2 and $SrTiO_3$ [13], the Ca $L_{2,3}$ spectra, etc. [14]. Another approach is the *ab initio* configuration interaction (CI) method [15, 16], which only applies to small cluster but not applicable for extended systems [17]. Moreover, the Bethe-Salpeter equation (BSE) approach provides another way to solve the many-body interaction problems. For example, the BSE method was embedded in the density functional theory (DFT) ground state treatment for the L-edge absorption spectra

calculation by P. Blaha, et al. [17]. The BSE approach is also embedded in the multiple scattering theoretical framework [18] and is currently available in the latest version of FEFF (version-9.6) [19].

In the following chapters, the EXAFS data analysis methods and the theoretical spectra calculation approaches will be applied to specific systems to explore the local structure of Ge QDs system.

References

[1] D. E. Ellis and G. S. Painter. Discrete variational method for the energy-band problem with general crystal potentials. *Phys. Rev. B*, 2:2887–2898, 1970.

[2] T. Huhne, C. Zecha, H. Ebert, P. H. Dederichs, and R. Zeller. Full-potential spin-polarized relativistic Korringa-Kohn-Rostoker method implemented and applied to bcc Fe, fcc Co, and fcc Ni. *Phys. Rev. B*, 58:10236–10247, 1998.

[3] D. Ahlers, G. Schutz, V. Popescu, and H. Ebert. Fully relativistic theory for the magnetic extended x-ray absorption fine structure. *J. Appl. Phys.*, 83:7082–7084, 1998.

[4] P. Blaha, K. Schwartz, P. Sorantin, and S. B. Trickey. Full-potential, linearized augmented plane-wave programs for crystalline systems. *Comp. Phys. Commun.*, 59:399–415, 1990.

[5] J. Q. Xu, P. Krüger, C. R. Natoli, K. Hayakawa, Z. Y. Wu, and K. Hatada. X-ray absorption spectra of graphene and graphene oxide by full-potential multiple scattering calculations with self-consistent charge density. *Phys. Rev. B*, 92:125408, 2015.

[6] Y. Joly. X-ray absorption near-edge structure calculations beyond the muffin-tin approximation. *Phys. Rev. B*, 63:125120, 2001.

[7] L. Hedin and B. I. Lundqvist. Explicit local exchange-correlation potentials. *J. Phys. C: Solid St. Phys.*, 4:2064–2083, 1971.

[8] X-ray absorption spectroscopy. http://xes.fysik.su.se//PDF/Lecture3.pdf, June 2010. online; accessed 13-May-2016.

[9] J. Stöhr. *NEXAFS spectroscopy*. Springer-Verlag Berlin Heidelberg, 1992.

[10] F. D. Groot. Multiplet effects in x-ray spectroscopy. *Coord. Chem. Rev.*, 249:31–63, 2005.

[11] E. Stavitski and F. D. Groot. The CTM4XAS program for EELS and XAS spectral shape analysis of transition metal L edges. *Micron*, 41:687–694, 2010.

[12] C. R. Natoli, M. Benfatto, C. Brouder, M. F. R. López, and D. F. Foulis. Multichannel multiple-scattering theory with general potentials. *Phys. Rev. B*, 42:1944–1968, 1990.

[13] P. Krüger. Multichannel multiple scattering calculation of $L_{2,3}$-edge spectra of TiO_2 and $SrTiO_3$: Importance of multiplet coupling and band structure. *Phys. Rev. B*, 81:125121, 2010.

[14] P. Krüger and C. R. Natoli. Theory of Ca $L_{2,3}$-edge xas using a novel multi-channel multiple-scattering method. *J. Synchrotron Rad.*, 12:80–84, 2005.

[15] H. Ikeno and I. Tanaka. Effects of breit interaction on the $L_{2,3}$ x-ray absorption near-edge structures of 3d transition metals. *Phys. Rev. B*, 77:075127, 2008.

[16] Y. Kumagai, H. Ikeno, and I. Tanaka. All-electron CI calculations of 3d transition-metal $L_{2,3}$ xanes using zeroth-order regular approximation for relativistic effects. *J. Phys. Condens. Matter*, 21:104209, 2009.

[17] R. Laskowski and P. Blaha. Understanding the $L_{2,3}$ x-ray absorption spectra of early 3*d* transition elements. *Phys. Rev. B*, 82:205104, 2010.

[18] J. J. Rehr, J. A. Soininen, and E. L. Shirley. Final-state rule vs the Bethe-Salpeter equation for deep-core x-ray absorption spectra. *Phys. Script.*, T115:207–211, 2005.

[19] Feff9.6 users' guide. http://leonardo.phys.washington.edu/feff/Docs/feff9/feff90/feff90_users_guide.pdf, February 2013. online; accessed 12-May-2016.

Chapter 5

Structure of colloidal matrix-free Ge quantum dots

In this chapter, the local structure analysis for the Ge QDs prepared by colloidal synthesis from GeO_2 and $GeCl_4$ precursors will be given. The as-prepared and annealed samples have been studied by the combination of EXAFS, PXRD, TEM and Raman. Details about the Ge QDs synthesis routes and sample characterization techniques will be presented first. This will be followed by the analysis and results discussion for the experimental results. Conclusions drawn from the comprehensive analysis will be given in the end as the final remarks.

5.1 Experiment

5.1.1 Synthesis

Two synthesis routes for Ge QDs were used. For the first route, bench-top colloidal synthesis [1] was utilized to prepare Ge QDs by reduction of GeO_2 at 60 °C at ambient pressure. In a typical experiment, GeO_2 powder (26 g, $> 99\%$) was dissolved in a solution of polyvinylpyrolidine (0.01 g, PVP, MW = 630.000) and of NaOH (10 mL, 0.15 M). Then HCl (0.5 mL, 0.5 M) was added to the flask to increase the pH to 7.0. At this point the solution was colourless and transparent. Heating the solution resulted in the formation of Ge nanoparticles by controlled addition of $NaBH_4$ (20 $mL \cdot h^{-1}$ of 10 mL of 0.75 M) via a syringe pump. Over 30 min the colour of the solution changed from colourless to yellow, then brown and finally dark brown. All chemicals were purchased from Sigma-Aldrich and used as purchased with-

out any purification. The formed Ge NPs were separated from the chemical residual using 10000 r.p.m. centrifugation and washed with ethanol several times. The formed Ge NPs were suspended in ethanol or kept in hexane. All samples were sealed in glass capillaries (0.7 mm) immediately after preparation to avoid prolonged exposure to air. The NPs produced via this synthesis route are referred to as CS1.
For the second route, $GeCl_4$ (265 mL) was reduced with a solution of ethylene glycol (10 mL) and PVP (0.05 g, MW = 630.000) [2]. Then triglyme (6 mL) was added with two different rates: 90 mL $\cdot$ h^{-1} for the first 2 mL and 9 mL $\cdot$ h^{-1} for the remaining 4 mL. This controlled addition process of the triglyme was performed with a syringe pump into a three-neck round-bottom flask in which the solution was bubbled continuously with Ar gas or a mixture of H_2 and Ar gas from a micro-tube inlet through the solution. The final product was separated from the colloidal chemical solution by centrifugation at 10000 r.p.m. for 10 min. All samples were sealed in glass capillaries (0.7 mm) immediately after preparation to avoid prolonged exposure to air. The NPs produced via this synthesis route are referred to as CS2. In addition to the synthesis, the Ge QDs were annealed in H_2/Ar gas and Ar gas mediums at a flow rate of 100 ccm at temperatures of 450 °C and 600 °C for 1 h. All samples were annealed immediately following synthesis and were sealed in glass capillaries (0.7 mm) immediately after annealing. All the sample synthesis work was done by Dr. Ali Karatutlu in our group.

5.1.2 Characterization

TEM (Jeol 2010) was employed to characterize size distribution and morphology. Energy dispersive X-ray spectroscopy (EDX) was used to analyse the chemical component. Raman measurements were carried out using a Renishaw Raman microscope equipped with a 632 nm He-Ne laser. The experimental spectral resolution was 0.5 cm^{-1}. PXRD (performed at beamline B18, X-ray energy 8047 eV) and EXAFS measurement (performed at beamline B18, X-ray energy continuous from 10800 eV to 12400 eV, step-size: 0.92 eV, energy resolution: $\Delta E/E = 1.4 \times 10^{-4}$) was carried out at the Diamond synchrotron light source. For PXRD measurements a multi-channel curved detector was used. EXAFS measurements were carried out in transmission mode using ionization chambers. Reference data for bulk crystalline Ge were collected to obtain the value of the passive reduction factor S_0^2 that was later used in the analysis of EXAFS data of the samples. The passive reduction factor in diamond-type bulk Ge was found to be 0.94 ± 0.06.

5.2 Results and Discussion

TEM images for as-prepared CS1 and CS2 samples are shown in Figs. 5.1 (a) and 5.1 (c), respectively. The size distribution of as- prepared samples (both CS1 and CS2) was calculated from TEM images (Figs. 5.1b and 5.1d), 60 particles were used to calculate

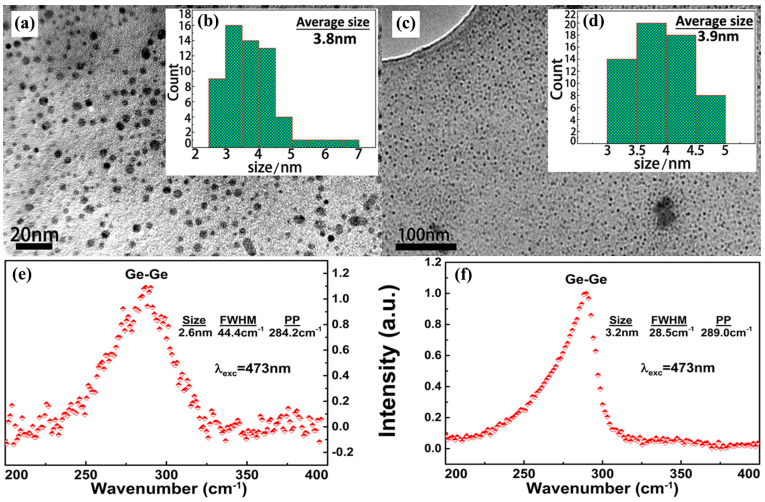

Fig. 5.1 (a,b) TEM and size distribution of CS1 as-prepared sample; (c,d) TEM and size distribution of CS2 as-prepared sample; (e,f) Raman spectrum for CS1 and CS2 as-prepared samples, respectively.

the size distribution. For CS1 and CS2 the QDs were found to have an average size of 3.8 ± 0.1 nm and 3.9 ± 0.1 nm, respectively. Raman spectra for as-prepared CS1 and CS2 samples are shown in Figs. 5.1 (e) and 5.1 (f). The observed peak can be assigned to the Ge-Ge vibration mode (around 300 cm^{-1} in bulk crystalline Ge). The asymmetry of the Raman peaks (49 : 27 and 44 : 16 at FWHM (full width at half maximum) for CS1 and CS2, respectively), which is especially clear for the CS2 sample (Fig. 5.1f), is due to particle size effects [3, 4]. The average particle sizes obtained from Raman using a fitting based on the phonon confinement model [3, 4] for CS1 and CS2 are 2.6 ± 0.5 nm and 3.2 ± 0.5 nm, respectively. This is in contrast to the TEM data where observed sample sizes are very similar. For CS2, the particle sizes obtained from TEM and Raman are similar. However, there is a clear discrepancy between Raman and TEM size analysis in CS1. In both samples the Raman peaks are downshifted (as compared with the bulk cGe) as expected, but the broader peak observed in the spectrum of CS1 may suggest a higher amorphous component. This would explain the discrepancy in sizes calculated from TEM (Fig. 5.1b) and Raman (Fig.

5.1e) since the quantum confinement model for particle size calculation [3, 4] assumes a crystalline sample. Furthermore, contribution from the amorphous content (higher in CS1) to the Raman signal may explain much less pronounced asymmetry of the signal from CS1 sample as compared with CS2.

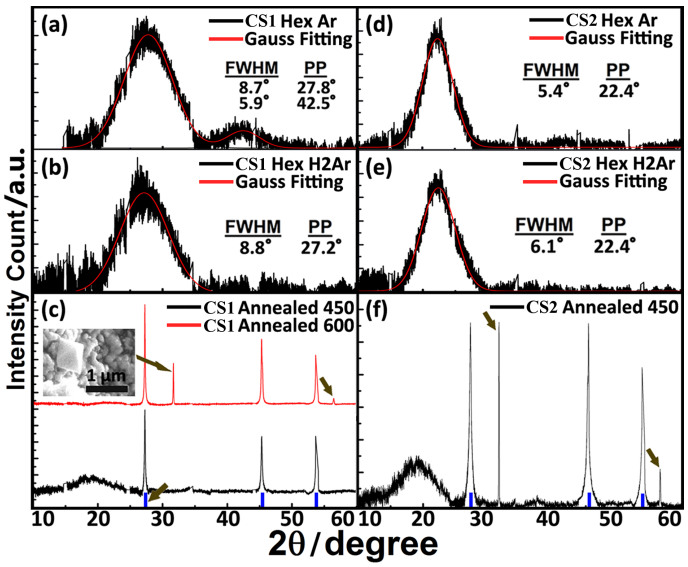

Fig. 5.2 Background-subtracted PXRD patterns (X-ray energy = 8047 eV) for all as-prepared and annealed CS1 (a – c) and CS2 (d – f)samples; reference for diamond-type Ge (JCPDS No. 4-545) is shown as blue marks at the bottom. 'Hex' in the sample name means a suspension in hexane; 'Ar' means synthesis with Ar gas protection and 'H2Ar' for a mixture of H_2 and Ar. The inset image is scanning electron microscope (SEM) image for CS1 annealed 600.

PXRD measurements were carried out to obtain long-range order information. Fig. 5.2 presents background-subtracted diffraction patterns for all CS1 and CS2 samples. CS1 (GeO_2 precursor) and CS2 ($GeCl_4$ precursor) as-prepared samples both show broad diffraction features typical of small nano- particles (or amorphous samples). However, the average peak positions are clearly different as can be seen in Figs. 5.2 (a), 5.2 (b), 5.2 (d) and 5.2 (e), where numerical values for the peak positions and of the FWHM are also shown, assuming Gaussian peak profile. Analysis of the FWHM of XRD peaks in the 20–30° range suggests a higher degree of disorder in as-prepared CS1 (FWHM of 8.7–9.6°) samples compared with as-prepared CS2 (FWHM of 5.4–6.1°). This is consistent with the Raman data shown earlier. However, FWHM for both samples are smaller than that of around 15° normally observed

in bulk [5] or thin-film [6, 7] amorphous Ge. Thus, XRD data suggest a higher degree of long-range order in all our as-prepared Ge QDs than in a typical amorphous Ge phase.

Table 5.1 d-spacing (in Å) calculated from PXRD patterns compared with JCPDS database for α-quartz, rutile GeO_2 and diamond-type Ge.

Sample	Experiment	α-quartz GeO_2 (JCPDS No. 361463)	Rutile GeO_2 (JCPDS No. 710651)	Diamond Ge (JCPDS No. 4-545)
CS1 Hex Ar	3.21 ± 0.03	3.43 (101)	3.11, (110)	3.25, (111)
	2.13 ± 0.01	2.16, (202)	2.11, (111)	2.00, (220)
CS1 Hex H_2Ar	3.28 ± 0.03	3.43, (101)	3.11, (110)	3.25, (111)
CS1 annealed 450	4.65 ± 0.06	4.32, (110)	NA	NA
	3.27 ± 0.03	3.43, (101)	3.11, (110)	3.25, (111)
	2.00 ± 0.01	2.02, (201)	1.97, (210)	2.00, (220)
	1.70 ± 0.01	1.73, (202)	NA	1.70, (311)
CS1 annealed 600	3.27 ± 0.03	3.43, (101)	3.11, (110)	3.25, (111)
	2.82 ± 0.02	2.49, $(2\bar{1}0)$	NA	NA
	2.00 ± 0.01	2.02, (201)	1.97, (210)	2.00, (220)
	1.70 ± 0.01	1.73, (202)	NA	1.70, (311)
	1.63 ± 0.01	1.63, $(3\bar{1}0)$	1.62, (212)	NA
CS2 Hex Ar	3.97 ± 0.04	4.32, (110)	NA	NA
CS2 Hex H_2Ar	3.97 ± 0.04	4.32, (110)	NA	NA
CS2 annealed 450	4.67 ± 0.06	4.32, (110)	NA	NA
	3.27 ± 0.03	3.43, (101)	3.11, (110)	3.25, (111)
	2.82 ± 0.02	2.49, $(2\bar{1}0)$	NA	NA
	2.00 ± 0.01	2.02, (201)	1.97, (210)	2.00, (220)
	1.70 ± 0.01	1.73, (202)	NA	1.70, (311)
	1.63 ± 0.01	1.63, $(3\bar{1}0)$	1.62, (212)	NA

Detailed comparison of d-spacing between experimental data and the reference (Ge and GeO_2 related) can be found in Table 5.1. The position of the first broad peak in PXRD data for CS1 (corresponding to a distance of around 3.28 Å) is consistent with the distance corresponding to the (111) plane of diamond-type (JCPDS No. 4-545) Ge structure. However, the peak position is different for CS2 as-prepared samples, as it corresponds to a distance of around 3.97 Å (see Table 5.1). This result is contrary to the XRD data previously reported for this synthesis route [2], but similar to the recently reported XRD data recorded for nanocrystalline Ge prepared by laser ablation [8].

We compared the PXRD signal for CS2 samples with a number of relevant metastable Ge phases (ST12 [9], mC16 [10] and BC8 [11]) in order to understand possible origins of the peak position. Our data together with the corresponding PXRD simulated for several Ge phases are shown in Fig. 5.3. One can see that out of all phases, only the recently reported mC16 phase [10] has several diffraction peaks that fall within the range of the observed broad peak.

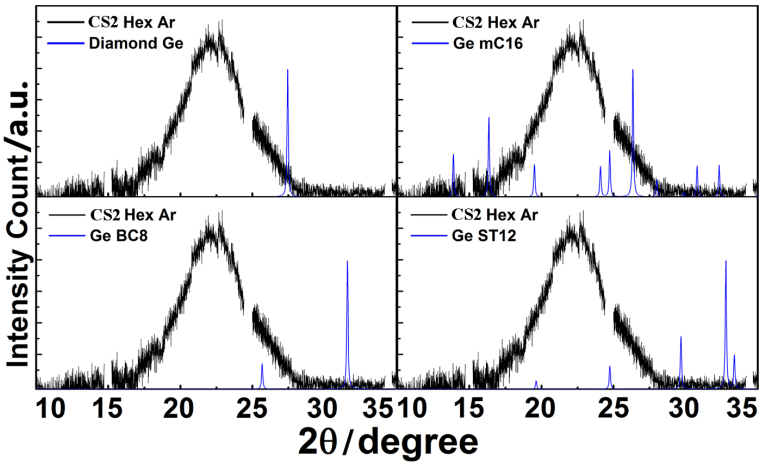

Fig. 5.3 Comparison if CS2 as-prepared sample PXRD pattern with Ge related phase: (a) diamond, (b) mC16, (c) BC8, (d) ST12. Gaps in the original data are due to dead areas between XRD detector segments.

Table 5.2 Comparison of two extra diffraction peaks in CS1 annealed samples with Ge metastable phases.

Experiment	BC8, Ge	ST12, Ge	mC16, Ge
2.82 Å	2.83 Å, (112)	2.72 Å, (201)	2.77 Å, $(0\bar{2}2)$
1.63 Å	1.63 Å, (114)	1.64 Å, (320)	1.62 Å, $(4\bar{2}2)$

We investigated the effects of annealing on the structure of as-repared Ge QDs further. As seen in Fig. 5.2, annealing results in crystallization of as-prepared CS1 and CS2 samples into diamond-type Ge. However, in all cases, besides the expected diamond-type Ge phase related peaks, there are additional reflections present. These diffraction peaks, labelled with arrows, for CS1 annealed 600 and CS2 annealed 450 (samples annealed at 450 °C and 600 °C) are not from diamond-type Ge. EDX measurements were carried out for these two samples to check impurities beyond Ge. Results show that these two annealed samples are both mainly composed of Ge, C (from the TEM grid) and O, which suggests that the two extra diffraction peaks can only come from a Ge-related phase.

Further comparison (see Table 5.2) with relevant Ge metastable phases suggests that these reflections are close to those found in the BC8 (cubic unit cell) phase. Interestingly, the inset (Fig. 5.2) scanning electron microscope (SEM) image for CS1 annealed 600 shows a pyramid of large size (around 1 mm), which could explain the sharpness of the arrow-labelled diffraction peak, while the pyramid shape is not inconsistent with a BC8 structure.

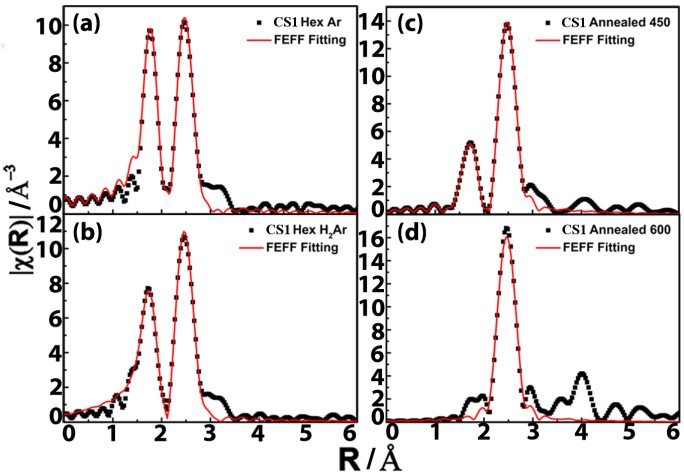

Fig. 5.4 (a,b) EXAFS fitting result for CS1 Hex Ar and CS1 Hex H_2Ar, respectively; (c,d) EXAFS fitting result for CS1 Ar annealed 450 and CS1 Ar annealed 600, respectively.

EXAFS measurements at the Ge K-edge were performed to determine the local atomic arrangements and to gain information on the local atomic distortions and possible surface termination since the technique selectively probes the environment of Ge atoms. EXAFS spectra were transformed into pseudo radial distribution functions to visualize the structural data (Fig. 5.4: CS1; Fig. 5.5: CS2). For as-prepared CS1 (GeO_2 precursor) samples, a clear signal from Ge-O bonding was observed. We conclude that Ge-O bonding is most likely to be associated with the surface, since no signal corresponding to Ge-O-Ge bonding (3.066 or 3.221 Å) [12] was observed in EXAFS and no reflections were found corresponding to GeO_2 in PXRD. Moreover, one can clearly see (Figs. 5.4a and 5.4b) that this feature is stronger for the sample where Ar rather than H_2Ar gas was used. Using the IFEFFIT algorithm, the fitted Ge-O bonding length (around 1.78 Å, Table 5.3) is found to be close to the bond length (1.87 Å) in rutile-type GeO_2 [13]. Here the shortening of the Ge-O bonding length for our sample as compared to the reference could be associated with the surface Ge-O bonding as mentioned above. A correlated Debye model was used to fit the Ge-Ge shell. From Table 5.3 it can be inferred that the fitted Debye temperature is close to the theoretical value of bulk Ge (373 K) [14]. The fitted Ge-Ge bond length is around 2.45 Å, which is consistent with that of diamond-type Ge. EXAFS results suggest that a GeO_2 shell may contribute to the overall particle size and thus further explain the size discrepancy between the TEM result and Raman calculation for as-prepared CS1 sample. For as-prepared CS2 (see Fig. 5.5), no other bonding features beyond Ge-Ge were observed. This indicates there could exist

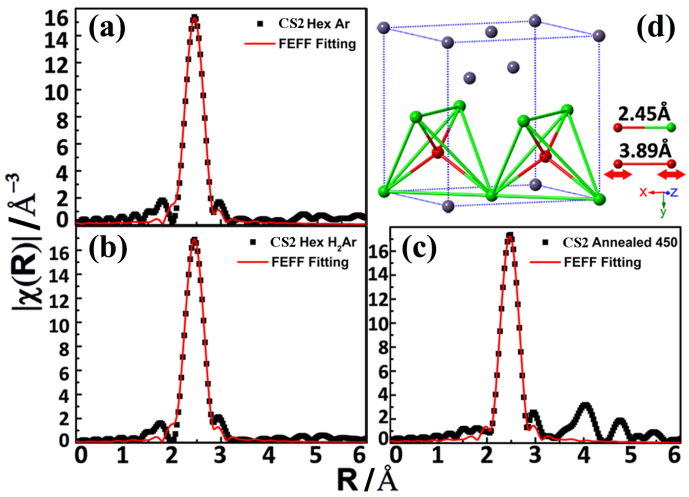

Fig. 5.5 (a,b) EXAFS fitting result for CS2 Hex Ar, CS2 Hex H_2Ar, respectively; (c) EXAFS fitting result for CS2 annealed 450. (d) The unit cell of diamond Ge.

dangling bonds on the surface of the as-prepared CS2 Ge QDs, or the surface atoms of the CS2 sample could possibly be terminated with hydrogen which cannot be seen

Table 5.3 EXAFS fitting result for CS1 samples.

For Ge-Ge bonding, the Debye correlated model was used for fitting, so the error was only provided for the Debye temperature but not for the DW factor. For the CS1 annealed 600 sample, the Debye temperature was fixed at 370 K to avoid non-physical fitting result. R_{eff} for diamond Ge: first shell 2.45 Å; for rutile GeO_2: first shell 1.87 Å.

Sample	Debye temperature (K)	σ^2_{Ge-Ge} (Å^2)	R_{Ge-Ge} (Å)	Coordination number	R_{Ge-O} (Å)
CS1 Hex Ar	325.3 ± 25.1	0.006	2.46 ± 0.01	2.5 ± 0.5	1.78 ± 0.01
CS1 Hex H_2Ar	309.8 ± 18.3	0.007	2.45 ± 0.01	2.9 ± 0.4	1.77 ± 0.01
CS1 annealed 450	355.6 ± 22.6	0.005	2.46 ± 0.01	2.9 ± 0.4	1.76 ± 0.01
CS1 annealed 600	370	0.005	2.45 ± 0.01	3.2 ± 0.4	NA

by the EXAFS measurements, due to the weak scattering by the hydrogen atoms. In either of the situations, the surface reconstruction effect is known to lead to the bond contraction [15]. As a matter of fact, the fitted first-shell Ge-Ge distance (2.42 ± 0.02 Å or 2.43 ± 0.02 Å, Table. 5.4) from the EXAFS analysis for the CS2 as-prepared sample is indeed shorter than that of the diamond-type Ge reference (2.45 Å).

For the annealed samples, the fitted Ge-Ge interatomic distances correspond well with that of diamond Ge. However, for the first Ge-Ge shell of CS1 annealed 600 and CS2 annealed 450 sample, the fitted DW factor does not decrease by any significant degree upon annealing (see Table 5.3) as would be expected. The DW factor includes dynamic and static contributions. The dynamic contribution is defined by the effective spring constant (or, the oscillator strength) of the Ge-Ge bonding. Here, all the as-prepared and annealed were measured at ambient condition, therefore the dynamic contribution to the DW factor is not expected to change in between samples (as-prepared and annealed). Hence a significant amount of static distortion should still exist in annealed samples. This static disorder can originate from distortions within tetrahedrons composed of local Ge atoms (red arrow in Fig. 5.5d), but can also be an indication of phases other than diamond-type Ge being present. The latter would be consistent with the analysis of PXRD data (see Fig. 5.2).

Table 5.4 EXAFS fitting result for CS2 samples.

Sample	Debye temperature (K)	σ^2_{Ge-Ge} (Å^2)	R_{Ge-Ge} (Å)	Coordination number
CS2 Hex Ar	349.4 ± 16.8	0.005	2.42 ± 0.02	3.3 ± 0.4
CS2 Hex H_2Ar	344.7 ± 22.7	0.006	2.43 ± 0.02	3.8 ± 0.5
CS2 annealed 450	381.6 ± 27.4	0.005	2.45 ± 0.02	3.2 ± 0.4

The first-shell coordination numbers are shown in Tables 5.3 and 5.4 for all as-prepared and annealed samples. The extracted coordination numbers were found to be lower than that of various known Ge phases (diamond: 4 at 2.45 Å; BC8: 1 at 2.41 Å, 3 at 2.50 Å; mC16: 3 at 2.42 Å, 1 at 2.45 Å; ST12: 4 at 2.48 Å). This is most likely due to the combination of large surface-to-volume ratios in nanoparticles and a correlation between Debye temperature and coordination numbers during data fitting. Neither of these factors affect the extracted interatomic distances.

Based on the analysis above, we suggest that two different synthesis routes seem to produce samples with a large degree of structural disorder. There could be several possibilities for the morphology of as-prepared CS1 and CS2 Ge nanoparticles, which are graphically summarised in Fig. 5.6. First of all, the discrepancy of sizes extracted from TEM and Raman indicates that a disordered component is present in our sample, which is consistent with PXRD data. Then PXRD patterns suggest that the long-range order in our as-prepared Ge QDs is better than that in amorphous Ge. Thus TEM/Raman/PXRD results comprehensively exclude cases (a) and (b) in Fig. 5.6. Moreover, the size discrepancy between TEM and Raman for CS1 could also come from GeO_2 on the surface. Furthermore, a mixture of

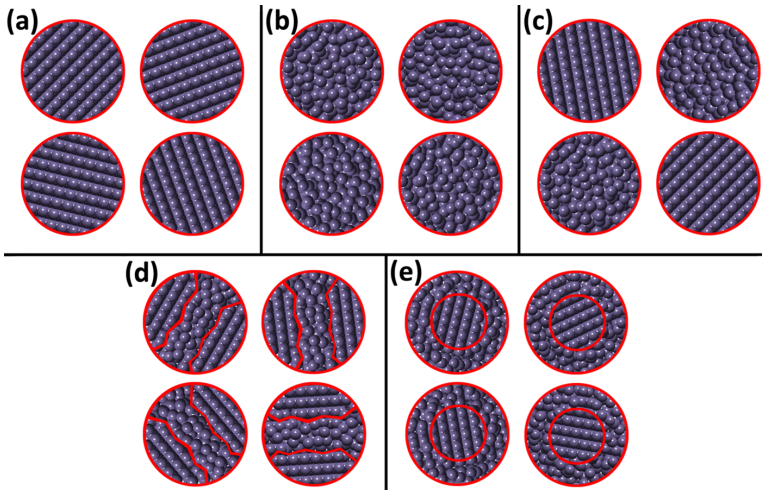

Fig. 5.6 Five general possibilities for as-prepared homogeneous and inhomogeneous Ge QDs. (a) Crystalline. (b) Amorphous. (c) Mixture of crystalline and amorphous QDs. (d) Mixed crystalline-amorphous within one single QD. (e) Single QD with nano-crystalline core and amorphous shell.

independent nano-crystalline and nano-amorphous QDs with the particle size observed in TEM (case-c, Fig. 5.6) would result in the observation of second (and possibly further) coordination shells in EXAFS data, which is not the case for as-prepared samples. Besides, a mixture of crystalline and amorphous Ge QDs would result in a non-Gaussian peak shape (broad amorphous background with a sharp crystalline peak on top) rather than the Gaussian diffraction peak we observed. A mixed phase (case-d, Fig. 5.6) in a single QD with size down to sub-nanometres can be excluded on the basis of thermodynamic considerations [16, 17].

Hence the most likely model for as-prepared Ge QDs is a core-shell one shown in Fig. 5.6 (e). This has been predicted from first-principle and molecular dynamics calculations [15, 18], but has not been confirmed by experimental data until now for colloidal Ge QDs. For CS1 as-prepared QDs, the surface is terminated with a GeO_2 shell based on EXAFS/TEM/Raman analysis. We believe CS1 as-prepared samples are terminated with hydrogen.

5.3 Conclusions

Ge QDs were synthesized by two colloidal routes: one of which by reducing GeO_2 (CS1 route) and the other by reducing $GeCl_4$ (CS2 route). Combined EXAFS/PXRD/Raman/

TEM characterization was carried out to reveal the short- and long-range order, and to access information on the atomic structure of the samples. It was found that as-prepared CS1 has diamond-type Ge structure with oxide-terminated surface. For the as-prepared CS2 sample, EXAFS analysis points to diamond-type structure, whereas the PXRD pattern indicates the possible existence of metastable phase. The annealing process crystallizes both the as-prepared CS1 and CS2 Ge QDs to diamond-type crystalline phase. But again, diffraction patterns that does not belong to the Ge diamond-type phase can be observed. Furthermore, based on the comprehensive results from Raman, TEM, PXRD and EXAFS, a core-shell model for the morphology of both as-prepared CS1 and CS2 Ge QDs was proposed.

To further verify the nature of phases in the as-prepared Ge QDs, we will focus in the next chapter on their behaviour under hydrostatic compression.

References

[1] J. H. Wu, Y. G. Sun, R. J. Zou, G. S. Song, Z. G. Chen, C. R. Wang, and J. Q. Hu. One-step aqueous solution synthesis of Ge nanocrystals from GeO_2 powders. *CrystEngComm*, 13:3674–3677, 2011.

[2] N. H. Chou, K. D. Oyler, N. E. Molt, and R. E. Schaak. Colloidal synthesis of germanium nanocrystals using room-temperature benchtop chemistry. *Chem. Mater.*, 21:4105–4107, 2009.

[3] I. H. Campbell and P. M. Fauchet. The effects of microcrystal size and shape on the one phonon Raman-spectra of crystalline semiconductors. *Solid State Commun.*, 58:739–741, 1986.

[4] H. Richter and Z. P. Wang. The one phonon Raman-spectrum in microcrystalline silicon. *Solid State Commun.*, 39:625–629, 1981.

[5] E. Muthuswamy, A. S. Iskandar, M. M. Amador, and S. M. Kauzlarich. Facile synthesis of germanium nanoparticles with size control: Microwave versus conventional heating. *Chem. Mater.*, 25:1416–1422, 2013.

[6] A. F. Khan, M. Mehmood, M. Aslam, and S. I. Shah. Nanostructured multilayer TiO_2-Ge films with quantum confinement effects for photovoltaic applications. *J. Collod. Interf. Sci.*, 343:271–280, 2010.

[7] A. F. Khan, M. Mehmood, A. M. Rana, and T. Muhammad. Effect of annealing on structural, optical and electrical properties of nanostructured Ge thin films. *Appl. Surf. Sci.*, 256:2031–2037, 2010.

[8] J. Liu, C. H. Liang, Z. F. Tian, S. Y. Zhang, and G. S. Shao. Spontaneous growth and chemical reduction ability of ge nanoparticles. *Sci. Rep.*, 3:1741, 2013.

[9] J. C. Kasper and S. M. Richards. Crystal structure of new forms of Si and Ge. *Acta. Crystallogr.*, 17:752–755, 1964.

[10] D. Selli, I. A. Baburin, R. Martonak, and S. Leoni. Novel metastable metallic and semiconducting germaniums. *Sci. Rep.*, 3:1466, 2013.

[11] R. J. Nelmes, M. I. McMahon, N. G. Wright, D. R. Allan, and J. S. Loveday. Stability and crystal-structure of BC8 germanium. *Phys. Rev. B*, 48:9883–9886, 1993.

[12] W. H. Baur and A. A. Khan. Rutile-type compounds. IV. SiO_2, GeO_2 and a comparison with other rutile-type structures. *Acta Crystallogr., Sect. B: Struct. Crystallogr. Cryt. Chem.*, B27:2133–2139, 1971.

[13] A. A. Bolzan, C. Fong, B. J. Kennedy, and C. J. Howard. Structural studies of rutile-type metal dioxide. *Act. Crystallogr., Sect. B: Struct. Sci.*, 53:373–380, 1997.

[14] G. R. Stewart. Measurement of low-temperature specific heat. *Rev. Sci. Instr.*, 54:1–11, 1983.

[15] L. Pizzagalli and G. Galli. Surface reconstruction effects on atomic properties of semiconducting nanoparticles. *Mater. Sci. Engin. B-Solid State Mater. Adv. Techn.*, 96:86–89, 2002.

[16] D. Yoreo and P. G. Vekilov. Principles of crystal nucleation and growth. *Rev. Mineral. Geochem.*, 54:57–93, 2003.

[17] J. D. Weeks and G. H. Gilmer. *Dynamics of Crystal Growth*, pages 157–228. John Wiley & Sons, Inc., 2007.

[18] L. Pizzagalli, G. Galli, J. E. Klepeis, and F. Gygi. Structure and stability of germanium nanoparticles. *Phys. Rev. B*, 63:165324, 2001.

Chapter 6

Phase transition of matrix-free Ge quantum dots under hydrostatic compression

The size effect of nanoscale systems tends to have significant influence on various physical properties of nanomaterials, from mechanical and optical to electrical properties. Also the size effect will result in distinctive phase or structural behaviour as compared to the corresponding bulk counterparts, such as the phase transition point (temperature, pressure), the transition pathways and the stability of various phases under different conditions, etc. [1]. Therefore looking into the pressure induced phase transition behaviour of nano-systems has been an interesting topic [2–5]. Moreover, it has been shown that the peculiar pressure-induced amorphization in nanoparticles (NPs), such as the BaF_2 NPs [6] and the porous Si nano-crystalline materials [7]. From the perspective of practical application, the exploration of pressure-induced amorphization is also interesting since it provides access to structures with novel electronic, optical and mechanical properties.

This chapter will focus on the phase transition behaviour of the colloidally prepared matrix-free Ge QDs under high pressure. Specifically, high pressure experiments were carried out to check if we do have a fully amorphous sample which will undergo the phase transition to β-tin at lower pressure than crystal. The methodology, including details about the experimental set-ups and simulation package in use, will be introduced in the first section. The main results and the corresponding discussion will be addressed in the second section, which will be followed by the conclusion section at the end.

6.1 Methodology

The sample synthesized following the CS2 route was subject to further hydrostatic compression study. The hydrostatic compression was conducted using the diamond anvil cell (DAC). The standard Bridgeman type DAC used (see Fig. 6.1) is capable of operating over the range of 1 – 50 GPa, and hence will be more than enough for investigating Ge QDs as amorphous Ge has a transition pressure of $\sim$ 6 GPa [8] and crystalline Ge has a transition pressure of $\sim$ 11 GPa [9]. Samples were either loaded into the DAC immediately following

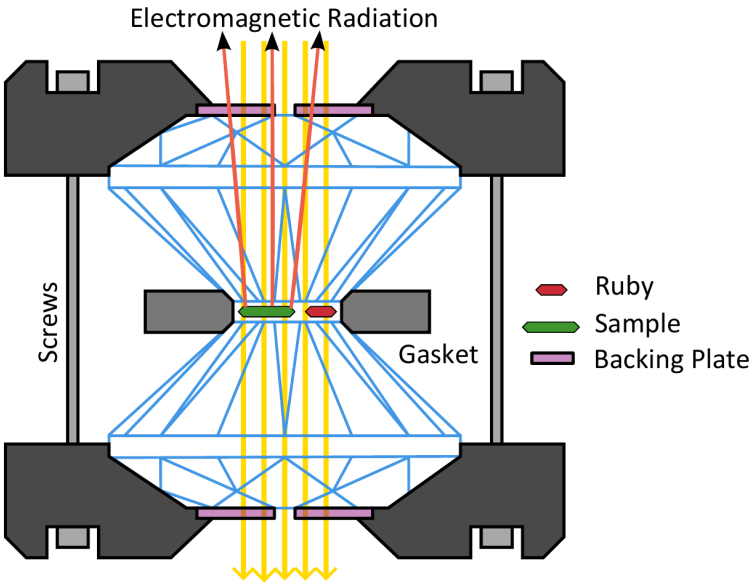

Fig. 6.1 The cross section of a Bridgeman-type Diamond Anvil Cell. The culet where the diamond faces make contact with sample is typically $\sim$ 0.6mm. The applied pressures is increased by tightening the screws. The ruby is present for calibrating the pressure. The gasket compromised of a hard metal foil is to prevent the diamond faces from coming into contact [10].

the synthesis or stored in oxygen-free atmosphere to avoid surface oxidation. The ruby fluorescence technique was used for the pressure measurements. We used methanol-ethanol and silicone oil as pressure transmitting media to check for possible steric effects. We found no detectable difference between these pressure-transmitting media. X-ray absorption data in a DAC were collected in the fluorescence detection mode to alleviate the problem of the diamond reflections that are particularly severe in the energy range around the Ge absorption K-edge [11, 12]. This approach allowed us to collect high quality data out to 12 Å.

For the *ab initio* simulation, ONESTEP code [13] which implements the electronic enthalpy method [14] was used to explore the structural evolution under pressure at the atomic level. As a representative model of a H-terminated Ge nanoparticle we studied the $Ge_{71}H_{60}$ system with the cGe (diamond-type) structure. The structure of the nanocrystal was initially optimized at 0 GPa and then pressure was applied in steps of 5 GPa or less to find the minimum enthalpy configuration. The HOMO-LUMO gap and the vibrational density of states (VDOS) were calculated on the relaxed structures using density functional perturbation theory implemented in the plane-wave DFT code CASTEP [15]. All the DFT calculation works mentioned in this chapter was carried out by Dr. N. R. Corsini.

6.2 Results and Discussion

As can be seen from Fig. 6.2 (a), the translucent Ge QD starts to become increasingly opaque only after 14.8 GPa, which suggests the band-gap closure and may indicate a transition to a metallic phase. However in bulk Ge, the transition to the metallic β-Sn phase occurs around 10 GPa. For amorphous bulk Ge, the transition can happen at even lower pressure of ~ 6 GPa [17]. For the Raman spectra of the Ge QDs under high pressure (see Fig. 6.2b), on one hand, the diamond-type Ge related peak can still be observed when the pressure was increased to 17.5 GPa, and meanwhile, the peak position shifts to higher wavenumber with increasing pressure. However, for bulk Ge, the Raman peak (corresponding to the diamond-type Ge) disappears as the system undergoes the transition to the metallic β-tin phase. On the other hand, the Raman peak is broadened as the pressure increases, which indicates increasing disorder. The quantitative result for the Raman peak analysis is presented in Fig. 6.2 (b). As compared to the linear shift of the Raman peak position as the function of pressure for bulk Ge (Fig. 6.2c, red circles), the small Ge QDs show peculiar behaviour (Fig. 6.2c, blue circles). The corresponding Raman peak position shows a linear up-shift with the pressure increasing before the shaded region (the grey strip in Fig. 6.2c), after which the Raman peak position appears to be constant as the pressure increases. Such peculiar non-linear behaviour of the Raman peak position as the function of pressure could be attributed to two aspects. On one side, the contraction of the Ge-Ge bonding as the result of high pressure contributes to the up-shift of the corresponding Raman peak position. On the other side, the increasing pressure leads to growing disorder in Ge QDs, which can be seen from the inset figure in Fig. 6.2c that shows the FWHM of the Raman peak increases linearly as the function of pressure. Such increase in the disordered component in Ge QDs would then result in a down-shift of the Raman peak position. We believe that the combination of the above two contributions

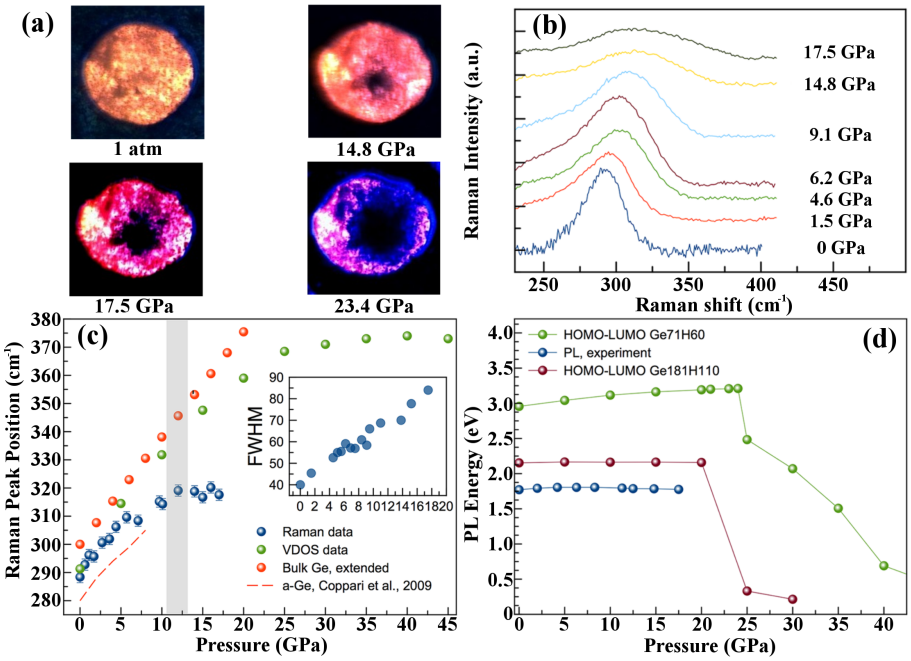

Fig. 6.2 (a) White light transmission through the sample as a function of pressure. (b) Evolution of the Raman spectra. (c) The Raman peak position extracted from the experimental data (blue circles) together with the DFT simulation result (green circles). The Raman peak position for the bulk c-Ge (red circles) linearly extrapolated beyond 11 GPa is also shown. The inset figures shows the changing of the FWHM of the experimental Raman peak as a function of pressure. (d) Pressure dependence of the photoluminescence peak position (blue circles) compared to the calculated HOMO-LUMO gaps for $Ge_{71}H_{60}$ (green circles) and $Ge_{181}H_{110}$ (purple circles) hydrogen-terminated clusters [16].

then leads to the observed non-linear behaviour of the Raman peak position as the function of pressure. The experimental result here is reproduced by the DFT calculation for the VDOS of Ge cluster terminated with hydrogen – see the green circles in Fig. 6.2 (c). Furthermore, the PL measurement for Ge QDs under high pressure shows the disappearance of the PL signal when the pressure increases to around 18 GPa (see Fig. 6.2d, blue circles), which indicates the band-gap closure. Such results, based on the PL measurements here, are consistent with the optical transmission result shown in Fig. 6.2 (a). Again, the band-gap closure behaviour of the small Ge QDs under high pressure was confirmed by the DFT calculation for the HOMO-LUMO gap as the function of pressure, as shown in Fig. 6.2 (d) (green and purple circles).

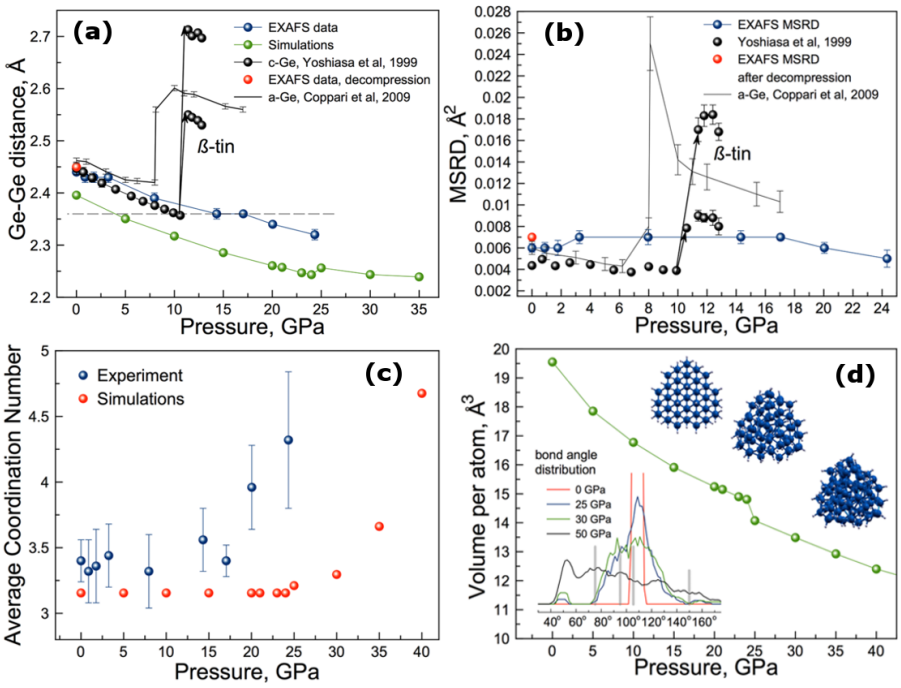

Fig. 6.3 (a) Ge-Ge nearest-neighbour distance obtained from EXAFS analysis and DFT simulations. The horizontal dashed line indicates the value of stability of Ge-Ge distance in crystalline bulk Ge. (b) DW factor of Ge-Ge bonding from EXAFS analysis. For (a) and (b), the corresponding behaviour of the crystalline [18] and amorphous [19] bulk Ge is also shown for comparison. (c) The 1st shell coordination number from EXAFS analysis and DFT simulation. (d) The changing of volume per atom as the function of pressure calculated from DFT. The corresponding $Ge_{71}H_{60}$ cluster and the bond angle distribution (the grey bars correspond to the β-Sn phase) are shown as the inset figures.

To further understand the phase transition behaviour of the Ge QDs under pressure from the perspective of local atomic structure, the result from EXAFS analysis was compared to DFT simulation. The comparison, together with the data for bulk crystalline and amorphous Ge, is shown in Fig. 6.3. As can be seen from Fig. 6.3 (a), for bulk crystalline Ge, the Ge-Ge nearest neighbour distance shows a sharp increase at $\sim$ 10 GPa, indicating the transition from semiconductor (diamond-type) to metallic β-Sn phase. The transition pressure for amorphous bulk Ge can be observed to be $\sim$ 8 GPa. However, no sharp change in the distance was observed for our Ge QDs throughout the whole pressure range, indicating that the application of pressure eventually results in compression of the bond beyond the stability value for the diamond-type Ge structure. This suggests metallization as observed by optical

transmission, Raman and PL measurements takes place within a local structure similar to diamond-type Ge and is primarily driven by the bond over-compression for the matrix-free Ge QDs. The result here is in contrast to the situation for crystalline and amorphous bulk Ge, where it has been shown that the semiconductor-to-metal phase transition is accompanied by the structural changes into the octahedral β-Sn arrangement. Similarly for the DW factor of Ge-Ge bonding, no sharp change was observed as compared to the situation for crystalline and bulk Ge (see Fig. 6.3b). Instead, the DW factor value stays around the same level as the pressure is raised. Now the Raman data discussed above suggests the increasing of the static disorder upon raising pressure. Since the overall DW factor stays the same within error, and it is expected that the dynamic contribution to the DW factor should decrease on increasing pressure.

Furthermore, in both the Ge-Ge bonding length (Fig. 6.3a) and the DW factor pattern (Fig. 6.3b), a kink can be observed around 15 GPa, which indicates the onset of phase transition. As can be seen from Fig. 6.3 (c), the phase transition is accompanied by an increase in the coordination number. Therefore the results from EXAFS analysis point to the low-density amorphous (LDA) to high-density amorphous (HDA) phase transition, which further confirms the proposition from the Raman data. The phase transition behaviour of the matrix-free Ge QDs, as indicated by the EXAFS data, was further supported by the DFT simulation on the $Ge_{71}H_{60}$ cluster. The changing Ge-Ge bonding length, DW factor and the coordination number from the EXAFS experiment are all consistent with the DFT calculation, except that the phase transition pressure was overestimated ($\sim$ 25 GPa). Such overestimation of the transition pressure could be due to the lack of dynamic effects in the DFT simulations and the small system size.

In Fig. 6.3 (d), the volume per atom (as the function of pressure) calculated from the DFT calculation is shown. The decreasing of the volume per atom throughout the whole pressure range reinforces the proposed phase transition mechanism – LDA to HDA transition. Again, at the phase transition pressure around 25 GPa, a kink was observed, corresponding to the small volume decrease ($\sim$ 5%) at the transition, which is in contrast to the large volume change (up to $\sim$ 19% [16]) in the usual transition to β-Sn phase for bulk Ge. Also, the bond angle distribution in the HDA phase obtained from the simulations (see inset in Fig. 6.3d) suggests that the structure of this HDA phase has more in common with liquid Ge phase [20, 21] rather than with β-Sn structure.

6.3 Conclusion

The experimental results (Raman, PL and EXAFS), together with DFT simulations, suggest that application of hydrostatic pressure on our small Ge QDs ($\sim$ 4 nm) leads to an increase in structural disorder followed by the gradual onset of LDA to HDA transition at around 15 GPa. This was accompanied by the semiconductor-to-metal transition. Here, we did not observe the usual transition to the β-tin phase (observed above 6 GPa in bulk a-Ge and 10 GPa in bulk c-Ge) up to the maximum pressure of 25 GPa. Thus, for the first time we conclusively observed an amorphous metallic phase of an elemental semiconductor. The exact nature of the transition on the atomic scale is still under debate, but our recent work [16] suggests that a geometric frustration due to competing requirements for bulk and surface atoms may be responsible. These results further support the core-shell model developed in preceding chapters.

Following the EXAFS analysis for Ge QDs based on conventionally used parameters fitting technique, the next chapter will move on to introduce our work upon combining the MD and FEFF simulation to go beyond the limitation of the traditional EXAFS analysis technique.

References

[1] A. San-Miquel. Nanomaterials under high-pressure. *Chem. Soc. Rev.*, 35:876–889, 2006.

[2] J. Z. Jiang, L. Gerward, and J. S. Oslen. Pressure induced phase transformation in nanocrystal SnO_2. *Scr. Mater.*, 44:1983–1986, 2001.

[3] Z. W. Wang and Q. X. Guo. Size-dependent structural stability and tuning mechanism: a case of zinc sulfide. *J. Phys. Chem. C*, 113:4286–4295, 2001.

[4] H. Lv, M. G. Yao, Q. J. Li, Z. P. Li, B. Liu, R. Liu, S. C. Lu, D. M. Li, J. Mao, and X. L. Ji. Effect of grain size on pressure-induced structural transition in Mn_3O_4. *J. Phys. Chem. C*, 116:2165–2171, 2012.

[5] L. Wang, W. G. Yang, Y. Ding, Y. Ren, S. G. Xiao, B. B. Liu, S. V. Sinogeikin, Y. Meng, D. J. Gosztola, and G. Y. Shen. Size-dependent amorphization of nanoscale Y_2O_3 at high pressure. *Phys. Rev. Lett.*, 105:095701, 2010.

[6] J. S. Wang, Q. L. Cui, T. J. Hu, J. H. Yang, X. Y. Li, Y. Q. Liu, B. Liu, W. Q. Zhao, H. Y. Zhu, and L. L. Yang. Pressure-induced amorhization in BaF_2 nanoparticles. *J. Phys. Chem. C*, 120:12249–12253, 2016.

[7] K. D. Sudip, M. Wilding, M. Somayazulu, and P. F. McMillan. Pressure-induced amorphization and an amorphous-amorphous transition in densified porous silicon. *Nature*, 414:528–530, 2001.

[8] O. Shimomura, S. Minomura, N. Sakai, K. Asaumi, K. Tamura, J. Fukushima, and H. Endo. Pressure-induced semiconductor-metal transitions in amorphous Si and Ge. *Philos. Mag.*, 29:547–558, 1974.

[9] C. S. Menoni, J. Z. Hu, and I. L. Spain. Germanium at high pressures. *Phy. Rev. B*, 34:362–368, 1986.

[10] W. R. Little. *Structure of and light emission in matrix-free germanium quantum dots*. PhD thesis, Queen Mary, University of London, London, UK, 2015.

[11] A. V. Sapelkin and S. C. Bayliss. X-ray absorption spectroscopy under high pressures in diamond anvil cells. *High Press. Res.*, 21:315–329, 2002.

[12] X. G. Hong, M. Newville, V. B. Prakapenka, M. L. Rivers, and S. R. Sutton. High quality x-ray absorption spectroscopy measurements with long energy range at high pressure using diamond anvil cell. *Rev. Sci. Instr.*, 80:073908, 2009.

[13] M. Cococcioni, F. Mauri, G. Ceder, and N. Marzari. Electronic-enthalpy functional for finite systems under pressure. *Phys. Rev. Lett.*, 94:145501, 2005.

[14] C. K. Skylaris, P. D. Haynes, A. A. Mostofi, and M. C. Payne. Introducing ONESTEP: linear-scaling density functional simulations on parallel computers. *J. Chem. Phys.*, 122:084119, 2005.

[15] K. Refson, P. R. Tulip, and S. J. Clark. Variational density-functional perturbation theory for dielectrics and lattice dynamics. *Phys. Rev. B*, 73:155114, 2006.

[16] N. R. Corsini, Y. P. Zhang, R. L. William, A. Karatutlu, O. Ersoy, P. D. Haynes, C. Molteni, N. D. M. Hine, I. Hernandez, J. Gonzalez, F. Rodriguez, V. V. Brazhkin, and A. Sapelkin. Pressure-induced amorphization and a new high density amorphous metallic phase in matrix-free Ge nanoparticles. *Nano Lett.*, 15:7334–7340, 2015.

[17] K. Tanaka. Amorphous-Ge under pressure. *Phys. Rev. B*, 43:4302–4307, 1991.

[18] A. Yoshiasa, T. Nagai, O. Ohtaka, O. Kamishima, and O. Shimomura. Pressure and temperature dependence of EXAFS Debye-Waller factors in diamond-type and white-tin-type germanium. *J. Synchrotron Radiat.*, 6:43–49, 1999.

[19] F. Coppari, J. C. Chervin, A. Congeduti, M. Lazzeri, A. Polian, E. Principi, and A. Di Cicco. Pressure-induced phase transitions in amorphous and metastable crystalline germanium by Raman scattering, x-ray spectroscopy, and ab initio calculations. *Phys. Rev. B*, 80:115213, 2009.

[20] R. V. Kulkarni, W. G. Aulbur, and D. Stroud. Ab initio molecular-dynamics study of the structural and transport properties of liquid germanium. *Phys. Rev. B*, 55:6896–6903, 1997.

[21] A. Arnold, N. Mauser, and J. Hafner. A molecular-dynamics study of the structure of liquid germanium. *J. Phys. Condens. Matter*, 1:965–980, 1989.

Chapter 7

Combined molecular dynamics and FEFF simulation for Ge quantum dots

The conventional EXAFS analysis relies on the assumption of an input structural model and the following spectra fitting will try to adjust the structural parameters based on the given model to best fit the experimental data. Such an approach is powerful in extracting structural parameters for certain systems. However, first of all, the modern EXAFS analysis based on the spectra fitting has significant limitations in that it returns a number of structural parameters associated with scattering paths, rather than a structural model that can be used as an input for subsequent analysis or further calculations. Secondly, the IFEFFIT algorithm commonly used for EXAFS spectra fitting treats the disorder of the system in question using the DW factor and higher order cumulants. In highly disordered systems, such as liquids, the cumulant expansion may become inadequate or fail altogether to describe the experimental EXAFS spectra [1–3].

Based on the aforementioned considerations, the program MD2FEFF was developed to combine the FEFF calculation for EXAFS spectra (using FEFF9.6) with the MD simulation (using DL_POLY_4). The program was designed to use the MD simulation as the structure evolution tool followed by the FEFF calculation for the resulted cluster. The configuration average over the whole cluster (with each atom as the absorber separately) would be calculated to take into account of the inhomogeneity of the system. The step-wise average (after each MD and FEFF running cycle) would also be calculated to account for the thermodynamic disorder of the system. The calculated spectra were then compared with the corresponding experimental EXAFS spectra to check the agreement. The developed MD2FEFF program was applied to two systems - amorphous GaSb (aGaSb) and Ge QDs systems. Here aGaSb was used as a reference system since it has been previously extensively studied [4, 5].

Technical details about the simulation works will be described in the first section, which will then be followed by results and the corresponding discussions. Conclusions drawn based on the combined MD-FEFF simulation will be presented in the end.

7.1 Methodology

The flowchart and description for the developed MD2FEFF code is given in Appendix-E, where the link for the source code and all the necessary programs/scripts for compiling and running MD2FEFF are also given. In simulating the aGaSb system, the ART program developed by N. Mousseau, et al. [6] was used to generate the amorphous GaSb model (with 3060 atoms, which corresponds to $7 \times 7 \times 7$ supercell of the crystalline form). The random

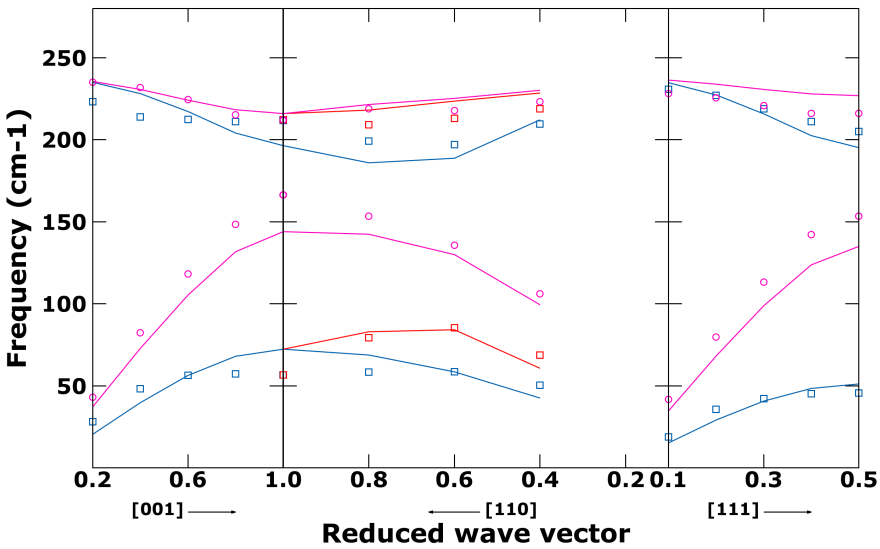

Fig. 7.1 The GaSb phonon dispersion curve fitting with Morse and screened harmonic three-body potential. The phonon frequencies (in dots) for GaSb (taken at 300 K) are from Ref. [7]. The reduced wave vector is given as: $\zeta = a_0 q/2\pi$, where the lattice constant $a_0 = 6.0959$ Å.

structural model generated with a C code developed by Barkema [8] was used as the input for ART running. For generating the amorphous Ge model (with 3060 atoms, which corresponds to the $7 \times 7 \times 7$ supercell of the crystalline form), the WWW code developed by Barkema, et al. [8] was utilized with a random configuration generated with the aforementioned C code by Barkema as the input. The WWW program was further revised to create the core-shell

model (with 3060 atoms) with different core radii, where the core keeps the crystalline form and the shell is amorphous. In generating the core-shell model, the crystalline Ge cluster ($7 \times 7 \times 7$ supercell) was used as the input. For the revision of the WWW code, the half box size of the original crystalline input was taken as the typical cluster size $r_{overall}$. Then an extra parameter (*Perct*) was introduced to account for the percentage of the crystalline region (which can be adjusted) in the finally obtained core-shell model. Therefore the core (crystalline) radius in the final core-shell model should be $r_{overll} \times Perct$.
For the MD simulation of GaSb system, the Morse potential (intramolecular) and the screened harmonic (shrm) three-body potential (TBP, intermolecular) was utilized:

$$\text{Morse potential: } U(r_{ij}) = E_0\left\{\left[1 - e^{-k(r_{ij}-r_0)}\right]^2 - 1\right\} \tag{7.1}$$

$$\text{shrm three-body potential: } U(\theta_{ijk}) = \frac{k}{2}(\theta_{ijk} - \theta_0)^2 e^{-(\frac{r_{ij}}{\rho_1} + \frac{r_{ik}}{\rho_2})} \tag{7.2}$$

The potential parameters were fitted to the phonon dispersion curve for GaSb provided in the report by M. K. Farr et al. [7] using GULP [9], and the fitting result is shown in Fig. 7.1. The fitted parameters for Morse and three-body potential are given in Table. 7.1.

Table 7.1 The fitted Morse and screened harmonic three-body potential for GaSb.

Morse (Ga-Sb)			shrm TBP (Sb-Ga-Sb)	shrm TBP (Ga-Sb-Ga)
E_0(eV)	1.068558	k (eV $\cdot$ rad^{-2})	1726.155936	459.419664
r_0 (Å)	2.64	θ_0 (°)	109.47	109.47
k(eV $\cdot$ rad^{-2})	1.642344	ρ_1 (Å)	0.579283	0.934626
		ρ_2 (Å)	0.619983	0.984919

For the Ge system, the highly successful and widely used environment-dependent Tersoff potential [10] was employed, which is particularly well suited for surface simulations where the atomic environment is different from that in the bulk:

$$U_{ij} = f_C(r_{ij})[f_R(r_{ij}) - \gamma_{ij} f_A(r_{ij})] \tag{7.3}$$

where:

$$f_R(r_{ij}) = A_{ij} e^{-a_{ij} r_{ij}} \tag{7.4}$$

$$f_A(r_{ij}) = B_{ij} e^{-b_{ij} r_{ij}} \tag{7.5}$$

$$f_C(r_{ij}) = \begin{cases} 1 & : r_{ij} < R_{ij} \\ \frac{1}{2} + \frac{1}{2} cos\left[\pi \frac{r_{ij} - R_{ij}}{S_{ij} - R_{ij}}\right] & : R_{ij} < r_{ij} < S_{ij} \\ 0 & : r_{ij} > S_{ij} \end{cases} \tag{7.6}$$

$$\gamma_{ij} = \chi_{ij}(1 + \beta_i^{\eta_i} \mathscr{L}_{ij}^{\eta_i})^{-\frac{1}{2\eta_i}} \tag{7.7}$$

$$\mathscr{L}_{ij} = \sum_{k \neq i,j} f_C(r_{ik}) \omega_{ik} g(\theta_{ijk}) \tag{7.8}$$

$$g(\theta_{ijk}) = 1 + \frac{c_i^2}{d_i^2} - \frac{c_i^2}{d_i^2 + (h_i - cos\theta_{ijk})^2} \tag{7.9}$$

$$a_{ij} = \frac{a_i + a_j}{2}, \quad b_{ij} = \frac{b_i + b_j}{2} \tag{7.10}$$

$$A_{ij} = (A_i A_j)^{1/2}, \quad B_{ij} = (B_i B_j)^{1/2} \tag{7.11}$$

$$R_{ij} = (R_i R_j)^{1/2}, \quad S_{ij} = (S_I S_j)^{1/2} \tag{7.12}$$

The potential parameters given in Ref. [10] was used (Table-7.2):

Table 7.2 Tersoff potential parameters for Ge system.

Parameter	Value
A (eV)	1.769×10^3
a ($\mathring{A}^{-1}$)	2.4451
B (eV)	4.1923×10^2
b ($\mathring{A}^{-1}$)	1.7047
R	2.80
S	3.10
β	9.0166×10^{-7}
η	7.5627×10^{-1}
c	1.0643×10^5
d	1.5610×10^1
h	-4.3884×10^{-1}

For the MD simulation of both aGaSb and Ge QDs systems, the periodic boundary condition in DL_POLY_4 was utilized.

7.2 Results and Discussion

First of all, the aGaSb was used as the reference system to test the validity of the combined FEFF and MD approach, where the aGaSb model was generated using the ART code. The

relaxation curve (Energy vs Relaxation events) is shown in Fig. 7.2. The amorphous structural model obtained finally, together with the PDF pattern of the initial (green triangle-line) and final (blue dot-line) structural configuration, is shown as the inset of Fig. 7.2. The corresponding first and second shell distances are given in Table. 7.3.

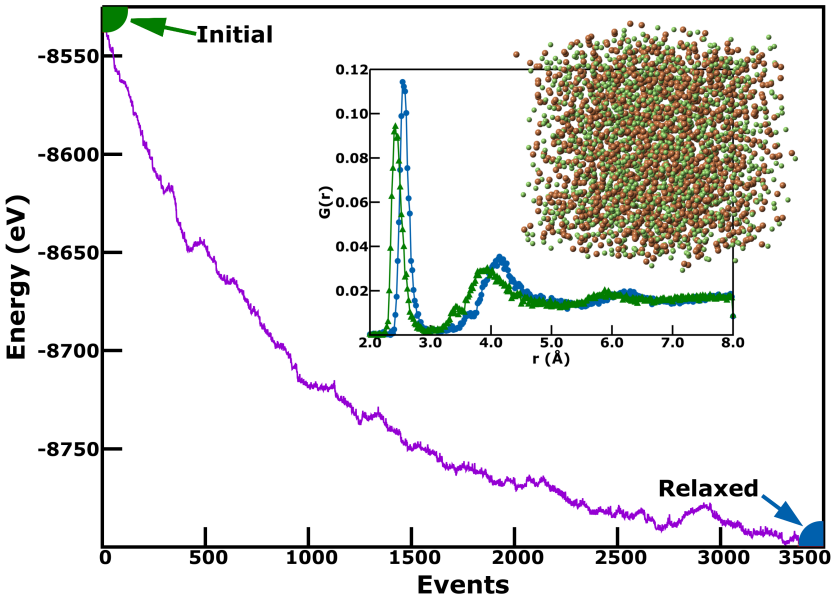

Fig. 7.2 The relaxation curve for the ART running. The inset figures are the finally obtained aGaSb model, together with the PDF pattern corresponding to the initial (green) and final (blue) structural configuration.

Table 7.3 The first and second shell distances for the initial and relaxed (for 3500 steps) aGaSb model, together with those for cGaSb [11] and aGaSb [12] reference.

	1st Shell (Å)	2nd Shell (Å)
Initial	2.48 ± 0.07	4.19 ± 0.43
Relaxed	2.60 ± 0.09	4.30 ± 0.35
cGaSb	2.64	4.32
aGaSb	2.64 ± 0.01	4.31 ± 0.01

The initial input model and the one obtained after $\sim$ 3500 steps relaxation were used as the input for the MD2FEFF code, respectively. The calculation result for each model was then compared to the experimental Ga K-edge EXAFS spectra for amorphous GaSb sample, which is shown in Fig.7.3 (a) and (b), respectively. As can be seen from Fig. 7.3, the experimental EXAFS spectra beyond 6 Å^{-1} are well reproduced with either of the two models as the input.

However, in the low-k region indicated by the green box in Fig. 7.3 (a) and (b), it can be observed that the agreement between the experimental and theoretical EXAFS spectra is better for the relaxed aGaSb model.

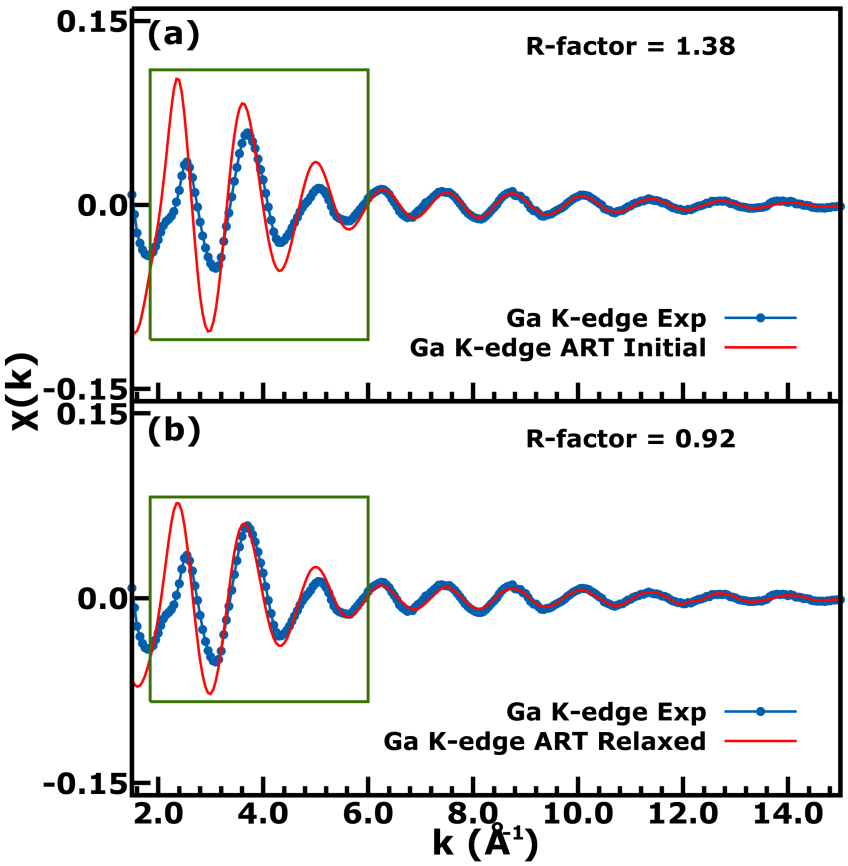

Fig. 7.3 The comparison of the Ga K-edge EXAFS experimental spectra (measured at 78 K) with the theoretical spectra obtained from MD2FEFF running for (a) the initial random aGaSb model and (b) the aGaSb model after $\sim$ 3500 steps relaxation as the input structural model. The numerical difference between the experimental and the theoretical spectra is also presented for each model in (a) and (b), respectively.

To further compare in between the two input models, the corresponding R-factor accounting for the point-by-point (from $k = 1.5$ Å^{-1} to $k = 15.0$ Å^{-1}) difference between the theoretical and the experimental EXAFS spectra was calculated for each. As presented in Fig. 7.3 (a) and (b), the R-factor corresponding to the relaxed aGaSb model (Fig. 7.3a, 0.92) is smaller than that of the initial random model (Fig. 7.3b, 1.38). The result here suggests that the ART

approach used to generate the amorphous GaSb model provides better fit to the experimental data.

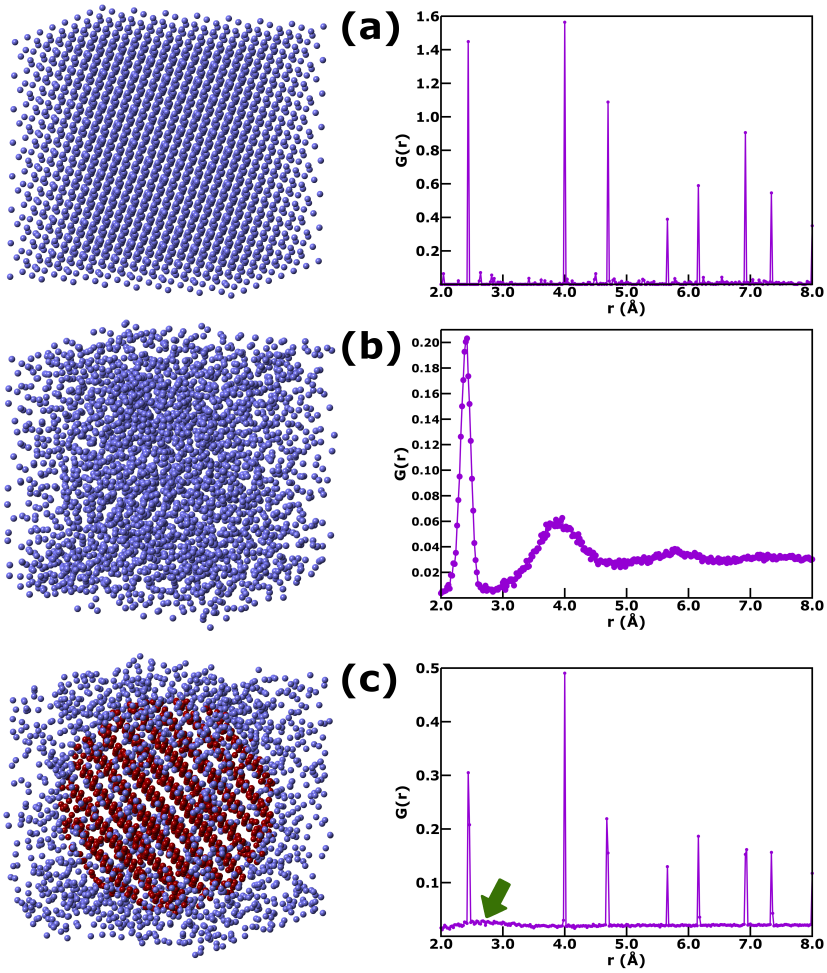

Fig. 7.4 The Ge (a) crystalline (b) amorphous and (c) core-shell (with the 90% crystalline region, atoms shown in red color) structural models and the corresponding PDF pattern for each model. The green arrow in (c) indicates contribution from the amorphous portion of the model as compared to that of the crystalline model.

Following the application of MD2FEFF on aGaSb system, the code was further applied to the Ge QDs system. Here three input Ge models are generated – the crystalline Ge model, the amorphous Ge model and the core-shell Ge model (for which the core is crystalline and the shell is amorphous). Generating the crystalline Ge model is straightforward, and here the NO. 53642 '.cif' file from ICSD database was used to build up the model. In generating of amorphous and core-shell Ge model, the WWW code and its revised version was utilized,

as described in the methodology section of this chapter. The illustration for the three Ge structural models is shown in Fig. 7.4, together with the corresponding PDF patterns. For the core-shell model, the one with 90% core crystalline region (atoms shown in red color in Fig. 7.4c) was taken as the representative example. As can be seen from Fig. 7.4 (c), the broad background peak (indicated by green arrow) in the PDF pattern corresponds to the contribution from the amorphous portion, while the sharp peaks (in the same positions as in the PDF of crystalline model shown in Fig. 7.4a) comes from the core crystalline region. We

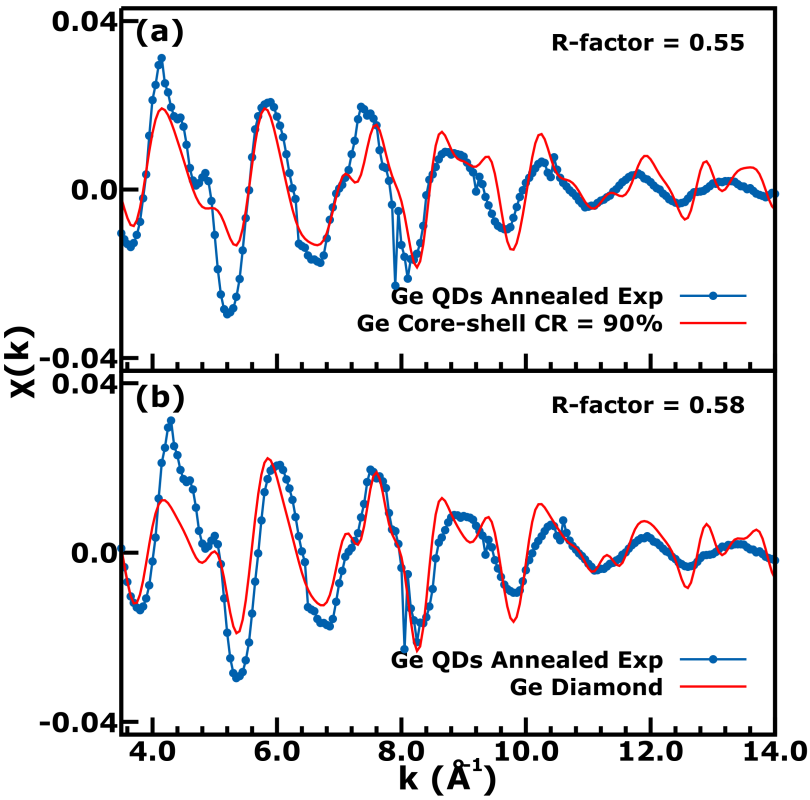

Fig. 7.5 The comparison of experimental EXAFS spectra for annealed Ge QDS with the theoretical spectra obtained from MD2FEFF running for (a) Ge core-shell model with 90% core crystalline region and (b) crystalline Ge model. The numerical difference (from $k = 3.5$ Å^{-1} to $k = 14.0$ Å^{-1}) between the experimental and theoretical spectra is also presented for each model in (a) and (b), respectively.

then used the generated crystalline and core-shell models as the input for MD2FEFF in order to compare with the experimental data for the annealed Ge QDs. For the core-shell model, the percentage of the crystalline (PC) region was adjusted from 20% up to 90%.

By checking the deviation from the experimental spectra of the annealed Ge QDs, it was found that the calculation result corresponding to the model with PC = 90% gives the best

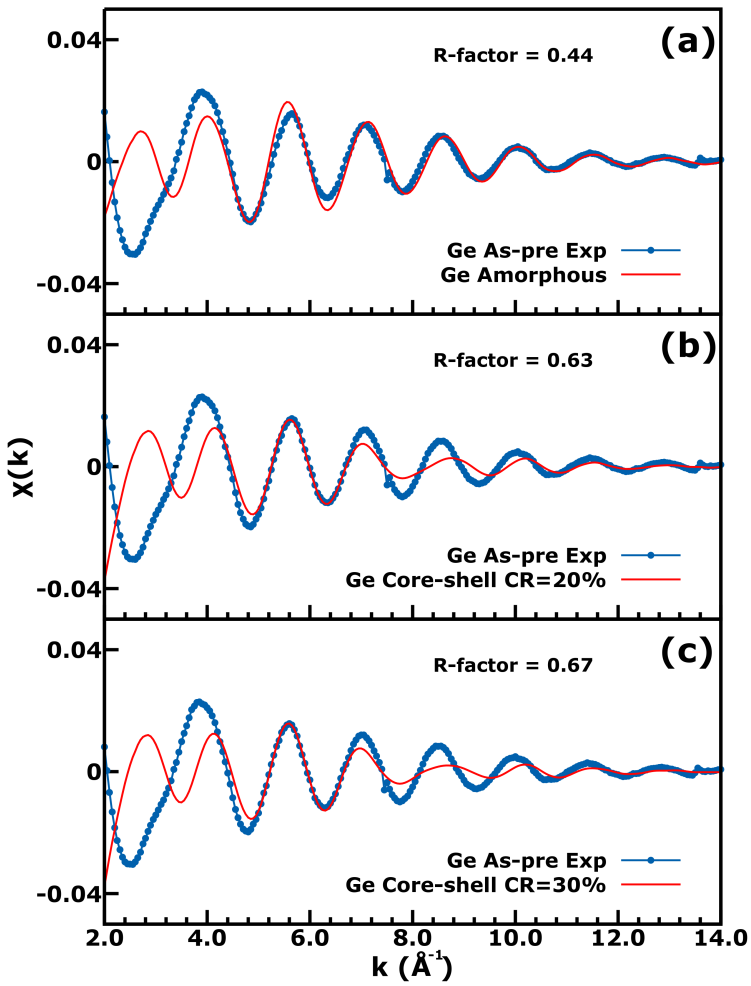

Fig. 7.6 The comparison of experimental EXAFS spectra for as-prepared Ge QDs with the theoretical spectra obtained from MD2FEFF running for (a) Ge amorphous model, (b) Ge core-shell model with 20% core crystalline region and (c) Ge core-shell model with 30% core crystalline region. The numerical difference (from $k = 3.5$ Å^{-1} to $k = 14.0$ Å^{-1}) between the experimental and theoretical spectra is also presented for each model in (a) - (c), respectively.

agreement among all the core-shells models. Furthermore, the theoretical spectra for the PC = 90% core-shell model was then compared to that of the crystalline Ge model to look at which gives better agreement with the experimental spectra, and the comparison is presented

in Fig. 7.5. It can be seen that neither of the two input models gives perfect consistency with the experimental spectra. However, for the PC = 90% core-shell model, the deviation from the experimental result seems to be smaller in the low-k region of the spectra. To further compare in between the two models, R-factors were calculated for each model and are presented in Fig. 7.5 (a) and (b), respectively. By comparison, the PC = 90% core-shell model gives better consistency with the experimental EXAFS spectra for the annealed Ge QDs. This further confirms the conclusion drawn from the previous XANES spectra analysis (will be discussed in Chapter-8).

As for the as-prepared Ge QDs, the amorphous and core-shell models (with different PC) were used as the input for MD2FEFF running. And the same procedures as goes for annealed sample described above was applied here. The comparison of the calculated spectra for various structural models with the experimental EXAFS spectra for as-prepared Ge QDs is presented in Fig. 7.6. For the core-shell models with various PC, the ones with PC = 20% and PC = 30% give the best agreement with experiment therefore were selected to be compared with the amorphous model. By inspection, it can be found that the amorphous model gives better agreement with the experimental spectra (see the numerical R-factor for each model, Fig. 7.6) instead of the core-shell model for the as-prepared Ge QDs. Hereby the combined MD+FEFF simulation results seem to suggest the uniform amorphous/disordered structure, in contrast to the previously proposed core-shell model (see Chapter-5). Here the reason could be that the developed core-shell model (with perfect crystalline core and an amorphous shell) for the combined MD+FEFF simulation is not an adequate model for describing the system. Instead, the real structural model could possibly be more complicated with a disordered surface and a less disordered inner region, where the degree of disorder may vary from the core to the surface.

7.3 Conclusion

In this chapter, the combined FEFF (for EXAFS spectra calculation) and MD simulation (accounting for the thermodynamic disorder) was realized by the developed MD2FEFF code. The running result for the reference aGaSb system demonstrates the validity of the combined simulation approach. The MD2FEFF code was then further applied to Ge QDs system, where the theoretical calculation results were compared to the experimental data for both as-prepared and annealed samples. For the annealed Ge QDs, it was shown that the core-shell model with 90% core crystalline region best describes the experimental EXAFS spectra. However, the simple core-shell model doesn't work well for the as-prepared samples

as compared to the uniform amorphous model. The reason could be that the generated core-shell model here over-simplifies the real structural configuration. In the real situation, the structural model could be more complicated, where the degree of disorder may vary from the core to the surface other than possessing a perfect crystalline core and an amorphous shell.

The next chapter will move on to discuss the application of XANES to look into the local symmetry of Ge QDs, with the help of the numerical calculation using FDMNES package.

References

[1] P. D'Angelo and A. Di Nola. An extended x-ray absorption fine structure study of aqueous solutions by employing molecular dynamics simulations. *J. Chem. Phys.*, 100:985–994, 1994.

[2] A. Filipponi and A Di Cicco. Short-range order in crystalline, amorphous, liquid, and supercooled germanium probed by x-ray-absorption spectroscopy. *Phys. Rev. B*, 51:12322–12336, 1995.

[3] S. W. T. Price, N. Zonias, C. K. Skylaris, A. E. Russel, and B. Ravel. The application of molecular dynamics to fitting EXAFS data. *J Phys. Conf. Ser.*, 430:012009, 2013.

[4] A. V. Sapelkin, S. C. Bayliss, A. G. Lyapin, V. V. Brazhkin, and A. J. Dent. Structure of bulk amorphous GaSb: a temperature-dependent EXAFS study. *Phys. Rev. B*, 56:11531–11535, 1997.

[5] C. S. Schnohr and M. C. Ridgway. *X-ray absorption spectroscopy of semiconductors*. Springer, USA, 2015.

[6] N. Mousseau and L. Lewis. Topology of amorphous tetrahedral semiconductors on intermediate length scales. *Phys. Rev. Lett.*, 78:1484–1487, 1997.

[7] M. K. Farr, J. G. Traylor, and S. K. Sinha. Lattice dynamics of GaSb. *Phys. Rev. B*, 11:1587–1594, 1975.

[8] N. Mousseau and G. T. Barkema. Fast bond-transposition algorithms for generating covalent amorphous structures. *Curr. Opin. Solid State Mater. Sci.*, 5:497–502, 2001.

[9] J. D. Dale. GULP: A computer program for the symmetry-adapted simulation of solids. *J. Chem. Soc.*, 93:629–637, 1997.

[10] J. Tersoff. Modeling solid-state chemistry: interatomic potentials for multicomponent systems. *Phys. Rev. B*, 39:5566–5568, 1989.

[11] V. M. Goldschmidt. Geochemische verteilungsgesetze der elemente. VIII. Untersuchungen *ü*ber bau and eigenschaften von krisallen. *Akad. Oslo, Mat. Naturvid*, 8:194, 1926.

[12] A. V. Sapelkin and S. C. Bayliss. X-ray absorption spectroscopy under high pressures in diamond anvil cells. *High Press. Res.*, 21:315–329, 2002.

Chapter 8

Local structure of bulk amorphous GaSb and Ge quantum dots by XANES

In Chapter-5 and 6, we saw that the EXAFS signal is restricted to the first shell for the highly disordered as-prepared Ge QDs. However, the PXRD pattern for the as-prepared QDs suggests the level of disorder below that of the amorphous Ge. Therefore, further information about the local symmetry is needed to solve ambiguity in the local structural configuration, and meanwhile, to distinguish between possible metastable phases observed in nanoscale systems.

At the same time, the near edge structure (XANES) is known to be sensitive to both the electronic properties (e.g. oxidation state, changes in the DOS around the Fermi level, etc.) and the local atomic structure beyond the first coordination shell (and hence to local symmetry). Therefore in this chapter, the XANES is employed to look at the local symmetry of Ge QDs system, based on the numerical calculation using FDMNES package. Here again, we used well-studied bulk amorphous GaSb [1, 2] as a reference and then extended our approach to matrix-free Ge QDs.

Details about the experimental measurements and theoretical calculation will be given in the first section, followed by the results and discussion for the GaSb reference and the Ge QDs system. Following the discussions on the XANES spectra analysis, the discussion for the optically detected XANES of the Ge QDs system will be presented. The last section will then summarize the main findings based on the discussion in current chapter.

8.1 Experiment and Calculation

In the analysis of GaSb XANES we used the XAS data obtained previously. [1] The synthesis routes for the two sets of Ge QDs samples (CS1 – oxygen-terminated, CS2 – oxygen-free) have already been described in Chapter-5 (section-5.1). For details about the XAS measurement, see section-5.1 in Chapter-5. The optically detected XAS (ODXAS) measurement was conducted using X-ray excited optical luminescence (XEOL) signal. The detection system consisted of a Triax 190 spectrometer equipped with a Synapse CCD and a Newport VIS Femtowatt photoreceiver. A Hamamatsu R3809U-50 MCP photomultiplier was used for low signal conditions. The light was delivered to the spectrometer using an optical fibre. All the optical detection experiments have been conducted at $T = 100$ K using a cryojet system. The XAS data reduction was carried out using Athena program as before. For the XANES numerical calculation, the FDM mode (which is described in section-4.1 of Chapter-4) was used. The typical time scale for the FDM mode calculation, e.g. the parallel calculation using five nodes for 7 Å diamond-type Ge cluster, was 2 – 3 days.

8.2 Bulk aGaSb as the reference system

Bulk amorphous (aGaSb) and crystalline (cGaSb) were used as a reference to verify the capability of our approach to distinguish between two possible structural arrangements and to test sensitivity to the local symmetry. We used the data collected previously [1], where the samples of aGaSb were prepared by compression of cGaSb with the zinc-blende structure to above a structural transition, followed by fast decompression from the high pressure β-tin structure of GaSb to ambient conditions. Thus, potentially there could be two possible local configurations in the ambient amorphous phase: the metastable β-tin-like structure (Ga and Sb occupy 4-fold tetrahedral sites) and stable zinc-blende-like (Ga and Sb occupy 6-fold octahedral sites) structure (see Fig. 8.1). It has been shown previously from by EXAFS analysis [1] that the bond angle in aGaSb is close to that of the zinc-blende structure, therefore the tetrahedral local symmetry is expected. To test that such result can be reproduced by XANES calculations, we constructed the two corresponding structural models (see Fig. 8.1a and b), calculated XANES signals for both structures and compared the results to the experimental data for cGaSb and aGaSb. The results for these calculations at Ga K-edge with cluster size of 7 Å (this was the minimum cluster size necessary to adequately reproduce all features observed in the experimental data for cGaSb) can be seen in Fig. 8.2 (a). The difference can be clearly seen (see features A, B, C, D and E) between calculated

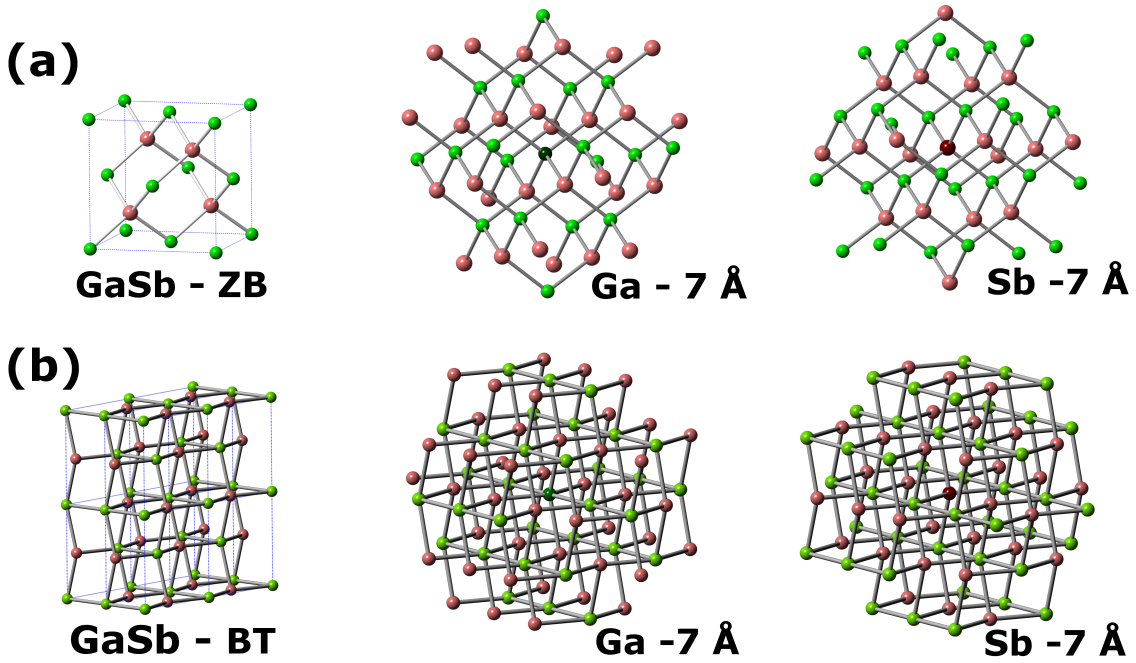

Fig. 8.1 (a) GaSb zinc blende (ZB) (b) GaSb β-tin (BT) unit cell together with the 7.0 Å cluster for XANES spectra calculation with Ga and Sb as the absorbing atom, respectively.

XANES signals for zinc-blende and β-tin structures, with the zinc-blend simulated spectrum most closely corresponding to the experimental cGaSb data. This suggests that XANES calculations can reliably reproduce experimental data and distinguish between the phases. We had a closer look at XANES signal from aGaSb (see Fig. 8.2b). The shape of the signal is very different from that calculated for the β-tin-like structure (see Fig. 8.2a and b) and is rather similar to cGaSb, except the features are less pronounced. The latter is related to the structural disorder in aGaSb. At this stage we can conclude that tetrahedral local symmetry corresponding to the zinc-blende structure is preserved in aGaSb, which is in line with the previous [1] EXAFS analysis. Furthermore, armed with a capability to calculate XANES signals as a function of cluster size, we can also examine the range over which the local symmetry is preserved. In order to do that we compared calculated XANES spectra for several different cluster sizes – 3.0 Å, 5.0 Å and 7.0 Å. One can see that the main features A, B, C and D (for aGaSb, feature E is missing in either experimental or theoretical spectra) observed both in cGaSb and aGaSb are only adequately reproduced for the largest cluster size of 7.0 Å (see Fig. 8.2b) indicating the extent of the short-range order (SRO). This indicates

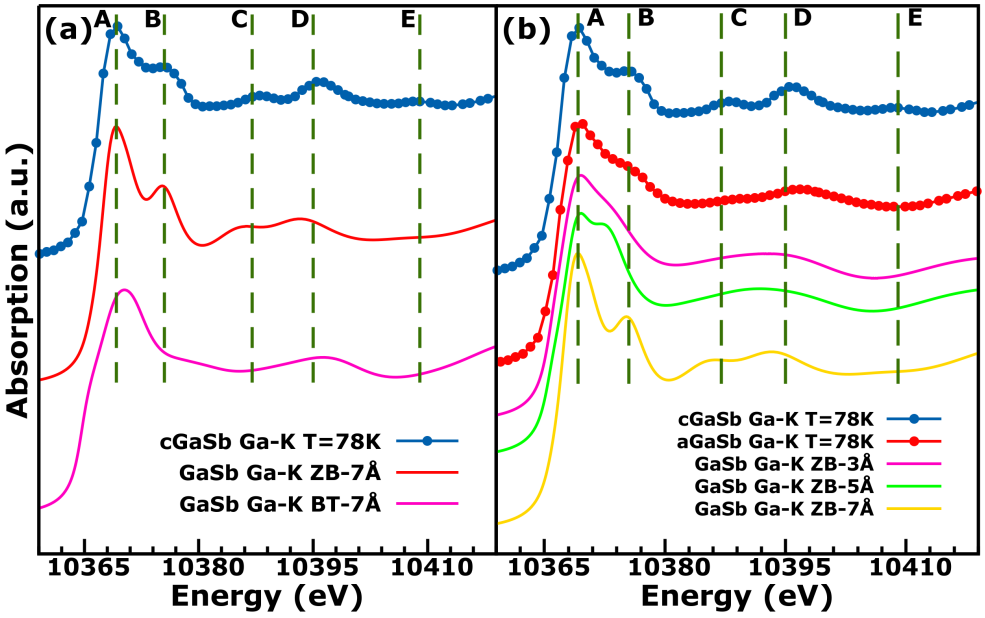

Fig. 8.2 (a) Ga K-edge XANES for GaSb compound at $T = 78$ K, together with the corresponding simulated XANES for zinc blende (ZB) structure. (b) The Ga K-edge XANES of both crystalline and amorphous GaSb compounds at $T = 78$ K, together with the corresponding simulated XANES spectra where the calculation cluster was set to 3.0 Å, 5.0 Å and 7.0 Å, respectively.

that numeric XANES analysis shows sufficient sensitivity to metastable phases and is capable of yielding information on the range over which the local order is preserved.

8.3 Local symmetry in matrix-free Ge QDs

We took advantage of the observed capability of numerical XANES analysis to explore the local symmetry to study matrix-free Ge QDs. First of all, the XANES spectra for CS1 Ge QDs is presented in Fig. 8.3, where the reference XANES of amorphous GeO_2 [3] is also shown. It can be seen that the main white line peak (labelled with 'A') for CS1 Ge QDs corresponds to Ge-O bonding environment. Meanwhile, the edge position as well as the feature labelled out in the green box both correspond to the Ge-Ge bonding. Moreover, a linear combination of the aGe (the XANES of aGe reference is not shown in Fig. 8.3 for clearness) and $aGeO_2$ reference spectra (aGe – 50%, $aGeO_2$ – 50%) is also shown in Fig. 8.3.

The result here indicates that the CS1 Ge QDs possess both Ge and GeO_2 features, which is consistent with the early EXAFS analysis.

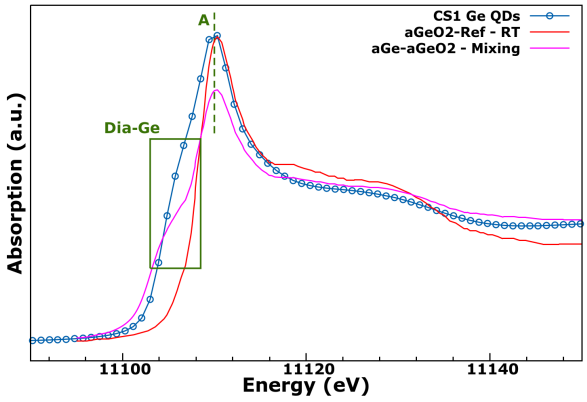

Fig. 8.3 The XANES spectra of CS1 Ge QDs, together with the reference spectra of $aGeO_2$ and the linear combination of aGe and $aGeO_2$ (aGe – 50%, $aGeO_2$ – 50%).

For the CS2 sample, the XANES spectra of both the as-prepared and annealed samples are shown in Fig.8.4 (a). The XANES spectra of the amorphous and crystalline Ge reference samples, together with the calculated XANES for the Ge diamond-type, BC8 and ST12 phases, are shown in Fig. 8.4 (a). First of all, the experimental XANES spectra for the CS2 Ge QDs (both as-prepared and annealed) are neither identical to that of the amorphous [4] nor the crystalline references, considering all the main features ('A' to 'D', labelled out in Fig. 8.4a). By comparing the experimental spectra (for CS2 Ge QDs) with the theoretical calculation for several phases of Ge (with the calculation cluster size $r = 7.0$ Å for each), it can be found that besides the main white line feature 'A' (11106 eV, Fig. 8.4a), the feature 'C' (11113 eV, Fig. 8.4a) observed in the annealed sample and the crystalline reference sample can be reproduced in all the three phases. However, the feature 'D' (labelled with dashed box) observed in both the as-prepared and annealed samples can only be found in the diamond-type phase. The results here indicate that for our small Ge QDs (both as-prepared and annealed), the diamond-type local symmetry is kept. Nevertheless, the feature 'B' observed in both the as-prepared and annealed samples is missing in all the calculated XANES spectra presented here. Therefore, to further explore the origins of these differences in the XANES spectra, we carried out an numerical XANES analysis. For the diamond-type Ge structure, the calculation cluster radius was set to a series of values from 3.0 Å up to 7.0 Å (Fig. 8.4b) to simulate the change in the local order effects on the XANES signal. The results are shown in Fig. 8.4 (b). When only the first shell was included (r = 3.0 Å), the simulated XANES spectrum is

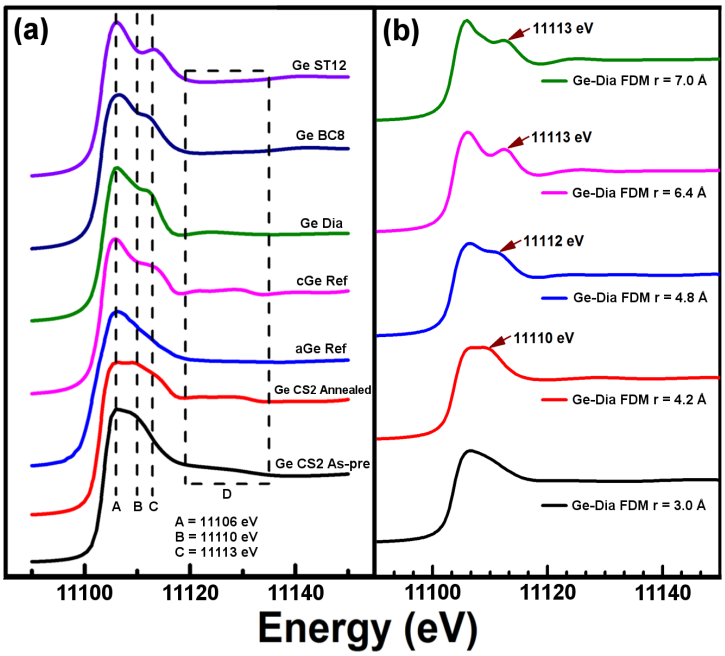

Fig. 8.4 (a) Comparison of XANES spectra for as-prepared, annealed Ge QDs, amorphous Ge [4], bulk (diamond-type) Ge references, theoretical calculation with diamond-type [5], BC8 [6] and ST12 [7] Ge phases (with the calculation cluster size $r = 7.0$ Å). The energy value corresponding to feature 'A' to 'C' is given at the bottom. (b) Simulated XANES spectra for diamond-type Ge structure by FDMNES using FDM mode, where the calculation cluster size was set from 3.0 Å to 7.0 Å. The arrows indicate the second main feature position in each spectrum.

featureless, which is consistent with the experimental spectra for amorphous Ge (see Fig. 8.4a). When the second shell was included (r = 4.2 Å), the second main feature (labelled with arrows in Fig. 8.4b) appears close to the white line. Furthermore, with increasing cluster size, the position of this second feature (obtained by analysing the second derivative of the spectrum, see the supporting information of our published paper: [8]) shifts to higher energy reaching 11113 eV for a cluster radius of 7.0 Å.

By directly comparing our calculations with the XANES spectra of as-prepared Ge QDs (see Fig. 8.5) we found that all the main features (designated as A, B and C around the region labelled by the rectangle) in the experimental spectra can be successfully reproduced only when at least two coordination shells (cluster size $r = 4.2$ Å) are included in the calculation. The analysis here thus shows that inclusion of a second shell is required to adequately reproduce the XANES of the as-prepared sample. This shows that the local symmetry

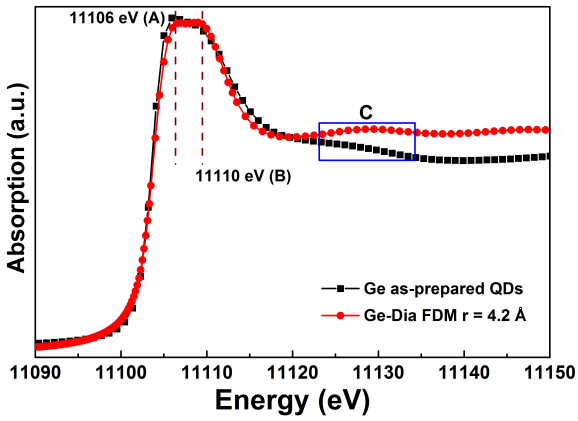

Fig. 8.5 Comparison of experimental XANES spectra of as-prepared Ge QDs with simulation, for which only the first two shells are included in the calculation cluster (radius $r = 4.2$ Å) using FDM mode.

corresponding to the diamond-type Ge phase is kept beyond the first coordination shell in CS2 sample, which is not seen from the EXAFS data analysis. The result here is consistent with our previous analysis [9] of the powder X-ray diffraction pattern for an as-prepared sample, which shows a narrower diffraction peak compared with a typical amorphous Ge signal. This further demonstrates that XANES can be used to provide local symmetry information in small nanoparticles when EXAFS data are limited to the first shell only.

We then turned our attention to the annealed samples. The positions of several features (marked by vertical dashed lines) just above the absorption edge for our annealed Ge QDs are shown in Fig. 8.6, designated as A, B and C. By comparison with the XANES of the diamond-type Ge reference, it can be seen that our annealed Ge QDs show an extra feature at around 11110 eV (designated as B; Fig. 8.6). The positions of the other two features (A and C) are identical to the crystalline reference. By comparing Figs. 8.5 and 8.6, one can see that the positions of features B are identical (11110 eV; Figs. 8.5 and 8.6) in both. This suggests similar structural origins of these features in the as-prepared and annealed samples. This, together with the theoretical XANES calculation shown in Figs. 8.4 and 8.5 and analysis for the as-prepared sample, indicates the presence of an amorphous-like component in the annealed Ge QDs with local order restricted to the first two coordination shells. Hence, the result here suggests that there must be two distinctly different regions of symmetry correlation lengths. Then, following arguments similar to the ones in Chapter-5, we conclude that the core-shell model is most appropriate (see the inset in Fig. 8.6). The finding here is consistent

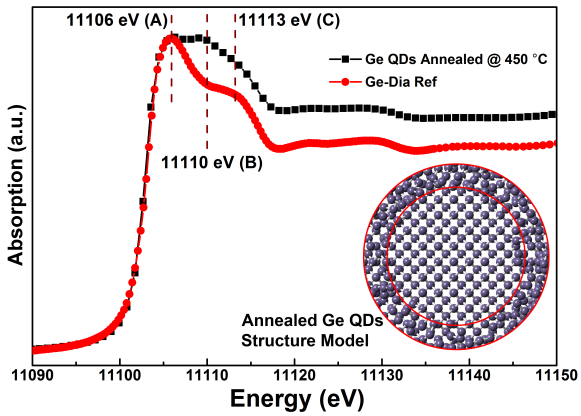

Fig. 8.6 Position of features in the XANES spectra of annealed Ge QDs and the diamond-type Ge reference. The feature in the middle cannot be observed in the reference XANES spectrum. The positions were obtained by taking the derivatives of the XANES spectra. The inset is an illustration of the proposed core-shell model for annealed Ge QDs.

with the results from the first-principle and empirical MD calculations by Pizzagalli, et al. [10].

We thus conclude that as-prepared matrix-free colloidal Ge QDs show a high degree of structural disorder, but preserve local diamond-like symmetry. Annealing of as-prepared nanoparticles in an oxygen-free environment for 1 h at 450 °C results in QDs crystallization, while surface disorder is still preserved.

8.4 Structural origins of PL in Ge QDs by OD-XANES

In our previous report [11], the optically detected EXAFS (OD-EXAFS) was employed, together with the MD simulation, to look into the origins of light emission in the etched hydrogen- and oxygen-terminated Ge QDs. It was shown that in the oxygen-terminated sample, it is the oxygen-rich regions that are responsible for optical emission. In the hydrogen-terminated sample, it was found the surface disordered layer ($\sim$ 5 Å thick) contributes to light emission. Here, since details about the local symmetry of our Ge QDs have been established based on the numerical XANES analysis discussed in last section, we further explored the relationship between the atomic-level structure and the photoluminescence (PL) emission in CS1 and CS2 samples using the optically detected XANES (OD-XANES). Two main optical emission windows of interest were used for the ODXAS data collection using

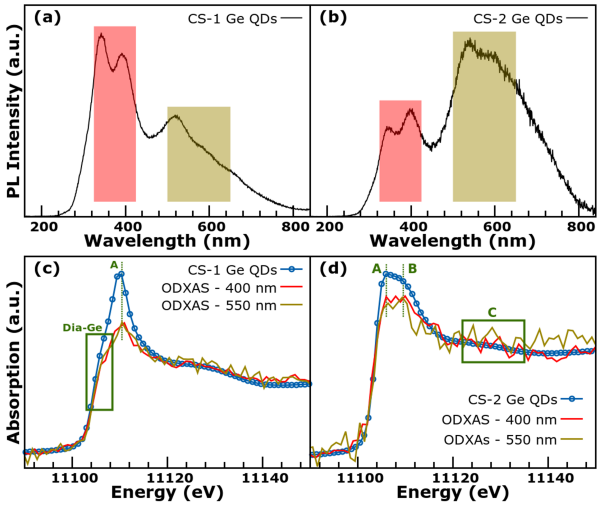

Fig. 8.7 (a) and (b) The two PL windows (350 – 450 nm and 500 – 650 nm) used to collect the OD-XANES spectra for CS1 and CS2 sample, respectively. (c) and (d) The comparison of OD-XANES (with PL window selected around 400 nm and 550 nm, respectively) and XANES (detected in transmission mode) spectra for CS1 and CS2 sample, respectively.

XEOL – 350 – 450 nm and 500 – 650 nm (see Fig. 8.7a and b), for both CS1 and CS2 samples here. The signal-to-noise ratio of the recorded absorption spectra in the extended region (above $\sim$ 11300 eV) was found to be too low to obtain a usable EXAFS signal. However, the XANES signal was found to be suitable for subsequent qualitative analysis (see Fig. 8.7c and d). Here, the advantage of high signal-to-noise of XANES spectra over EXAFS is reflected, as mentioned in section-3.5 of Chapter-3. One can see that OD-XANES retained the key features of the transmission XANES data. In case of CS1 sample the data suggest that there is no difference in structural origins of emission between two spectral windows. However, comparison of the normalized transmission and optically detected data show that the amplitude of the white line corresponding to GeO_2 (feature A in Fig. 8.7c) is noticeably reduced. The strength of various features in an absorption signal in multi-component systems is proportional to the atomic fraction of the contributing structure [12]. For example, a reduction in the signal associated with the GeO_2 in a transmission signal of GeO_2-Ge mixture would indicate a lower fraction of the GeO_2 phase. However, since the transmission and optically detected data were collected simultaneously, the observed result here should not be the effect of sample changing (e.g. oxidization) during measurements. Hence, to understand the origins of the difference we must turn to the nature of ODXAS.

In ODXAS, given the signal was taken in the thin limit [13, 11], such reduction indicates lower light yield from the corresponding phase. This suggests that although the oxygen-rich surface regions do contribute to the emission in CS1 Ge QDs, the contribution from the pure Ge channel is disproportionally higher. As mentioned at the beginning of this section, our previous OD-EXAFS based analysis for the oxygen-terminated sample shows the light emission mainly comes from the oxygen-rich regions. Combined with such findings, the result here indicates that photoelectrons may propagate beyond the local excited regime before decaying to emit light, owing to the long EMFP in the XANES region. This tends to mix the contributions to the optical emission from the pure-Ge and Ge-O regions for CS1 sample.

For CS2 Ge QDs, the comparison of XANES and OD-XANES spectra are shown in Fig. 8.7d. One can see that the OD-XANES spectra for two spectral windows are similar to the transmission XANES of CS2 sample (compare the positions of the typical feature A and B). This indicates that pure Ge structures contribute to the light emission in CS2 sample. Similarity in the position of the features A and B further suggests that the structure with the diamond-type symmetry is the source of light emission. However, the intensity of these features is somewhat reduced in OD-XANES compared to the transmission data. This effect suggests that optical signal is dominated by the emission from a subset of atoms in the sample, as discussed above for the CS1 sample. In the previous report (from our group) [11] on matrix free hydrogen-terminated Ge QDs prepared by etching, it was shown that optical emission within the core-shell model (crystalline core, disordered shell) can be localized to a disordered substructure extending to around 5 Å from the surface. This is consistent with our findings here since coordination shells out to ~ 4.2 Å have to be included to explain XANES signal observed in CS2 sample, while OD-XANES signal is similar to the transmission data. We should stress here that in bulk systems the correspondence between the X-ray absorption signal detected in transmission and in optically detected modes may or may not be straightforward [14]. Problems associated with sample preparation, thickness and energy transfer between luminescent centers and matrix has been observed and extensively discussed previously [13, 15]. However, this work and our recent report [11] indicate that optically-detected XAS measurements can become a valuable asset in understanding the relationship between atomic structure and emission in nanoparticles. This is, in part, due to relatively straightforward ability to work in the thin limit [13]. However, addressing the question of selectivity of the technique on nanoscale and understanding specific challenges in ODXAS in low dimensional systems is currently limited by availability of experimental information. On the other hand, such applications have a potential to become an extremely powerful

tool (certainly much more so than in the bulk systems) since a vast number of nanoscale systems (importantly, including both semiconductors and metals) can exhibit strong light emission. As an example, such methods can be very useful indeed for distinguishing between the size-effect and doping contribution (e.g. boron and phosphorous doping [16], etc.) to the blue or red shift of PL emission from doped Ge in QDs.

8.5 Conclusion

In this chapter, the numerical XANES calculation is used as the main method for probing the local structure of both aGaSb and matrix-free Ge QDs systems. The test on the well-studied bulk aGaSb system demonstrated that such an approach based on XANES spectra analysis can reliably identify the local symmetry of different phases. Further analysis for the matrix-free Ge QDs system shows that XANES indeed can provide information about medium-range order (i.e. local order beyond the first coordination shell) for highly disordered system, which is, however, not accessible by EXAFS. Specifically, detailed XANES analysis clearly points to diamond-like local symmetry for the oxygen-free Ge QDs (i.e. CS2 sample), where the local order is retained up to the second coordination shell.
ODXAS signals were recorded for both samples by selecting two XEOL emission windows – 350-450 nm and 500-650 nm. The comparison of the transmission and optically detected XANES shows that for CS1 Ge QDs the contribution from pure Ge channel is disproportionally higher than the oxygen-rich surface regions. In oxygen-free CS2 Ge QDs it was found that pure Ge structure contributes to the light emission. Based on the analysis for the XANES detected using the transmission mode, the similarity between the optically and transmission detected XANES indicates that the optical emission in the pure Ge QDs is strongly correlated to the local structural configuration of CS2 sample – highly disordered with local diamond-type symmetry extending to the second coordination shell.

The next (final) chapter will summarize the main approach used in this thesis to address the problems in structure characterization for small Ge QDs. The main conclusions for the specific case studies presented in Chapter-5 to 8 will be given. As the final remarks, the prospects for future work will also be addressed.

References

[1] A. V. Sapelkin, S. C. Bayliss, A. G. Lyapin, V. V. Brazhkin, and A. J. Dent. Structure of bulk amorphous GaSb: a temperature-dependent EXAFS study. *Phys. Rev. B*, 56:11531–11535, 1997.

[2] C. S. Schnohr and M. C. Ridgway. *X-ray absorption spectroscopy of semiconductors*. Springer, USA, 2015.

[3] J. P. Itie, A. Polian, G. Calas, J. Petiau, A. Fontaine, and H. Tolentino. Pressure-induced coordination changes in crystalline and vitreous GeO_2. *Phys. Rev. Lett.*, 63:398–401, 1989.

[4] M. Backman, F. Djurabekova, O. H. Pakarinen, and K. Nordlund. Amorphization of Ge and Si nanocrystals embedded in amorphous SiO_2 by ion irradiation. *Phys. Rev. B*, 80:144109, 2009.

[5] N. Shaw and Y. H. Liu. X-ray measurement of the thermal expansion of germanium, silicon, indium antimonide and gallium arsenenide. *Acta Phys. Sin-CH ED*, 20:699–704, 1964.

[6] R. J. Nelmes, M. I. McMahon, N. G. Wright, D. R. Allan, and J. S. Loveday. Stability and crystal structure of BC8 germanium. *Phys. Rev. B*, 48:9883–9886, 1993.

[7] J. C. Kasper and S. M. Richards. Crystal structure of new forms of Si and Ge. *Acta. Crystallogr.*, 17:752–755, 1964.

[8] Y. P. Zhang, O. Ersoy, A. Karatutlu, W. Little, and A. Sapelkin. Local structure of Ge quantum dots determined by combined numerical analysis of EXAFS and XANES data. *J. Synchrotron Rad.*, 23:253–259, 2016.

[9] Y. P. Zhang, A. Karatutlu, O. Ersoy, W. Little, G. Cibin, A. Dent, and A. Sapelkin. Structure and effects of annealing in colloidal matrix-free ge quantum dots. *J. Synchrotron Rad.*, 22:105–112, 2015.

[10] L. Pizzagalli and G. Galli. Surface reconstruction effects on atomic properties of semiconducting nanoparticles. *Mater. Sci. Engin. B-Solid State Mater. Adv. Techn.*, 96:86–89, 2002.

[11] W. Little, A. Karatutlu, D. Bolmatov, K. Trachenko, A. V. Sapelkin, G. Cibin, R. Taylor, F. Mosselmans, A. J. Dent, and G. Mountjoy. Structural origin of light emission in germanium quantum dots. *Sci. Rep.*, 4:7372, 2014.

[12] L. L. Araujo, R. Giulian, D. J. Sprouster, C. S. Schnohr, D. J. Llewellyn, P. Kluth, D. J. Cookson, G. J. Foran, and M. C. Ridgway. Size-dependent characterization of embedded ge nanocrystals: Structural and thermal properties. *Phys. Rev. B*, 78:094112, 2008.

[13] S. Emura, T. Moriga, J. Takizawa, M. Nomura, K. R. Bauchspiess, T. Murata, K. Harada, and H. Maeda. Optical-luminescence yield spectra produced by x-ray excitation. *Phys. Rev. B*, 47:6918–6930, 1993.

[14] L. Soderholm, G. K. Liu, M. R. Antonio, and F. W. Lytle. X-ray excited optical luminescence (XEOL) detection of x-ray absorption fine structure (XAFS). *J. Chem. Phys.*, 109:6745–6752, 1998.

[15] J. T. P. Goulon, P. M. Lemonnier, and J. Dexpert-Ghys. On a site-selective EXAFS experiment using optical emission. *Chem. Phys.*, 78:347–356, 1983.

[16] N. Sustersic, L. Nataraj, M. Weiland, M. Coppinger, M. V. Shaleev, A. V. Novikov, R. Opila, S. G. Cloutier, and J. Kolodzey. Effects of boron and phosphorus doping on the photoluminescence of self-assembled germanium quantum dots. *Appl. Phys. Lett.*, 94:183103, 2009.

Chapter 9

Conclusion and Future work

9.1 Summary

In this thesis, X-ray absorption spectroscopy was employed to explore the local structure of Ge QDs. Specifically, two sets of samples were examined – the oxygen-terminated sample prepared with GeO_2 as the precursor (CS1 sample) and oxygen-free sample with $GeCl_4$ as the precursor (CS2 sample). First of all, the EXAFS spectra analysis methodology (mainly introduced in Chapter-3) was applied on the two sets of Ge QDs samples both with size around 4 nm. Combined with the results from TEM, Raman and PXRD, it was shown that the as-prepared CS1 Ge QDs was terminated by oxygen bonding. Whereas the as-prepared oxygen-free sample was believed to be terminated with hydrogen. Furthermore, based on comprehensive analysis, a core-shell model was proposed for the as-prepared Ge QDs (CS2, oxygen-free), where the core is crystalline and shell is amorphous. Further annealing processing crystallizes the as-prepared Ge QDs to the diamond-type Ge phase. The extra diffraction peak in the PXRD pattern for the two sets of annealed Ge QDs then indicates that a metastable phase may possibly be present in the small Ge QDs due to the size effect.
The EXAFS analysis was then combined with optical and Raman spectroscopy to explore the phase transition behaviour of the as-prepared matrix-free Ge QDs under hydrostatic compression. It was found that with increasing pressure, the commonly observed transition to metallic β-tin in bulk Ge (either crystalline or amorphous) was frustrated in Ge QDs due to the size effect. Instead, the transition from low-density to high-density (metallic) amorphous phase was observed, as revealed by the comprehensive EXAFS, optical transmission, PL and Raman analysis. The proposed phase transition mechanism for the small Ge QDs was further supported by the DFT simulation for a $Ge_{71}H_{60}$ cluster.

To go beyond the limitation of the conventionally used EXAFS fitting technique based on the given structural model, a Fortran code MD2FEFF was developed, intending to combine the EXAFS calculation (using FEFF9.6) and molecular dynamics simulation (using DL_POLY_4). For the FEFF calculation, the configuration average over the whole cluster was calculated. The average was further taken over all the FEFF calculation results after each MD running to take account of the dynamic disorder of the system. The developed code was applied to both aGaSb and Ge QDs system. The results from the aGaSb reference system show the validity of the combined FEFF and MD simulation approach. The application of MD2FEFF code on annealed Ge QDs suggests that the Ge core-shell model with 90% core crystalline region best describes the experimental spectra.
For the as-prepared oxygen-free Ge QDs (CS2 sample), the PXRD pattern indicates higher crystallization as compared to the completely amorphous sample. However, the EXAFS spectra in *R*-space only shows the peak corresponding to the first-shell coordination. To solve such ambiguity about the local structural configuration, XANES spectra were utilized, which is more sensitive to the local environment as described in section-1.4 of Chapter-1 and section-3.5 of Chapter-3. The theoretical XANES was calculated using the FDMNES package (see section-4.1 of Chapter-3), which was further compared with the experimental spectra for probing the local structural configuration. The application of such methodology on the GaSb system showed that XANES can be reliably used to obtain information about local symmetry in systems where the lack of periodicity precludes the use of powerful diffraction methods. Further application of the numerical XANES analysis on CS2 Ge QDs demonstrates that the as-prepared oxygen-free Ge QDs is highly disordered, whereas local symmetry corresponding to the diamond-type structure is generally extended to the second coordination shell on average. Furthermore, based on the numerical XANES analysis, a core-shell model (core – crystalline; shell – amorphous) was also proposed for the annealed CS2 Ge QDs. On the basis of the numerical analysis for the XANES detected in transmission mode, the optically detected XAS was further considered to link the local structure with the optical emission behaviour in the Ge QDs system. For the oxygen-terminated CS1 sample, it was found that light emission comes from both Ge-Ge and Ge-O bonding environment (i.e. as the light emission center). However, the comparison of the transmission and optically detected XANES shows that for CS1 Ge QDs, the contribution from pure Ge channel is disproportionally higher than the oxygen-rich surface regions. For oxygen-free Ge QDs (CS2 sample), it was found that the optical emission in pure Ge QDs is strongly correlated to the local structural configuration of CS2 Ge QDs – highly disordered with local diamond-type symmetry extending to the second coordination shell.

9.2 Future work

Recently, our group has been cooperating with other groups working on the bio-application of carbon QDs. For carbon systems, the features of the XANES spectra are richer than that of the Ge system. The complex local bonding environment around the carbon atom, owing to the strong covalent property of carbon, leaves space for utilizing XANES spectra to investigate local and medium-range symmetry. Therefore the application of XANES theoretical calculation to probe the local symmetry of carbon QDs could be one of the future research concerns. Although there is work reported on the application of XAS on carbon nanostructures [1], from our knowledge, there are limited reports concerning the implementation of the theoretical calculation of XANES for carbon nanostructure studies. The main difficulty lies in that the theoretical approach based on the conventional multiple scattering theory fails to reproduce the rich features of the experimental XANES spectra. As mentioned in section-4.1, a full potential multiple scattering approach, which goes beyond the limitation of muffin-tin approximation for calculating XANES spectra of light-element system (e.g. Carbon) by J. Q. Xu, et al. [2]. Meanwhile, the main approach used in this thesis for XANES calculation – FDMNES – is also designed to go beyond the limitation of the muffin-tin approximation. Therefore for the future work, it will be beneficial to examine in detail the validity of the two available approaches here on various carbon-related systems with different chemical environments and/or local symmetry.

Furthermore, the developed MD2FEFF code could be applied to more systems to help examining structural configurations. As an example, it can be employed to compare among the several possible structural models for various binary metallic nanoparticles, including independent nanoparticles, core-shell model and alloy model, etc. Moreover, for now, the kernel of the MD2FEFF code is to use the MD simulation as the tool for structural evolution, which is designed to taken into account of the dynamic disorder of the system. However, the potential parameters for the MD simulation cannot be adjusted during the simulation. This could be a problem when the potential parameters from literature (e.g. the Tersoff potential parameters for Ge, see Chapter-7) may not be appropriate for the complex structural configuration in simulation (e.g. the core-shell model for Ge QDs, see Chapter-7). By introducing the capability to adjust the potential parameters for MD simulation on-the-run (according to the agreement between FEFF calculation result and the experimental spectra, in each running cycle), it is expected that the MD2FEFF simulation could give better agreement with the experimental EXAFS spectra. This is beneficial for either comparing between different input models or predicting structural model for certain systems.

References

[1] J. Zhong, H. Zhang, X. H. Sun, and S. T. Lee. Synchrotron soft x-ray absorption spectroscopy study of carbon and silicon nanostructures for energy applications. *Adv. Mater.*, 16:7786–7806, 2014.

[2] J. Q. Xu, P. Krüger, C. R. Natoli, K. Hayakawa, Z. Y. Wu, and K. Hatada. X-ray absorption spectra of graphene and graphene oxide by full-potential multiple scattering calculations with self-consistent charge density. *Phys. Rev. B*, 92:125408, 2015.

Appendix A

Nyquist-Shannon theorem

In mathematics, analog signals can be described as the continuous function in time domain. However for practical signal measurement, the obtained signals can never be really continuous. In another word, what the measurement does is actually sampling the continuous signal to obtain a series of data at discrete sampling points. Then comes the important question that whether the sampling can successfully rebuild the real signal. If not, the measurement is not a good representative of the real signal or in another way, part of the information in the real signal is missing in the measurement. This is where the Nyquist-Shannon theorem comes to help. Since the theorem concerns about the validity of the signal samplings, therefore it is also called the Sampling theorem. To understand the Sampling theorem, it is better to first look at how the sampling works mathematically.
First of all, the continuous signal in time domain is given as $f(t)$, and the sampling is realized through multiplying $f(t)$ by a sampling function $p(t)$:

$$f_d(t) = f(t)p(t) \tag{A.1}$$

where $f_d(t)$ represents the obtained sampling signal (discrete), and the sampling function is given as the sum of a series of δ function:

$$p(t) = \sum_{n=-\infty}^{\infty} \delta(r - nT_s) \tag{A.2}$$

T_s here refers to the sampling interval. Let $F(\omega)$ and $P(\omega)$ represent the Fourier transform $\mathscr{F}$ of $f(t)$ and $p(t)$, respectively, i.e.:

$$F(\omega) = \mathscr{F}[f(t)] \tag{A.3}$$

$$P(\omega) = \mathscr{F}[p(t)] \tag{A.4}$$

Then according to the convolution theorem, the Fourier transform of the sampled signal $f_d(t)$ can be given as:

$$\begin{aligned} F_d(\omega) = \mathscr{F}[f_d(t)] &= \mathscr{F}[f(t)p(t)] \\ &= \mathscr{F}[f(t)] \otimes \mathscr{F}[p(t)] \\ &= F(\omega) \otimes P(\omega) \end{aligned} \tag{A.5}$$

where the symbol '$\otimes$' represents the convolution operation. Since the given sampling function $p(t)$ is periodic (with the periodicity of T_s), the corresponding Fourier transform function $P(\omega)$ is then discrete and only takes value at $\omega = \omega_s, 2\omega_s, 3\omega_s, \ldots$, where $\omega_s = 2\pi/T_s$ is the baseband angular frequency. Mathematically, the $P(\omega)$ function can be written in the following form:

$$P(\omega) = \sum_{n=-\infty}^{\infty} P_n \delta(\omega - n\omega_s) \tag{A.6}$$

where

$$P_n = \frac{1}{T_s} \int_{t_0}^{t_0+T_s} p(t) e^{-jn\omega_s t} dt \tag{A.7}$$

Then the equation-A.5 can be further given as:

$$\begin{aligned} F_d(\omega) &= F(\omega) \otimes P(\omega) \\ &= F(\omega) \otimes \sum_{n=-\infty}^{\infty} P_n \delta(\omega - n\omega_s) \\ &= \sum_{n=-\infty}^{\infty} P_n [F(\omega) \otimes \delta(\omega - \omega_s)] \\ &= \sum_{n=-\infty}^{\infty} F(\omega - n\omega_s) \end{aligned} \tag{A.8}$$

From A.8, it can be seen that the Fourier transform $F_d(\omega)$ of the sampled signal $f_d(t)$ is the sum of a series of replica of the Fourier transform $F(\omega)$ of the original continuous signal $f(t)$. For jth component, the corresponding replica of $F(\omega)$ is shifted to the right by $j\omega_s$ (when j is negative, the shift is to the left), and such idea is depicted in Fig. A.1. In Fig. A.1, the blue curve corresponds to the original continuous signal and the green curves are the shifted components of the Fourier transform corresponding to the sampled signal. If assuming the bandwidth (frequency) of the original continuous signal is $2B$ ($-B \rightarrow B$, given

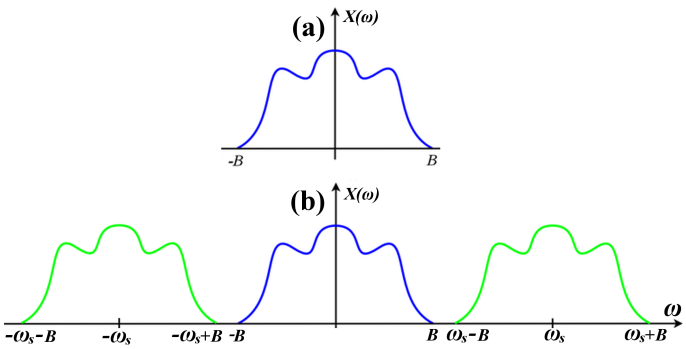

Fig. A.1 The illustration for the Fourier transform of (a) the original continuous signal (in time domain) and (b) the sampled signal. The picture was reproduced based on the original image: [1]

in angular frequency, the bandwidth is $2\pi B$), then it can be seen clearly from Fig. A.1 that it is the baseband angular frequency ω_s, therefore the sampling interval T_s ($\omega_s = 2\pi/T_s$), that determines whether shifted components in the Fourier transform of the sampled signal overlap with each other.

Theorem T.A1. *In order for a band-limited (i.e., one with a zero power spectrum for frequencies $f > B$) baseband ($f > 0$) signal to be reconstructed fully, it must be sampled at a rate $f_s \geq 2B$ [2].*

To reconstruct the original signal, the shifted components must not overlap with each other, since otherwise the adjacent components will be mixed up and it then becomes impossible to separate the single component in the Fourier transform which corresponds to the original continuous signal. This is the basic idea of the *Nyquist-Shannon sampling theorem*, which is expressed exactly by theorem-T.A1 [2], i.e.:

$$f_s = 2\pi\omega_s \geq 2B \tag{A.9}$$

Accordingly, the sampling interval T_s should meet the following requirement for the successful reconstruction of the original signal:

$$\begin{gathered} \frac{1}{T_s} \geq 2B \\ \Downarrow \\ T_s \leq \frac{1}{2B} \end{gathered} \tag{A.10}$$

To demonstrate the idea of the sampling theorem, three simple signals are presented in Fig. A.2. As shown in Fig. A.2 (a), the sampling interval T_s is smaller than half the periodicity

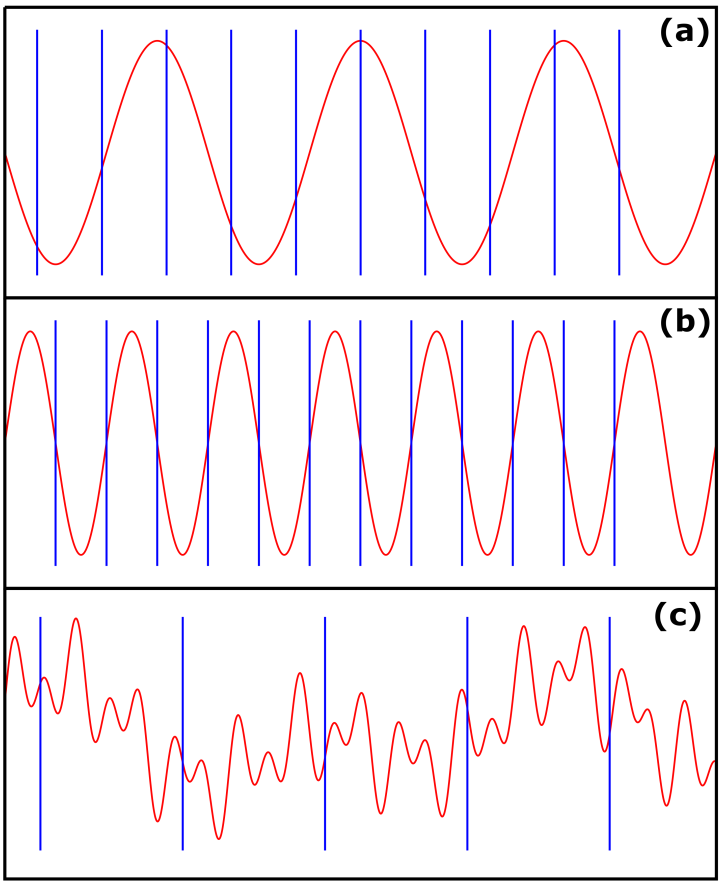

Fig. A.2 The illustration for the sampling theorem using three artificial signals in (a), (b) and (c), respectively. The blue lines indicate the sampling points in time domain.

of the *cosine* signal, which satisfies the requirement A.10. Therefore the sampling in this case is fine enough to reconstruct the original *cosine* signal. Fig. A.2 (b) shows the critical situation where the equal sign is taken in A.10. As for the case presented in Fig. A.2 (c), the requirement of A.10 is not met therefore the original signal cannot be completely reconstructed. In another word, the information contained in the fine vibrations located in between the sampling intervals is lost.

References

[1] Nyquist–shannon sampling theorem. https://en.wikipedia.org/wiki/Nyquist%E2%80%93Shannon_sampling_theorem, May 2016. online; accessed 19-May-2016.

[2] Sampling theorem. http://mathworld.wolfram.com/SamplingTheorem.html, May 2016. online; accessed 19-May-2016.

Appendix B

Multiple scattering theory

In this appendix, the basic scattering theory and how it is embedded into the XAFS simulation will be introduced. The first section will be about the basic introduction to the quantum scattering theory based on Chapter-7 of Sakurai's book *Modern Quantum Mechanics* [1]. The second section will focus on the theoretical method used for XAFS spectra calculation in FEFF, based on the quantum scattering theory.

B.1 Quantum scattering theory

B.1.1 Lippmann-Schwinger equation

In quantum mechanics, the scattering problem is treated as the influence of the existing scattering potential V on the propagation of the electron wave. First of all, if without the scattering potential, i.e. $V = 0$, the corresponding Schr$\ddot{o}$dinger equation is:

$$\mathscr{H}_0|\phi\rangle = E|\phi\rangle \tag{B.1}$$

where $\mathscr{H}_0 = \mathbf{p}^2/2m$ stands for the kinetic energy operator, and the solution of (B.1) is just the free particle state $|\mathbf{p}\rangle$. When the scattering potential is non-zero, the corresponding Schr$\ddot{o}$dinger equation is given as:

$$(\mathscr{H}_0 + V)|\psi\rangle = E|\psi\rangle \tag{B.2}$$

Here the kernel of the quantum scattering problem is to solve equation-(B.2), and it should be followed that when $V \to 0$, there should be $|\psi\rangle \to |\phi\rangle$. Written in the symbolic format,

the solution for (B.2) could be given as:

$$|\psi\rangle = \frac{1}{E-\mathscr{H}_0}V|\psi\rangle + |\phi\rangle \tag{B.3}$$

When $V \to 0$, the solution-(B.3) reduces to $|\psi\rangle \to |\phi\rangle$. It is straightforward to verify (B.3) by multiplying $(E-\mathscr{H}_0)$ on both sides, which returns to the equation-B.2, if considering (B.1). The problem of the singular nature of the operator $1/(E-\mathscr{H}_0)$ was then solved by making E a bit complex to give the corrected version of the solution:

$$|\psi^{(\pm)}\rangle = |\phi\rangle + \frac{1}{E-\mathscr{H}_0 \pm i\eta}V|\psi^{(\pm)}\rangle \tag{B.4}$$

which is called the **Lippmann-Schwinger equation**. Here the '$\pm$' sign represents the outgoing or back-scattered wave, which can be seen clearly when considering the scattered wave in large distances (will be discussed later on). The operator $1/(E-\mathscr{H}_0 \pm i\varepsilon)$ is the Green's function (about Green's function method, see Appendix-C) corresponding to the free particle Schr*ö*dinger equation-(B.1), which, according to Sakurai's book, can be given in the position space as following:

$$G_{\pm}(\mathbf{x},\mathbf{x}') = -\frac{1}{4\pi}\frac{2m}{\hbar^2}\frac{e^{\pm ik|\mathbf{x}-\mathbf{x}'|}}{|\mathbf{x}-\mathbf{x}'|} \tag{B.5}$$

The next step is to cast the solution for the scattered wavefunction (B.4) specifically to position space. First of all it was assumed that the potential V is local, which means there is no correlation between potential in different spatial positions, i.e.:

$$\langle \mathbf{x}'|V|\mathbf{x}''\rangle = V(\mathbf{x}')\delta^{(3)}(\mathbf{x}'-\mathbf{x}'') \tag{B.6}$$

Considering the assumption for the scattering potential and also the form of Green's function given by (B.5), (B.4) can be cast to the position space as following:

$$\begin{aligned}\langle \mathbf{x}|\psi^{(\pm)}\rangle &= \langle \mathbf{x}|\phi\rangle + \int d^3x' \left\langle \mathbf{x}\right| \frac{1}{E-\mathscr{H}_0 \pm i\varepsilon}\left|\mathbf{x}'\right\rangle \langle \mathbf{x}'|\mathbf{V}|\psi^{(\pm)}\rangle \\ &= \langle \mathbf{x}|\phi\rangle - \frac{2m}{\hbar^2}\int d^3x' \frac{e^{\pm ik|\mathbf{x}-\mathbf{x}'|}}{4\pi|\mathbf{x}-\mathbf{x}'|}\langle \mathbf{x}'|\mathbf{V}|\psi^{(\pm)}\rangle \\ &= \langle \mathbf{x}|\phi\rangle - \frac{2m}{\hbar^2}\int d^3x' \frac{e^{\pm ik|\mathbf{x}-\mathbf{x}'|}}{4\pi|\mathbf{x}-\mathbf{x}'|}\Big(\int d^3x'' \langle \mathbf{x}'|V|\mathbf{x}''\rangle\langle \mathbf{x}''|\psi^{(\pm)}\rangle\Big)\end{aligned} \tag{B.7}$$

$$= \langle \mathbf{x}|\phi\rangle - \frac{2m}{\hbar^2}\int d^3x' \frac{e^{\pm ik|\mathbf{x}-\mathbf{x}'|}}{4\pi|\mathbf{x}-\mathbf{x}'|}\Big(\int d^3\mathbf{x}'' V(\mathbf{x}')\delta^{(3)}(\mathbf{x}'-\mathbf{x}'')\langle \mathbf{x}''|\psi^{(\pm)}\rangle\Big)$$
$$= \langle \mathbf{x}|\phi\rangle - \frac{2m}{\hbar^2}\int d^3x' \frac{e^{\pm ik|\mathbf{x}-\mathbf{x}'|}}{4\pi|\mathbf{x}-\mathbf{x}'|}V(\mathbf{x}')\langle \mathbf{x}'|\psi^{(\pm)}\rangle \tag{B.8}$$

B.1.2 Scattering amplitude

In practice, it is always the position far from the scattering potential field is important, since the observation point (e.g. experimental detector) for the scattered wavefunction is always located at large distances as compared to the size of the scattering potential field. Mathematically:

$$|\mathbf{x}| \gg |\mathbf{x}'| \tag{B.9}$$

therefore:

$$\begin{aligned} |\mathbf{x}-\mathbf{x}'| &= \sqrt{x^2 - 2xx' cos\alpha + r'^2} \\ &= x\Big(1 - \frac{2x'}{x}cos\alpha + \frac{x'^2}{x^2}\Big)^{1/2} \\ &\simeq x - \hat{\mathbf{x}}\cdot\mathbf{x}' \end{aligned} \tag{B.10}$$

where $\hat{\mathbf{x}} = \mathbf{x}/|\mathbf{x}|$ is the unit vector in $\mathbf{x}$ direction, and $\alpha = \angle(\mathbf{x},\mathbf{x}')$ is the angle between the observation and field position. Moreover, if defining:

$$\mathbf{k}' \equiv k\hat{\mathbf{r}} \tag{B.11}$$

as the wave vector of the scattered wave, one could have:

$$e^{\pm ik|\mathbf{x}-\mathbf{x}'|} \simeq e^{\pm ikr}e^{\mp i\mathbf{k}'\cdot\mathbf{x}'} \tag{B.12}$$

Considering the approximation given here, the scattered wavefunction of (B.8) at large distance can be given as ($\mathbf{p}$ replaced by $\mathbf{k}$ considering $\mathbf{k} = \mathbf{p}/\hbar$):

$$\begin{aligned} \langle \mathbf{x}|\psi^{(\pm)}\rangle &\overset{\text{large r}}{=} \langle \mathbf{x}|\mathbf{k}\rangle - \frac{1}{4\pi}\frac{2m}{\hbar^2}\int d^3x' \frac{e^{\pm ikr}e^{\mp i\mathbf{k}'\cdot\mathbf{x}'}}{r}V(\mathbf{x}')\langle \mathbf{x}'|\psi^{(\pm)}\rangle \\ &= \langle \mathbf{x}|\mathbf{k}\rangle - \frac{1}{4\pi}\frac{2m}{\hbar^2}\frac{e^{\pm ikr}}{r}\int d^3x' e^{\mp i\mathbf{k}\cdot\mathbf{x}'}V(\mathbf{x}')\langle \mathbf{x}'|\psi^{(\pm)}\rangle \\ &= \frac{1}{(2\pi)^{2/3}}\Big[e^{i\mathbf{k}\cdot\mathbf{x}} + \frac{e^{\pm ikr}}{r}f(\mathbf{k},\mathbf{k}')\Big] \end{aligned} \tag{B.13}$$

where r is assigned as $r = |\mathbf{x}|$, and the factor $f(\mathbf{k}^{'},\mathbf{k})$ is given as:

$$\begin{aligned} f(\mathbf{k},\mathbf{k}^{'}) &= -\frac{1}{4\pi}\frac{2m}{\hbar^2}(2\pi)^3 \int d^3x^{'} \frac{e^{\mp i\mathbf{k}^{'}\cdot\mathbf{x}^{'}}}{(2\pi)^{3/2}} V(\mathbf{x}^{'})\langle\mathbf{x}^{'}|\psi^{(\pm)}\rangle \\ &= -\frac{1}{4\pi}\frac{2m}{\hbar^2}(2\pi)^3 \int d^3x^{'} \langle\pm\mathbf{k}^{'}|\mathbf{x}^{'}\rangle V(\mathbf{x}^{'})\langle\mathbf{x}^{'}|\psi^{(\pm)}\rangle \\ &= -\frac{1}{4\pi}\frac{2m}{\hbar^2}(2\pi)^3 \int d^3x^{'} \langle\pm\mathbf{k}^{'}|V(\mathbf{x}^{'})|\mathbf{x}^{'}\rangle\langle\mathbf{x}^{'}|\psi^{(\pm)}\rangle \\ &= -\frac{1}{4\pi}(2\pi)^3\frac{2m}{\hbar^2}\langle\pm\mathbf{k}^{'}|V|\psi^{(\pm)}\rangle \end{aligned} \tag{B.14}$$

From (B.13), it can be seen that the result of the scattering event can be decomposed to two components – the initial plane wave (the first term in (B.13)) and the modulated (by $f(\mathbf{k},\mathbf{k}^{'})$) spherical wave (the second term in (B.13)). The meaning of the '$\pm$' sign in the scattered wavefunction is now clear – it represents either the outgoing ('$+$') or back-scattered ('$-$') spherical wave. Considering the initial state which is the incoming plane wave, the spherical wave component in (B.13) then corresponds to the scattering effect of the existing potential V. Furthermore, considering the amplitude 1 and $f(\mathbf{k},\mathbf{k}^{'})$ for the incident and scattered wave, respectively, the *differential cross section* (in classic theory, it refers to the effective interaction area between the incoming and scatterer particle) $d\sigma/d\Omega$ can be given as:

$$\frac{d\sigma}{d\Omega}d\Omega = \frac{r^2|\mathbf{j}_{scatt}|d\Omega}{|\mathbf{j}_{incid}|} = |f(\mathbf{k}^{'},\mathbf{k})|^2 d\Omega \tag{B.15}$$

which infers:

$$\frac{d\sigma}{d\Omega} = |f(\mathbf{k}^{'},\mathbf{k})|^2 \tag{B.16}$$

Here the factor $f(\mathbf{k}^{'},\mathbf{k})$ is called the ***scattering amplitude***. From (B.16), it can seen that the scattering amplitude $f(\mathbf{k}^{'},\mathbf{k})$ is indeed an important notion since it is directly linked to the effective scattering effect (the differential cross section). Furthermore, it is just one of the important parameters that is calculated in FEFF for further EXAFS spectra fitting as mentioned earlier.

B.1.3 Born approximation

It could be noticed that in the solution given by (B.4), the unknown scattered wavefunction is contained in both the left and right hand sides. Therefore (B.4) does not directly give the solution of the scattered wave. To further solve the problem, the transition operator T is

defined at first in the following way:

$$V|\psi^{+}\rangle = T|\phi\rangle \tag{B.17}$$

Here it should be be pointed out that for the convenience of discussion, only the '+' sign (therefore the outgoing portion) in the scattered wave is considered. By multiplying both sides of (B.4) with V and representing the free propagator $1/(E-\mathscr{H}_0+i\varepsilon)$ with the symbol G_0, B.4 becomes:

$$V|\psi^{+}\rangle = V|\phi\rangle + VG_0V|\psi^{+}\rangle \tag{B.18}$$

$$\Downarrow$$

$$T|\phi\rangle = V|\phi\rangle + VG_0T|\phi\rangle \tag{B.19}$$

Here the plane wave state $|\phi\rangle$ is not a specially chosen state and also the plane wave can form a complete
space. Therefore (B.19) infers:

$$T = V + VG_0T \tag{B.20}$$

Furthermore, the scattering amplitude given by (B.14) can be further written as:

$$f(\mathbf{k}',\mathbf{k}) = -\frac{1}{4\pi}\frac{2m}{\hbar^2}(2\pi)^3\langle\mathbf{k}'|T|\mathbf{k}\rangle \tag{B.21}$$

Therefore the transition operator T is sufficient to determine the scattering amplitude $f(\mathbf{k}',\mathbf{k})$. To solve the transition operator T, it should be noticed that (B.20) can be written in an iterative way:

$$T = V + VG_0V + VG_0VG_0V + \cdots \tag{B.22}$$

which is called the *Born series*. Accordingly, the scattering amplitude $f(\mathbf{k}',\mathbf{k})$ can be decomposed as:

$$f(\mathbf{k}',\mathbf{k}) = \sum_{1}^{\infty} f^{(n)}(\mathbf{k}',\mathbf{k}) \tag{B.23}$$

where each term is in correspondence with that in (B.22), e.g.:

$$f^{(1)} = -\frac{1}{4\pi}\frac{2m}{\hbar^2}(2\pi)^3\langle\mathbf{k}'|V|\mathbf{k}\rangle \tag{B.24}$$

$$f^{(2)}(\mathbf{k}',\mathbf{k}) = -\frac{1}{4\pi}\frac{2m}{\hbar^2}(2\pi)^3\langle\mathbf{k}'|VG_0V|\mathbf{k}\rangle \tag{B.25}$$

$$\vdots$$

Taking the second term $f^{(2)}$ as an example, it can be further calculated:

$$\begin{aligned} f^{(2)}(\mathbf{k}',\mathbf{k}) &= -\frac{1}{4\pi}\frac{2m}{\hbar^2}(2\pi)^3\int d^3x'\int d^3x''\langle\mathbf{k}'|\mathbf{x}'\rangle\langle\mathbf{x}'|VG_0V|\mathbf{x}''\rangle\langle\mathbf{x}''|\mathbf{k}\rangle \\ &= -\frac{1}{4\pi}\frac{2m}{\hbar^2}(2\pi)^3\int d^3x'\int d^3x''\langle\mathbf{k}'|\mathbf{x}'\rangle V(\mathbf{x}')\langle\mathbf{x}'|G_0|\mathbf{x}''\rangle V(\mathbf{x}'')\langle\mathbf{x}''|\mathbf{k}\rangle \\ &= -\frac{1}{4\pi}\frac{2m}{\hbar^2}(2\pi)^3\int d^3x'\int d^3x''e^{-i\mathbf{k}'\cdot\mathbf{x}'}V(\mathbf{x}')\big[\frac{2m}{\hbar^2}G(\mathbf{x}',\mathbf{x}'')\big]V(\mathbf{x}'')e^{i\mathbf{k}\cdot\mathbf{x}''} \end{aligned} \tag{B.26}$$

By inspecting (B.26) from right to the left, it can be found that the second term of the Born series can be viewed as a two-step scattering process. First of all, the incoming plane wave interacts with the potential located at $\mathbf{x}''$ after which the scattered wave propagates to $\mathbf{x}'$ through the free propagator $G(\mathbf{x}',\mathbf{x}'')$. Then the scattered wave further interacts with the potential located at $\mathbf{x}'$ and propagates away in the direction of $\mathbf{k}'$.
From the Born series expansion of the transition operator T (thus the scattering amplitude), one can see the basic idea of multiple scattering. The idea here will be further extended to the scattering problem in real complex atomic structures, which will be addressed later on when discussing the implementation of such multiple scattering treatment in FEFF.

B.1.4 Partial-wave expansion

To further calculate the scattering amplitude given by (B.21), the partial-wave expansion method is crucial. In practice, the partial-wave expansion is based on the representation changing from the momentum space (as given in (B.21)) to the spherical-wave state (i.e. the $|E,l,m\rangle$ representation), employing the spherical expansion of the incident plane wave. Detailed derivations can be found in Chapter-7 of Sakurai's book [1], and here is only listed the main results:

$$\langle\mathbf{k}|E,l,m\rangle = \frac{\hbar}{\sqrt{mk}}\delta\big(E-\frac{\hbar^2k^2}{2m}\big)Y_l^m(\hat{\mathbf{k}}) \tag{B.27}$$

$$\langle\mathbf{x}|E,l,m\rangle = \frac{i^l}{\hbar}\sqrt{\frac{2mk}{\pi}}j_l(kr)Y_l^m(\hat{\mathbf{r}}) \tag{B.28}$$

$$\frac{e^{i\mathbf{k}\cdot\mathbf{x}}}{(2\pi)^{3/2}} = \frac{1}{(2\pi)^{3/2}}\sum_l(2l+1)i^l j_l(kr)P_l(\hat{\mathbf{k}}\cdot\hat{\mathbf{r}}) \tag{B.29}$$

where Y_l^m is the spherical harmonics indexed by (l,m), j_l is the spherical Bessel function of the first kind of order l, and P_l is the Legendre polynomials of order l. Based on the representation transformation expression from (B.27) to (B.29), the scattering amplitude $f(\mathbf{k}',\mathbf{k})$ can be further given in the spherical-wave basis. Here before the following discussion,

it is important to introduce a crucial assumption – spherically symmetric scattering potential, which is actually one of the two main assumptions in the muffin-tin approximation as mentioned at the beginning of this chapter. With the spherically symmetric potential, the transition operator will then be independent of m in the $|E,l,m\rangle$ representation, or in another word, T commutes with L^2. Based on such assumption, $f(\mathbf{k}^{'},\mathbf{k})$ can be calculated in the $|E,l,m\rangle$ representation:

$$\begin{aligned}
f(\mathbf{k}^{'},\mathbf{k}) &= -\frac{1}{4\pi}\frac{2m}{\hbar^2}(2\pi)^3\langle\mathbf{k}^{'}|T|\mathbf{k}\rangle \\
&= -\frac{1}{4\pi}\frac{2m}{\hbar^2}(2\pi)^3\sum_l\sum_m\sum_{l'}\sum_{m'}\int dE\int dE^{'}\langle\mathbf{k}^{'}|E^{'}l^{'}m^{'}\rangle\langle E^{'}l^{'}m^{'}|T|Elm\rangle\langle Elm|\mathbf{k}\rangle \\
&= -\frac{1}{4\pi}\frac{2m}{\hbar^2}(2\pi)^3\sum_l\sum_m\sum_{l'}\sum_{m'}\int dE\int dE^{'}\Big[\frac{\hbar}{\sqrt{mk^{'}}}\delta(E^{'}-\frac{\hbar^2k^{'2}}{2m})Y_l^{m^{'}*}(\hat{\mathbf{k}}^{'})\Big] \\
&= \times T_l(E,E^{'})\delta_{mm'}\Big[\frac{\hbar}{\sqrt{mk}}\delta(E-\frac{\hbar^2k^2}{2m})Y_l^m(\hat{\mathbf{k}})\Big] \\
&= -\frac{1}{4\pi}\frac{2m}{\hbar^2}(2\pi)^3\frac{\hbar^2}{mk}\sum_l\sum_m T_l(E)\Big|_{E=\hbar^2k^2/2m}Y_l^m(\hat{\mathbf{k}}^{'})Y_l^{m*}(\hat{\mathbf{k}}) \\
&= -\frac{4\pi^2}{k}\sum_l\sum_m T_l(E)\Big|_{E=\hbar^2k^2/2m}Y_l^m(\hat{\mathbf{k}}^{'})Y_l^{m*}(\hat{\mathbf{k}})
\end{aligned} \tag{B.30}$$

Here for the derivation, it was assumed the scattering is elastic, i.e. $E=\hbar^2k^2/2m=\hbar^2k^{'2}/2m=E^{'}$, and also the orthogonality of the spherical harmonics was applied. Furthermore, if taking the incident wave propagation direction $\hat{\mathbf{k}}$ as the positive z-direction of the selected coordinate system, $Y_l^m(\hat{\mathbf{k}})$ is given as:

$$\begin{aligned}
Y_l^m(\hat{\mathbf{k}}) &= \sqrt{\frac{2l+1}{4\pi}}P_l(cos0)\delta_{m0} \\
&= \sqrt{\frac{2l+1}{4\pi}}\delta_{m0}
\end{aligned} \tag{B.31}$$

The δ function in (B.31) indicates that only the terms containing $m=0$ contributes, therefore if taking $\theta=\angle(\mathbf{k}^{'},\mathbf{k})$, the other spherical harmonics term in (B.30) can be given as:

$$Y_l^0(\hat{\mathbf{k}}^{'}) = \sqrt{\frac{2l+1}{4\pi}}P_l(cos\theta) \tag{B.32}$$

Then the scattering amplitude can be further given as:

$$
\begin{aligned}
f(\mathbf{k}^{'},\mathbf{k}) &= -\frac{4\pi}{k}\sum_{l} T_l(E)\sqrt{\frac{2l+1}{4\pi}}\sqrt{\frac{2l+1}{4\pi}}P_l(cos\theta) \\
&= \sum_{l=0}^{\infty}(2l+1)\Big[-\frac{\pi T_l(E)}{k}\Big]P_l(cos\theta) \\
&= \sum_{l=0}^{\infty}(2l+1)f_l(k)P_l(cos\theta) = f(\theta)
\end{aligned}
\tag{B.33}
$$

where the ***partial-wave scattering amplitude*** $f_l(k)$ is defined as:

$$
f_l(k) = -\frac{\pi T_l(E)}{k} \tag{B.34}
$$

Here the importance of introducing $f_l(k)$ can be reflected when looking at the scattered wave at large distances. Based on the spherical expansion of the plane, the asymptotic behavior of the spherical Bessel function j_l and also the expression for $f(\theta)$ given in (B.33), the scattered wave (B.13) is given as (for detailed derivation, refer to (7.6.8) in Sakurai's book [1]):

$$
\langle \mathbf{x}|\psi^{(+)}\rangle \overset{\text{large r}}{=} \frac{1}{(2\pi)^{3/2}}\sum_{l}(2l+1)\frac{P_l}{2ik}\Big[[1+2ikf_l(k)]\frac{e^{ikr}}{r} - \frac{e^{-i(kr-l\pi)}}{r}\Big] \tag{B.35}
$$

It can be seen from (B.35) that if without the scattering potential, the incoming plane wave can be decomposed to a series spherically outgoing and back-coming components. The existing of the scattering potential modulates the outgoing spherical components by changing the amplitude:

$$
1 \rightarrow 1+2ikf_l(k) \tag{B.36}
$$

without influencing the back-coming components. Here the important of the partial-wave scattering amplitude $f_l(k)$ (or $f(\theta)$) should be highlighted, since it is directly correlated to the modulation for the outgoing spherical components.

B.1.5 Phase shift

In the time-independent frame, the incoming and outgoing flux during the scattering process should be equal to each other to keep the net flux 0:

$$
\oint \mathbf{j}\cdot d\mathbf{S} = 0 \tag{B.37}
$$

Considering (B.35), if defining:

$$S_l(k) \equiv 1 + 2ikf_l(k) \tag{B.38}$$

there should be:

$$|S_l(k)| = 1 \tag{B.39}$$

which further indicates that $S_l(k)$ can be written in the following way:

$$S_l(k) = e^{2i\delta_l(k)} \tag{B.40}$$

Then $f_l(k)$ can be worked out based on (B.38) and (B.40):

$$\begin{aligned} f_l(k) &= \frac{e^{2ik\delta_l(k)} - 1}{2ik} \\ &= \frac{cos[2\delta_l(k)] + isin[2\delta_l(k) - 1]}{2ik} \\ &= \frac{1 - 2sin^2\delta_l(k) + 2isin[\delta_l(k)]cos[\delta_l(k)] - 1}{2ik} \\ &= \frac{2sin[\delta_l(k)]\Big[icos[\delta_l(k)] - sin[\delta_l(k)]\Big]}{2ik} \\ &= \frac{e^{i\delta_l(k)}sin[\delta_l(k)]}{k} \end{aligned} \tag{B.41}$$

Finally, the full scattering amplitude is given as:

$$\begin{aligned} f(\theta) &= \sum_{l=0}^{\infty}(2l+1)f_l(k)P_l(cos\theta) \\ &= \frac{1}{k}\sum_{l=0}^{\infty}(2l+1)e^{i\delta_l(k)}sin[\delta_l(k)]P_l(cos\theta) \end{aligned} \tag{B.42}$$

where the real quantity $\delta_l(k)$ is defined as the ***phase shift***. Here it should be noticed that based on the priciple of zero net flux (which promises the definition (B.38) and the following equation (B.39)), the only influence (at large distances) of the scattering potential is to change to the phase of the outgoing spherical wave – thus reflecting the importance of the phase shift (of the partial wave) $\delta_l(k)$ defined here.

B.2 Scattering theory in FEFF

B.2.1 Basic theoretical formulation

First of all, the Fermi's golden rule for calculating the absorption coefficient given by (3.15) could be written in a more accurate way, considering the contributions from all possible final states [2]:

$$\mu(E) \propto \sum_{f}^{E_f > E_F} |\langle f|\varepsilon\hat{\cdot}\mathbf{r}|i\rangle|^2 \delta(E - E_f) \tag{B.43}$$

$$= \sum_{f}^{Ef > E_F} \langle i|\hat{\varepsilon}^* \cdot \mathbf{r}|f\rangle \delta(E - E_f) \langle f|\hat{\varepsilon} \cdot \mathbf{r}|i\rangle \tag{B.44}$$

where E_F refers to the Fermi level, and also the dipole approximation is assumed here. If writing the final states related term in (B.44) compactly as [3]:

$$-\frac{1}{\pi} Im\, G = \sum_{f}^{E_f > E_F} |f\rangle \delta(E - E_f) \langle f| \tag{B.45}$$

then the absorption coefficient can be written as [2, 3]:

$$\mu(E) = -\frac{1}{\pi} Im \langle|\hat{\varepsilon}^* \cdot \mathbf{r} G \hat{\varepsilon} \cdot \mathbf{r}|i\rangle \Theta(E - E_F) \tag{B.46}$$

where Θ is the Heaviside step function assuring that the cross section is non-zero only above the Fermi level E_F [2]. Considering the specific form of the one-particle Green's function corresponding to the final state Schrödinger equation with the Hamiltonian $H = H_0 + V_{int} + \delta V$:

$$G(\mathbf{r}, \mathbf{r}'; E) = \sum_{n} \frac{\psi_n(\mathbf{r}')\psi_n^*(\mathbf{r})}{E - E_n + i\eta} \tag{B.47}$$

it can be seen that the function G in (B.45) is just the Green's function corresponding to the final state. For the full Hamiltonian mentioned above, H_0 refers to the kinetic energy of the free propagating plane wave, V_{int} is the interstitial potential energy and δV is the scattering potential around atoms in a material. Here V_{int} is flat and δV is spherically symmetric within the muffin-tin potential approximation. In Fig. B.1, it was presented the comparison between the full potential and the muffin-tin potential. Detailed discussion about the building up of the muffin-tin potential will be presented in the end of this section as one of the final remarks.

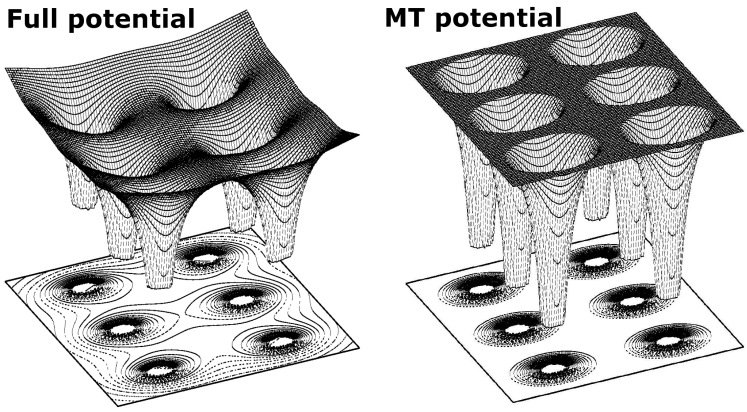

Fig. B.1 Depiction of the full potential and the muffin-tin potential. Reproduced from Ref. [4].

With equation-(B.46), the kernel of the absorption coefficient calculation then resides in the full, one-electron Green's function in the presence of the scattering potential. To solve the full Green's function, the Lippmann-Schwinger equation-(B.4) should be revisited, and considering the definition of the transition operator T given in (B.17), one could have:

$$\begin{aligned} |\psi\rangle &= |\phi\rangle + G_0 V |\psi\rangle \\ &= |\phi\rangle + G_0 T |\phi\rangle \end{aligned} \tag{B.48}$$

Owing to the linearity of the Green's function method, the full Green's propagator could be given as:

$$G = G_0 + G_0 T G_0 \tag{B.49}$$

according to (B.48), and (B.49) here is called the *Dyson equation*. Furthermore, if considering the Born expansion of the transition operator T, together with the corresponding physical explanation for each term of the Born series – the stepwise scattering, the transition operator T here corresponding to the multiple sites scattering problem could be written as:

$$T = t + tG_0t + tG_0tG_0t + \cdots \tag{B.50}$$

in analogy with (B.22) while t here represents the single site scattering matrix (i.e. the lower case 't' here is the upper case 'T' in B.1, e.g. in equation-(B.22)). Putting (B.50) into the Dyson equation (B.49), one could have the multiple expansion:

$$G = G_0 + G_0tG_0 + G_0tG_0tG_0 + \cdots \tag{B.51}$$

Based on equation (B.51), the idea of the stepwise scattering could be recast here in terms of the multiple sites scattering. Taking the second term in (B.51) as an example, once the photoelectron is excited, it propagates to a scatterer (atomic site) through the free-electron propagator G_0, which corresponds to the flat interstitial potential V_{int} within the frame of the muffin-tin approximation mentioned earlier. The following t represents the scattering effect

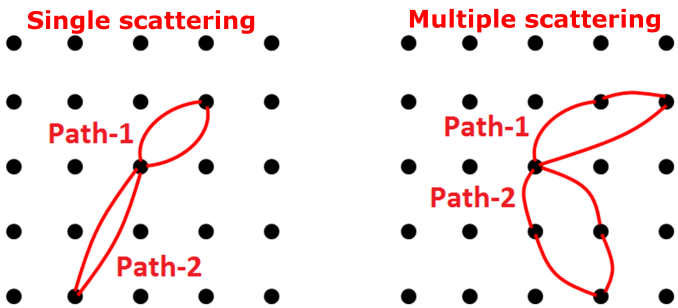

Fig. B.2 The illustration for the single and multiple scattering paths.

of potential located at the scatterer (atomic site), after which the photoelectron travels back to the absorber, again, through the free propagator G_0. Actually, the second term in (B.51) refers to all the single-leg scattering events described above. Similarly, all the remaining terms in (B.51) then correspond to the contributions from the multiple-legs scattering. Here the single and multiple scattering paths are depicted in Fig. B.2. Moreover, the importance of the muffin-tin approximation should be highlighted, which makes it convenient to carry out the Born expansion for calculating the full propagator G, with the free propagator G_0 as the connector between different scattering events.

To further work out the full propagator given by (B.51), partial-wave expansion method could used to calculate the matrix t at each scattering site. However, it should be pointed out that the partial-wave method relies on the assumption that the incoming wave is free propagating plane wave. As a matter of fact, in the multiple-site scattering problem, once the excited photoelectron is scattered at one site, the outgoing wave is no longer plane wave (instead, it should be spherical, according to (B.13)). Therefore in principle the partial wave method cannot be directly applied to calculate the single site scattering matrix t in the continuous multiple-scattering problem. To deal with such difficulty, one of the approaches is based on the plane wave approximation (PWA), where all the outgoing spherical waves are approximated as plane waves.

Within the PWA, the scattering matrix t at each single site is given as (in spherical-wave state representation):

$$t_l = e^{i\delta_l} sin(\delta_l) \tag{B.52}$$

where δ_l refers to the phase shift of the partial wave. As mentioned in **??**, δ_l should be the function of k, and here for convenience the variable k is eliminated (the same goes as following). Accordingly, the single site scattering amplitude is given as:

$$f(\theta) = \sum_l (2l+1) t_l P_l(cos\theta) \tag{B.53}$$

which is a bit different (by a factor k) from the usual definition (B.42) [5]. Once the single site scattering matrix t is available (i.e. the single site scattering amplitude is available), the full propagator G can be built up according to (B.51). Then if only focusing on the scattering effect for the moment, the polarization-averaged XAFS signal $\chi^{N-1}(k)$ corresponding to a multiple-scattering path with N legs (i.e. $N-1$ scatters) can be given as [5]:

$$\begin{aligned}\chi^{(N-1)}(k) &= Im\Big[\frac{e^{2i\delta_1}}{2l+1}\sum_m G^{(N-1)}_{lm,lm}(\mathbf{R}_1,\cdots,\mathbf{R}_N)\Big] \\ &= Im\Big[\frac{e^{i(\rho_1+\rho_2+\cdots+\rho_N)+2i\delta_1}}{\rho_1\rho_2\cdots\rho_N}(\hat{\rho}_1\cdot\hat{\rho}_N) f_{N-1}(\theta_{N-1})\cdots f_2(\theta_2) f_1(\theta_1)\Big]\end{aligned} \tag{B.54}$$

where k is the photoelectron wave number, $\mathbf{r}_i = k(\mathbf{R}_{i+1} - \mathbf{R}_i)$ is the dimensionless bond vector, and $\theta_i = cos^{-1}(\hat{\mathbf{R}}_i \cdot \hat{\mathbf{R}}_{i+1})$ is the scattering angle at site i. The terms like $e^{i\rho_i}/\rho_i$ corresponds to the free propagator G_0 in (B.51), $f_i(\theta_i)$ is just the aforementioned plane-wave scattering amplitude at the ith scatterer, which corresponds to the single site scattering matrix t in (B.51). Hereby, there are two more aspects to point out about (B.54). The first one is that $\chi^{(N-1)}(k)$ is obtained by calculating the average value of the propagator G matrix over the spherical-wave basis (i.e. the $|E,l,m\rangle$ representation). The second aspect is that for the calculation of G matrix average value, the complete spherical-wave basis could be inserted in between each two adjacent matrices in the N-legs scattering term in (B.51). Therefore the product of matrices then becomes the simple product over scattering amplitude $f_i(\theta_i)$ as given in (B.54).

The theoretical description here based on the PWA works well for energy regime far beyond the absorption edge. However as the photoelectron energy approaches the edge, the curved-wave effects become increasingly important, therefore the validity of the PWA breaks down. To solve the problem of PWA, Rehr and Albers [5] showed that the form of the multiple scattering expansion (B.54) could be kept if replacing the single site scattering amplitude

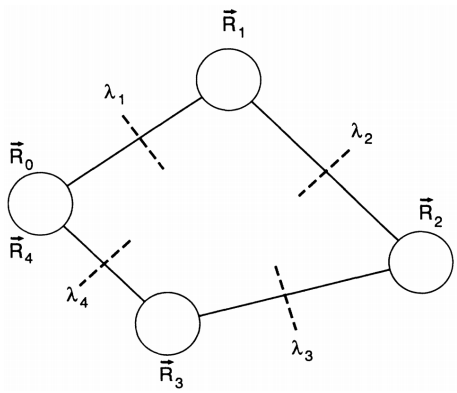

Fig. B.3 Illustration of four-leg multiple scattering. Circles represent the scatterers, and line represents the Green's propagator connecting each two adjacent atoms. λ is the spherical expansion index and the dashed line represents the separable representation of the Green's propagator for each leg. Reproduced from Ref. [5].

$f_i(\theta_i)$ with the corresponding scattering matrix $\mathbf{F}^i$. This was realized by separating the representation of the free propagator G_0 to two parts for each scattering leg, as depicted in Fig. B.3. Detailed mathematical formulation can be found in the above mentioned reference by Rehr and Albers: [5].

Both the approaches mentioned above, no matter following the PWA or beyond PWA, are based on the multiple scattering expansion (i.e. equation-(B.51)). In the near-edge region, however, the expansion series given by (B.51) may or may not converge, even taking the curved-wave effects into consideration following Rehr and Alber's approach [3]. This is where the so-called *full multiple scattering* (FMS) method comes to help. As a matter of fact, the multiple scattering expansion for the Dyson equation given by (B.51) could be recognized as a Taylor series:

$$\begin{aligned} G &= G_0 + G_0 t G_0 + G_0 t G_0 t G_0 + \cdots \\ &= (1 - G_0 t)^{-1} G_0 \end{aligned} \tag{B.55}$$

which provides a direct way to obtain the full propagator G by inversing the $(1 - G_0 t)$ matrix. Such method is equivalent to include the multiple scattering term to the infinite order, therefore is called full multiple scattering. This is important for the calculation of XANES spectra, where the multiple scattering effects play a crucial role. However FMS method is computationally expensive because of the scaling of the matrix inversion. According

to (B.30), when written in the spherical-wave representation, the scale of the single site scattering matrix is determined by:

$$\mathscr{L} = 1+3+5+\cdots+(2l_{max}+1) = l_{max}(l_{max}+1) \tag{B.56}$$

where each term in the sum represents the number of magnetic quantum number m given the angular quantun number l. Considering all the scattering sites, the size of the scattering matrix is:

$$\mathscr{L} = \sum_i l^i_{max}(l^i_{max}+1) \tag{B.57}$$

where i labels the scattering site. In (B.56) and (B.57), the maximum number of angular moment states to be considered is reasonably limited by the pre-set muffin-tin radius R_{MT} [6]:

$$l_{max} \simeq kR_{MT} \tag{B.58}$$

where k is the photoelectron wavenumber. Moreover, the computation memory required scales as the square of the matrix size, and the computation time scales as the cube. Therefore although it is technically possible to carry out the EXAFS calculation using FMS in FEFF, it is, however, computationally prohibited due to the large l_{max} (see (B.58)) far beyond the edge. Furthermore, the multiple scattering effects barely contributes to the EXAFS signal, therefore besides the consideration of computation power bottleneck, it is also not necessary to do the FMS calculation from the perspective of physics.

Hereby, the main theoretical framework of embedding quantum scattering theory in FEFF, including the multiple scattering expansion and FMS method, was briefly covered. As the final remarks before the end of this section, there are several more aspects that worth mentioning, and the first one as following is about the building up of scattering potential in FEFF.

B.2.2 Scattering potential in FEFF

In FEFF, the free atomic potentials of each atomic type are initially calculated using a relativistic Dirac-Fock atom code. The overall potential is then built up by overlapping all the individual potentials following the Mattheiss prescription, i.e. the muffin-tin approximation, as depicted in Fig. B.4.

In Fig. B.4, the solid blue and green circles represents the fixed muffin-tin radius for the corresponding atoms, and the dashed circle outside the solid one refers to the total spherically averaged potential of each atom. The red area then indicates the interstitial region where the potential is set to be flat. Here for the choice of the muffin-tin radius, there are several

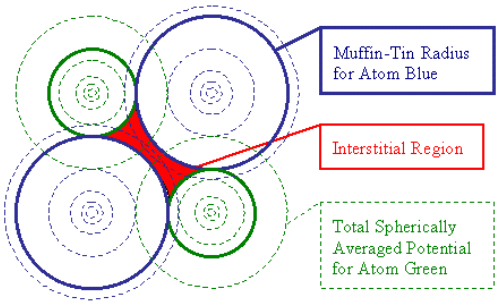

Fig. B.4 Illustration for the building up of the muffin-tin potential in 2D space. The idea for 3D situation is similar. Reproduced from Re. [7].

available criteria to follow, including the atomic, Pauling and ionic radii, etc. of atoms. In FEFF, the Norman radii is used – the charge inside the muffin-tin radius equals to that of the atom [3]. In general, the muffin-tin spheres touch, but do not overlap with each. However in FEFF, this is not the case and the muffin-tin spheres are set to overlap by default, since '*it typically leads to better results than non-overlapping muffin-tin spheres*' [8]. To further account for the exchange correlation in the system, the Hedin-Lundqvist potential is introduced in FEFF calculation.

From FEFF8, the scattering potential can be determined in a self-consistent way. Based on the initial muffin-tin potential built up following the approach mentioned above, the phase shift δ (see the following discussion about the determination of phase shift) and therefore the scattering amplitude f (or the scattering matrix F) can be obtained. This further allows the calculation of the full propagator G and the corresponding fine structure function χ. Accordingly, the new electronic densities of states for atoms can be calculated [9]:

$$\rho_{new} = \rho_0(1+\chi) \tag{B.59}$$

Then the obtained new electronic density can be used as the input potential for the next round of calculation for G and χ. Such cycling calculation will be repeated until the convergence of the obtained electronic density.

B.2.3 Determination of Phase shift, amplitude factor and EMFP

From the discussion through this section, it can be seen that the phase shift is the kernel of the quantum scattering theory and also the FEFF calculation. Once the phase shift is

calculated, it can be used to calculate the scattering amplitude (in the PWA, see (B.42) and (B.53)) or the scattering matrix (beyond the PWA in FEFF). The following calculations, including the full propagator G, the absorption fine structure χ and electronic densities, etc., are all based on the obtained phase shift and scattering amplitude (matrix). In FEFF, based on the pre-determined muffin-tin potential, the Schrödinger equation of the system is then solved separately in each individual region (both the interstitial regions and those surrounding atoms). The phase shift is then obtained by matching the solution at the muffin-tin radius [10].

The passive amplitude factor S_0^2 can be set as the parameter for fitting the experimental EXAFS spectra. In theory, the S_0^2 parameter accounts for the non-perfect overlapping (in real space) between the wavefunctions of the initial and final states [3]. Following this theoretical principle, S_0^2 can be estimated in FEFF, by calculating the square of determinant of overlap integrals for core orbitals calculated with and without core hole [8].

As for another important parameter in XAFS formulation (based on the quantum scattering theory) – EMFP $\lambda(k)$, it is not allowed to be fitted in Artemis. Instead, FEFF will take care of the EMFP theoretically, and in practice the EMFP is determined from the imaginary part of the average interstitial potential [10].

References

[1] J. J. Sakurai. *Modern Quantum Mechanics*. Addison-Wesley Publishing Company, 1994.

[2] B. Ravel. A practical introduction to multiple scattering theory. *J. Alloys Compd.*, 401:118–126, 2005.

[3] G. Bunker. *Introduction to XAFS: A Practical Guide to X-ray Absorption Fine Structure Spectroscopy*. Cambridge University Press, 2010.

[4] DFT electronic structure calculations by muffin tin orbital based basis. http://institute.loni.org/dft2011/documents/TanusriLec1.pdf, July 2011. online; accessed 10-May-2016.

[5] J. J. Rehr and R. C. Albers. Scattering-matrix formulation of curved-wave multiple-scattering theory: application to x-ray-absorption fine structure. *Phys. Rev. B*, 41:8139–8149, 1990.

[6] J. M. Deleon, J. J. Rehr, S. I. Zabinsky, and R. C. Albers. ab initio curved-wave x-ray absorption fine structure. *Phys. Rev. B*, 9:4146–4156, 1991.

[7] Constructing the muffin-tin potential. http://hermes.phys.uwm.edu/projects/elecstruct/mufpot/MP/MP.Theory4.html, April 1999. online; accessed 12-May-2016.

[8] Feff9.6 users' guide. http://leonardo.phys.washington.edu/feff/Docs/feff9/feff90/feff90_users_guide.pdf, February 2013. online; accessed 12-May-2016.

[9] A. L. Ankudinov, B. Ravel, J. J. Rehr, and S. D. Conradson. Real-space multiple-scattering calculation and interpretation of x-ray-absorption near-edge structure. *Phys. Rev. B*, 58:7565–7576, 1998.

[10] *Ab initio* multiple-scattering x-ray absorption fine structure and x-ray absorption near edge structure code. http://www.feffproject.org/FEFF/Docs/feff6/feff6.html#toc2, August 1995. online; accessed 12-May-2016.

Appendix C

Green's function method

In general, Green's function refers to the integral kernel corresponding to certain differential equation. In mathematics, given the differential equation:

$$Lu(x) = f(x) \tag{C.1}$$

where the symbol 'L' represents the differential operation. The idea of Green's function method is to find the integral operation (kernel), i.e. the inverse operation (L^{-1}) of L, corresponding to equation-C.1. Mathematically:

$$\begin{aligned} u(x) &= L^{-1} f(x) \\ &= \int G(x,\xi) f(\xi) d\xi \end{aligned} \tag{C.2}$$

The integral kernel $G(x,\xi)$ is just the Green's function corresponding to equation-C.1. From C.2, it can be seen that the power of Green's function method lies in that once the Green's function corresponding to a certain differential equation (given boundary conditions) can be found, the solution for the unknown function (i.e. $u(x)$ in C.1) is then as straightforward as calculating the integration following C.2. In physics, the Green's function method plays important role in solving problems involving the second-order differential equations, such as the Poisson's equation of electric field, the heat conduction problems, etc. Here following is given an example of the Green's function in the problem of electric field caused by electrostatic charge distribution. As shown in Fig. C.1, the distribution of the electrostatic charge in vacuum space is given as the function ρ. The corresponding Poisson's equation of the system is then given as:

$$\nabla^2 u = -\frac{\rho}{\varepsilon_0} \tag{C.3}$$

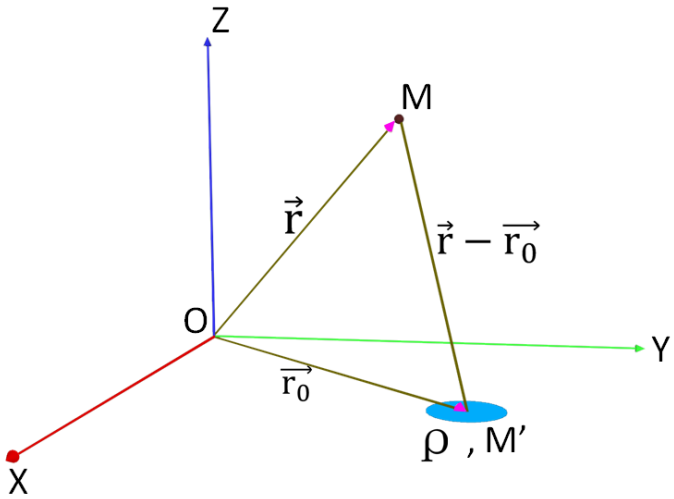

Fig. C.1 The electric field caused by the electrostatic charge distribution in space.

where u is the potential field function in space, and ε_0 is the vacuum permittivity. Given the specific form of the charge distribution function ρ, the potential field of the system can be solved following equation-C.3. Meanwhile, the potential field can be solved in another way by assuming the charge distribution is composed of infinite number of point charges. For the point charge located at $\vec{r}_0$ as illustrated in Fig. C.1, the potential at the field point $\vec{r}$ is given as:

$$G(\vec{r},\vec{r}_0) = \frac{1}{4\pi\varepsilon_0}\frac{1}{|\vec{r}-\vec{r}_0|} \tag{C.4}$$

Then according to the superposition principle, the potential field in space can be given as:

$$\begin{aligned} u(\vec{r}) &= \int_V \frac{\rho(\vec{r}_0)}{4\pi\varepsilon_0|\vec{r}-\vec{r}_0|}dV \\ &= \int_V G(\vec{r},\vec{r}_0)\rho(\vec{r}_0)dV \end{aligned} \tag{C.5}$$

It can be seen from C.5 that the Green's function corresponding to the Poisson's equation-C.3 is just the potential field function of the point charge – C.4. Here it should be pointed out that the discussion given here applies only for the situation of infinite boundary. For other systems with other boundary conditions, the way to obtain the Green's function may not be straightforward. But the basic idea of Green's function method can be seen from the simple situation discussed here.

More examples for the Green's function in various differential equation problems can be found in Ref-[1] and [2]. In this thesis, the FEFF package used for XAFS spectra calculation utilizes Green's function method to deal with the final states Schrödinger equation. Therefore in the following part, the Green's function for the static Schrödinger equation will be briefly discussed based on the summary given by J. Schueler [3]. First of all, considering the inhomogeneous differential equation given in the following general form:

$$[z - L(r)]u(r) = f(r) \tag{C.6}$$

where L is a linear Hermitian operator (e.g. the Hamiltonian operator in Schrödinger equation) with a series of eigenvalue λ_n and the corresponding eigenfunction $\phi_n(r)$, $f(r)$ is the known inhomogeneous term and $u(r)$ is the unknown function to be solved. z here is the introduced complex identity. According to the introduction to the Green's function method given above, the solution for $u(r)$ in equation-C.6 can be given in the following form:

$$u(r) = \begin{cases} \int G(r,r';z)f(r')dr', & z \neq \lambda_n \\ \int G^{\pm}(r,r';z)f(r')dr' + \phi_n(r), & z = \lambda_n \end{cases} \tag{C.7}$$

The first expression in C.7 is just the basic form of the solution given with the Green's function $G(r,r';z)$ as in C.2, while the second expression corresponds to the special situation where $z = \lambda_n$. The following discussion will start from the first expression and the special situation when $z = \lambda_n$ will be mentioned in the end. By putting the solution form given in C.7 (the first expression) into C.6, it can be obtained:

$$\begin{aligned} [z - L(r)]u(r) &= [z - L(r)] \int G(r,r';z)f(r')dr' \\ &= \int [z - L(r)]G(r,r';z)f(r')dr' = f(r) \end{aligned} \tag{C.8}$$

To let the equation-C.8 stand, considering the property of δ function: $\int \delta(x - x_0)f(x) = f(x_0)$, it can be deduced that:

$$[z - L(r)]G(r,r';z) = \delta(r - r') \tag{C.9}$$

Putting C.9 back to C.8, there should be:

$$\int [z - L(r)]G(r,r';z)f(r')dr' = \int f(r')\delta(r - r')dr' = f(r) \tag{C.10}$$

Therefore C.9 is just the equation that the Green's function corresponding to the differential

equation C.6 should satisfy. To solve the equation-C.9, the following relations should be given:

$$L(r)\phi_n(r) = \lambda_n \phi_n(r) \tag{C.11}$$

$$\int_\omega \phi_n^*(r)\phi_m(r)dr = \delta_{mn} \tag{C.12}$$

$$\sum_n \phi_n(r)\phi^*(r^{'}) = \delta(r-r^{'}) \tag{C.13}$$

where

$$\delta(r-r^{'}) = \begin{cases} 0 & (r-r^{'}) \neq 0 \\ \infty & (r-r^{'}) = 0 \end{cases} \tag{C.14}$$

Employing the Bra-Ket representation, the following fundamental relations (and definitions) are also needed:

$$\phi_n(r) = \langle r|n\rangle \tag{C.15}$$

$$\delta(r-r^{'})L(r) \equiv \langle r|L|r^{'}\rangle \tag{C.16}$$

$$G(r,r^{'};z) \equiv \langle r|G(z)|r^{'}\rangle \tag{C.17}$$

$$\langle r|r^{'}\rangle = \delta(r-r^{'}) \tag{C.18}$$

$$\int dr|r\rangle\langle r| = 1 \tag{C.19}$$

Considering C.15 to C.19, the equation-C.9, together with C.11 to C.13 could be given as:

$$(z-L)G(z) = 1 \tag{C.20}$$

$$L|\phi_n\rangle = \lambda_n|\phi_n\rangle \tag{C.21}$$

$$\langle\phi_n|\phi_m\rangle = \delta_{mn} \tag{C.22}$$

$$\sum_n |\phi_n\rangle\langle\phi_n| = 1 \tag{C.23}$$

Here the equivalence of C.20 and C.9 needs some proof. Based on C.20, it can be deduced that:

$$\begin{aligned} \langle r|(z-L)G(z)|r^{'}\rangle &= \langle r|1|r^{'}\rangle \\ &= \langle r|r^{'}\rangle \\ &= \delta(r-r^{'}) \end{aligned} \tag{C.24}$$

For the left-hand side of C.24:

$$\begin{aligned}
\langle r|(z-L)G(z)|r^{'}\rangle &= \langle r|zG(z)|r^{'}\rangle - \langle r|LG(z)|r^{'}\rangle \\
&= zG(r,r^{'};z) - \langle r|LG(z)|r^{'}\rangle \\
&= zG(r,r^{'};z) - \int ds\langle r|L|s\rangle\langle s|G(z)|r^{'}\rangle \\
&= zG(r,r^{'};z) - \int ds\delta(r-s)L(r)\langle s|G(z)|r^{'}\rangle \\
&= zG(r,r^{'};z) - L(r)\langle r|G(z)|r^{'}\rangle \\
&= zG(r,r^{'};z) - L(r)G(r,r^{'};z) \\
&= [z-L(r)]G(r,r^{'};z) \qquad \text{(C.25)}
\end{aligned}$$

Therefore C.20 and C.9 is equivalent, and the Green's function corresponding equation-C.6 can be solved:

$$G(z) = \frac{1}{z-L} \qquad \text{(C.26)}$$

Considering equation-C.23, the solution for the Green's function can be given in the representation of the eigenstates of operator L:

$$G(z) = \frac{1}{z-L}\sum_n |\phi_n\rangle\langle\phi_n| \qquad \text{(C.27)}$$

$$= \sum_n \frac{1}{z-L}|\phi_n\rangle\langle\phi_n| \qquad \text{(C.28)}$$

$$= \sum_n \frac{|\phi_n\rangle\langle\phi_n|}{z-\lambda_n}, \quad z \neq \lambda_n \qquad \text{(C.29)}$$

Here from C.28 to C.29, the Taylor expansion for the operator could be imagined in between the two expressions (therefore the operator L in the denominator of C.28 becomes the corresponding λ_n in C.29). Also it should be noticed that in the final solution for the Green's function C.29, $z = \lambda_n$ are the singular points. The common way to solve the singularity problem is by making the eigenvalue of operator L a bit complex [3]. The corresponding form of the Green's function is defined as:

$$G^{\pm}(r,r^{'};\lambda_n) \equiv \lim_{s\to 0^+} G(r,r^{'};\lambda \pm is) \qquad \text{(C.30)}$$

The corresponding solution for the original differential equation-C.6 could be written in the form of C.7.

Then for the static Schrödinger equation:

$$H\psi = E\psi \Rightarrow [E - H(r)]\psi(r) = 0 \tag{C.31}$$

it is a special case of the differential equation in the general form of C.6, and the following replacement can be made:

$$L(r) \rightarrow H(r) \tag{C.32}$$

$$\lambda_n \rightarrow E_n \tag{C.33}$$

$$z = \lambda \pm is \rightarrow z = E \pm is \tag{C.34}$$

$$\phi_n \rightarrow \psi_n \tag{C.35}$$

Based on the discussion given above, the solution for the time-independent Schrödinger equation can be given as:

$$u(r) = \begin{cases} \int G(r,r^{'};E)f(r^{'})dr^{'}, & E \neq E_n \\ \int G^{\pm}(r,r^{'};E)f(r^{'})dr^{'} + \psi_n(r), & E = E_n \end{cases} \tag{C.36}$$

where the corresponding Green's function is given as:

$$G(r,r^{'};z) = \begin{cases} \sum_n \frac{\psi_n^*(r^{'})\psi_n(r)}{E - E_n}, & E \neq E_n \\ \sum_n \frac{\psi_n^*(r^{'})\psi_n(r)}{E - E_n \pm is}, & E = E_n \end{cases} \tag{C.37}$$

This is just the Green's function corresponding to the time-independent Schrödinger equation, which is the kernel of the XAFS spectra calculation (see B.47 in B.2 of Chapter-4).

References

[1] K. A. Shah. *Mathematical modeling of malignant skin tumor in Human Body*. PhD thesis, Veer Narmad South Gujarat University, November 2011.

[2] Solving nonhomogeneous PDEs (eigenfunction expansions). http://math.kennesaw.edu/~plaval/math4490/fall2009/lesson12.pdf, August 2015. online; accessed 20-May-2016.

[3] Green's functions and their applications to quantum mechanics. https://www.math.washington.edu/~morrow/336_11/papers/jeff.pdf, June 2011. online; accessed 20-May-2016.

Appendix D

Finite difference method

The finite difference method (FDM) is one of the effective ways to numerically solve the partial differential equations, which is widely applied in the area of physics and among others. The basic idea of the FDM approach is to represent the function (to be solved) by its value at certain grid point and the derivatives are approximated by the difference between the function values of the surrounding points. Accordingly the two basic steps for solving the partial differential equation with FDM are:

1) Discretize the domain to be solved and transform the partial differential equation to its corresponding FDM form.

2) Solve the linear equations group to obtain the function values at each grid point.

First of all, the Taylor expansion of the function value at the neighbouring points can be given:

$$f(x_i - h) = f(x_i) - hf^{'}(x_i) + \frac{h^2}{2}f^{''}(x_i) - \frac{h^3}{3!} + \cdots \tag{D.1}$$

$$f(x_i + h) = f(x_i) + hf^{'}(x_i) + \frac{h^2}{2}f^{''}(x_i) + \frac{h^3}{3!} + \cdots \tag{D.2}$$

By ignoring the high order terms, D.1−D.2 will give:

$$f^{'}(x_i) \approx \frac{f(x_i + h) - f(x_i - h)}{2h} \tag{D.3}$$

Similarly the approximation for the first order differential of function $f(x)$ at point x_i in the

forward $[f'_+(x_i)]$ and backward $[f'_-(x_i)]$ can be given as:

$$f'_+(x_i) \approx \frac{f(x_i+h)-f(x_i)}{h} \tag{D.4}$$

$$f'_-(x_i) \approx \frac{f(x_i)-f(x_i-h)}{h} \tag{D.5}$$

Furthermore, D.1+D.2 will give:

$$f''(x_i) \approx \frac{f(x_i+h)-2f(x_i)+f(x_i+h)}{h^2} \tag{D.6}$$

D.3 to D.6 are the mathematical basis of the FDM approach, based on which the differential

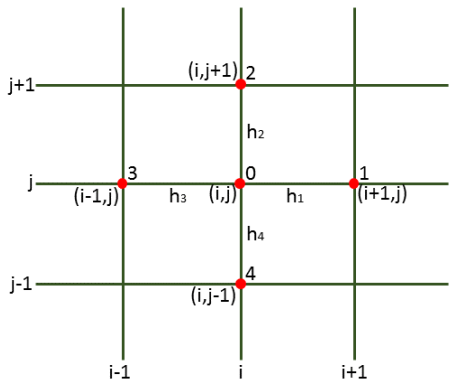

Fig. D.1 Example of the discretization of the domain.

equation can transformed (approximately) to its linear form involving the difference between the function values of neighbouring grid points. An example of discretizing the domain is shown in Fig. D.1. The cross points are the nodes where the differential equation is going to be solved. Taking the node-0 in Fig. D.1 as an example, the Laplacian operator at node-0 can be approximated by the function values of the four nearest neighbouring points in the following way (assuming equidistant grid, i.e. $h_1 = h_2 = h_3 = h_4$):

$$f_3 + f_1 \approx 2f_0 + h^2 f_{xx} \tag{D.7}$$

$$f_4 + f_2 \approx 2f_0 + h^2 f_{yy} \tag{D.8}$$

$$\nabla^2 f \approx \frac{f_1+f_2+f_3+f_4-f_0}{h^2} \tag{D.9}$$

For further discussion about the implementation of the FDM approach, the following general form of partial differential equation in two dimension will be considered:

$$\frac{\partial^2\phi}{\partial x^2}+\frac{\partial^2 y}{\partial y^2}+f(x,y)\phi=q(x,y) \tag{D.10}$$

Given any partial differential equation, the corresponding boundary conditions (BC) are necessary to obtain certain solutions, and in general, the BC can be compactly written as:

$$\phi|_G+g_1(s)\frac{\partial\phi}{\partial n}\Big|_G=g_2(s) \tag{D.11}$$

where $g_1(s)$ and $g_2(s)$ are the function defined at the boundary of the domain. According to its different form, the BC can be divided into three types:

(1) The first one, also called Dirichlet type BC ($g_1(s)=0$, $g_2(s)\neq 0$):

$$\phi|_G=g(s) \tag{D.12}$$

(2) The second one, also called Neumann type BC ($g_1(s)\neq 0$, $g_2(s)=0$):

$$\frac{\partial\phi}{\partial n}\Big|_G=g(s) \tag{D.13}$$

(3) The third one is the mixed type ($g_1(s)\neq 0$, $g_2(s)\neq 0$)

Following the above discussion, to solve equation-D.11 provided specific BC, the first step is to evaluate the differential function at each grid point by the function values at the neighbouring points. Taking node-0 in Fig. D.1 as the example, the corresponding first and second order differential function values can be written as [1]:

$$\left(\frac{\partial\phi}{\partial x}\right)_0\approx\frac{h_3^2(\phi_1-\phi_0)-h_1^2(\phi_3-\phi_0)}{h_1h_3(h_1+h_3)} \tag{D.14}$$

$$\left(\frac{\partial^2\phi}{\partial x^2}\right)_0\approx 2\frac{h_3(\phi_1-\phi_0)+h_1(\phi_3-\phi_0)}{h_1h_3(h_1+h_3)} \tag{D.15}$$

$$\left(\frac{\partial\phi}{\partial y}\right)_0\approx\frac{h_4^2(\phi_2-\phi_0)-h_2^2(\phi_4-\phi_0)}{h_2h_4(h_2+h_4)} \tag{D.16}$$

$$\left(\frac{\partial^2\phi}{\partial y^2}\right)_0\approx 2\frac{h_4(\phi_2-\phi_0)+h_2(\phi_4-\phi_0)}{h_2h_4(h_2+h_4)} \tag{D.17}$$

By putting D.15 and D.17 into D.10, the differential equation at each node (i,j) can be written as:

$$(\nabla^2\phi)_{i,j}=2\Big[\frac{h_3(\phi_{i+1,j}-\phi_{i,j})+h_1(\phi_{i-1,j}-\phi_{i,j})}{h_1h_3(h_1+h_3)}$$

$$+\frac{h_4(\phi_{i+1,j}-\phi_{i,j})+h_2(\phi_{i-1,j}-\phi_{i,j})}{h_2h_4(h_2+h_4)}\Big]+f_{i,j}\phi_{i,j}$$
$$=q_{i,j} \tag{D.18}$$

When $h_1=h_2=h_3=h_4=h$, the equation-D.10 can be given in its FDM form:

$$\phi_{i+1,j}+\phi_{i-1,j}+\phi_{i,j+1}+\phi_{i,j-1}+(h^2f_{i,j}-4)\phi_{i,j}=h^2q_{i,j} \tag{D.19}$$

Considering the Dirichlet type of BC (for the simplicity of discussion), the partial differential equation-D.10 together with the corresponding BC then becomes the following group of linear equations which contains the value of the function ϕ at each node point as the unknowns:

$$\phi_{i,j}-\frac{1}{4-h^2f_{i,j}}(\phi_{i+1,j}+\phi_{i-1,j}+\phi_{i,j+1}+\phi_{i,j-1})=\frac{h^2}{4-h^2f_{i,j}}q_{i,j} \tag{D.20}$$

$$\phi_{i,j}=q_{i,j}, \quad \text{at the boundary} \tag{D.21}$$

For the discretization, it is further assumed that the domain is divided into N equal sections in both the x and y directions. Also for the convenience of discussion, it is assumed that all the boundary points are located at the grid points. To directly solve the group of equations given by D.20 and D.21, it is convenient to write them in matrix form. For simplicity, $f(x,y)$ in the original equation-D.10 is assumed to be 0, i.e. $f_{i,j}$ in D.20 is 0.
By defining:

$$\phi_j=\begin{bmatrix}\phi_{1,j}\\ \phi_{2,j}\\ \vdots\\ \phi_{N-1,j}\end{bmatrix}, \qquad q_j=-\frac{h^2}{4}\begin{bmatrix}q_{1,j}\\ q_{2,j}\\ \vdots\\ q_{N-1,j}\end{bmatrix} \tag{D.22}$$

and denoting:

$$\Phi=\begin{bmatrix}\phi_1\\ \phi_2\\ \vdots\\ \phi_{N-1}\end{bmatrix}, \qquad B=\begin{bmatrix}b_1\\ b_2\\ \vdots\\ b_{N-1}\end{bmatrix} \tag{D.23}$$

where the column matrix b is the modified version of column matrix q, for example the first

two components of b is given as:

$$b_1 = -\frac{1}{4}\begin{bmatrix} h^2 q_{1,1} - g_{0,1} - g_{1,0} \\ h^2 q_{2,1} - g_{2,0} \\ \vdots \\ h^2 q_{N-1,1} - g_{N-1,1} - q_{N-1,0} \end{bmatrix} \tag{D.24}$$

$$b_2 = -\frac{1}{4}\begin{bmatrix} h^2 q_{1,2} - g_{0,2} \\ h^2 q_{2,2} \\ \vdots \\ h^2 q_{N-1,2} - q_{N,2} \end{bmatrix} \tag{D.25}$$

then the group of equations given by D.20 and D.21 can be written in a compact way:

$$K\Phi = B \tag{D.26}$$

The matrix K in D.26 is given as:

$$K = \begin{bmatrix} G & -I/4 & \cdots & 0 \\ -I/4 & G & -I/4 & \vdots \\ \vdots & \ddots & \ddots & -I/4 \\ 0 & \cdots & -I/4 & G \end{bmatrix} \tag{D.27}$$

where I represents the unit matrix of order $(N-1)^2$, and G is matrix of order $(N-1)^2$ given by:

$$G = \begin{bmatrix} 1 & -1/4 & \cdots & 0 \\ -1/4 & 1 & -1/4 & \vdots \\ \vdots & \ddots & \ddots & -1/4 \\ 0 & \cdots & -1/4 & 1 \end{bmatrix} \tag{D.28}$$

Here to demonstrate the equivalence of D.26 and D.10, one can take the first component of the column matrix on both sizes of D.26 as an example:

$$G\phi_1 - \frac{1}{4} I\phi_2 = b_1 \tag{D.29}$$

Then by putting G (D.28), I, ϕ_1 and ϕ_2 (D.22) and b_1 (D.24) into D.29, one gets the following

matrix equation:

$$\begin{bmatrix} 1 & -1/4 & \cdots & 0 \\ -1/4 & 1 & -1/4 & \vdots \\ \vdots & \ddots & \ddots & -1/4 \\ 0 & \cdots & -1/4 & 1 \end{bmatrix} \begin{bmatrix} \phi_{1,1} \\ \phi_{2,1} \\ \vdots \\ \phi_{N-1,1} \end{bmatrix} - \frac{1}{4} \begin{bmatrix} 1 & 0 & \cdots & 0 \\ 0 & 1 & \ddots & \vdots \\ \vdots & \ddots & \ddots & 0 \\ 0 & \cdots & 0 & 1 \end{bmatrix} \begin{bmatrix} \phi_{1,2} \\ \phi_{2,2} \\ \vdots \\ \phi_{N-1,2} \end{bmatrix}$$
$$= \frac{1}{4} \begin{bmatrix} h^2 q_{1,1} - g_{0,1} - g_{1,0} \\ h^2 q_{2,1} - g_{2,0} \\ \vdots \\ h^2 q_{N-1,1} - g_{N-1,1} - q_{N-1,0} \end{bmatrix} \tag{D.30}$$

Here it should be pointed out that in D.27, D.28 and D.30, all the eclipsed elements are 0. Again, taking the first component of the column matrix on both sides of D.30 as an example:

$$\phi_{1,1} - \frac{1}{4}\phi_{2,1} - \frac{1}{4}\phi_{1,2} = -\frac{1}{4}h^2 q_{1,1} + \frac{1}{4}g_{0,1} + \frac{1}{4}g_{1,0} \tag{D.31}$$

By rearranging D.31, one gets:

$$g_{0,1} + \phi_{2,1} + g_{1,0} + \phi_{1,2} + 4\phi_{1,1} = h^2 q_{1,1} \tag{D.32}$$

This is just the combination of D.20 and D.21 at the node point of $(1,1)$, from which one can see the equivalence between the matrix equation D.26 and equations group composed of D.20 and D.21.

Based on the matrix equation-D.26, the solution for the function $\phi(x,y)$ at each node point can be directly given as:

$$\Phi = K^{-1}B \tag{D.33}$$

which involves the inversion of matrix K. Whereas in practice, the size of matrix K may be quite large. In that case if matrix K is not sparse it will be difficult to directly calculate the inverse. There are several alternative methods to solve the equations-D.20 and D.21, including Monte Carlo method, direct iteration method, Gauss–Seidel iteration method and successive over-relaxation method, which will not be covered in this thesis. More details can be found in Ref-[1] and [2].

References

[1] Finite difference method (in chinese). http://www.bb.ustc.edu.cn/jpkc/xiaoji/jswl/skja/chapter4.pdf, 2005. online; accessed 21-May-2016.

[2] Finite difference methods for differential equations. http://disciplinas.stoa.usp.br/pluginfile.php/41896/mod_resource/content/1/LeVeque%20Finite%20Diff.pdf, September 2005. online; accessed 21-May-2016.

Appendix E

MD2FEFF Codes

The MD2FEFF program was written in Fortran 90/95. The main flowchart is presented in Fig. E.1, and separate files containing subroutines responsible for different functions are also shown (indicated by dashed line). For speeding up the program, the FEFF calculation for each single cluster is designed to be carried out in parallel. Here the shared-memory approach OPENMP based on multithread processing was utilized for parallelization. The bash script responsible for executing FEFF calculation is generated on-the-run by the 'main.f90' routine (the main program file for MD2FEFF). For the FEFF calculation result, the configuration average is taken over all results from each individual cluster. Also the step-wise average is taken over all previous steps (including the current step) to simulate the dynamic disorder of the system. The reading-in of all the FEFF calculation results is also carried out in parallel (the 'read_xmu.f90' file as shown in Fig. E.1). For comparing the difference between the calculation and experimental data, the two sets of data should be interpolated to the same grid. This was realized using a Fortran interpolation library, the details of which will be described in the following. The structural evolution was carried using the MD simulation package DL_POLY_4. Moreover, all the global variables and parameters are included in a separate file named 'defs.h'.
Here following are all the Fortran program files of MD2FEFF code, and for saving space, the program files are stored online in Ubuntu pastebin, the links of which are given following each file name as following:

- main.f90 → Ref. [1]
- fileio.f90 → Ref. [2]
- pre_feff.f90 → Ref. [3]

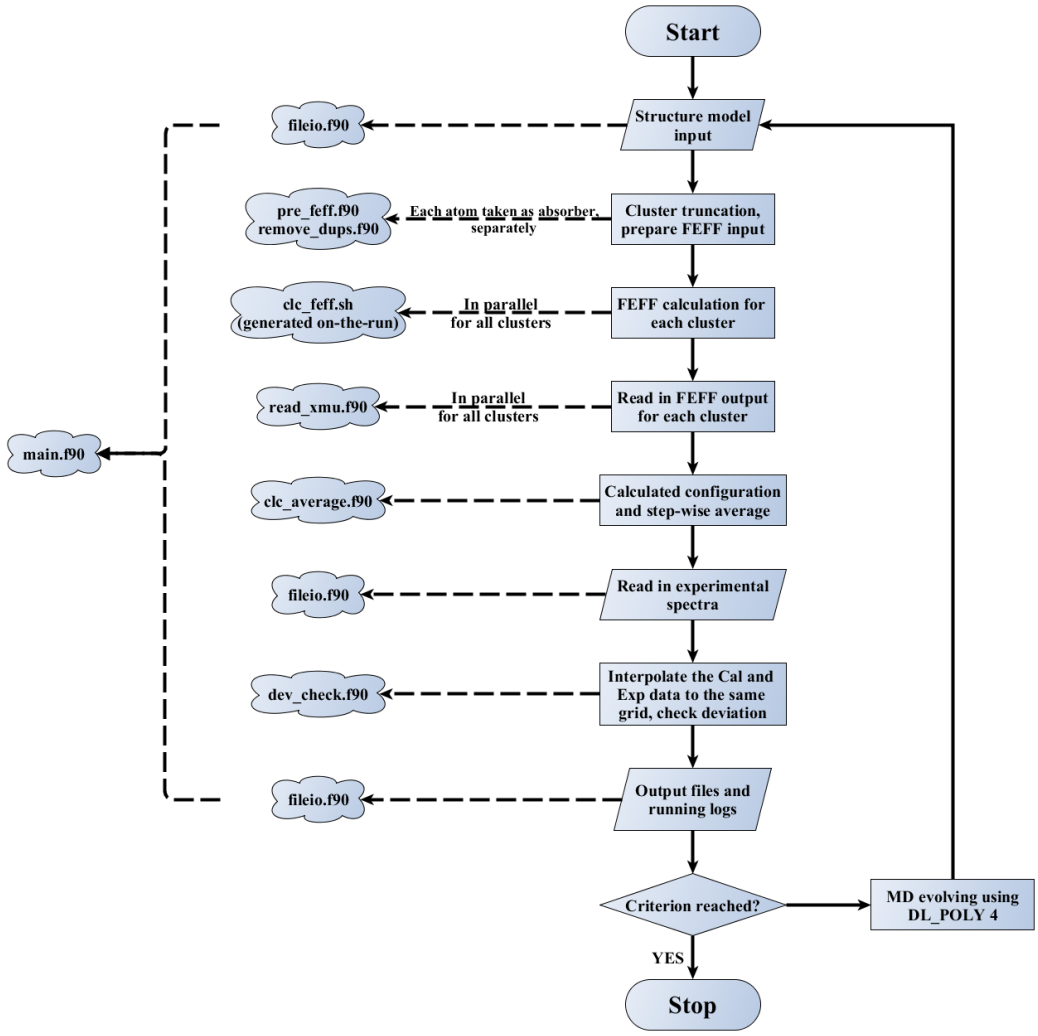

Fig. E.1 The flowchart of MD2FEFF code.

- remove_dups.f90 → Ref. [4]
- read_xmu.f90 → Ref. [5]
- clc_average.f90 → Ref. [6]
- dev_check.f90 → Ref. [7]
- defs.h → Ref. [8]

As mentioned above, an external Fortran interpolation library is used by the MD2FEFF code. Here the library related files/programs are compressed into a tarball which can be

downloaded here: [9]. Following are the descriptions for each file contained in the above tarball:

- interp.f90 → The main interpolation library file.
- interp.sh → The script for configuring and installing the library.
- f90split → A program responsible for splitting the 'interp.f90' file to separate program files, which will be compiled to obtain the final binary library file that can be directly called by the MD2FEFF code. The program will be called within the 'interp.sh' script.
- readme.txt → Licence and library source information, configuration guidance, etc.

For the compiling of the MD2FEFF code, a 'Makefile' was prepared so one can just type 'make' on command line (under Unix-like platform only) to get the executable 'MD2FEFF' program. Here is the link for the prepared 'Makefile': [10]. It should be pointed out that the path for the interpolation library specified in the 'Makefile' should be changed according to configuration specified in the 'interp.sh' file given above.

References

[1] main.f90. http://paste.ubuntu.com/16599723/. online; accessed 08-July-2016.

[2] fileio.f90. http://paste.ubuntu.com/16599824/. online; accessed 08-July-2016.

[3] pre_feff.f90. http://paste.ubuntu.com/16599787/. online; accessed 08-July-2016.

[4] remove_dups.f90. http://paste.ubuntu.com/16599846/. online; accessed 08-July-2016.

[5] xmu_read.f90. http://paste.ubuntu.com/16599867/. online; accessed 08-July-2016.

[6] clc_average.f90. http://paste.ubuntu.com/16599909/. online; accessed 08-July-2016.

[7] dev_check.f90. http://paste.ubuntu.com/16599888/. online; accessed 08-July-2016.

[8] defs.h. http://paste.ubuntu.com/16599948/. online; accessed 08-July-2016.

[9] Fortran interpolation library. https://www.dropbox.com/s/w5m6xhgi8320j04/interp_lib.tar.gz?dl=0. online; accessed 08-July-2016.

[10] Makefile. http://paste.ubuntu.com/16599973/. online; accessed 08-July-2016.